

**WYDZIAŁ INŻYNIERII  
MATERIAŁOWEJ  
POLITECHNIKA WARSZAWSKA  
UL. WOŁOSKA 141A  
02-507 WARSZAWA**

za pośrednictwem:  
**Rady Doskonałości Naukowej**  
pl. Defilad 1  
00-901 Warszawa  
(Pałac Kultury i Nauki, p. XXIV, pok. 2401)

**ANNA DOBKOWSKA**  
Wydział Inżynierii Materiałowej  
Politechnika Warszawska

## **Wniosek**

z dnia 29.01.2025

o przeprowadzenie postępowania w sprawie nadania stopnia doktora  
habilitowanego w dziedzinie **nauk inżynieryjno – technicznych** w dyscyplinie  
**inżynieria materiałowa**

Wnoszę – na podstawie art. 221 ust. 10 ustawy z dnia 20 lipca 2018 r. Prawo o  
szkolnictwie wyższym i nauce (Dz. U. z 2021 r. poz. 478 zm.) – aby komisja habilitacyjna  
podejmowała uchwałę w sprawie nadania stopnia doktora habilitowanego w głosowaniu  
**tajnym/jawnym**\*<sup>1</sup>

*Zostałem poinformowany, że:*

*Administratorem w odniesieniu do danych osobowych pozyskanych w ramach postępowania w  
sprawie nadania stopnia doktora habilitowanego jest Przewodniczący Rady Doskonałości  
Naukowej z siedzibą w Warszawie (pl. Defilad 1, XXIV piętro, 00-901 Warszawa).*

*Kontakt za pośrednictwem e-mail: [kancelaria@rdn.gov.pl](mailto:kancelaria@rdn.gov.pl) , tel. 22 656 60 98 lub w siedzibie  
organu. Dane osobowe będą przetwarzane w oparciu o przesłankę wskazaną w art. 6 ust. 1 lit.  
c) Rozporządzenia UE 2016/679 z dnia z dnia 27 kwietnia 2016 r. w związku z art. 220 - 221  
oraz art.*

*232 – 240 ustawy z dnia 20 lipca 2018 roku - Prawo o szkolnictwie wyższym i nauce, w  
celu*

*przeprowadzenie postępowania o nadanie stopnia doktora habilitowanego oraz realizacji praw i  
obowiązków oraz środków odwoławczych przewidzianych w tym postępowaniu.*

*Szczegółowa informacja na temat przetwarzania danych osobowych w postępowaniu dostępna  
jest na stronie [www.rdn.gov.pl/klauzula-informacyjna-rodo.html](http://www.rdn.gov.pl/klauzula-informacyjna-rodo.html)*

*Anna Dobkowska.....*  
(podpis wnioskodawcy)

---

<sup>1</sup> \* Niepotrzebne skreślić.

Załączniki:

Załącznik 1: Dane wnioskodawcy w języku polskim

Załącznik 2: Kopia dokumentu potwierdzającego posiadanie stopnia doktora

Załącznik 3: Autoreferat w języku polskim

Załącznik 4: Publikacje A1-A7

Załącznik 5: Oświadczenia współautorów o ich zakresie prac w publikacjach współautorskich

Załącznik 6: Wykaz osiągnięć naukowych albo artystycznych, stanowiący znaczny wkład w rozwój określonej dyscypliny w języku polskim

Załącznik 7: Publikacja potwierdzająca inne osiągnięcia naukowe dotycząca wytwarzania proszków ze stopów Mg niedostępnych w sprzedaży komercyjnej

Załącznik 8: Potwierdzenie zgłoszenia patentowego P.437777

Załącznik 9: Publikacja potwierdzająca inne osiągnięcia naukowe dotycząca opisu odporności powłok miedzianych stosowanych na kontenerach stalowych do składowania odpadów radioaktywnych w zależności od metod ich wytwarzania

Załącznik 10: Potwierdzenie zatrudnienia w University of Western Ontario na stanowisku Postdoctoral Associate (post doc); dokument w języku angielskim

Załącznik 11: Potwierdzenie uzyskania międzynarodowych kwalifikacji akademickich (International Academic Qualifications, World Educational Services); dokument w języku angielskim

Załącznik 12: Dokumenty potwierdzające kierowanie projektami

Dane wnioskodawcy w języku polskim

## Dane wnioskodawcy

1. Imię i Nazwisko: Anna Dobkowska
2. Miejsce pracy: Wydział Inżynierii Materiałowej, Politechnika Warszawska
3. Adres korespondencyjny: [REDACTED]
4. Nr telefonu: +4 [REDACTED]
5. Adres e-mail: anna.dobkowska@pw.edu.pl
6. Numer PESEL: [REDACTED]



(podpis wnioskodawcy)

Autoreferat w języku polskim

## Spis treści

1. Imię i nazwisko .....	2
2. Posiadane dyplomy, stopnie naukowe lub artystyczne – z podaniem podmiotu nadającego stopień, roku ich uzyskania oraz tytułu rozprawy doktorskiej.....	2
3. Informacja o dotychczasowym zatrudnieniu w jednostkach naukowych lub artystycznych	2
4. Omówienie osiągnięć, o których mowa w art. 219 ust. 1 pkt. 2 ustawy z dnia 20 lipca 2018 r. Prawo o szkolnictwie wyższym i nauce (Dz. U. z 2021 r. poz. 478 z późn. zm.). Omówienie to winno dotyczyć merytorycznego ujęcia przedmiotowych osiągnięć, jak i w sposób precyzyjny określać indywidualny wkład w ich powstanie, w przypadku, gdy dane osiągnięcie jest dziełem współautorskim, z uwzględnieniem możliwości wskazywania dorobku z okresu całej kariery zawodowej.....	3
4.1. Tytuł osiągnięcia naukowego.....	3
4.2. Wykaz publikacji stanowiących osiągnięcie naukowe .....	3
4.3. Omówienie celu naukowego cyklu artykułów i osiągniętych wyników wraz z omówieniem ich potencjalnego zastosowania.....	7
4.3.1. Wprowadzenie.....	7
4.3.2. Cel naukowy.....	12
4.3.3. Materiały do badań.....	12
4.3.4. Metodyka prac badawczych.....	14
4.3.5. Wpływ rozdrobnienia mikrostruktury na odporność korozyjną czystego technicznie Mg odkształcanego metodą KoBo bez nagrzewania materiału wsadowego	16
4.3.6. Wpływ tekstury i wydzielen typy $\beta$ -Mg <sub>17</sub> Al <sub>12</sub> na odporność korozyjną stopów z serii Mg-Al-Zn odkształczanych metodą KoBo.....	20
4.3.7. Wpływ mikrostruktury jednofazowej $\alpha$ (Mg) oraz dwufazowej $\alpha$ (Mg) + $\beta$ (Li) na odporność korozyjną stopów na bazie Mg z dodatkiem Li odkształczanych metodą KoBo	23
4.3.8. Wpływ rozdrobnienia ziarna oraz wydzielen faz wtórnych na odporność korozyjną stopów z serii Mg-Y-RE po odkształceniu tradycyjnym i metodą KoBo przy różnych stopniach wyciskania.....	25
4.3.9. Analiza porównawcza czynników mikrostrukturalnych wpływających na odporność korozyjną czystego Mg, stopów z serii Mg-Zn-Al, Mg-Li oraz Mg-Y-RE ...	29
4.3.10. Podsumowanie .....	33
4.3.11. Wkład w rozwój dyscypliny.....	35
5. Informacja o wykazywaniu się istotną aktywnością naukową albo artystyczną realizowaną w więcej niż jednej uczelni, instytucji naukowej lub instytucji kultury, w szczególności zagranicznej.....	39
6. Informacja o osiągnięciach dydaktycznych, organizacyjnych oraz popularyzujących naukę lub sztukę.....	40
7. Oprócz kwestii wymienionych w pkt. 1-6, wnioskodawca może podać inne informacje, ważne z jego punktu widzenia, dotyczące jego kariery zawodowej. ....	41
Literatura do rozdziału 4 .....	46

### **1. Imię i nazwisko**

Anna Dobkowska

### **2. Posiadane dyplomy, stopnie naukowe lub artystyczne – z podaniem podmiotu nadającego stopień, roku ich uzyskania oraz tytułu rozprawy doktorskiej**

- 17.09.2017 Politechnika Warszawska, Wydział Inżynierii Materiałowej  
Stopień naukowy Doktora Nauk Technicznych w dziedzinie nauk technicznych, w dyscyplinie Inżynierii Materiałowa

Tytuł rozprawy doktorskiej: „Odporność korozyjna stopów Mg-Li”

Promotor: prof. dr hab. inż. Jarosław Mizera, Wydział Inżynierii Materiałowej Politechnika Warszawska

Promotor pomocniczy: dr inż. Bogusława Adamczyk-Cieślak, Wydział Inżynierii Materiałowej Politechnika Warszawska

Recenzent: dr hab. inż. Łukasz Kaczmarek, prof. nadzw. PŁ, Politechnika Łódzka Wydział Mechaniczny, Instytut Inżynierii Materiałowej

Recenzent: dr hab. inż. Maria Sozańska, prof. nzw. Pol. Śl., Politechnika Śląska, Instytut Nauki o Materiałach

- 9.12.2011 Tytuł zawodowy magister inżyniera, Politechnika Warszawska, Wydział Inżynierii Materiałowej, kierunek Inżynieria Materiałowa, specjalność: nanomateriały i nanotechnologie

Tytuł pracy magisterskiej: „Odporność korozyjna stopów aluminium-lit w zależności od stopnia zgniotu”

Promotor: dr hab. inż. Joanna Zdunek, prof. PW

- 8.02.2010 Tytuł zawodowy inżyniera, Politechnika Warszawska, Wydział Inżynierii Materiałowej, kierunek Inżynieria Materiałowa

Tytuł pracy inżynierskiej: „Nanokompozytowe warstwy Ni/Si<sub>3</sub>N<sub>4</sub> wytwarzane metodą elektrochemiczną”

Promotor: prof. nzw. dr inż. Maria Trzaska

### **3. Informacja o dotychczasowym zatrudnieniu w jednostkach naukowych lub artystycznych**

Od 02.11.2017 Politechnika Warszawska. Wydział Inżynierii Materiałowej

Zajmowane stanowiska:

- 01.02.2024 – obecnie  
Adiunkt w grupie pracowników badawczo-dydaktycznych w Zakładzie Projektowania Materiałów
- 01.02.2022 – 31.01.2024

- Adiunkt w grupie pracowników badawczych w Zakładzie Projektowania Materiałów
- 01.07.2020 – 31.01.2022  
Technolog w Zakładzie Projektowania Materiałów
- 02.11.2017 – 01.06.2018  
Technolog w Zakładzie Projektowania Materiałów

**01.06.2018-30.05.2020** Postdoctoral Fellowship, Chemistry Department, The University of Western Ontario, London, Ontario, Kanada

- Realizacja badań w ramach projektu “Defining Cu coating specifications - effect of impurities on copper corrosion behaviour” współfinansowanego przez Nuclear Waste Management Organization, Toronto, Kanada. Wsparcie działu inżynierskiego w Nuclear Waste Management Organization, Toronto, Kanada.

**4. Omówienie osiągnięć, o których mowa w art. 219 ust. 1 pkt. 2 ustawy z dnia 20 lipca 2018 r. Prawo o szkolnictwie wyższym i nauce (Dz. U. z 2021 r. poz. 478 z późn. zm.). Omówienie to winno dotyczyć merytorycznego ujęcia przedmiotowych osiągnięć, jak i w sposób precyzyjny określać indywidualny wkład w ich powstanie, w przypadku, gdy dane osiągnięcie jest dziełem współautorskim, z uwzględnieniem możliwości wskazywania dorobku z okresu całej kariery zawodowej**

Jako osiągnięcie naukowe wynikające z art. 219 ust. 1 pkt. 2 ustawy z dnia 20 lipca 2018r. Prawo o szkolnictwie wyższym i nauce (Dz. U. z 2021r. poz. 478 z późn. zm.) i stanowiące podstawę ubiegania się o uzyskanie stopnia naukowego doktora habilitowanego wskazuję cykl powiązanych tematycznie 7 publikacji naukowych.

**4.1. Tytuł osiągnięcia naukowego**

**Wpływ mikrostruktury na kształtowanie odporności korozyjnej Mg i jego stopów odkształczanych metodą wyciskania współbieżnego z oscylującą matrycą**

**4.2. Wykaz publikacji stanowiących osiągnięcie naukowe**

Poniżej przedstawiam cykl powiązanych tematycznie 7 publikacji naukowych. Dla każdej publikacji wskazano całkowitą liczbę cytowań wg. bazy Web of Science (Z<sub>wos</sub>) i Scopus (Z<sub>s</sub>) - w nawiasach liczba cytowań po odliczeniu cytowań własnych, impact factor (IF) czasopisma obowiązujący w roku opublikowania artykułu (w przypadku roku 2022 wskazano dane za rok 2021), oraz liczbę punktów zgodnie z listą Ministerstwa Nauki i Szkolnictwa Wyższego obowiązującą w roku opublikowania artykułu. Dla artykułów opublikowanych w roku 2024 podano dane za rok 2024 wg wykazu czasopism naukowych opublikowanego przez Ministra Nauki 5 stycznia 2024. **We wszystkich przedstawionych publikacjach jestem pierwszym autorem.** Sumaryczny IF cyklu publikacji wynosi 43,7.

---

[A1] **A. Dobkowska**, B. Adamczyk-Cieślak, M. Gonzalez, W. Bednarczyk, J. Gubicza, P. Jenei, K. Mukhartova, M. Tkocz, D. Kuc, J. Mizera, Effect of high deformation ratios without preheating of the initial billet using KoBo, *Metals* 2024, 14, 949. <https://doi.org/10.3390/met14080949>

Zwos: 0(0) Zs:0(0) **IF 2,6; 70 pkt MNiSW**

Mój wkład w powstanie publikacji polegał na opracowaniu koncepcji badań, przygotowaniu przeglądu literaturowego, zaplanowaniu eksperymentów i dobór metod badawczych, przeprowadzeniu i analizie badań korozyjnych, wykonaniu pomiarów EBSD oraz obserwacji zniszczeń korozyjnych. Następnie przygotowałam pierwszą wersję tekstu manuskryptu, zinterpretowałam wyniki badań, opracowałam je graficznie. Przeprowadziłam dyskusję wyników. W trakcie recenzji przygotowałam odpowiedzi dla recenzentów, edytowałam manuskrypt i przygotowałam jego ostateczną wersję.

---

[A2] **A. Dobkowska**, B. Adamczyk-Cieślak, M. Chlewicka, A. Towarek, A. Zielińska, M. Koralnik, D. Kuc, J. Mizera, Evolution of microstructure dependent corrosion properties of ultrafine AZ31 under conditions of extrusion with a forward backward oscillating die, *J. Mater. Res. Technol.* 18 (2022) 4486–4496. <https://doi.org/10.1016/j.jmrt.2022.04.131>

Zwos: 5(2) Zs:6(4) **IF 6,2; 100 pkt MNiSW**

W artykule pełniłam rolę autora wiodącego. Opracowałam koncepcję badań, wykonałam i przeanalizowałam wyniki badań korozyjnych, policzyłam szybkość korozji materiałów oraz opracowałam wyniki obserwacji mikroskopowych zniszczeń korozyjnych. Przygotowałam wstępną wersję manuskryptu, opracowałam wyniki graficznie, wysnułam wnioski. W trakcie recenzji przygotowałam odpowiedzi dla recenzentów, edytowałam manuskrypt i przygotowałam jego ostateczną wersję.

---

[A3] **A. Dobkowska**, A. Zielińska, I. Paulin, Č. Donik, M. Łojkowski, M. Koralnik, B. Adamczyk-Cieślak, K. Paradowski, M. Tkocz, D. Kuc, J. Kubasek, M. Godec, W. Świążkowski, Microstructure and properties of an AZ61 alloy after extrusion with a forward-backward oscillating die without preheating of the initial billet, *J. Alloys Compd.* (2023) 169843. <https://doi.org/10.1016/j.jallcom.2023.169843>

Zwos: 3(3) Zs:6(2) IF 5,8; 100 pkt MNiSW

Mój wkład w powstanie publikacji polegał na opracowaniu koncepcji badań, przygotowaniu przeglądu literaturowego, zaplanowaniu eksperymentów i dobór metod badawczych, przeprowadzeniu i analizie badań korozyjnych oraz wykonaniu obserwacji zniszczeń korozyjnych. Zaplanowałam i zorganizowałam badania mikrostrukturalne we współpracy z naukowcami z jednostek zagranicznych, w tym z Institute of Metals and Technology, Słowenia oraz z University of Chemistry and Technology, Praga, Czechy. Następnie przygotowałam pierwszą wersję tekstu manuskryptu, zestawiałam i zinterpretowałam wyniki badań, opracowałam je graficznie. Przeprowadziłam dyskusję wyników. W trakcie recenzji przygotowałam odpowiedzi dla recenzentów, edytowałam manuskrypt i przygotowałam jego ostateczną wersję.

---

[A4] A. Dobkowska, M. Korallnik, B. Adamczyk-Cieślak, D. Kuc, W. Chromiński, J. Kubasek, J. Mizera, The Effect of Extrusion Ratio on the Corrosion Resistance of Ultrafine-Grained Mg-4Li-3Al-Zn Alloy Deformed Using Extrusion with a Forward-Backward Oscillating Die, J. Mater. Eng. Perform. (2022). <https://doi.org/10.1007/s11665-022-06895-1>

Zwos: 6(4) Zs:6(4) IF 2,2; 70 pkt MNiSW

Mój wkład w powstanie publikacji polegał na opracowaniu koncepcji badań, przygotowaniu przeglądu literaturowego, zaplanowaniu eksperymentów i dobór metod badawczych, przeprowadzeniu i analizie badań korozyjnych oraz wykonaniu obserwacji zniszczeń korozyjnych. Przeprowadziłam pomiary EBSD. Przygotowałam pierwszą wersję tekstu manuskryptu, zestawiałam i zinterpretowałam wyniki badań, opracowałam je graficznie. Przeprowadziłam dyskusję wyników. W trakcie recenzji przygotowałam odpowiedzi dla recenzentów, edytowałam manuskrypt i przygotowałam jego ostateczną wersję.

---

[A5] A. Dobkowska, B. Adamczyk – Cieślak, M. Korallnik, W. Chromiński, J. Kubasek, J. Ciftci, D. Kuc, J. Mizera, Corrosion behavior of fine-grained Mg-7.5Li-3Al-1Zn fabricated by extrusion with a forward-backward rotating die (KoBo), J. Magnes. Alloy. 10 (2022) 811–820. <https://doi.org/10.1016/j.jma.2021.08.020>

Zwos: 29(21) Zs:33(27) IF 17,6; 100 pkt MNiSW

Mój wkład w powstanie publikacji polegał na opracowaniu koncepcji badań, przygotowaniu przeglądu literaturowego, zaplanowaniu eksperymentów i dobór metod badawczych, przeprowadzeniu i analizie badań korozyjnych oraz wykonaniu obserwacji zniszczeń korozyjnych. Przygotowałam pierwszą wersję tekstu manuskryptu, zestawiałam i zinterpretowałam wyniki badań, opracowałam je graficznie. Przeprowadziłam dyskusję wyników. W trakcie recenzji przygotowałam odpowiedzi dla recenzentów, edytowałam manuskrypt i przygotowałam jego ostateczną wersję.

---

**[A6] A Dobkowska, A. Zielińska, I. Paulin, C. Donik, M. Korallnik, B. Adamczyk-Cieślak, M. Wieczorek-Czarnecka, D. Kuc, J. Kubasek, T. Mikuszewski, M. Godec, J. Mizera, Microstructural, corrosion and mechanical properties of a WE43 alloy : conventional extrusion versus SPD, J. Alloys Compd. 976 (2024). <https://doi.org/10.1016/j.jallcom.2023.173090>**

Zwos: 2(1) Zs:2(1) IF 6,2; 100 pkt MNiSW

Mój wkład w powstanie publikacji polegał na opracowaniu koncepcji badań, przygotowaniu przeglądu literaturowego, zaplanowaniu eksperymentów i dobór metod badawczych, przeprowadzeniu i analizie badań korozyjnych oraz wykonaniu obserwacji zniszczeń korozyjnych. Zaplanowałam i zorganizowałam badania mikrostrukturalne we współpracy z naukowcami z jednostek zagranicznych, w tym z Institute of Metals and Technology, Słowenia oraz z University of Chemistry and Technology, Praga, Czechy. Następnie przygotowałam pierwszą wersję tekstu manuskryptu, zestawiałam i zinterpretowałam wyniki badań, opracowałam je graficznie. Przeprowadziłam dyskusję wyników. W trakcie recenzji przygotowałam odpowiedzi dla recenzentów, edytowałam manuskrypt i przygotowałam jego ostateczną wersję.

---

**[A7] A. Dobkowska, J. Kubasek, On the possibility of the deformation of Mg and alloys without preheating of initial billets: understanding their corrosion performance via electrochemical tests, Materials (Basel). 17 (2024) 1–10. <https://doi.org/doi.org/10.3390/ma17246182>**

Zwos: 0(0) Zs:0(0) IF 3,1; 140 pkt MNiSW

Mój wkład w opracowanie artykułu wynosi 80%: opracowałam koncepcję artykułu oraz zaplanowałam i zrealizowałam badania odporności korozyjnej metodami elektrochemicznymi. Następnie przygotowałam pierwszą wersję tekstu manuskryptu, zestawiałam i zinterpretowałam

wyniki badań, opracowałam je graficznie. Przeprowadziłam dyskusję wyników. W trakcie recenzji przygotowałam odpowiedzi dla recenzentów, edytowałam manuskrypt i przygotowałam jego ostateczną wersję.

Publikacje [A1-A7] zestawiałam w **Załączniku 4**, zaś oświadczenia współautorów o ich zakresie prac w publikacjach współautorskich zawarłam w **Załączniku 5**.

### **4.3. Omówienie celu naukowego cyklu artykułów i osiągniętych wyników wraz z omówieniem ich potencjalnego zastosowania**

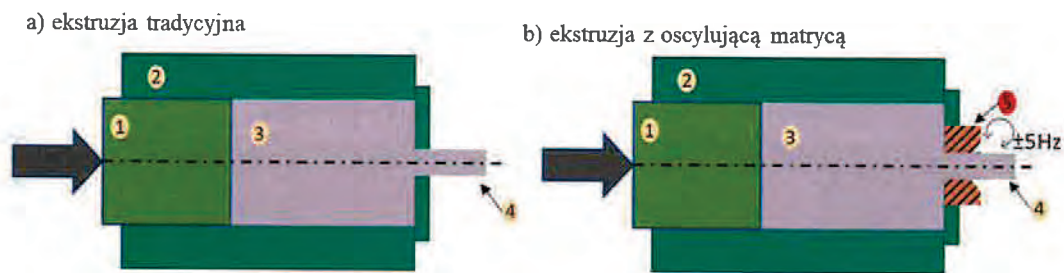
#### **4.3.1. Wprowadzenie**

Rosnące zainteresowanie magnezem (Mg) i jego stopami wynika z połączenia dwóch kluczowych właściwości tych materiałów – niskiej masy z dobrymi właściwościami mechanicznymi. Dzięki takiej kombinacji właściwości, Mg i jego stopy mają ogromny potencjał w zastosowaniu do projektowania lekkich konstrukcji inżynierskich wraz z zachowaniem odpowiednich właściwości mechanicznych. Niższy ciężar konstrukcji bądź systemów inżynierskich obniża znacznie koszty zużycia energii, co jest obecnie priorytetem gospodarczym zgodnym z wytycznymi zrównoważonego rozwoju.

**Należy jednak podkreślić, że szerokie zastosowanie Mg i jego stopów jest ograniczone z powodu licznych blokad technologicznych, z których najważniejsze są wysokie koszty przerobu oraz, w porównaniu do stopów aluminium, niska odporność korozyjna. Z punktu widzenia nauki są to kluczowe zagadnienia, których poznanie pozwoli na przełamanie barier stojących na drodze szerokiego zastosowania Mg i jego stopów. Dogłębne poznanie czynników kształtujących zachowanie korozyjne tych materiałów przyczyni się do rozwoju obszaru inżynierii materiałowej, w której kluczowym wątkiem badawczym jest określenie decydujących czynników determinujących właściwości korozyjne materiałów lekkich o strukturze heksagonalnej odkształcanych bez wstępnego nagrzewania materiału odkształcanego, co do tej pory nie było rozpoznane.**

Mg i jego stopy krystalizują w sieci heksagonalnej, przez co liczba niezależnych systemów poślizgu aktywowanych w temperaturze pokojowej jest ograniczona [1,2]. To z kolei uniemożliwia odkształcenie tych materiałów bez nagrzewania materiału wsadowego, generując wysokie koszty wytwarzania. W związku z tym poszukiwane są nowe technologie, które w sposób znaczący mogą ograniczyć koszty, ale także i czas produkcji. Jedną z takich metod jest wyciskanie współbieżne z oscylującą matrycą umieszczoną na końcu ekstrudera (tzw. metoda KoBo). Metoda KoBo została opracowana w latach 90-tych, a jej odkrywcami

są prof. Włodzimierz Bochniak z Wydziału Metali Nieżelaznych i prof. Andrzej Korbel z Wydziału Inżynierii Mechanicznej i Robotyki, Akademii Górniczo-Hutniczej im. Stanisława Staszica w Krakowie (stąd nazwa metody KoBo) [3]. KoBo łączy w sobie cechy odkształcania konwencjonalnego z oscylacjami wprowadzonymi przez ruch rewersyjny matrycy pod ustalonym kątem i z określoną częstotliwością, co w konsekwencji pozwala na wyciskanie materiałów w warunkach trwałej destabilizacji mikrostruktury, tj. poprzez zastosowanie dużej szybkości odkształcenia, w wyniku której powstaje mikrostruktura drobnoziarnista (o wielkości ziarna poniżej kilku  $\mu\text{m}$ ) [4]. Na rys. 1a przedstawiono schemat konwencjonalnej metody wyciskania oraz schemat wyciskania współbieżnego z oscylującą matrycą (rys. 1b). Metoda wyciskania współbieżnego z oscylującą matrycą jest nowatorska i pozwala na wyciskanie metali trudno-odkształcalnych bez zastosowania układu grzewczego [5–7]. Cykliczne obustronne skręcanie wyciskanego metalu wprowadza go w stan płynięcia plastycznego, dzięki czemu odkształcenie metalu o strukturze heksagonalnej jest możliwe bez uprzedniego nagrzewania wsadu [8,9].



Rysunek 1. Porównanie schematów metod wyciskania: a) tradycyjnego, b) z oscylującą matrycą (1- stempel 2 – tuleja ekstrudera, 3 – materiał preciskany, 4 – materiał przeciśnięty, 5 – oscylująca matryca) [A6]

Dotychczas metodą KoBo preciskano m. in. stopy Al [10], Ti [11], Zn [12], oraz dwufazowe stopy z serii MgLiAl [5]. Dostępne dane literaturowe skupiają się na opisie mikrostruktury po procesie KoBo i jej wpływu na właściwości mechaniczne materiałów, bądź na wpływie odkształcenia plastycznego w trakcie wyciskania KoBo na procesy wydzieleniowe. Badania wykazały, że właściwości mechaniczne stopów odkształcanych KoBo w stosunku do ich odpowiedników odkształcanych konwencjonalnie są dużo wyższe. Przykładem jest Zn, którego granica plastyczności i wytrzymałości na rozciąganie po wyciskaniu metodą KoBo wzrosła odpowiednio o 67% i 37% w porównaniu do prętów wyciskanych konwencjonalnie [12]. W pracy [A6] wykazałam, że wartość granicy plastyczności dla stopu WE43 wyciskanego metodą KoBo wzrosła 3-krotnie, oraz odnotowałam 1,5-krotny wzrost wytrzymałości na rozciąganie w porównaniu do materiału wyciskanego tradycyjnie w temperaturze 400 °C.

Według mojej wiedzy, nie ma dostępnych danych literaturowych, które opisują właściwości korozyjne metali i ich stopów odkształcanych metodą KoBo bez uprzedniego nagrzewania materiału odkształcanego.

Jak już wspomniałam, czynnikiem ograniczającym szerokie zastosowanie Mg i jego stopów jest ich niska odporność korozyjna w porównaniu do innych materiałów konstrukcyjnych. Mg jest pierwiastkiem aktywnym chemicznie, posiada potencjał standardowy  $-2.737\text{ V vs SHE}$ , co świadczy o jego wysokiej aktywności elektrochemicznej. Mg ulega pasywacji, w kontakcie z powietrzem pokrywa się cienką warstwą tlenku magnezu MgO lub wodorotlenku magnezu  $\text{Mg(OH)}_2$ , co częściowo chroni go przed postępującymi reakcjami korozyjnymi. Ze względu na ilość i różnorodność czynników, które wpływają na zachowanie korozyjne Mg i jego stopów, podwyższenie odporności korozyjnej tych materiałów jest jednym z najbardziej skomplikowanych i wymagających rozwiązania problemów współczesnej inżynierii materiałowej. Zachowaniem korozyjnym Mg i jego stopów można sterować dwutorowo: i) poprzez zmianę składu chemicznego oraz ii) modyfikację mikrostruktury. W przedstawionym cyklu publikacji rozważałam nie tylko wpływ modyfikacji mikrostruktury metodą KoBo na odporność korozyjną Mg i jego stopów, ale równolegle badałam, w jaki sposób, zmiana składu chemicznego kształtuje ich zachowanie w środowisku korozyjnym. Symultaniczne oddziaływanie czynników mikrostrukturalnych i składu chemicznego na odporność na korozję Mg i jego stopów odkształcanych metodą KoBo, pozwoliło na określenie najkorzystniejszych rozwiązań w kontekście przyszłych zastosowań tych materiałów.

Rozważania na temat odporności korozyjnej Mg i jego stopów warto rozpocząć od wyróżnienia czynników wpływających na kształtowanie odporności korozyjnej materiałów polikrystalicznych. **Należy podkreślić, że opisany w cyklu publikacji problem badawczy jest złożony ze względu na mnogość czynników mikrostrukturalnych, które mają kluczowy wpływ na ukształtowanie zachowania korozyjnego stopów Mg w danych warunkach badawczych bądź eksploatacyjnych.** Wśród nich wyróżnia się: wielkość ziarna, gęstość dyslokacji, teksturę, typ, rozmiar i rozmieszczenie wydzieleń drugiej fazy. **Kluczowe w moich badaniach było określenie korelacji mikrostruktura – odporność korozyjna Mg i jego stopów po odkształceniu stosując wysoki stopień odkształcenia bez nagrzewania materiału odkształcanego.** W moim podejściu innowacją jest kompleksowe podejście i określenie, jak mikrostruktura wpływa na zachowanie korozyjne Mg i jego stopów odkształcanych bez nagrzewania wsadu, co do tej pory nie było rozeznane i szczegółowo analizowane.

Istnieją prace badawcze, które definiują wpływ wielkości ziarna na odporność czystego Mg odkształcanego metodami „na gorąco”. Op't Hoog i wsp. [13] wykazali, że rozdrobnienie ziarna w czystym Mg poddanym procesowi przeciskania przez kanał kątowy (z ang. *equal channel angular pressing, ECAP*) podwyższa jego odporność na korozję. Gollapudi [14] potwierdził ich doniesienia, i udowodnił, że w przypadku czystego Mg, rozdrobnienie mikrostruktury przyspiesza oraz intensyfikuje kinetykę reakcji pasywacji. Opublikowano również prace badawcze, które jasno wskazują, że rozdrobnienie mikrostruktury poprzez kilkukrotne przeciskanie przez kanał kątowy zmniejsza wielkość ziarna z ok 800  $\mu\text{m}$  do ok 50  $\mu\text{m}$ , co wpływa na obniżenie odporności korozyjnej czystego Mg poprzez tworzenie się wyższej ilości defektów krystalicznych w postaci granic ziaren, które są miejscami inicjacji procesów korozyjnych [15,16]. Kolejnym istotnym czynnikiem wpływającym na odporność na korozję materiałów polikrystalicznych jest obecność wydzielen obcych faz. W przypadku stopów z serii Mg-Al-Zn (AZXX) odporność na korozję można podwyższyć poprzez obecność wydzielen typu  $\beta\text{-Mg}_{17}\text{Al}_{12}$  bądź obecność fazy AlMn [17,18]. Dlatego zasadnym jest przypuszczać, że metody dużego odkształcenia plastycznego, poprzez podział lub jednorodne rozmieszczanie cząstek drugiej fazy, mogą być efektywnym procesem podwyższenia odporności korozyjnej stopów z serii AZXX. Warto jednak zwrócić uwagę, że rola wydzielen  $\beta\text{-Mg}_{17}\text{Al}_{12}$  w kształtowaniu mechanizmów korozyjnych w stopach Mg nie jest jeszcze do końca poznana i zdefiniowania, gdyż zależy ona od wielu czynników, m. in. takich jak fragmentacja i rozmieszczenie fazy w osnowie [19–21]. Wyniki niektórych prac wskazują na pozytywny efekt występowania fazy  $\beta\text{-Mg}_{17}\text{Al}_{12}$  zmniejszając aktywność elektrochemiczną mechanizmów korozji i tworząc barierę przed ich rozprzestrzenianiem się [22–25]. W innych pracach dowiedziono, że faza  $\beta\text{-Mg}_{17}\text{Al}_{12}$  posiada inny potencjał niż otaczająca osnowa intensyfikując powstawanie reakcji mikro-galwanicznych [26].

Najniższą masą właściwą pośród materiałów na osnowie Mg cechują się stopy z dodatkiem Li, którego ilość może obniżyć gęstość Mg aż do 1.3  $\text{g}/\text{cm}^3$  [27]. W zależności od zawartości Li, wyróżnia się stopy o budowie jednofazowej  $\alpha(\text{Mg})$  zawierające do 5,5 % mas. Li, stopy dwufazowe o strukturze  $\alpha(\text{Mg})+\beta(\text{Li})$  i zawartości Li pomiędzy 5,5 a 10,8 % mas., zaś dodatek powyżej 10,8 % mas. Li kształtuje stopy o budowie jednofazowej typu  $\beta(\text{Li})$  [28]. Istotnym jest, że Li podwyższa formowalność stopów Mg już w temperaturze otoczenia [29], ale może obniżać ich odporność korozyjną. Ze względu na to, że dodatek Li do stopów Mg może powodować powstawanie wielu różnych, w tym metastabilnych faz, ich zachowanie korozyjne nie jest poznane. Jeszcze bardziej skomplikowanym zjawiskiem jest korozja stopów Mg-Li o strukturze dwufazowej  $\alpha(\text{Mg})+\beta(\text{Li})$ . Dzięki niskiej masie oraz zaskakująco dobrej

podatności do odkształcenia plastycznego dwufazowe stopy Mg-Li stanowią doskonałą alternatywę dla tradycyjnych stopów na osnowie Mg [30,31]. Do tej pory zastosowano różne metody poprawy ich odporności na korozję, np. wyciskanie w temperaturze 300 °C i 350 °C [32], stopowanie dodatkiem Sn [33], Y [34] bądź Gd [35]. Dodatek 3 % mas. Al do stopów Mg-Li o budowie jednofazowej  $\alpha(\text{Mg})$ , dzięki formowaniu się wydzielen  $\text{Al}_3\text{Li}$  podwyższa ich właściwości mechaniczne, ale obecność tych wydzielen sprzyja formowaniu korozji mikro-galwanicznej [36]. Dodatek Ca do stopów Mg-Li powoduje wydzielanie się fazy typu  $\text{Mg}_2\text{Ca}$ , której obecność w odniesieniu do właściwości korozyjnych jest kontrowersyjna. Z jednej strony jest to czynnik zwiększający szybkość korozji [37], z drugiej zaś może blokować postępujące reakcje korozyjne [38,39].

Stopy Mg-Y-RE z dodatkiem pierwiastków ziem rzadkich (z ang. rare earth, RE) są stopami o wysokiej wytrzymałości i odporności na korozję w podwyższonej temperaturze [40]. Wydzielenia zawierające pierwiastki ziem rzadkich są stabilne termodynamicznie w temperaturze nawet do 300 °C [41,42]. Szybkość korozji komercyjnie dostępnego stopu WE43 jest prawie 100-krotnie niższa niż szybkość korozji czystego Mg [43]. W trakcie zanurzenia w środowiskach wodnych na powierzchni stopu tworzy się stabilna warstwa produktów korozji [44], która pełni funkcję warstwy ochronnej przed otaczającym środowiskiem. Odporność na korozję stopu WE43, podobnie jak omówionych wyżej stopów na osnowie Mg, jest zależna od wielu czynników. Jednym z mechanizmów korozji występującym w stopach WE43 jest korozja mikro-galwaniczna zachodząca pomiędzy wydzieleniami a osnową [45]. Zjawisko to można zminimalizować poprzez fragmentację wydzielen w trakcie odkształcenia plastycznego na gorąco [46] albo poprzez wyżarzanie prowadzące do redystrybucji wydzielen drugiej fazy [47].

**Jak opisano powyżej, odporność na korozję Mg i jego stopów jest zjawiskiem niezwykle złożonym, zależnym głównie od składu chemicznego, mikrostruktury, historii technologicznej i środowiska korozyjnego. Wszystkie podjęte dotychczas próby podwyższenia odporności korozyjnej stopów na bazie Mg poprzez odkształcenie plastyczne dotyczą metod, które ze względu na ich niską podatność na odkształcenia, muszą być prowadzone w podwyższonej temperaturze. Przedstawiony cykl publikacji obejmuje najnowsze badania nad odpornością korozyjną Mg i jego stopów Mg wyciskanych metodą wyciskania współbieżnego z oscylującą matrycą. Czynnikiem wyróżniającym KoBo spośród innych metod jest możliwość odkształcenia materiałów o strukturze heksagonalnej bez wstępnego nagrzewania wlewka.**

### 4.3.2 Cel naukowy

Głównym celem badań było wykonanie szczegółowej analizy wpływu mikrostruktury na kształtowanie się odporności korozyjnej nowoczesnych stopów na osnowie Mg wyciskanych współbieżnie z oscylującą matrycą umieszczoną na końcu ekstrudera, bez wstępnego nagrzewania materiału odkształcanego. Celem szczegółowym badań było określenie, czy możliwa jest poprawa odporności korozyjnej Mg i jego stopów poprzez wyciskanie współbieżnie z oscylującą matrycą umieszczoną na końcu ekstrudera oraz, jeśli to możliwe, wykazanie, które elementy mikrostrukturalne mają decydujący wpływ na kształtowanie zachowania korozyjnego tych materiałów w warunkach obróbki plastycznej prowadzonej bez uprzedniego nagrzewania wsadu.

W moich badaniach szczegółowo omówiłam zmiany mikrostrukturalne wywołane w Mg i jego stopach przy różnych stopniach wyciskania metodą KoBo, oraz określiłam wpływ tych zmian na odporność korozyjną. Uzyskane wyniki stanowią istotne ogniwo w poznaniu mechanizmów kształtujących właściwości użytkowe stopów na bazie Mg, zwłaszcza ich odporności korozyjnej, poprzez formowanie mikrostruktury w trakcie odkształcenia bez nagrzewania materiału wsadowego, co do tej pory w literaturze polskiej, jak i światowej nie było analizowane.

### 4.3.3. Materiały do badań

W przedstawionym cyklu publikacji omówiłam wpływ wyciskania metodą KoBo na odporność korozyjną i formowanie mechanizmów korozyjnych w czterech najważniejszych z punktu widzenia zarówno naukowego, jak i aplikacyjnego, grupach materiałów na bazie Mg. Czysty Mg odkształcony metodą KoBo przy trzech różnych stopniach wyciskania w temperaturze pokojowej umożliwił mi zbadanie wpływu wielkości ziarna na formowanie się mechanizmów korozyjnych w materiale, w którym mogłam ograniczyć udział wydzielen innych faz [A1]. W kolejnych pracach analizowałam wpływ odkształcenia metodą KoBo na mikrostrukturę i odporność korozyjną stopów z następujących serii:

- Mg-Al-Zn (stop AZ31 [A2] oraz AZ61 [A3]),
- Mg-Al-Zn-Li (stop AZ31+4Li % mas. [A4] oraz stopu AZ31+7.5Li % mas. [A5]),
- Mg-Y-RE (stop WE43 [A6]).

Analizę porównawczą wpływu mikrostruktury na odporność korozyjną badanych w pracach [A1-A6] materiałów zawarłam w pracy [A7].

**W każdej z przedstawionych prac badawczych analizowałam wpływ mikrostruktury na odporność korozyjną materiałów na osnowie Mg. W moich rozważaniach wzięłam pod uwagę następujące czynniki: wielkość ziaren, ich orientację krystalograficzną i wzajemne rozmieszczenie, uzyskane po odkształceniu przy różnych stopniach odkształcenia bez nagrzewania materiału wsadowego. Następnie określiłam rolę rodzaju, ilości i rozmieszczenia wydzielen oraz gęstości dyslokacji na odporność korozyjną badanych stopów. Wszystkie prace dotyczą materiałów odkształczanych przy wysokich stopniach odkształcenia w pojedynczym cyklu przejścia przez zespół matryc.**

Poznając mechanizmy i czynniki determinujące odporność korozyjną czystego technicznie Mg, przeprowadziłam prace badawcze nad grupą stopów z serii Mg-Al-Zn (AZXX), w których głównymi pierwiastkami stopowymi są Al i Zn (X oznacza zawartość odpowiednio Al i Zn). W publikacjach [A2] i [A3] opisałam wpływ mikrostruktury ukształtowanej w wyniku odkształcenia plastycznego przy różnych stopniach odkształcenia na odporność korozyjną stopów AZ31 oraz AZ61, które ze względu na niską cenę i dobrą wytrzymałość są jednymi z najpowszechniej stosowanymi komercyjnie stopami na bazie Mg.

Kolejną grupą badanych materiałów były stopy z serii Mg-Li, w szczególności AZ31 z dodatkiem Li, które cechują się niższą masą właściwą oraz lepszą formowalnością podczas odkształcenia plastycznego w odniesieniu do stopów z serii Mg-Al-Zn. W pracach [A4] oraz [A5] przedstawiłam, w jaki sposób odkształcenie metodą KoBo wpływa na kształtowanie się mikrostruktury stopów AZ31 z dodatkiem 4 oraz 7,5 mas. % Li. Określiłam wpływ struktury jednofazowej typu  $\alpha(\text{Mg})$  oraz dwufazowej  $\alpha(\text{Mg})+\beta(\text{Li})$  na kształtowanie się mechanizmów korozyjnych oraz wytypowałam czynniki, które determinują odporność korozyjną tych grup stopów Mg.

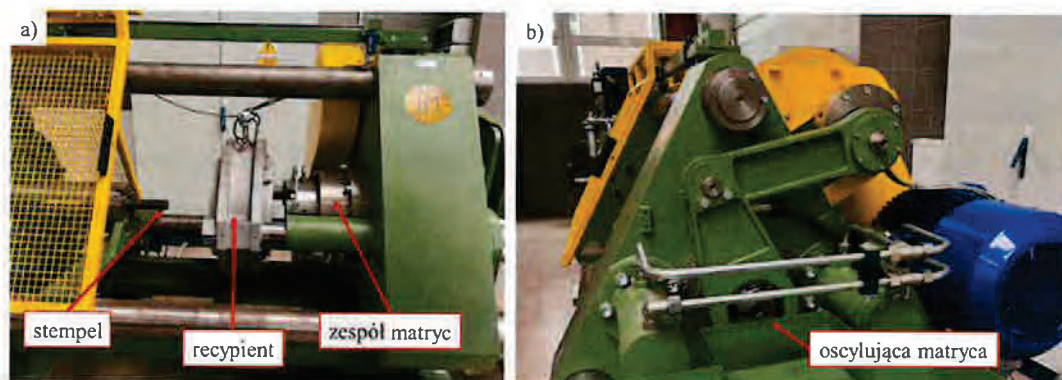
W pracy [A6] przeanalizowałam możliwość wyciskania metodą KoBo stopów Mg z dodatkiem pierwiastków ziem rzadkich (grupa Mg-Y-RE) bez nagrzewania wlewka oraz zdefiniowałam główne czynniki mikrostrukturalne wpływające na odporność korozyjną tej grupy materiałów. Badania prowadziłam na przykładzie stopu WE43, który jako główny składnik stopowy zawiera Y w ilości ok. 4% oraz pierwiastki ziem rzadkich (RE).

W pracy [A7] dokonałam podsumowania i zestawienia wpływu poszczególnych czynników mikrostrukturalnych dla analizowanych grup stopów na bazie Mg: czystego Mg, stopów z serii Mg-Al-Zn, Mg-Li oraz Mg-Y-RE. W tej samej pracy porównałam odporność korozyjną stopów z analizowanych grup materiałów, a następnie wyszczególniłam czynniki, które mają decydujący wpływ na wyselekcjonowanie stopów Mg o najwyższej odporności korozyjnej. W tym celu, do badań porównawczych wybrałam stopy z prac [A1-A6]

o najwyższej odporności korozyjnej spośród poprzednio zbadanych stopni odkształcenia, a następnie wykonałam pomiary odporności korozyjnej.

#### 4.3.4. Metodyka prac badawczych

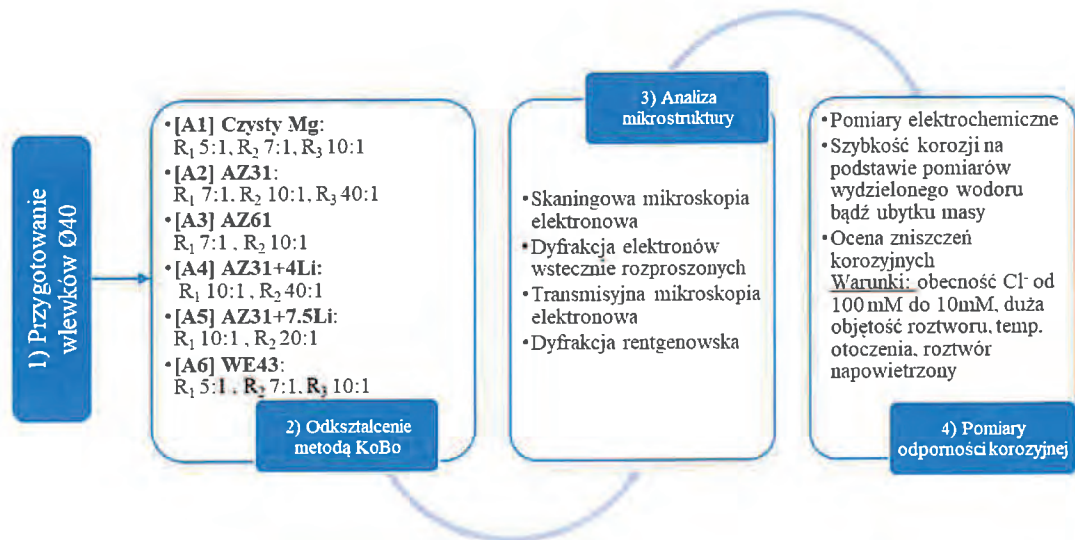
Wszystkie badane materiały były odlane do form o średnicy  $\varnothing 40$  mm, a następnie odkształcane przy użyciu prasy Hydromet w Katedrze Technologii Materiałowych na Wydziale Inżynierii Materiałowej Politechniki Śląskiej (rys. 2).



Rysunek 2. Prasa hydrauliczna Hydromet do wyciskania z oscylującą matrycą (metoda KoBo): a) widok układu wytłaczania ze stemplem, tuleją recypienta  $\varnothing 40 \times 160$  mm wraz z zespołem matryc, b) widok z przodu: układ oscylującej matrycy o częstotliwości od 1 Hz do 10 Hz i amplitudzie kąta skrętu od  $2^\circ$  do  $12^\circ$

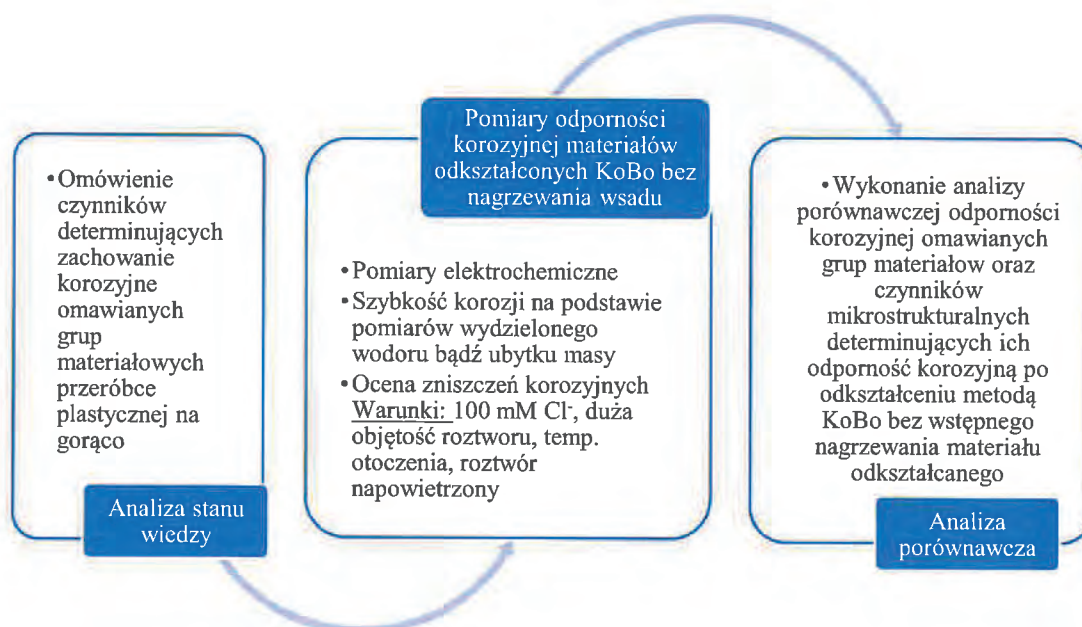
W każdej z prac [A1-A6] problem naukowy rozpatrywałam zgodnie ze schematem badawczym przedstawionym na rys. 3. Stopnie odkształcenia, jakie dobrałam dla poszczególnych stopów różnią się między sobą, gdyż były zależne od warunków i możliwości technologicznych. Po odkształceniu materiałów metodą KoBo, analizowałam ich mikrostrukturę (stopnie odkształcenia R podano na rys. 3). W tym celu przeprowadzono obserwacje mikrostrukturalne na skaningowym mikroskopie elektronowym (z ang. *scanning electron microscopy*, SEM), dyfrakcję elektronów wstecznie rozproszonych (z ang. *electron backscattered diffraction*, EBSD), obserwacje wysokorozdzielcze na transmisyjnym mikroskopie elektronowym (z ang. *transmission electron microscopy*, TEM). Analizę składu fazowego, a w wybranych przypadkach również pomiar naprężeń własnych, przeprowadzono przy użyciu dyfrakcji rentgenowskiej (z ang. *X-ray diffraction*, XRD). Ze względu na duże zdefektowanie po odkształceniu metodą KoBo oraz wysoką zawartość Li nie udało się wykonać pomiarów EBSD dla stopu AZ31 zawierającego 7.5 % mas. Li. Odporność korozyjną wszystkich materiałów badałam w wodnym roztworze chlorku sodu (NaCl) o zawartości 10 mM NaCl bądź 100 mM NaCl. Badania wykonałam przy użyciu technik elektrochemicznych (pomiaru potencjału

otwartego, EoCP, elektrochemiczna spektroskopia impedancyjna, EIS, oraz testy potencjodynamiczne). Dla wszystkich materiałów obliczyłam szybkość korozji w oparciu o ilość uwolnionego wodoru w trakcie zanurzenia w środowisku korozyjnym, bądź na podstawie pomiarów ubytku masy. Morfologię zniszczeń korozyjnych oceniłam na podstawie zdjęć SEM powierzchni materiałów po zanurzeniu w roztworze korozyjnym oraz po chemicznym usunięciu produktów korozji w 180 g/L Cr<sub>2</sub>O<sub>3</sub>.



Rysunek 3. Schemat badań prowadzonych w przedstawionych do oceny publikacjach [A1-A6] zawierających opis czynników wpływających na odporność korozyjną Mg i jego stopów po odkształceniu metodą KoBo

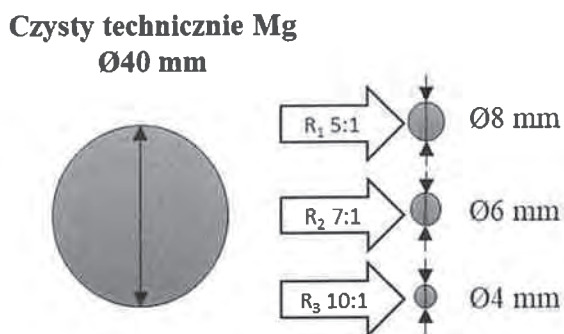
W pracy [A7] dokonałam przeglądu wszystkich badanych materiałów i zestawiałam główne parametry mikrostrukturalne, które decydowały o zachowaniu badanych materiałów w danym środowisku korozyjnym. W celu wykonania analizy porównawczej z każdej badanej grupy wytypowałam najbardziej odporny na korozję materiał [A1-A6], a następnie dla wytypowanych materiałów przeprowadziłam testy korozyjne w takich samych warunkach, tj. w roztworze naturalnie napowietrzonym zawierającym 100 mM NaCl oraz w temperaturze otoczenia (rys. 4).



*Rysunek 4. Schemat badań prowadzonych w publikacji [A7] zawierającej analizę porównawczą czynników wpływających na odporność korozyjną Mg i jego stopów po odkształceniu metodą KoBo bez wstępnego nagrzewania materiału wsadowego*

#### **4.3.5. Wpływ rozdrobnienia mikrostruktury na odporność korozyjną czystego technicznie Mg odkształcanego metodą KoBo bez nagrzewania materiału wsadowego**

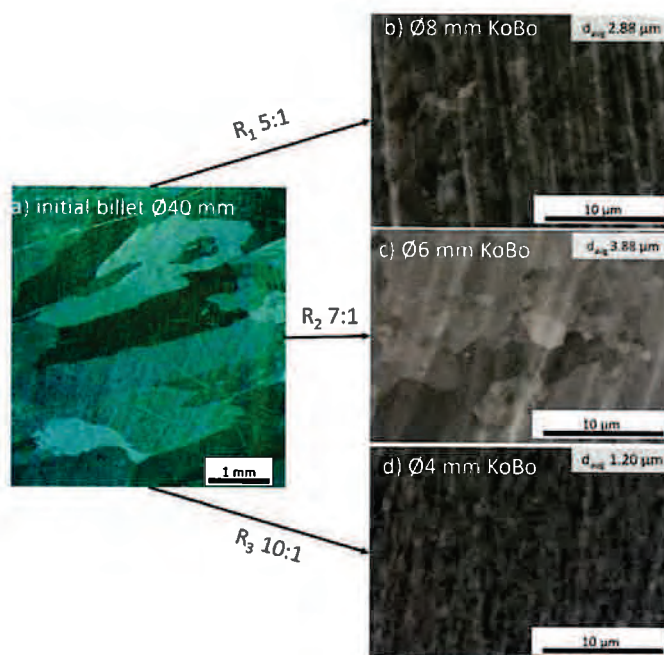
Trudnością w zdefiniowaniu głównych czynników determinujących odporność korozyjną stopów wieloskładnikowych jest heterogeniczność mikrostruktury, a co za tym idzie, duża ilość elementów mikrostrukturalnych, które jednocześnie wpływają na ich zachowanie korozyjne. W moim podejściu badawczym w pierwszej kolejności wyeliminowałam udział obcych faz w formowaniu się mechanizmów korozyjnych i określiłam zależność mikrostrukturalną vs. odporność korozyjną dla czystego technicznie Mg odkształconego metodą KoBo bez nagrzewania materiału wsadowego [A1]. Badania prowadziłam dla materiału wsadowego oraz dla materiałów po odkształceniu. W pracy przeanalizowałam 3 różne stopnie odkształcenia czystego Mg z początkowej średnicy  $\varnothing 40$  mm, odpowiednio do 8 mm ( $R_1$  5:1), 6 mm ( $R_2$  7:1) oraz 4 mm ( $R_3$  10:1), rys. 5.



*Rysunek 5. Stopnie odkształcenia ( $R$ ) zastosowane dla czystego technicznie Mg przerobionego metodą KoBo bez wstępnego nagrzewania wsadu [A1]*

Dzięki odkształceniu przy użyciu metody KoBo nastąpiła znaczna redukcja wielkości ziarna. Ze struktury gruboziarnistej o średniej wielkości kilkudziesięciu  $\mu\text{m}$  otrzymano materiały o średniej wielkości ziarna  $d_{\text{avg}} = 2,9 \mu\text{m}$  dla  $R_1$  5:1,  $d_{\text{avg}} = 3,9 \mu\text{m}$  dla  $R_2$  7:1, oraz  $d_{\text{avg}} = 1,2 \mu\text{m}$  dla  $R_3$  10:1 (rys.6), gdzie  $d$  definiuje się jako średnią średnicę ekwiwalentną. Wyniki uzyskane metodą EBSD wykazały, że w materiale zaszły procesy rekrytalizacji dynamicznej i zdrowienia dynamicznego, ale w zależności od stopnia odkształcenia intensywność tych procesów była różna. Najwięcej zrekrystalizowanych ziaren, ok 85% całej populacji, zaobserwowano w przypadku czystego Mg odkształconego przy parametrach  $R_1$  5:1 i  $R_3$  10:1. W materiale odkształconym  $R_2$  7:1 w pełni zrekrystalizowało ok. 80% wszystkich analizowanych ziaren, oraz zaobserwowano powstałą substrukturę w środku dużych ziaren. Ponadto, największą gęstość dyslokacji obliczono dla stopnia odkształcenia  $R_1$  5:1 i  $R_3$  10:1.

Analiza wyników badań elektrochemicznych wskazuje, że zmiany mikrostrukturalne, powstałe w trakcie odkształcenia metodą KoBo bez wstępnego nagrzewania materiału wsadowego, podwyższyły odporność korozyjną materiałów odkształconych w odniesieniu do materiału odlewanego, niezależnie od stopnia odkształcenia. Nie zaobserwowano jednak, by wraz ze zwiększającym się stopniem odkształcenia, w sposób wzrastający ulegała poprawie odporność korozyjna czystego Mg. Spośród odkształconych próbek, najwyższą odpornością korozyjną cechował się czysty Mg wyciskany przy zadanym stopniu odkształcenia  $R_2$  7:1, niższą odpornością charakteryzował się materiał odkształcony przy  $R_1$  5:1, zaś najniższa odporność korozyjna została zarejestrowana dla najniższego stopnia odkształcenia  $R_3$  10:1.

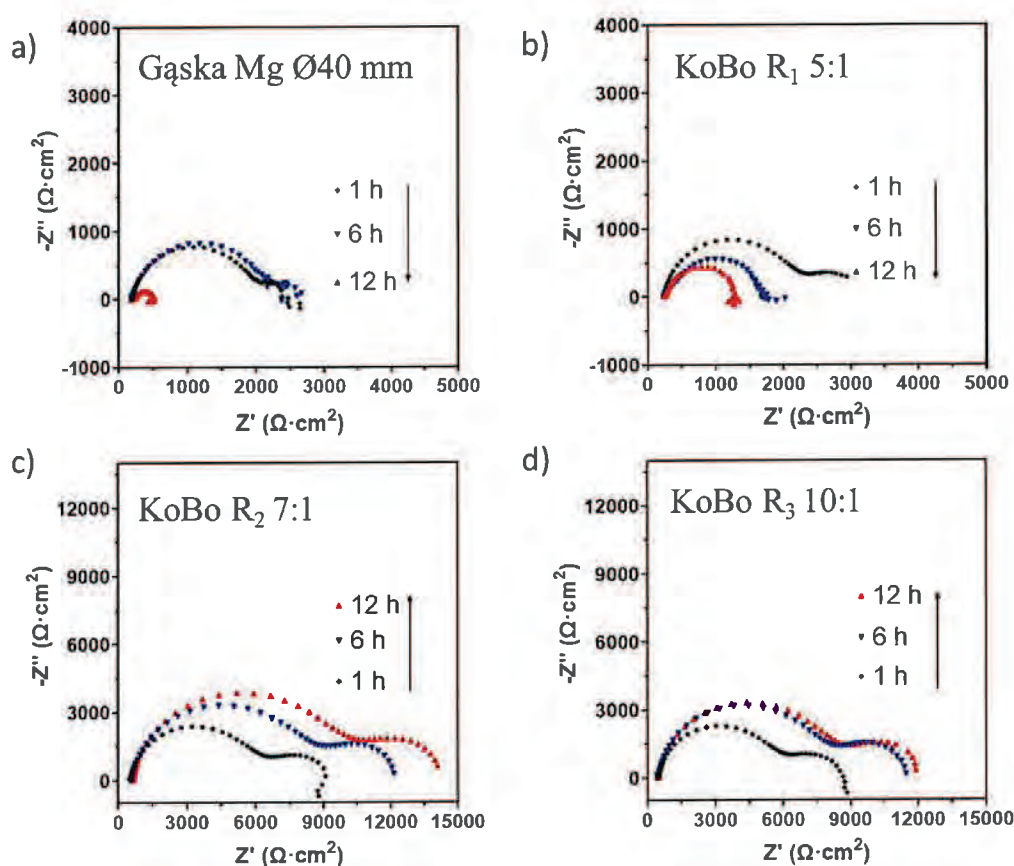


Rysunek 6. Mikrostruktura czystego odlewanego Mg oraz czystego Mg po przeróbce metodą KoBo w pojedynczym cyklu przejścia przez zespół matryc bez wstępnego nagrzewania wsadu [AI] przy zastosowaniu różnych stopni odkształcenia: a) materiał wsadowy (odlew), b) R<sub>1</sub> 5:1, c) R<sub>2</sub> 7:1 oraz c) R<sub>3</sub> 10:1

W pracy udowodniono, że stopień odkształcenia miał wpływ na zmianę mechanizmów korozyjnych. W przypadku materiałów wyciskanych przy najniższym stopniu odkształcenia R<sub>1</sub> 5:1 nie zaobserwowano zmiany mechanizmu korozyjnego w odniesieniu do materiału wyjściowego – obydwa materiały aktywnie korodowały w analizowanym medium. Próbki wyciskane przy wyższych stopniach odkształcenia, R<sub>2</sub> 7:1 oraz R<sub>3</sub> 10:1, ulegały pasywacji, przy czym wyższą odporność na korozję typu lokalnego wykazała próbka odkształcona przy stopniu odkształcenia R<sub>2</sub> 7:1. Takie zmiany w mechanizmach odporności korozyjnej czystego Mg po odkształceniu metodą KoBo są zależne od przebiegu procesów rekrytalizacji dynamicznej oraz wzajemnej intensywności rekrytalizacji dynamicznej i zdrowienia dynamicznego. Obydwa te procesy są zależne od szybkości odkształcenia, co z kolei oprócz stopnia odkształcenia, w przypadku metody KoBo, jest dodatkowo uwarunkowane wielkością odkształcenia powstałego w trakcie cyklu skręcania matrycy.

Dodatkową zmienną, którą analizowałam w tej publikacji był wpływ czasu ekspozycji w środowisku korozyjnym na zmianę odporności korozyjnej czystego Mg w stanie wyjściowym, jak i po odkształceniu metodą KoBo. Jak pokazano na rys. 7a, odporność korozyjna materiału wyjściowego drastycznie zmalała po 12 godzinach od zanurzenia. Podobny trend odnotowano w przypadku czystego Mg wyciskanego przy najniższym stopniu odkształcenia, przy czym odporność na korozję po 12 godzinach zanurzenia tego materiału

jest wyższa niż odporność materiału wyjściowego (rys. 7b). Jak już wspomniano, próbki wyciśnięte przy wyższych stopniach odkształcenia są mniej aktywne w analizowanym medium korozyjnym, a dzięki tworzeniu się warstwy pasywnej, która częściowo chroni ich powierzchnię przed postępującymi reakcjami korozyjnymi, ich odporność na działanie roztworu zawierającego jony chlorkowe jest wyższa niż w poprzednich dwóch przypadkach (rys. 7c i rys 7d). Dodatkowo, dla czystego Mg odkształconego przy  $R_2$  7:1 odnotowano ciągły wzrost odporności korozyjnej (rys. 7c). W przypadku odkształcenia  $R_3$  10:1 krzywe Nyquista po 6 i 12 godzinach zanurzenia nakładają się, nie zaobserwowano ani spadku ani podwyższenia odporności korozyjnej po 12 godzinach zanurzenia.



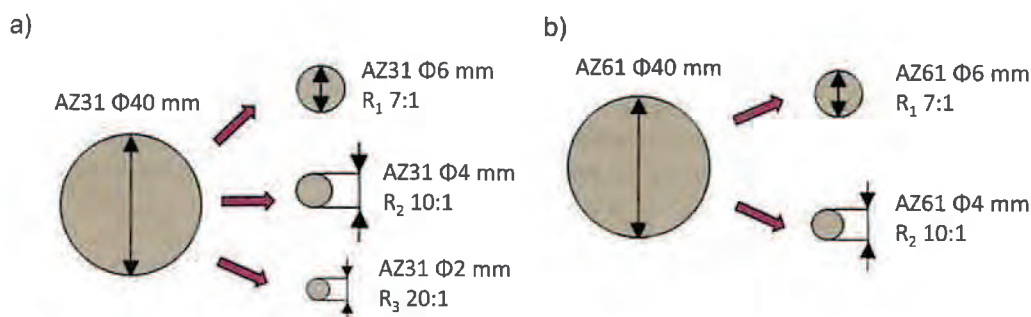
Rysunek 7. Krzywe Nyquista zarejestrowane dla czystego Mg w stanie wyjściowym i po odkształceniu metodą KoBo dla różnych stopni odkształcenia w trakcie zanurzenia środowisku zawierającym jony chlorkowe przez 1, 6 i 12 godzin: przy zastosowaniu różnych stopni odkształcenia: a) materiał wsadowy (odlew), b)  $R_1$  5:1, c)  $R_2$  7:1 oraz c)  $R_3$  10:1

Przedstawione w pracy [A1] wyniki, potwierdzają, że wyciskanie czystego Mg metodą KoBo bez nagrzewania materiału wsadowego umożliwia znaczącą redukcję średnicy, tym samym zmniejszając wielkość ziarna z kilkunastu  $\mu\text{m}$  do nawet 1  $\mu\text{m}$ . Zmiana wielkości

ziarna nie postępuje liniowo w stosunku do zwiększającego się stopnia odkształcenia. Największą wielkość ziarna otrzymano dla średniej wielkości stopnia odkształcenia, co związane jest z różną intensywnością procesów rekrytalizacji dynamicznej w trakcie wyciskania zachodzących przy różnych stopniach odkształcenia. Dzięki zmianom mikrostrukturalnym wywołanym w trakcie procesu KoBo odporność na korozję czystego Mg uległa poprawie w odniesieniu do materiału wyjściowego. Nie mniej jednak poprawa odporności na korozję czystego Mg nie postępuje liniowo wraz ze zmniejszającą się wielkością ziarna. Najlepszą odpornością korozyjną charakteryzuje się czysty Mg o najmniejszym rozdrobieniu ziarna. Oprócz dużej ilości granic ziaren będącymi miejscami anodowymi w zachodzących procesach korozyjnych, na odporność korozyjną czystego Mg po odkształceniu metodą KoBo ma wpływ gęstość dyslokacji. Wyższa gęstość dyslokacji przy mniejszej wielkości ziarna sprzyja formowaniu się ognisk korozyjnych i ich rozprzestrzenianiu, co jest przyczyną niskiej odporności korozyjnej czystego Mg o największym rozdrobieniu mikrostruktury.

#### 4.3.6. Wpływ tekstury i wydzieleni typu $\beta$ -Mg<sub>17</sub>Al<sub>12</sub> na odporność korozyjną stopów z serii Mg-Al-Zn odkształcanych metodą KoBo

Kolejnym aspektem moich badań było określenie, czy te same warunki wpływające na zmianę odporności korozyjnej w przypadku czystego Mg odkształcanego metodą KoBo, dotyczą również zjawisk korozyjnych w przypadku stopów wieloskładnikowych. Jeżeli w przypadku wieloskładnikowych stopów na bazie Mg zachodzą inne mechanizmy korozyjne niż te pokazane w pracy [A1], celem kolejnych prac, było ich zdefiniowanie oraz wskazanie głównych czynników kontrolujących odporność korozyjną tych materiałów. Do badań wybrano dwa stopy o różnej zawartości Al z serii Mg-Al-Zn (AZ31 [A2] oraz AZ61 [A3]). Stopy odkształcono metodą KoBo wg schematu zamieszczonego na rys. 8.

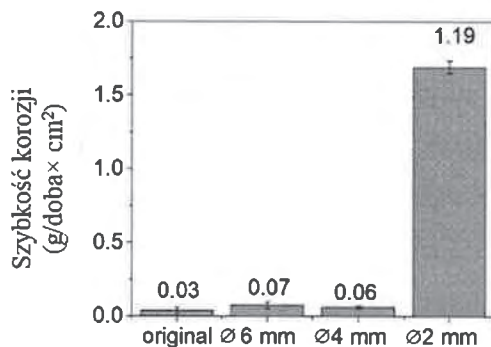


Rysunek 8. Stopnie odkształcenia (R) metodą KoBo bez wstępnego nagrzewania wsadu a) stopu AZ31 oraz b) stopu AZ61 [A3]

W przypadku stopu AZ31 wraz ze zwiększającym się stopniem odkształcenia wielkość ziarna ulegała zmniejszeniu, przy czym średnia wielkość ziarna po wyciskaniu przy stopniu odkształcenia  $R_1$  7:1 oraz  $R_2$  10:1 nie różni się znacząco i wynosi odpowiednio 5,0  $\mu\text{m}$  i 4,4  $\mu\text{m}$  (z początkowej wielkości kilkudziesięciu  $\mu\text{m}$ ). W obydwu materiałach utworzyły się mikrostruktury o bimodalnym charakterze rozkładu wielkości ziarna. Zadając stopień odkształcenia  $R_1$  7:1 w stopie uformowały się duże, pierwotne ziarna otoczone łańcuszkiem małych zrekrytalizowanych ziaren. W stopie po odkształceniu  $R_2$  10:1 duże ziarna otoczone są małymi zrekrytalizowanymi ziarnami, ale ich wielkość jest większa niż w przypadku ziaren zrekrytalizowanych przy wyciskaniu  $R_1$  7:1. Po wyciskaniu przy stopniu  $R_3$  20:1 utworzyła się drobnoziarnista mikrostruktura równoosiowa o największym stopniu zdefektowania i wielkości ziarna 1,9  $\mu\text{m}$ . W stopach AZ31 nie zidentyfikowano obecności fazy  $\beta\text{-Mg}_{17}\text{Al}_{12}$ . Orientacja krystalograficzna ziaren zależna jest od stopnia wyciskania: w trakcie wyciskania  $R_1$  7:1 uformowały się ziarna zorientowane w kierunku  $\langle 0001 \rangle$  w stosunku do osi wyciskania, w trakcie wyciskania  $R_2$  10:1 powstały ziarna o orientacji  $\langle 10\bar{1}0 \rangle$  i  $\langle 2\bar{1}\bar{1}0 \rangle$  w stosunku do osi wyciskania. Ziarna w mikrostrukturze powstałej przy największym odkształceniu są zorientowane przypadkowo.

Na podstawie przeprowadzonych badań stwierdzono, że obróbka plastyczna metodą KoBo bez nagrzewania wsadu nie prowadzi do podwyższenia odporności korozyjnej stopu AZ31. Zarówno, bimodalny rozkład wielkości ziaren, jak i obecność dużej gęstości dyslokacji wywołanej działaniem oscylującej matrycy nie sprzyja podwyższeniu odporności korozyjnej stopu AZ31. W mikrostrukturze o bimodalnym rozkładzie wielkości ziaren skupiska małych zrekrytalizowanych ziaren stanowią anodę w odniesieniu do dużych pierwotnych ziaren, które pełnią funkcję katody. To właśnie stosunek wielkości ziaren zrekrytalizowanych do obszaru ziaren pierwotnych jest kluczowym czynnikiem decydującym o szybkości korozji zachodzącej w tego typu materiałach. Duży obszar katodowy, dążąc do utrzymania stanu równowagowego reakcji cząstkowych, wymusza na mniejszym obszarze anodowym szybsze reakcje roztwarzania. Mikrostruktury uformowane w trakcie odkształcenia przy zadanym stopniu wyciskania  $R_1$  7:1 i  $R_2$  10:1 cechują się niższą odpornością na korozję niż materiał wsadowy, ale wyższą niż pręt odkształcony przy  $R_3$  20:1 (rys. 9). W tym ostatnim przypadku uzyskano mikrostrukturę drobnoziarnistą zbliżoną do równoosiowej, w której granice ziaren stanowią miejsca anodowe w mechanizmach korozyjnych. Duży udział granic ziaren w stosunku do ich wnętrza oraz wysoka gęstość splotów dyslokacyjnych skumulowanych w trakcie odkształcenia stanowiła miejsca inicjacji reakcji mikro-galwanicznych z osnową, co zdecydowanie obniżyło odporność na korozję tego materiału. Podsumowując, zastosowana metoda odkształcenia,

pomimo dużego rozdrobnienia wielkości ziarna, ze względu na uformowanie się dużej ilości defektów struktury krystalicznej, nie wpłynęła na poprawę odporności korozyjnej stopu AZ31 w odniesieniu do materiału wyjściowego.

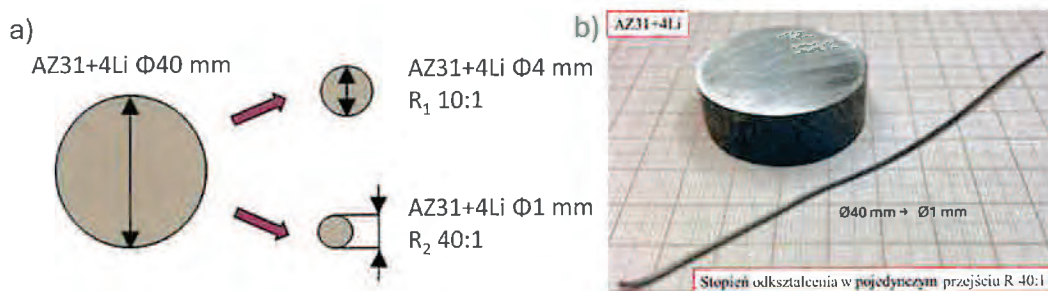


Rysunek 9. Szybkość korozji stopu odlewanego stopu AZ31 oraz po wyciskaniu metodą KoBo bez wstępnego nagrzewania wsadu przy stopniach odkształcenia  $R_1$  7:1,  $R_2$  10:1 i  $R_3$  20:1 w środowisku 100 mM NaCl [A2]

Mikrostruktura stopu AZ61 po wyciskaniu przy zadanych stopniach odkształcenia  $R_1$  7:1 oraz  $R_2$  10:1, podobnie jak w stopie AZ31, uległa przekształceniu i znacznemu rozdrobnieniu. Osiągnięto rozdrobnienie ziarna z 20,4  $\mu\text{m}$  do 6,6  $\mu\text{m}$  oraz 4,3  $\mu\text{m}$ , odpowiednio dla  $R_1$  7:1 oraz  $R_2$  10:1. W obydwu odkształconych przypadkach uformowały się ziarna równoosiowe zorientowane w kierunkach  $\langle 10\bar{1}0 \rangle$  oraz  $\langle 2\bar{1}10 \rangle$  w stosunku do osi wyciskania. W obydwu materiałach wykryto również obecność fazy  $\beta\text{-Mg}_{17}\text{Al}_{12}$  rozmieszczonej głównie na granicach ziaren. Odporność korozyjna stopów po odkształceniu uległa obniżeniu w porównaniu do materiału wyjściowego. Wyższą odpornością na korozję cechował się stop odkształcony przy  $R_1$  7:1, zaś wyższa gęstość dyslokacji we wnętrzu ziaren, wpłynęła na obniżenie odporności korozyjnej stopu o mikrostrukturze cechującej się mniejszą wielkością ziarna, która powstała w trakcie wyciskania przy  $R_2$  10:1. W przypadku stopu AZ61, oprócz dużej gęstości dyslokacji, obecność fazy  $\beta\text{-Mg}_{17}\text{Al}_{12}$  na granicach ziaren, sprzyjała formowaniu się ogniw mikro-galwanicznych, akcelerując procesy degradacji materiałów po odkształceniu, dlatego stop AZ61 odkształcony metodą KoBo bez nagrzewania wsadu, niezależnie od stopnia odkształcenia, posiada niższą odporność na korozję niż stop AZ31.

#### 4.3.7. Wpływ mikrostruktury jednofazowej $\alpha(\text{Mg})$ oraz dwufazowej $\alpha(\text{Mg}) + \beta(\text{Li})$ na odporność korozyjną stopów na bazie Mg z dodatkiem Li odkształczanych metodą KoBo

Następny etap badań dotyczył stopów na bazie Mg zawierających Li. Dodatek Li znacząco redukuje gęstość stopów Mg, a dodatkowo poprawia ich formowalność [48]. W tej części badań odkształciliśmy stop o budowie jednofazowej  $\alpha(\text{Mg})$  o składzie chemicznym Mg-4Li-3Al-1Zn (AZ31+4 mas. % Li) [A4]. Wymiary materiału wsadowego sukcesywnie zredukowano, bez nagrzewania materiału wyjściowego, ze średnicy  $\text{Ø}40$  mm do  $\text{Ø}4$  mm ( $R_1$  10:1) oraz ze średnicy  $\text{Ø}40$  mm do  $\text{Ø}1$  mm ( $R_2$  40:1), w pojedynczym przejściu przez zespół matryc (rys. 10). Nie odnalazłam danych literaturowych, dotyczących tak znaczącego odkształcenia stopów na bazie Mg bez nagrzewania materiału wsadowego (stopień przerobu dla tego materiału wynosił  $\lambda=1600$ ). Publikacja [A4] jest pierwszą publikacją opisującą odkształcenie metalu o strukturze heksagonalnej przy tak dużym zredukowaniu średnicy materiału w pojedynczym przejściu przez zespół matryc bez wstępnego nagrzewania materiału (rys. 10b).

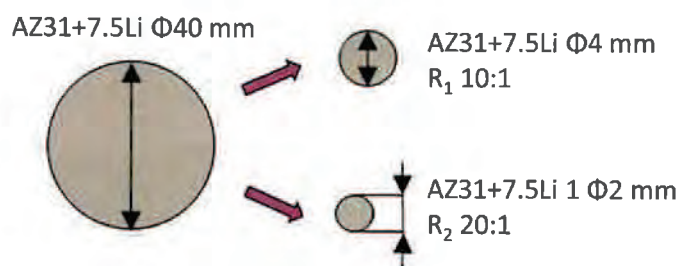


Rysunek 10. Odkształcenie metodą KoBo stopu AZ31+4Li w pojedynczym przejściu przez zespół matryc bez wstępnego nagrzewania materiału odkształcanego (wlewka) [A4]: a) stopnie odkształcenia, b) zdjęcie stopu AZ31+4Li przed i po wyciskaniu KoBo ze średnicy  $\text{Ø}40$  mm do  $\text{Ø}1$  mm (stopień odkształcenia  $R=40:1$ ) w pojedynczym przejściu przez zespół matryc

W obydwu wyciskanych materiałach ukształtowała się mikrostruktura o ziarnach zbliżonych do równoosiowych, ale w odróżnieniu od czystego Mg (rozdział 4.3.5) i stopów z serii Mg-Al-Zn (rozdział 4.3.6), wraz ze zwiększeniem stopnia odkształcenia nastąpił nieznaczny rozrost średniej wielkości ziarna z  $3.2 \mu\text{m}$  do  $3.9 \mu\text{m}$ , odpowiednio dla  $R_1$  10:1 i  $R_2$  40:1. Orientacja krystalograficzna ziaren w obydwu odkształconych materiałach była podobna; ziarna były głównie zorientowane w kierunku  $\langle 10\bar{1}0 \rangle$  oraz  $\langle 2\bar{1}\bar{1}0 \rangle$  w stosunku do osi wyciskania. W stopie odkształconym do 4 mm ( $R_1$  10:1) zidentyfikowano obecność obojętnej korozyjnie wydzieleń AlLi, zaś we wnętrzu ziaren stopie odkształconym do 1 mm ( $R_2$  40:1) wydzielili się  $\beta\text{-Mg}_{17}\text{Al}_{12}$  oraz  $\text{Li}_{0.81}\text{Mg}_{0.19}$ . Obecność  $\beta\text{-Mg}_{17}\text{Al}_{12}$  oraz  $\text{Li}_{0.81}\text{Mg}_{0.19}$

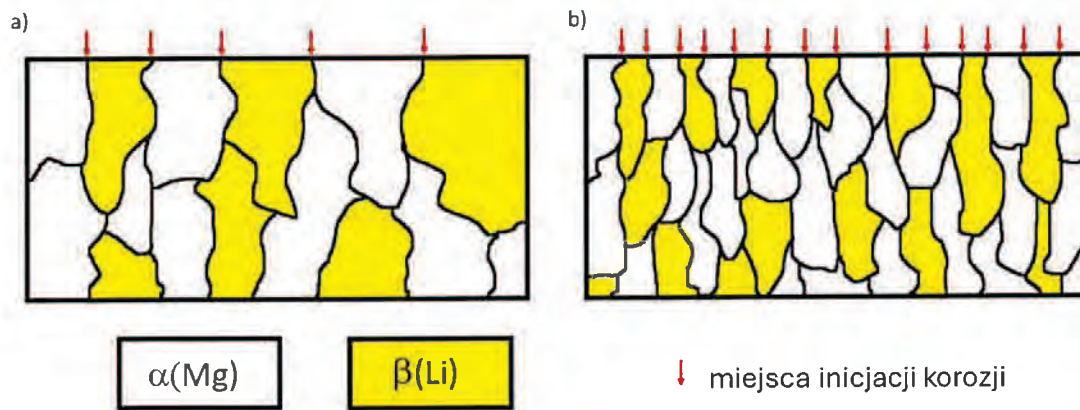
spowodowała zwiększenie ilości miejsc inicjacji reakcji mikro-galwanicznych z osnową magnezową. Stop ten charakteryzował się dwukrotnie wyższą szybkością korozji niż stop o średnicy 4 mm ( $R_1$  10:1). Podsumowując, oprócz wielkości ziarna, istotny wpływ na obniżenie odporności korozyjnej stopu Mg-4Li-3Al-1Zn o budowie jednofazowej  $\alpha(\text{Mg})$  ma ilość i rodzaj powstałych w trakcie odkształcenia faz: gruboziarnista faza AlLi nie ma wpływu na tworzenie się mikro-ogniw korozyjnych, zaś drobne wydzielenia  $\beta\text{-Mg}_{17}\text{Al}_{12}$  oraz  $\text{Li}_{0.81}\text{Mg}_{0.19}$  tworzą mikro-ogniwa z osnową Mg.

Odmienny mechanizm korozyjny zidentyfikowałam w trakcie badań nad stopem o budowie dwufazowej  $\alpha(\text{Mg})+\beta(\text{Li})$  o składzie chemicznym Mg-7.5Li-3-Al-1Zn (AZ31+7.5Li) [A5]. Materiał odkształcono przy dwóch różnych stopniach wyciskania  $R_1$  10:1 i  $R_2$  20:1 (rys. 11).



Rysunek 11. Stopnie odkształcenia metodą KoBo bez wstępnego nagrzewania wsadu stopu AZ31 z dodatkiem 7.5Li [A5]

Prace nad tym materiałem rozpoczęłam od analizy ilościowej zawartości fazy  $\alpha(\text{Mg})$  oraz fazy  $\beta(\text{Li})$  w obydwu odkształconych prętach. Wraz ze zwiększającym się stopniem odkształcenia zmniejszył się udział fazy  $\alpha(\text{Mg})$ , z 34,1% do 27,2% dla  $R_1$  10:1 i  $R_2$  20:1, wzrósł zaś udział fazy  $\beta(\text{Li})$ , z 63,2% do 71,2%. Obserwacje SEM wykazały, że wraz ze zwiększaniem stopnia odkształcenia, nastąpiło rozdrobnienie fazy  $\beta(\text{Li})$  w osnowie  $\alpha(\text{Mg})$  oraz jej równomiernie rozłożenie. W przypadku stopu Mg-7.5Li-3Al-1Zn zmiany mikrostrukturalne wywołane odkształceniem KoBo, wpłynęły na podwyższenie odporności korozyjnej materiałów odkształconych w porównaniu do materiału wsadowego. Nie mniej jednak wraz ze wzrostem stopnia odkształcenia szybkość korozji również wzrosła.



Rysunek 12. Schemat mechanizmu korozyjnego w stopie Mg-7.5Li-3Al-1Zn zachodzący w środowisku jonów chlorkowych po wyciskaniu metodą KoBo bez wstępnego nagrzewania wsadu dla następujących stopni odkształcenia: a)  $R_1$  10:1, b)  $R_2$  20:1 [A5]

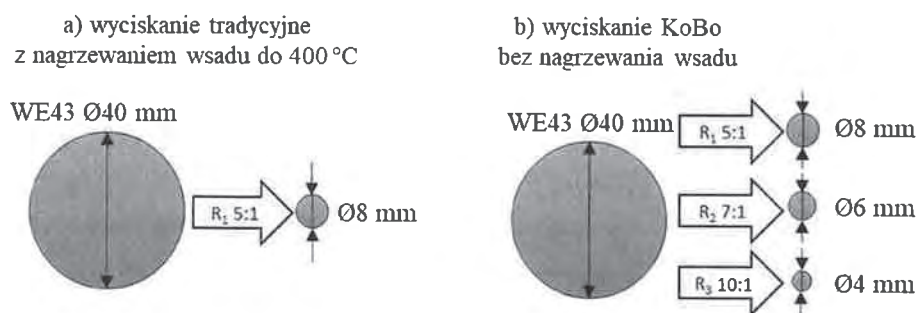
Spośród odkształconych stopów Mg-7.5Li-3Al-1Zn, wraz z wyższym stopniem wyciskania nastąpiło rozdrobnienie mikrostruktury i fragmentacja fazy  $\beta(\text{Li})$  w osnowie  $\alpha(\text{Mg})$ , co jednak nie wpłynęło na poprawę odporności korozyjnej. Zjawisko podwyższenia szybkości korozji należy przypisać utworzeniu się dużej ilości ognisk korozyjnych (głównie granic ziaren), co schematycznie pokazano na rys. 12. Atak korozyjny w przypadku analizowanych stopów o bardziej rozdrobnionej mikrostrukturze rozpoczynał się na granicach ziaren, gdzie tworzyły się drobne wydzielenia  $\text{MgLi}_2\text{Al}$ . W przypadku wyższego stopnia odkształcenia nastąpiła fragmentacja fazy  $\beta(\text{Li})$ , co doprowadziło do uformowania się większej ilości granic ziaren. Dodatkowo, obecność fazy  $\text{MgLi}_2\text{Al}$  na granicach ziaren sprzyjała inicjowaniu reakcji anodowych, które nie były kompensowane przez reakcje prowadzące do powstania warstwy ochronnej. Następnie, miejscowy atak korozyjny przechodził w korozję typu mikrogalwanicznego występującą pomiędzy bardziej aktywną fazą  $\beta(\text{Li})$ , a mniej aktywną fazą  $\alpha(\text{Mg})$ . W związku z tym, im większe rozdrobnienie fazy  $\beta(\text{Li})$  w osnowie  $\alpha(\text{Mg})$ , tym szybciej postępują procesy korozyjne. Jest to główny czynnik regulujący szybkość degradacji stopów na bazie Mg z Li o strukturze dwufazowej  $\alpha(\text{Mg}) + \beta(\text{Li})$ .

#### 4.3.8. Wpływ rozdrobnienia ziarna oraz wydzieleni faz wtórnych na odporność korozyjną stopów z serii Mg-Y-RE po odkształceniu tradycyjnym i metodą KoBo przy różnych stopniach wyciskania

Grupę stopów Mg, które w porównaniu do materiałów opisanych w rozdziałach 4.3.5. – 4.3.7, cechują się wyższą wytrzymałością, dobrą odpornością na pełzanie i dobrymi właściwościami odlewniczymi, stanowią stopy z serii Mg-Y-RE. Stopy z dodatkiem Y są najdroższe spośród dostępnych na rynku stopów na bazie Mg, w związku z tym zasadne jest

podjęcie badań zmierzających do obniżenia ich kosztów produkcji, co można osiągnąć przez odkształcenie metodą KoBo, w którym eliminuje się proces nagrzewania. W tej części badań podjęłam próbę wyciskania współbieżnego KoBo bez nagrzewania materiału wsadowego stopu WE43. W pracy [A6] podjęłam dwa aspekty badawcze:

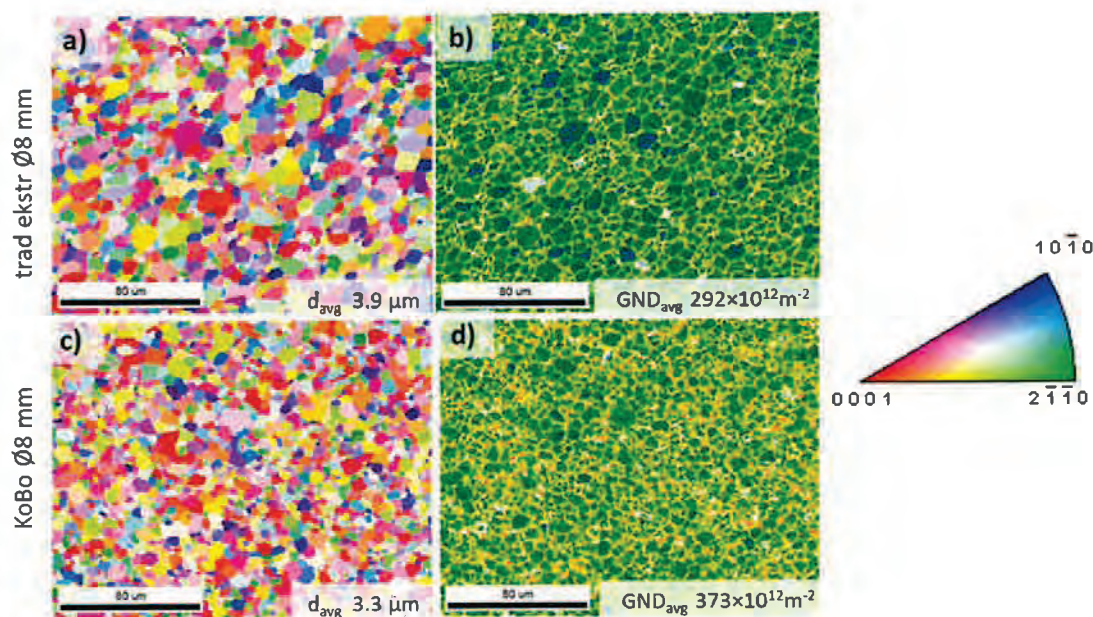
- porównałam mikrostrukturę i właściwości stopu WE43 wyciskanego ze średnicy  $\varnothing 40$  mm do  $\varnothing 8$  mm ( $R_1$  5:1) zarówno metodą tradycyjnego wyciskania w temperaturze  $400\text{ }^\circ\text{C}$ , oraz metodą KoBo bez nagrzewania wsadu (rys. 13),
- porównałam wpływ różnego stopnia odkształcenia metodą KoBo na właściwości korozyjne oraz mechaniczne uzyskanych prętów. Wyciśnięto pręty ze średnicy  $\varnothing 40$  mm do  $\varnothing 8$  mm ( $R_1$  5:1),  $\varnothing 40$  mm do  $\varnothing 6$  mm ( $R_2$  7:1) oraz  $\varnothing 40$  mm do  $\varnothing 4$  mm ( $R_3$  10:1), rys. 13b.



Rysunek 13. Stopnie odkształcenia metodą KoBo stopu WE43: a) metodą tradycyjnej ekstruzji w temperaturze  $400\text{ }^\circ\text{C}$ , b) metodą KoBo bez wstępnego nagrzewania materiału odkształcanego [A6]

Wyniki badań przeprowadzone w celu opisu mikrostruktury stopu WE43 wyciskanego tradycyjnie przy tym samym stopniu odkształcenia  $R_1$  5:1, w podwyższonej temperaturze oraz metodą KoBo bez nagrzewania materiału, wyjściowego wykazały zasadnicze różnice w mikrostrukturach obu stopów. W wyniku odkształcenia metodą KoBo uzyskano większe rozdrobnienie mikrostruktury stopu. Średnia wielkość ziarna materiału odkształconego tradycyjnie na gorąco wyniosła  $3,9\text{ }\mu\text{m}$  (rys. 14a), zaś materiału wyciskanego KoBo średnia wielkość ziarna wyniosła  $3,3\text{ }\mu\text{m}$  (rys. 14b). W obu materiałach ukształtowały się ziarna zbliżone do równoosiowych o przypadkowej orientacji krystalograficznej z przewagą ziaren o orientacji  $\langle 0001 \rangle$  w stosunku do osi wyciskania. Zmiana drogi odkształcenia jakiej poddawany jest materiał w czasie wyciskania Kobo, czyli obustronne skręcanie wsadu, powoduje wzrost gęstości defektów sieci krystalicznej w trakcie odkształcenia. Wzrost koncentracji naprężeń ujawniły obserwacje wykonane przedstawione na rys. 14b i 14d. Nawet tak nieduża zmiana w rozdrobnieniu mikrostruktury, doprowadziła do akumulacji dyslokacji

geometrycznie niezbędnych (z ang. *geometrically necessary dislocation, GND*) na granicach ziaren.

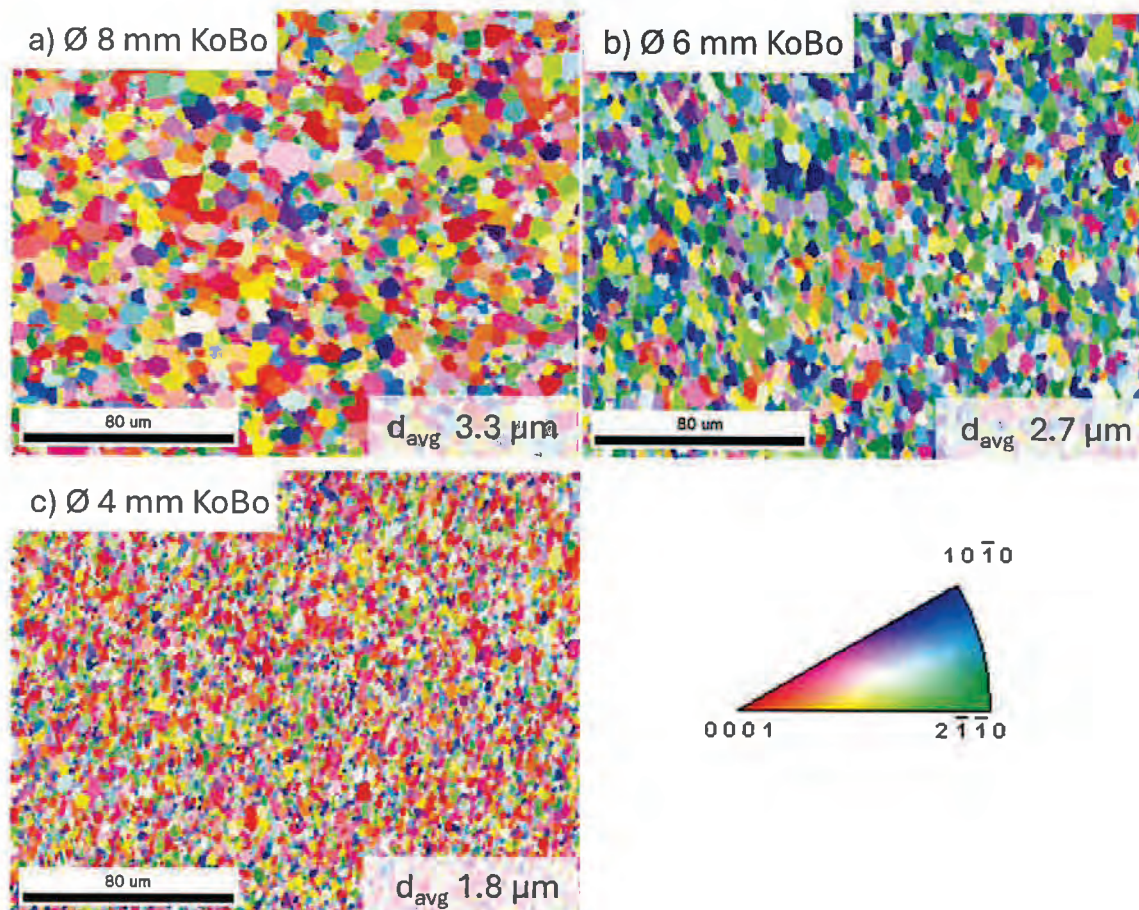


Rysunek 14. Wyniki EBSD dla stopu WE43: a) mapa rozkładu orientacji ziaren stopu odkształconego tradycyjną ekstruzją na gorąco  $R_1$  5:1, b) rozkład dyslokacji geometrycznie niezbędnych (GND) w stopie odkształconym tradycyjną ekstruzją na gorąco  $R_1$  5:1, c) mapa rozkładu orientacji ziaren stopu odkształconego metodą KoBo bez nagrzewania materiału wsadowego  $R_1$  5:1, d) rozkład dyslokacji geometrycznie niezbędnych (GND) w stopie odkształconym metodą KoBo bez nagrzewania materiału wsadowego  $R_1$  5:1 [A6]

W wyniku zmian, które zaszły w mikrostrukturze stopu wyciskanego metodą KoBo, nastąpiło podwyższenie właściwości mechanicznych, a także wzrost odporności korozyjnej, w odniesieniu do stopu wyciskanego metodą tradycyjną. Głównym czynnikiem wpływającym na podwyższenie odporności na korozję stopu WE43 odkształconego metodą KoBo jest większe rozdrobnienie ziaren, prowadzące do bardziej równomiernego rozkładu potencjału cząstkowych reakcji korozyjnych, w których granice ziaren odgrywają rolę miejsc anodowych, zaś wnętrza ziaren są lokalnymi katodami.

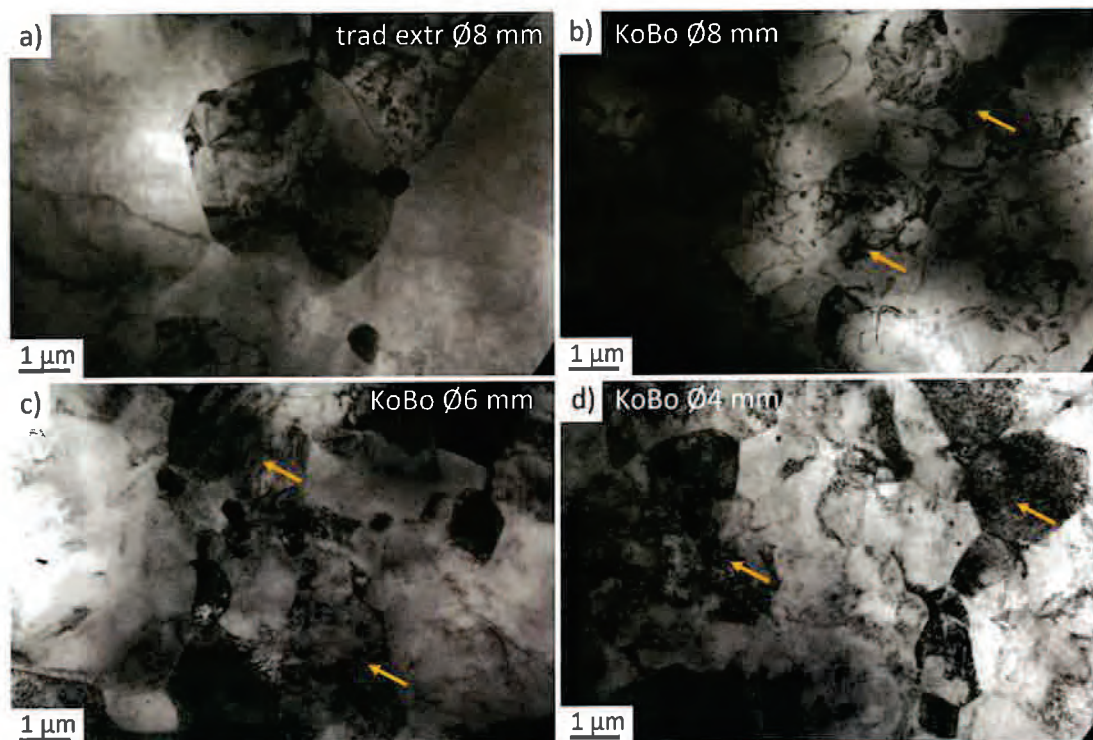
Wiedząc, że w wyniku wyciskania KoBo możliwe jest uzyskanie wyższej odporności korozyjnej stopu WE43 niż w przypadku wyciskania tradycyjnego na gorąco, w dalszej części prac skupiłam się na określeniu wpływu stopnia wyciskania na odporność korozyjną WE43. We wszystkich materiałach odkształconych metodą KoBo ukształtowała się mikrostruktura o ziarnach zbliżonych do równoosiowych. W trakcie wyciskania  $R_2$  7:1 uformowały się ziarna o średniej wielkości na poziomie 2,7 µm zaś w trakcie wyciskania przy  $R_3$  10:1 na poziomie 1,8 µm. W wyniku wyciskania przy stopniu odkształcenia  $R_2$  7:1 nastąpiła zmiana orientacji

ziaren. Zaobserwowano, że większa liczba ziaren zorientowana jest w kierunku  $\langle 10\bar{1}0 \rangle$  oraz  $\langle 2\bar{1}\bar{1}0 \rangle$  w stosunku do osi wyciskania, które są mniej odporne na korozję niż ziarna o orientacji  $\langle 0001 \rangle$  w stosunku do osi wyciskania, rys. 15a-c.



Rysunek 15. Mapy rozkładu orientacji krystalograficznych ziaren dla stopu WE43 odkształconego metodą KoBo bez nagrzewania materiału wsadowego przy różnych stopniach wyciskania: a)  $R_1$  5:1 b)  $R_2$  7:1, c)  $R_3$  10:1 [A6]

Wraz ze zwiększającym się stopniem odkształcenia uzyskano większe rozdrobnienie ziarna, zmianę orientacji ziaren, ale również zwiększenie gęstości dyslokacji, co potwierdziły obserwacje TEM (rys. 16). W wyniku tych zmian nastąpił gwałtowny spadek odporności korozyjnej stopu WE43, co jednoznacznie wskazuje, że w przypadku wyciskania przy stopniach  $R_2$  7:1 oraz  $R_3$  10:1 dominującą rolę w zachodzących procesach korozyjnych odgrywa duża gęstość dyslokacji wygenerowanych w trakcie odkształcenia. Granice ziaren są miejscami inicjacji procesów korozyjnych, w związku z tym, im większe rozdrobnienie ziarna, tym intensywniejsze procesy korozyjne mogą występować w materiale polikrystalicznym. W stopie WE43 odkształconym metodą KoBo, reakcje korozyjne są dodatkowo intensyfikowane obecnością trójskładnikowych nanowydzieleń typu Mg-Zn-Y.



Rysunek 16. Obserwacje TEM dla stopu WE43 odkształconego metodą tradycyjną w podwyższonej temperaturze (a) i metodą KoBo bez nagrzewania materiału wsadowego przy różnych stopniach wyciskania: b)  $R_1$  5:1 c)  $R_2$  7:1, d)  $R_3$  10:1 [A6]

#### 4.3.9. Analiza porównawcza czynników mikrostrukturalnych wpływających na odporność korozyjną czystego Mg, stopów z serii Mg-Zn-Al, Mg-Li oraz Mg-Y-RE

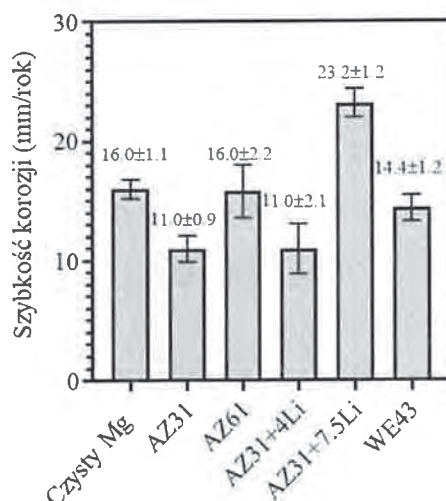
Metoda Kobo wykazuje duży potencjał w odkształcaniu Mg i jego stopów bez nagrzewania materiału wsadowego. Odkształcanie Mg i jego stopów metodą KoBo prowadzi do znaczącej redukcji średnicy wsadów, oraz do zmniejszenia wielkości ziarna i redystrybucji wydzielen drugiej fazy w ich mikrostrukturze. Najwyższy stopień ekstruzji, przy jakim sukcesywnie odkształciliśmy metal o strukturze heksagonalnej wynosi  $R$  40:1 dla stopu AZ31 z dodatkiem 4,5 mas. % Li (wyciskanie ze średnicy początkowej  $\varnothing 40$  mm do  $\varnothing 1$  mm, stopień przerobu  $\lambda=1600$ ) [A4]. Na podstawie przeprowadzonych badań należy stwierdzić, że rozdrobnienie ziaren w Mg i jego stopach po odkształceniu metodą KoBo nie zależy bezpośrednio od stopnia wyciskania, ale od intensywności procesów dynamicznej rekrytalizacji i zdrowienia dynamicznego wywołanych złożonym stanem odkształcenia wynikającym z dodatkowego rewersyjnego ruchu obrotowej matrycy wprowadzającej materiał w stan płynięcia plastycznego. Na skutek zachodzących w trakcie odkształcenia zmian mikrostrukturalnych, odporność korozyjna Mg i jego stopów zmienia się wraz ze zmianą stopnia odkształcenia, ale zależność ta nie jest liniowa.

Odporność na korozję stopów Mg zależy od ich składu chemicznego, a także, co stwierdzono na podstawie wyników zamieszczonych w pracach [A1-A6] dominującą rolę w kształtowaniu odporności korozyjnej stopów Mg odkształcanych KoBo odgrywa wielkość ziaren i gęstość dyslokacji powstałych w trakcie wyciskania. Jednoznacznie można stwierdzić, że im wyższa gęstość dyslokacji, a mniejsza wielkość ziaren, tym niższą odpornością korozyjną cechują się stopy Mg odkształcane metodą KoBo bez nagrzewania materiału wsadowego. W przypadku stopów wieloskładnikowych procesy korozyjne intensyfikowane są również obecnością wydzieleni wspierających procesy mikro-galwaniczne. Na podstawie przeprowadzonych badań określono, że odporność na korozję w środowisku zawierającym jony chlorkowe w przypadku Mg i jego stopów odkształconych metodą KoBo zmienia się w następujący sposób (rys. 17):

**AZ31 > AZ31+4Li >> WE43 > czysty Mg > AZ61 >> AZ31+7,5Li.**

W celu zdefiniowania czynników, która mają najistotniejszy wpływ na szybkość korozji w przypadku analizowanych stopów Mg, szybkość korozji odniesiono do ich cech mikrostrukturalnych zestawionych w Tabeli 1.

Spośród analizowanych materiałów najbardziej odporny na działanie medium korozyjnego jest stop AZ31 o średniej wielkości ziarna  $4,4 \mu\text{m}$  i ziarnach zorientowanych w kierunkach  $\langle 10\bar{1}0 \rangle$  i  $\langle 2110 \rangle$  w stosunku do osi wyciskania. W stopie AZ31 po odkształceniu metodą KoBo nie uformowały się wydzielenia typu  $\beta\text{-Mg}_{17}\text{Al}_{12}$ . Zbliżoną odpornością na korozję do stopu AZ31 cechuje się stop AZ31 z dodatkiem 4 % mas. Li. Ze względu na to, że stopy AZ31 i AZ31+4Li posiadają zbliżoną wielkość ziarna, zasadnym jest wnioskowanie, że czynnikiem sprzyjającym wyższej odporności na korozję stopu AZ31 jest krystalograficzna orientacja ziaren utworzonych w AZ31. Ze względu na to, że płaszczyzna  $\{0001\}$  jest płaszczyzną o dużej gęstości upakowania, ziarna zorientowane w kierunku  $\langle 0001 \rangle$  w stosunku do osi wyciskania są bardziej odporne na korozję niż  $\langle 10\bar{1}0 \rangle$  i  $\langle 2110 \rangle$  [35,49].



Rysunek 17. Szybkość korozji Mg i jego stopów odkształconych metodą KoBo bez wstępnego nagrzewania wsadu obliczona na podstawie wydzielonego wodoru w roztworze zawierającym jony chlorkowe [A7]

Niższą odporność na korozję niż AZ31 i AZ31+4Li cechuje się stop WE43, czysty Mg oraz AZ61. Na wymienionych materiałach zauważono formowanie się produktów korozji, które częściowo mogą chronić powierzchnię przed postępującymi reakcjami korozyjnymi. W stopie AZ61 na granicach ziaren powstały wydzielania  $\beta$ -Mg<sub>17</sub>Al<sub>12</sub>, które intensyfikują procesy mikro-galwaniczne, czego nie zauważono w przypadku wydzielen tego typu rozmieszczonych we wnętrzu ziaren AZ31. Czysty Mg odkształcony KoBo również posiada niższą odporność na korozję niż stop AZ31. Taka informacja jasno wskazuje, że istotne znaczenie w przypadku stopów z serii Mg-Zn-Al ma ilość i rozmieszczenie fazy  $\beta$ -Mg<sub>17</sub>Al<sub>12</sub>. Jeśli faza ta wydzieli się we wnętrzu ziarna, jej obecność sprzyja podwyższeniu odporności na korozję. Wraz ze zwiększającą się zawartością Al w stopie, faza  $\beta$ -Mg<sub>17</sub>Al<sub>12</sub> wydzieli się na granicach ziaren, co wzmaga procesy mikro-galwaniczne, zachodzące na granicach ziaren powodując ich szybkie rozpuszczanie. Ponieważ wielkość ziaren zarówno dla czystego Mg, jak i AZ31 jest porównywalna, należy wnioskować, że czynnikiem sprzyjającym wyższej odporności na korozję stopu AZ31 jest obecność ziaren zorientowanych w kierunku <0001> w stosunku do osi wyciskania.

Tabela 1. Podsumowanie podstawowych cech mikrostrukturalnych charakterystycznych dla badanych materiałów [A7]

	Struktura fazowa	Wielkość ziarna	Wydzielenia	Orientacja ziaren	Ref.
Mg	$\alpha(\text{Mg})$	3,9 $\mu\text{m}$	brak	$\langle 10\bar{1}0 \rangle$ $\langle 2\bar{1}10 \rangle$	[A1]
AZ31	$\alpha(\text{Mg})$	4,4 $\mu\text{m}$ ; rozkład bimodalny	duże wydzielienia $\text{Al}_5\text{Mn}_8$	$\langle 10\bar{1}0 \rangle$ $\langle 2\bar{1}10 \rangle$	[A2]
AZ61	$\alpha(\text{Mg})$	6,6 $\mu\text{m}$	duże wydzielienia $\text{Al}_5\text{Mn}_8$ nanowydzielienia $\beta\text{-Mg}_{17}\text{Al}_{12}$ zlokalizowane na granicach ziaren	$\langle 10\bar{1}0 \rangle$ $\langle 2\bar{1}10 \rangle$	[A3]
AZ31+4Li	$\alpha(\text{Mg})$	3,2 $\mu\text{m}$	duże wydzielienia AlLi	$\langle 10\bar{1}0 \rangle$ $\langle 2\bar{1}10 \rangle$	[A4]
AZ31+7.5Li	$\alpha(\text{Mg})+\beta(\text{Li})$	brak danych EBSD, na podstawie zdjęć SEM kilka $\mu\text{m}$	duże wydzielienia AlLi, $\text{MgLi}_2\text{Al}$ rozmiar ok 1 $\mu\text{m}$ , nanowydzielienia $\beta\text{-Mg}_{17}\text{Al}_{12}$ zlokalizowane w środku ziaren	brak danych	[A5]
WE43	$\alpha(\text{Mg})$	3,3 $\mu\text{m}$	$\text{Mg}_{41}\text{Nd}_5$ , $\text{Mg}_{24}\text{Y}_5$ , $\text{Mg}_{12}\text{Nd}$ , potrójne nanowydzielienia Mg-Nd-Y	przypadkowa	[A6]

Interesującym zagadnieniem jest zachowanie korozyjne stopów o strukturze dwufazowej  $\alpha(\text{Mg})+\beta(\text{Li})$ . Zdecydowanie wyższą odporność na korozję w środowisku jonów chlorkowych zaobserwowano się dla stopów jednofazowych  $\alpha(\text{Mg})$  niż dla stopów o strukturze dwufazowej typu  $\alpha(\text{Mg})+\beta(\text{Li})$ . Odporność korozyjna stopów AZ31+7.5Li jest kontrolowana stosunkiem udziału fazy  $\alpha(\text{Mg})$  do fazy  $\beta(\text{Li})$ . Jak podano w pracy [A5] im większe rozdrobnienie faz w materiale, tym niższa odporność na korozję. Mechanizm ten wyłumaczono w rozdziale 4.3.8.

Stop WE43 cechuje się zupełnie odmiennym składem chemicznym od wszystkich analizowanych materiałów, ale posiada zbliżoną wielkość ziarna i słabo wykształconą teksturę. Wyniki opisane w pracy [A6] jednoznacznie wskazują, że dla określonych parametrów odkształcenia metodą KoBo możliwe jest podwyższenie odporności korozyjnej stopu w odniesieniu do wyciskania tradycyjnego na gorąco. Jest to wynikiem uzyskania większego rozdrobnienia mikrostruktury w trakcie procesu KoBo. Rozważając wpływ stopnia odkształcenia metodą KoBo na odporność korozyjną stopu WE43, należy zwrócić uwagę, że im większe rozdrobnienie tym niższa odporność na korozję. Procesy korozyjne postępujące na granicach ziaren są wzmożone przez obecność trójskładnikowych nanowydzieleń o składzie

Mg-Nd-Y, których rolę w kształtowaniu odporności korozyjnej stopów z serii Mg-Y-RE metodą KoBo, w przyszłych badaniach należy opisać w sposób bardziej szczegółowy.

#### 4.3.10. Podsumowanie

Na podstawie analizy wyników badań przedstawionych w przedłożonym cyklu „Wpływ mikrostruktury na kształtowanie odporności korozyjnej Mg i jego stopów odkształcanych metodą wyciskania współbieżnego z oscylującą matrycą” sformułowałam następujące wnioski:

- ✓ Metoda wyciskania współbieżnego z oscylującą matrycą (KoBo) umożliwia wyciskanie Mg i jego stopów przy wysokich stopniach odkształcenia bez nagrzewania materiału wsadowego. Najwyższy stopień odkształcenia, jaki zastosowano w trakcie wyciskania metodą KoBo bez nagrzewania materiału wsadowego wynosi R 40:1 dla stopu na bazie Mg z dodatkiem 4 mas. % Li.
- ✓ Istnieje graniczne odkształcenie plastyczne generowane podczas wyciskania metodą KoBo, które sprzyja powstawaniu dużej ilości defektów struktury krystalicznej, głównie w postaci dyslokacji, a ich obecność intensyfikuje procesy korozyjne prowadząc do obniżenia odporności korozyjnej materiału.
- ✓ W wyniku odkształcenia metodą KoBo czystego Mg, osiągnięto znaczącą redukcję średniej wielkości ziaren. Nie zaobserwowano jednak jednoznacznej zależności pomiędzy zwiększającym się stopniem odkształcenia a zmianą rozdrobnienia mikrostruktury. Rozdrobnienie ziarna jest regulowane przez intensywność procesów, w wyniku których następuje przebudowa mikrostruktury, tj. rekrytalizacji i zdrowienia dynamicznego. Odkształcenie metodą KoBo czystego Mg prowadzi do znacznego rozdrobnienia mikrostruktury oraz do poprawy jego odporności korozyjnej, przy czym nie można w tym przypadku zdefiniować prostej zależności. Nie zaobserwowano, by wraz ze zwiększającym się stopniem odkształcenia, nastąpiło podwyższenie odporności korozyjnej czystego Mg, co jest sprzeczne z powszechnie panującą wiedzą. W wyniku działania złożonego stanu naprężeń w trakcie odkształcenia metodą KoBo bez nagrzewania materiału wsadowego, w mikrostrukturze czystego technicznie Mg powstaje duża gęstość dyslokacji. Największą gęstość dyslokacji we wnętrzu ziaren uzyskano dla materiału o najmniejszym rozmiarze ziarna. Dodatkowo, znaczne rozdrobnienie mikrostruktury spowodowało utworzenie dużej ilości granic ziaren - miejsc inicjacji korozji (im mniejsze ziarno, tym wyższa ilość granic ziaren). Obecność wysokiej gęstości dyslokacji we wnętrzu rozdrobionych ziaren intensyfikowała procesy degradacji materiału.

- ✓ Odporność korozyjna wieloskładnikowych stopów na bazie Mg w trakcie procesu odkształcania metodą KoBo bez nagrzewania materiału wsadowego jest zjawiskiem niezwykle złożonym. Zależy nie tylko od składu chemicznego, stopnia odkształcenia i uformowanej w wyniku odkształcenia mikrostruktury, ale również od wpływu złożonego stanu naprężeń. Należy podkreślić, że duża ilość defektów struktury krystalicznej gromadzonych we wnętrzu ziaren w trakcie odkształcenia przy udziale złożonego stanu naprężeń jest dodatkowo generowana w trakcie zmiany drogi odkształcenia wywołanego ruchami oscylującej matrycy.
- ✓ KoBo jest efektywną metodą rozdrobnienia mikrostruktury dla wieloskładnikowych stopów z serii Mg-Al-Zn. W przypadku prętów AZ31 odkształconych metodą KoBo, odnotowano wzrost granicy plastyczności, ale odporność korozyjna była niższa niż odporność materiału przed odkształceniem. Tak złożonego wpływu odkształcenia na właściwości materiałów, w przypadku stosowania różnych metod odkształcenia plastycznego, do tej pory nie odnotowano, zwłaszcza dla materiałów o strukturze heksagonalnej. Niska odporność korozyjna stopu AZ31 jest wynikiem zarówno utworzenia się mikrostruktury o bimodalnym rozkładzie wielkości ziarna, jak i obecności dużej gęstości dyslokacji.
- ✓ Głównym mechanizmem korozyjnym, tak jak w przypadku innych metod odkształcenia stopów Mg-Al-Zn, jest korozja mikro-galwaniczna, a postępujące reakcje są zależne od ilości Al w stopie. Przy zawartości Al na poziomie 3% mas. nie odnotowano w stopach po odkształceniu obecności fazy  $\beta$ -Mg<sub>17</sub>Al<sub>12</sub>, a mikro-ogniwa tworzyły się pomiędzy granicami ziaren o anodowym charakterze a wnętrzami ziaren, które pełniły rolę lokalnej katody. W tym przypadku, im mniejsza wielkość ziarna, tym niższa odporność na korozję. Przy wyższej zawartości Al, faza  $\beta$ -Mg<sub>17</sub>Al<sub>12</sub> wydzieliła się na granicach ziaren, co spowodowało dodatkowy czynnik powstawania mikro-ogniw galwanicznych, tym samym przyspieszając degradację materiału.
- ✓ W przypadku stopów na bazie Mg z dodatkiem Li, odporność korozyjna zależna jest udziału Li w osnowie Mg, czyli od jego budowy fazowej. Zarówno dla stopu jedno, jak i dwufazowego wraz ze zwiększeniem stopnia odkształcenia następuje spadek odporności korozyjnej, przy czym stop odkształcony KoBo jest bardziej odporny na korozję niż materiał wsadowy. Spośród odkształconych stopów o budowie jednofazowej wyższą odpornością cechuje się stop o mniejszym rozdrobnieniu ziarna osiągniętym dla niższego stopnia odkształcenia. W trakcie wyciskania stopu przy wyższym stopniu odkształcenia we wnętrzu ziaren wydzieliła się faza  $\beta$ -Mg<sub>17</sub>Al<sub>12</sub>, której obecność zintensyfikowała zachodzące procesy korozyjne. Mechanizm korozyjny w stopach o budowie dwufazowej  $\alpha$ (Mg)+ $\beta$ (Li) postępuje

głównie pomiędzy fazami  $\alpha(\text{Mg})$  i  $\beta(\text{Li})$  oraz jest zależny od ich rozdrobnienia i wzajemnego rozłożenia. Wyższy stopień odkształcenia powoduje rozdrobnienie mikrostruktury stopu, tym samym powodując fragmentację fazy  $\beta(\text{Li})$  w osnowie fazy  $\alpha(\text{Mg})$  skutkując przyspieszeniem reakcji korozyjnych. Dzieje się tak, ponieważ w układzie heterogenicznym, korozja typu mikro-galwanicznego kontrolowana jest przez stosunek fazy  $\beta(\text{Li})$  do  $\alpha(\text{Mg})$ , oraz ich wzajemne rozmieszczenie. W tym przypadku rolę anody pełni faza  $\beta(\text{Li})$ . Wyższe rozdrobnienie faz skutkowało powstaniem większej ilości mikro-ogniwi lokalnych. Reakcje te były przyspieszone poprzez obecność fazy  $\text{MgLi}_2\text{Al}$  zidentyfikowanej na granicach ziaren.

- ✓ Zmiany mikrostrukturalne wywołane w trakcie odkształcenia metodą KoBo spowodowały poprawę właściwości stopu WE43 reprezentującego serię stopów na bazie Mg o składzie chemicznym Mg-Y-RE, ale tylko w ograniczonym przedziale parametrów wyciskania, tj. przy najniższym zastosowanym stopniu odkształcenia. Wraz ze zwiększającym się stopniem odkształcenia, wielkość ziarna ulegała redukcji. Zmiany mikrostrukturalne wywołane odkształceniem metodą KoBo bez wstępnego nagrzewania stopu z serii Mg-Y-RE, w porównaniu do tego samego stopu wyciskanego konwencjonalnie w temperaturze 400 °C, spowodowały wyraźny wzrost zarówno granicy plastyczności, jak i wytrzymałości na rozciąganie w temperaturze otoczenia, niezależnie od stopnia odkształcenia. Poprawę odporności korozyjnej odnotowano tylko dla najniższego stopnia odkształcenia bez wstępnego nagrzewania materiału odkształcanego metodą KoBo w odniesieniu do stopu wyciskanego na gorąco. Spadek odporności korozyjnej wraz ze zwiększającym się stopniem odkształcenia związany jest z powstaniem większej ilości granic ziaren pełniących funkcję lokalnych anod oraz obecności trójskładnikowych nanowydzieleń typu Mg-Nd-Y, które najprawdopodobniej przyspieszają formowanie się lokalnych mikro-ogniwi.

#### **4.3.11. Wkład w rozwój dyscypliny**

Wyniki badań przedstawione w cyklu publikacji stanowiącym osiągnięcie naukowe, które jest podstawą do uzyskania stopnia naukowego doktora habilitowanego, wnoszą znaczący wkład w rozwój dyscypliny Inżynieria Materiałowa. Przedstawiony do oceny cykl publikacji zawiera oryginalne wyniki i opisuje nowatorski pomysł odkształcania metali o strukturze heksagonalnej zmodyfikowaną metodą wyciskania, w trakcie której wyeliminowany jest proces grzania, co pozwala na znaczną redukcję kosztów ich przerobu. Odkształcenie plastyczne Mg i jego stopów bez wstępnego nagrzewania materiału wsadowego metodą KoBo, dzięki której

możliwe jest uzyskanie półwyrobów o użytecznej wielkości, stanowi nowość w formowaniu właściwości stopów Mg bez wstępnego nagrzewania materiału odkształcanego. Opublikowane przeze mnie prace jednoznacznie wskazują, że ze względu na złożony stan mikrostruktury tworzący się podczas odkształcenia stopów o różnym składzie chemicznym, nie można sformułować jednoznacznej zależności pomiędzy mikrostrukturą Mg i jego stopów odkształczanych metodą KoBo bez wstępnego nagrzewania materiału a ich odpornością na korozję. Tym samym należy podkreślić, że do tej pory nie istniały prace badawcze wskazujące na możliwość odkształcenia Mg i jego stopów przy tak wysokich stopniach wyciskania bez wstępnego nagrzewania materiału odkształcanego.

**Mój wkład w rozwój dyscypliny inżynierii materiałowej polega na:**

- wykazaniu, że duże rozdrobnienie ziarna uzyskane w pojedynczym cyklu przejścia przez zespół matryc w trakcie procesu odkształcania metodą KoBo bez wstępnego nagrzewania materiału wsadowego nie zawsze prowadzi do podwyższenia odporności korozyjnej materiałów na bazie Mg. Podwyższenie odporności korozyjnej wywołane rozdrobnieniem ziarna uzyskano dla czystego Mg oraz dla następujących stopów: AZ31+4Li, AZ31+7,5Li oraz dla WE43. W przypadku stopów z serii AZXX odporność korozyjna uległa obniżeniu,
- wykazaniu, że wysoka wartość odkształcenia uzyskana w trakcie wyciskania czystego Mg metodą KoBo powoduje akumulację dużej energii odkształcenia, co jest powodem tworzenia się wysokiej gęstości splotów dyslokacyjnych. Z jednej więc strony metoda KoBo pozwala na uzyskanie mikrostruktury drobnoziarnistej, ale w środku ziaren następuje gromadzenie dużej ilości dyslokacji, które są główną przyczyną spadku odporności korozyjnej,
- opisie odporności korozyjnej stopów z serii AZXX (AZ31 i AZ61) po odkształceniu metodą KoBo i wskazaniu głównych czynników, które wpłynęły na obniżenie ich odporności korozyjnej w stosunku do materiału wsadowego. Udowodniłam, że pomimo dużego rozdrobnienia wielkości ziaren, zarówno wysoka gęstość dyslokacji wygenerowanych w trakcie odkształcenia, jak i obecność fazy  $\beta$ -Mg<sub>17</sub>Al<sub>12</sub>, która przy wyższym niż 3 % mas. Al wydziela się na granicach ziaren, powodują zwiększenie ilości mikro-ogniw korozyjnych na granicach ziaren powodując szybką degradację materiału,
- wykazaniu, że duże rozdrobnienie ziarna uzyskane w trakcie wyciskania metodą KoBo stopów na bazie Mg z dodatkiem Li nie sprzyja podwyższeniu ich odporności korozyjnej. W przypadku stopów o zawartości Li poniżej 5,5 mas.% (struktura

jednofazowa) wyższy stopień odkształcenia prowadzi do wydzielenia się faz  $\beta$ -Mg<sub>17</sub>Al<sub>12</sub> oraz Li<sub>0,81</sub>Mg<sub>0,19</sub>, których obecność zwiększa ilość miejsc inicjacji reakcji mikro-galwanicznych z osnową magnezową. W przypadku stopów Mg-Li o zawartości Li ok. 7,5 mas.% (struktura dwufazowa) im większe rozdrobnienie jednej fazy w drugiej, tym bardziej intensywnie zachodzą reakcje korozyjne. Powodem takiego zachowania jest tworzenie się korozji mikro-galwanicznej pomiędzy bardziej aktywną fazą  $\beta$ (Li), a mniej aktywną fazą  $\alpha$ (Mg),

- wykazaniu, że wyciskanie stopu WE43 metodą KoBo bez wstępnego nagrzewania materiału odkształcanego przy R<sub>1</sub> 5:1 pozwala na uzyskanie mikrostruktury drobnoziarnistej, o mniejszej wielkości ziaren, niż te uformowane w trakcie wyciskania tradycyjnego przy tych samych parametrach, ale w temperaturze 400 °C. Nie mniej jednak, wyższa gęstość dyslokacji i tworzenie się nanowydzielen typy Mg-Nd-Y, przy wyższych stopniach odkształcenia, wspomagają tworzenie się reakcji mikro-galwanicznych.

**Oprócz przedstawionego cyklu publikacji wskazanego jako osiągnięcie w pkt 4 załącznika 3, posiadam również inne osiągnięcia przedstawione w załączniku 6.**

Wśród nich na szczególną uwagę zasługuje wątek badawczy dotyczący wytwarzania proszków ze stopów na osnowie Mg o składach chemicznych niedostępnych w sprzedaży komercyjnej. Działania te podjęłam wspólnie z firmą Amazemet Sp z o.o. Z przygotowanych proszków podjęłam próbę wytworzenia materiałów metodą laserowego stapiania w złożu proszkowym (z ang. *Laser Powder Bed Fusion, LPBF*) oraz metodą spiekania impulsowo- plazmowego (z ang. *Pulse Plasma Sintering, PPS*). Przykładem jest publikacja dotycząca opisu właściwości stopu dwufazowego Mg-7,5Li-3Al-Zn % mas. (**Załącznik 7**):

- **A. Dobkowska, Ł. Żrodowski, M. Chlewicka, M. Korallnik B. Adamczyk-Cieślak, J. Ciftci, B. Morończyk, M.J. Kruszewski, J. Jaroszewicz, D. Kuc, W. Świążkowski, J. Mizera, A comparison of the microstructure-dependent corrosion of dual-structured Mg-Li alloys fabricated by powder consolidation methods: Laser powder bed fusion vs pulse plasma sintering, Journal of Magnesium and Alloys, 2022, DOI:10.1016/j.jma.2022.06.003, IF 17,6; 100 pkt MNiSW**

W przedstawionej pracy wykorzystałam proszek o składzie chemicznym Mg-7,5Li-3Al-Zn (% mas.) wytworzony w systemie indukcyjnym na urządzeniu RePowder firmy Amazemet Sp z o.o. Następnie porównałam mikrostrukturę i właściwości otrzymanych materiałów ze stopem wyciskany na gorąco. Na uwagę zasługuje fakt, że w mikrostrukturze

materiałów drukowanych powstały liczne błędy ułożenia, które są odpowiedzialne za podwyższenie właściwości mechanicznych drukowanego stopu Mg-7,5Li-3Al-Zn (% mas.) w odniesieniu do materiałów wytwarzanych innymi metodami. Wyniki przeprowadzonych pomiarów odporności korozyjnej są również obiecujące – jeśli uda się zoptymalizować parametry drukowania w taki sposób, by uzyskać stop bez obecności porów, jego odporność korozyjna będzie wyższa niż stopów o takim samym składzie chemicznym wytwarzanych metodami tradycyjnymi. Można to uzyskać dzięki możliwości kształtowania mikrostruktury o zmiennym udziale fazy  $\alpha$ (Mg) do  $\beta$ (Li), co z kolei wpływa na intensywność zachodzących w materiale procesów korozyjnych.

Wyniki badań dotyczące wytwarzania proszków ze stopów na osnowie Mg o składach chemicznych niedostępnych w sprzedaży komercyjnej były również podstawą do złożenia zgłoszenia patentowego „Sposób wytwarzania stopów Mg-Li-Al-Zn o ultra niskiej gęstości i ich zastosowanie” (**Załącznik 8**), w którym jestem pierwszym autorem.

Ważnym osiągnięciem naukowym w trakcie mojej kariery naukowej było również określenie zależności wielkość ziarna vs. odporność korozyjna dla czystej miedzi produkowanej różnymi metodami, stosowanej do wytwarzania powłok na kontenerach służących do przechowywania odpadów radioaktywnych. Wyniki przeprowadzonych w tym zakresie badań zawarłam w publikacji przedstawionej w **Załączniku 9**:

- **A.Dobkowska**, M. D. Castillo, J. Turnbull, S. Ramamurthy, D. Zagidulin, D. Moser, M. Behazin, P. Keech, D.W. Shoemsmith, J.J. Noël, *A comparison of the corrosion behaviour of copper materials in dilute nitric acid*, Corrosion Science, vol. 192, 2021, 109778, s. 1-12, DOI:10.1016/j.corsci.2021.109778, IF 7,205; 140 pkt MNiSW.

W publikacji jednoznacznie określiłam wpływ wielkości ziaren na zachodzące zjawiska korozyjne na miedzi w obecności napowietrzonego kwasu azotowego, którego śladowe ilości mogą tworzyć się w warunkach składowania odpadów radioaktywnych w wyniku obecności promieniowania gamma. Udowodniłam, że w przypadku mikrostruktury gruboziarnistej kluczowym czynnikiem wpływającym na postępujące mechanizmy korozyjne jest orientacja krystalograficzna ziaren i ich wzajemne ułożenie determinujące stosunek powierzchni anodowej do katodowej postępujących reakcji. Przy czym, zmienna szybkość korozji jest zależna nie tylko od orientacji krystalograficznej ziaren, ale także od adsorpcji jonów  $\text{NO}_3^-$ , który ma różne energie adsorpcji w zależności od kierunku ułożenia ziaren. W przypadku miedzi o mikrostrukturze drobnoziarnistej zaobserwowałam zdecydowane obniżenie szybkości korozji w stosunku do materiału gruboziarnistego. Wykazałam, że w przypadku mikrostruktury

drobnoziarnistej reakcje korozyjne zdominowane są przez mechanizm mikro-galwaniczny oddziaływania wnętrza ziaren (katod) z granicami ziaren (anod), gdzie większe ziarno sprzyja postępowaniu reakcji korozyjnych na granicach ziaren. Na podstawie przeprowadzonych badań zaproponowałam również sekwencję reakcji korozyjnych postępujących na miedzi, w mikrostrukturze której obecne są liczne pory (wytwarzanej metodą natryskiwania na zimno). Określiłam, że lokalna zmiana środowiska korozyjnego w obszarze porów nie jest rezultatem redukcji  $O_2$ , gdyż jego transport do środka porów jest ograniczony, a wynika z obecności jonów  $Cu^+$  i innych utleniaczy, które inicjują cykl korozji katalitycznej. Opublikowane wyniki stanowiły podstawę do rozszerzenia zakresu badań odporności korozyjnej dla miedzi natryskiwanej na zimno stosowanej do wytwarzania powłok na stalowych kontenerach służących do składowania odpadów radioaktywnych, a także do optymalizacji parametrów natryskiwania na zimno przez grupę inżynierów pracujących w Nuclear Waste Management Organization (NWMO) w Kanadzie. Ich zadaniem jest taki dobór parametrów natryskiwania powłoki miedzianej na stalowym kontenerze, żeby zminimalizować, a jeśli to możliwe - wyeliminować powstawanie porów w mikrostrukturze natryskiwanej powłoki miedzianej.

**5. Informacja o wykazywaniu się istotną aktywnością naukową albo artystyczną realizowaną w więcej niż jednej uczelni, instytucji naukowej lub instytucji kultury, w szczególności zagranicznej.**

W latach 2018 - 2020 odbyłam staż doktorski w renomowanej na światową skalę jednostce naukowej University of Western Ontario, London, Kanada. W ramach projektu „Effect of impurities on copper corrosion behaviour” współfinansowanego przez Nuclear Waste Management Organization w Toronto (NWMO), współpracowałam z grupą inżynierską NWMO oraz naukowcami z Chemistry Department oraz Surface Science Western, Western University of Ontario (**Załącznik 10**). W trakcie trwania projektu pracowałam nad powłoką wykonaną z czystej miedzi na kontenerze przeznaczonym na odpady radioaktywne. Głównym celem moich prac było określenie poziomów tolerancji dla różnych zanieczyszczeń powstających w trakcie procesu technologicznego (C, O, S, H i P) w powłoce miedzi bez pogorszenia jej właściwości korozyjnych. Powłoka musiała spełniać założenia ochrony katodowej kontenera na odpady radioaktywne określone przez normy NWMO. Efektem moich działań był udział w 5 konferencjach międzynarodowych oraz opublikowanie artykułu przedstawionego w **Załączniku 9**:

- **A.Dobkowska**, M. D. Castillo, J. Turnbull, S. Ramamurthy, D. Zagidulin, D. Moser, M. Behazin, P. Keech, D.W. Shoesmith, J.J. Noël, *A comparison of the corrosion*

*behaviour of copper materials in dilute nitric acid*, Corrosion Science, vol. 192, 2021, 109778, s. 1-12, DOI:10.1016/j.corsci.2021.109778, IF 7,205; MNiSW 140 pkt.

W trakcie stażu pracowałam również w ramach projektu „Characterizing the 1 billion year old Native Copper of the Lake Superior region, North America”. W tym projekcie współpracowałam z Zircon and Accessory Phase Laboratory, University of Western Ontario. Uzyskane wyniki prac zostały zaprezentowane w trakcie spotkania z firmą SKB Solna w Szwecji oraz na konferencji EGU General Assembly 2020:

- D. Moser, J.J Noël, **A. Dobkowska**, D. Zagidulin, J. Perritt, P. Keech, M. Behazin, J. Binns, G. Arcuri, and B. Langelier, *Learning from 1 billion year old copper*, EGU General Assembly 2020, Online, 4–8 May 2020, EGU2020-12231, <https://doi.org/10.5194/egusphere-egu2020-12231>, 2020.

W ramach studiów doktoranckich, w roku 2013 oraz 2015, odbyłam dwumiesięczny staż w laboratorium korozyjnym, Department of Metals and Corrosion Engineering, University of Chemistry and Technology (UCT) w Pradze. Brałam udział w wielu warsztatach naukowych, np. „Corrosion Chemistry - Faraday Discussion”, Chemistry Centre, Burlington House, Londyn, Wielka Brytania, “Introduction to vibrational spectroscopy” UCT, Praga czy “Nondestructive evaluation and characterization of materials”, ParisTech we Francji. Wszystkie te aktywności rozwinęły moje umiejętności w zakresie badań korozyjnych i ukierunkowały przyszłą pracę naukową.

## **6. Informacja o osiągnięciach dydaktycznych, organizacyjnych oraz popularyzujących naukę lub sztukę.**

### *Osiągnięcia dydaktyczne*

W roku 2022, wzorując się na kanadyjskich standardach kształcenia, stworzyłam autorski przedmiot „*Corrosion engineering of light metals and their alloys*” prowadzony w jęz. angielskim dla studentów studiów magisterskich, który składa się z dwóch części: wykładowej oraz projektowej. W semestrze zimowym roku akademickiego 2024/2025 prowadziłam projekt badawczy w ramach przedmiotu „Research Project – Biomaterials” oraz laboratorium „Badanie właściwości mechanicznych różnych materiałów do zastosowań biomedycznych” w ramach cyklu „Materiały i ich zastosowania”. Prowadzę również prace dyplomowe inżynierskie oraz magisterskie. W latach 2022 – 2024 wypromowałam 10 studentów, wszystkie prace napisane zostały w języku angielskim. Jedną z prac prowadzona była we współpracy z firmą SWERIM AB ze Szwecji i dotyczyła wpływu metody wodorowania na wchłanianie wodoru w stalach

konstrukcyjnych. Jestem również promotorem pomocniczym doktoratu Marlene Gonzalez „Advanced research on bioabsorbable Zn alloys”, który rozpoczął się w semestrze letnim roku akademickiego 2023/2024.

*Osiągnięcia organizacyjne:*

Przed uzyskaniem stopnia doktora, w latach 2013-2015 byłam przewodniczącą Wydziałowej Rady Doktorantów oraz członkiem Wydziałowej Komisji ds. Jakości Kształcenia. Po uzyskaniu stopnia doktora, od roku 2017 jestem opiekunem laboratorium metalograficznego oraz laboratorium korozyjnego na Wydziale Inżynierii Materiałowej Politechniki Warszawskiej. W roku 2022, pomagałam przy organizacji konferencji European Materials Research Society (19-21.09.2022 Warszawa).

*Osiągnięcia popularyzujące naukę:*

Od roku 2023, jestem członkiem Academic Advisory Committee w konkursie stypendialnym „The Kościuszko Foundation – Exchange to US”. Aktywnie recenzuję publikacje naukowe dla czasopism takich jak: Journal of Magnesium and Alloys, Journal of Alloys and Compounds czy Acta Biomaterialia. W latach 2022-2024 wygłosiłam 4 wykłady na zaproszenie:

- 17.04.2024 Upsalla University, Upsalla, Szwecja “Corrosion properties of ultralight Mg-Li alloys”,
- 17.11.2022 Institute of Metals and Technology, Ljubljana, Słowenia, "Review of Mg-Li alloys",
- 18.11.2022 University of Ljubljana, Faculty of Natural Sciences and Engineering, Słowenia, "Microstructure dependent corrosion of Mg-Li alloys",
- 16.04.2021 University of Chemistry and Technology, Praga, Czechy, "Effect of microstructural features on corrosion resistance of pure Cu".

W latach 2020 – 2022 kilkakrotnie byłam zaproszona jako oceniający podczas sympozjum młodych naukowców NACE Southern Ontario Student Section (SOSS).

**7. Oprócz kwestii wymienionych w pkt. 1-6, wnioskodawca może podać inne informacje, ważne z jego punktu widzenia, dotyczące jego kariery zawodowej.**

W roku 2012, po ukończeniu studiów magisterskich, rozpoczęłam studia doktoranckie na Wydziale Inżynierii Materiałowej Politechniki Warszawskiej. W trakcie doktoratu opracowałam podstawowy model mechanizmów korozyjnych występujących w odlewanych stopach Mg-Li. Wyniki uzyskane w trakcie studiów doktoranckich przedstawiłam

na 17 konferencjach krajowych i zagranicznych. Za pracę doktorską otrzymałam **nagrodę I stopnia** przyznaną przez **Polskie Stowarzyszenie Korozyjne (2019)**.

W roku 2020, po powrocie ze stażu podoktorskiego, kontynuowałam współpracę z grupą badawczą dr hab. inż. Dariusza Kuca, prof. Pol. Śl., w zakresie przetwarzania stopów na bazie Mg różnymi metodami, w tym metodami tradycyjnymi na gorąco, takimi jak wyciskanie, walcowanie, a także technikami nowatorskimi takimi jak ekstruzja z oscylującą matrycą (tzw KoBo) czy też przeciskanie przez śrubowy kanał kątowy (z ang. tubular channel angular pressing, TCAP). Przeprowadzone przeze mnie prace badawcze prowadzone dla różnych serii stopów na bazie Mg wyciskanych metodą KoBo zostały zawarte w cyklu publikacji, które stanowią osiągnięcie naukowe będące postawą do uzyskania stopnia naukowego doktora habilitowanego. Wyniki badań dotyczące metod przeróbki plastycznej stopów Mg prowadzonej w podwyższonej temperaturze zostały opublikowane w następujących w czasopismach z listy JCR:

- I. Bednarczyk, **A. Dobkowska**, O. Hilšer, S. Rusz, M. Pastrňák, R. Čada, M. Jabłońska, M. Tkocz, K. Kowalczyk, D. Pałgan, D. Necas, J. Mizera, Influence of temperature and number of passes during twist channel angular pressing (TCAP) on the microstructural, mechanical, and corrosion properties of Mg–4Li–Ca, Arch. Civ. Mech. Eng. 24 (2024) 1–15. <https://doi.org/10.1007/s43452-024-00903-y>, IF 4,4; 140 pkt MNiSW
- **A. Dobkowska**, B. Adamczyk – Cieślak, J. Kubásek, D. Vojtěch, D. Kuc, E. Hadasik, J. Mizera, Microstructure and corrosion resistance of a duplex structured Mg–7.5Li–3Al–1Zn, J. Magnes. Alloy. 9 (2021) 467–477. <https://doi.org/10.1016/j.jma.2020.07.007>, IF 10,088; 100 pkt MNiSW
- **A. Dobkowska**, B. Adamczyk – Cieślak, D. Kuc, E. Hadasik, T. Płociński, E. Ura-Bińczyk, J. Mizera, Influence of bimodal grain size distribution on the corrosion resistance of Mg–4Li–3Al–1Zn (LAZ431), J. Mater. Res. Technol. 13 (2021) 346–358. <https://doi.org/10.1016/j.jmrt.2021.04.078>, IF 6,267; 100 pkt MNiSW
- **A. Dobkowska**, B. Adamczyk-Cieślak, A. Towarek, P. Maj, E. Ura-Bińczyk, M. Momeni, D. Kuc, E. Hadasik, J. Mizera, The Influence of Microstructure on Corrosion Resistance of Mg-3Al-1Zn-15Li (LAZ1531) Alloy, J. Mater. Eng. Perform. 29 (2020) 2679–2686. <https://doi.org/10.1007/s11665-020-04775-0>, IF 2,2; 70 pkt MNiSW

W trakcie pracy nad materiałami na osnowie Mg, nawiązałam współpracę z naukowcami z Politechniki Białostockiej. W ramach projektu "Metal Matrix Composites with natural filler (Grant No. 2018/31/D/ST8/00890 NCN) powstała publikacja dotycząca roli wzmocnienia w kompozytach o osnowie magnezowej:

- I. Zgłobicka, **A. Dobkowska**, A. Zielińska, E. Borucinska, M. J. Kruszewski, R. Zybala, T. Płociński, J. Idaszek, J. Jaroszewicz, K. Paradowski, B. Adamczyk-Cieślak, K. Nikiforow, B. Bucholc, W. Świąszkowski, K.J. Kurzydłowski: In-depth analysis of the influence of bio-silica filler (*Didymosphenia geminata* frustules) on the properties of Mg matrix composites, *Journal of Magnesium and Alloys*, Elsevier B.V, vol. 11, nr 8, 2023, s. 2853-2871, DOI:10.1016/j.jma.2023.08.001, IF 17,6; 100 pkt MNiSW

Równolegle, podjęłam współpracę z firmą Amazemet Sp z o.o. w zakresie produkcji proszków i druku ultralekkich stopów Mg. Jako pierwsi na świecie sukcesywnie zatimizowaliśmy stopy z dodatkiem Li, a proszki wydrukowaliśmy metodą laserowego stapiania w złożu proszkowym. Współpraca z Amazemet Sp z o.o. odbywa się na wielu obszarach pracy z metalami lekkimi. Efekty tej współpracy są opublikowane w wymienionych poniżej artykułach oraz pracy dyplomowej:

- **A. Dobkowska**, Ł. Żrodowski, M. Chlewicka, M. Korallnik B. Adamczyk-Cieślak, J. Ciftci, B. Morończyk, M.J. Kruszewski, J. Jaroszewicz, D. Kuc, W. Świąszkowski, J. Mizera, A comparison of the microstructure-dependent corrosion of dual-structured Mg-Li alloys fabricated by powder consolidation methods: Laser powder bed fusion vs pulse plasma sintering, *Journal of Magnesium and Alloys*, 2022, DOI:10.1016/j.jma.2022.06.003, IF 17,6; 100 pkt MNiSW
- Ł. Żrodowski, R. Wróblewski, M. Leonowicz, B. Morończyk, T. Choma, J. Ciftci, W. Świąszkowski, **A. Dobkowska**, E. Ura-Bińczyk, P. Błyskun, J. Jaroszewicz, A. Krawczyńska, K. Kulikowski, B. Wysocki, T. Cetner, How to control the crystallization of metallic glasses during laser powder bed fusion? Towards part-specific 3D printing of in situ composites, *Additive Manufacturing*, , vol. 76, 2023, Numer artykułu: 103775, s. 1-40, DOI:10.1016/j.addma.2023.103775, IF 10,998; 200 pkt MNiSW
- **A. Dobkowska**, M.J. Kruszewski, J. Ciftci, B. Morończyk, I. Zgłobicka, R. Zybala, Ł. Żrodowski, Microstructure and Corrosion of Mg-Based Composites Produced from Custom-Made Powders of AZ31 and Ti6Al4V via Pulse Plasma

Sintering. *Materials* **2024**, *17*, 1602. <https://doi.org/10.3390/ma17071602>, IF 3,4; 140 pkt MNiSW

- Burak Bolat, Influence of manufacturing method on properties of AZ31/Ti and AZ31/Ti6Al4V composites”, praca dyplomowa magisterska, 2023

Na okoliczność wykorzystania proszków powstałych we współpracy z firmą Amazemet Sp z o.o. pozyskałam również projekt badawczy „Nowe możliwości kształtowania mikrostruktury i właściwości korozyjnych dwufazowych stopów Mg-Li” w ramach programu Miniatura 6 finansowanego przez NCN. Równolegle, w zakresie badań elektrochemicznych, wspierałam również zadania w projekcie europejskim „Promoting safety by a novel combination of imaging technologies for biodegradable magnesium implants, MgSafe”, European Union’s Horizon 2020 Marie Skłodowska-Curie Action (MSCA), numer grantu 811226. Uzyskane wyniki zostały opublikowane:

- D.C. Martinez, A. Borkam-Schuster, H. Helmholz, **A. Dobkowska**, B. Luthringer-Feyerabend, T. Płociński, R. Willumeit-Römer, W. Świąszkowski, Bone cells influence the degradation interface of pure Mg and WE43 materials: Insights from multimodal in vitro analysis, *Acta Biomater.* 187 (2024) 471–490. <https://doi.org/10.1016/j.actbio.2024.08.015>, IF 9,4; 140 pkt MNiSW
- D. Martinez, **A. Dobkowska**, R. Marek, H. Ćwieka, J. Jaroszewicz, T. Płociński, Č. Donik, H. Helmholz, B. Luthringer-Feyerabend, B. Zeller-Plumhoff, R. Willumeit-Römer, W. Świąszkowski, In vitro and in vivo degradation behavior of Mg-0.45Zn-0.45Ca (ZX00) screws for orthopedic applications, *Bioactive Materials*, vol. 28, 2023, s. 132-154, DOI:10.1016/j.bioactmat.2023.05.004, IF 18,56; 200 pkt MNiSW

Od roku 2022 biorę udział w międzynarodowym projekcie OPUS LAP „Nowe stale ODS do zastosowań w ekstremalnych warunkach z wykorzystaniem ultradźwiękowej dyspersji nanotlenków w połączeniu z SLM i PPS” prowadzonym we współpracy trójstronnej z Institute of Metals and Technology w Słowenii oraz University of Chemistry and Technology w Pradze. Byłam pomysłodawcą i głównym autorem projektu. Biorę również udział w międzynarodowym projekcie finansowanym przez NCBiR w ramach grupy wyszehradzkiej V4 „Rozwój zaawansowanych stopów magnezu przeznaczonych do pracy w warunkach ekstremalnych”, rozpoczęłam współpracę z Magnesium Research Center, Kumamoto, Japonia nad stopami na bazie Mg umacnianymi fazami LPSO (z ang. *long period stacking ordered phases*). W ramach prac badawczych prowadzę badania odporności korozyjnej stopów Mg-LPSO w różnych środowiskach, czego wynikiem są publikacje oraz prace dyplomowe:

- **A. Dobkowska**, F. Lofaj, M.A. González García, D.C. Martinez, K. Kulikowski, A. Paradiso, J. Idaszek, J. Gubicza, P. Jenei, M. Kabátová, L. Kvetková, M. Lisnichuk, S. Inoue, Y. Kawamura, W. Świąszkowski, Structural, mechanical, corrosion, and early biological assessment of tantalum nitride coatings deposited by reactive HiTUS, *Surf. Coatings Technol.* 493 (2024). <https://doi.org/10.1016/j.surfcoat.2024.131267>, IF 5,3; 100 pkt MNiSW
- D. Pałgan, **A. Dobkowska**, A. Zielińska, D. Drozdenko, K. Máthis, W. Świąszkowski, The Role of LPSO Structures in Corrosion Resistance of Mg-Y-Zn Alloys, *Crystals*, 2022 (12), IF 2,670; 70 pkt MNiSW
- Mahmoud Abubakra, Influence of manufacturing method on biocorrosion behaviour of Mg-1Ca-0.5Zn-0.1Y-0.03Mn (at.%) alloy, praca dyplomowa magisterska, 2024
- Riddhi Vasant Rajkuwar, Influence of annealing on corrosion resistance of Mg-1Ca-0.5Zn-0.1Y-0.03Mn alloy, praca dyplomowa magisterska, 2023
- Marlene Gonzalez, Microstructural, corrosive and mechanical properties of tantalum nitride coatings produced on Mg substrate by a novel High Target Utilization Sputtering (HITUS), praca dyplomowa magisterska, 2023.

Moje obecne zainteresowania naukowe skupiają się wokół zastosowania metod addytywnych w opracowaniu materiałów na bazie Mg i Zn stosowanych w biomedycynie. Na tę okoliczność, nawiązałam współpracę z grupą badawczą Francesco Di'Elia z Department of Materials Science and Engineering, Uppsala University. W ramach naszej współpracy prowadzimy intensywne działania dążące do opracowania parametrów wydruku jedno- i dwufazowych stopów Mg zawierających Li oraz Ca.

Brałam udział w licznych szkoleniach podnoszących moje kompetencje, m. in. ukończyłam kurs „The language of conference presentations” zorganizowany przez Centre for Teaching and Learning, The University of Western Ontario w London, Kanada oraz kurs Agile PM Foundation zakończony egzaminem, kurs „Modelling of corrosion for nuclear reactors” organizowany przez INSTN w Saclay we Francji. Posiadam również zweryfikowane międzynarodowe kwalifikacje akademickie potwierdzone certyfikatem International Academic Qualifications, World Educational Services (**Załącznik 11**).

Wynikiem mojej dotychczasowej działalności naukowej jest **37 publikacji opublikowanych w czasopiśmie z JCR**. Po uzyskaniu stopnia doktora brałam udział w **26 konferencjach krajowych i międzynarodowych**. Brałam udział w **5 projektach finansowanych przez NCN i NCBiR oraz w 2 projektach finansowanych przez University of Western Ontario i Nuclear Waste Management Organization (Kanada)**. Byłam kierownikiem **3 projektów (Załącznik 12)**. Biorę aktywny udział w recenzowaniu prac naukowych w czasopiśmie z JCR. Za swoje osiągnięcia naukowe w latach 2021-2022 otrzymałam **Indywidualną Nagrodę I stopnia JM Rektora Politechniki Warszawskiej**

W tabeli przedstawiam moje wskaźniki bibliometryczne (stan na dzień 10.01.2025)

	Wskaźniki bibliometryczne	
	wg Scopus	wg Web of Science
Indeks Hirsha bez autocytowań	9	9
Liczba publikacji	36	35
Liczba cytowań	301	269
Liczba cytowań bez autocytowań	248	220
Liczba publikacji jako jedyny autor	0	0
Liczba publikacji jako pierwszy autor	20	19

#### Literatura do rozdziału 4

- [1] F. Pan, Q. Wang, B. Jiang, J. He, Y. Chai, J. Xu, An effective approach called the composite extrusion to improve the mechanical properties of AZ31 magnesium alloy sheets, Mater. Sci. Eng. A. 655 (2016) 339–345. <https://doi.org/10.1016/j.msea.2015.12.098>.
- [2] Q. Yang, B. Jiang, Y. Tian, W. Liu, F. Pan, A tilted weak texture processed by an asymmetric extrusion for magnesium alloy sheets, Mater. Lett. 100 (2013) 29–31. <https://doi.org/10.1016/j.matlet.2013.02.118>.
- [3] A. Korbel, W. Bochniak, Method of plastic forming of materials, EP 0 711 210 B1, 2000.
- [4] K. Sztwiertnia, J. Kawalko, M. Bieda, M. Jaskowski, K. Pieła, W. Bochniak, Microstructure and texture of zinc deformed by extrusion with forward-backward rotating die (KoBo), IOP Conf. Ser. Mater. Sci. Eng. 82 (2015) 1–4. <https://doi.org/10.1088/1757-899X/82/1/012084>.
- [5] J. Dutkiewicz, P. Bobrowski, S. Rusz, O. Hilser, T.A. Tański, W. Borek, M. Łagoda, P. Ostachowski, P. Pałka, G. Boczek, D. Kuc, T. Mikuszewski, Effect of Various SPD Techniques on Structure and Superplastic Deformation of Two Phase MgLiAl Alloy, Met. Mater. Int. 24 (2018) 1077–1089. <https://doi.org/10.1007/s12540-018-0118-3>.
- [6] J. Maciejewski, Z. Mróz, An upper-bound analysis of axisymmetric extrusion assisted by cyclic torsion, J. Mater. Process. Technol. 206 (2008) 333–344. <https://doi.org/10.1016/j.jmatprotec.2007.12.061>.

- [7] A. Korbel, W. Bochniak, Refinement and control of the metal structure elements by plastic deformation, *Scr. Mater.* 51 (2004) 755–759. <https://doi.org/10.1016/j.scriptamat.2004.06.020>.
- [8] W. Bochniak, A. Korbel, P. Ostachowski, S. Ziółkiewicz, J. Borowski, Extrusion of metals and alloys by KOBO method, *Obróbka Plast. Met.* XXIV (2013).
- [9] W. Bochniak, A. Korbel, P. Ostachowski, M. Łagoda, Plastic flow of metals under cyclic change of deformation path conditions, *Arch. Civ. Mech. Eng.* 18 (2018) 679–686. <https://doi.org/10.1016/j.acme.2017.11.004>.
- [10] P. Koprowski, M. Bieda, S. Boczkal, A. Jarzębska, P. Ostachowski, J. Kawałko, T. Czeppe, W. Maziarz, M. Łagoda, K. Sztwiertnia, AA6013 aluminium alloy deformed by forward-backward rotating die (KoBo): Microstructure and mechanical properties control by changing the die oscillation frequency, *J. Mater. Process. Technol.* 253 (2018) 34–42. <https://doi.org/10.1016/j.jmatprotec.2017.10.043>.
- [11] J. Kawałko, P. Bobrowski, P. Koprowski, A. Jarzębska, M. Bieda, M. Łagoda, K. Sztwiertnia, Microstructure evolution of CP titanium during deformation in KoBo process followed by cold rolling, *J. Alloys Compd.* 707 (2017) 298–303. <https://doi.org/10.1016/j.jallcom.2016.11.202>.
- [12] K. Pięta, M. Wróbel, K. Sztwiertnia, M. Jaskowski, J. Kawałko, M. Bieda, M. Kiper, A. Jarzębska, Zinc subjected to plastic deformation by complex loading and conventional extrusion: Comparison of the microstructure and mechanical properties, *Mater. Des.* 117 (2017) 111–120. <https://doi.org/10.1016/j.matdes.2016.12.056>.
- [13] C. Op't Hoog, N. Birbilis, Y. Estrin, Corrosion of pure Mg as a function of grain size and processing route, *Adv. Eng. Mater.* 10 (2008) 579–582. <https://doi.org/10.1002/adem.200800046>.
- [14] S. Gollapudi, Grain size distribution effects on the corrosion behaviour of materials, *Corros. Sci.* 62 (2012) 90–94. <https://doi.org/10.1016/j.corsci.2012.04.040>.
- [15] D. Song, A. Bin Ma, J. Jiang, P. Lin, D. Yang, J. Fan, Corrosion behavior of equal-channel-angular-pressed pure magnesium in NaCl aqueous solution, *Corros. Sci.* 52 (2010) 481–490. <https://doi.org/10.1016/j.corsci.2009.10.004>.
- [16] S.K. Woo, B.C. Suh, H.S. Kim, C.D. Yim, Effect of processing history on corrosion behaviours of high purity Mg, *Corros. Sci.* 184 (2021) 109357. <https://doi.org/10.1016/j.corsci.2021.109357>.
- [17] R.C. Zeng, J. Zhang, W.J. Huang, W. Dietzel, K.U. Kainer, C. Blawert, W. Ke, Review of studies on corrosion of magnesium alloys, *Trans. Nonferrous Met. Soc. China (English Ed.)* 16 (2006). [https://doi.org/10.1016/S1003-6326\(06\)60297-5](https://doi.org/10.1016/S1003-6326(06)60297-5).
- [18] G. Song, A. Atrens, Understanding magnesium corrosion. A framework for improved alloy performance, *Adv. Eng. Mater.* 5 (2003) 837–858. <https://doi.org/10.1002/adem.200310405>.
- [19] F.R. Cao, H. Ding, Y.L. Li, G. Zhou, J.Z. Cui, Superplasticity, dynamic grain growth and deformation mechanism in ultra-light two-phase magnesium–lithium alloys, *Mater. Sci. Eng. A.* 527 (2010) 2335–2341. <https://doi.org/10.1016/j.msea.2009.12.029>.
- [20] A. Tripathi, S.V.S.N. Murty, P.R. Narayanan, Microstructure and texture evolution in AZ31 magnesium alloy during caliber rolling at different temperatures, *J. Magnes.*

- Alloy. 5 (2017) 340–347. <https://doi.org/10.1016/j.jma.2017.07.001>.
- [21] S. Leleu, B. Rives, N. Causse, N. Pébère, Corrosion rate determination of rare-earth Mg alloys in a Na<sub>2</sub>SO<sub>4</sub> solution by electrochemical measurements and inductive coupled plasma-optical emission spectroscopy, *J. Magnes. Alloy.* 7 (2019) 47–57. <https://doi.org/10.1016/j.jma.2018.12.002>.
- [22] A. Dobkowska, B. Adamczyk-Cieślak, A. Towarek, P. Maj, E. Ura-Bińczyk, M. Momeni, D. Kuc, E. Hadasik, J. Mizera, The Influence of Microstructure on Corrosion Resistance of Mg-3Al-1Zn-15Li (LAZ1531) Alloy, *J. Mater. Eng. Perform.* 29 (2020) 2679–2686. <https://doi.org/10.1007/s11665-020-04775-0>.
- [23] H.J. Martin, M.F. Horstemeyer, P.T. Wang, Structure-property quantification of corrosion pitting under immersion and salt-spray environments on an extruded AZ61 magnesium alloy, *Corros. Sci.* (2011). <https://doi.org/10.1016/j.corsci.2010.12.025>.
- [24] D. Thirumalaikumarasamy, K. Shanmugam, V. Balasubramanian, Comparison of the corrosion behaviour of AZ31B magnesium alloy under immersion test and potentiodynamic polarization test in NaCl solution, *J. Magnes. Alloy.* 2 (2014) 36–49. <https://doi.org/10.1016/j.jma.2014.01.004>.
- [25] J.Y. Kim, J.W. Byeon, Quantitative relation of discontinuous and continuous Mg<sub>17</sub>Al<sub>12</sub> precipitates with corrosion rate of AZ91D magnesium alloy, *Mater. Charact.* 174 (2021) 111015. <https://doi.org/10.1016/j.matchar.2021.111015>.
- [26] A. Atrens, M. Liu, N.I. Zainal Abidin, Corrosion mechanism applicable to biodegradable magnesium implants, in: *Mater. Sci. Eng. B Solid-State Mater. Adv. Technol.*, 2011. <https://doi.org/10.1016/j.mseb.2010.12.017>.
- [27] D. Hanwu, W. Limin, L. Ke, W. Lidong, J. Bin, P. Fusheng, Microstructure and deformation behaviors of two Mg-Li dual-phase alloys with an increasing tensile speed, *Mater. Des.* (2016). <https://doi.org/10.1016/j.matdes.2015.10.111>.
- [28] W. Gasiór, Z. Moser, W. Zakulski, G. SCHWITZGEBEL, Thermodynamic studies and the phase diagram of the Li-Mg system, *Metall. Mater. Trans. A.* 27A (1996) 1996–2419. [https://doi.org/10.1016/0364-5916\(80\)90009-7](https://doi.org/10.1016/0364-5916(80)90009-7).
- [29] H. Matsunoshita, K. Edalati, M. Furui, Z. Horita, Ultrafine-grained magnesium–lithium alloy processed by high-pressure torsion: Low-temperature superplasticity and potential for hydroforming, *Mater. Sci. Eng. A.* 640 (2015) 443–448. <https://doi.org/https://doi.org/10.1016/j.msea.2015.05.103>.
- [30] G. Liu, W. Xie, G. Wei, Y. Yang, J. Liu, T. Xu, W. Xie, X. Peng, Dynamic recrystallization behavior and corrosion resistance of a dual-phase Mg-Li alloy, *Materials (Basel)*. 11 (2018) 1–11. <https://doi.org/10.3390/ma11030408>.
- [31] Z. Ma, G. Li, Z. Su, G. Wei, Y. Huang, N. Hort, A. Hadadzadeh, M.A. Wells, Hot deformation behavior and microstructural evolution for dual-phase Mg–9Li–3Al alloys, *J. Mater. Res. Technol.* 19 (2022) 3536–3545. <https://doi.org/10.1016/j.jmrt.2022.06.047>.
- [32] R.C. Zeng, L. Sun, Y.F. Zheng, H.Z. Cui, E.H. Han, Corrosion and characterisation of dual phase Mg-Li-Ca alloy in Hank's solution: The influence of microstructural features, *Corros. Sci.* 79 (2014) 69–82. <https://doi.org/10.1016/j.corsci.2013.10.028>.
- [33] G. Tian, J. Wang, C. Xue, S. Wang, X. Yang, H. Su, Q. Li, X. Li, C. Yan, Z. Yang,

- Improving corrosion resistance of Mg–Li alloys by Sn microalloying, *J. Mater. Res. Technol.* 26 (2023) 199–217. <https://doi.org/10.1016/j.jmrt.2023.07.205>.
- [34] M. Gu, G. Wei, J. Zhao, W. Liu, G. Wu, Influence of yttrium addition on the corrosion behaviour of as-cast Mg–8Li–3Al–2Zn alloy, *Mater. Sci. Technol. (United Kingdom)*. 33 (2017) 864–869. <https://doi.org/10.1080/02670836.2016.1244140>.
- [35] Y. Sun, F. Zhang, R. Wang, C. Peng, J. Ren, G. Song, Improving the corrosion resistance of Mg–8Li–3Al–2Zn alloy by combining Gd alloying and hot extrusion, *J. Alloys Compd.* 964 (2023) 171205. <https://doi.org/10.1016/j.jallcom.2023.171205>.
- [36] C. Zhang, L. Wu, Z. Zhao, G. Huang, B. Jiang, A. Atrens, F. Pan, Effect of Al on the microstructure, corrosion behavior and mechanical properties of Mg–4Li, *Anti-Corrosion Methods Mater.* 67 (2020) 31–37. <https://doi.org/10.1108/ACMM-06-2019-2146>.
- [37] J. Sha, M. Qiao, J. Bao, H. Liu, S. Yin, W. Liu, Z. Zhao, Z. Zhao, J. Cui, Z. Zhang, Improving the electrochemical behaviors and discharge performance of as-rolled Mg–4Li alloys through multicomponent alloying, *J. Alloys Compd.* 895 (2022) 162536. <https://doi.org/10.1016/j.jallcom.2021.162536>.
- [38] N. Sriraman, P.B. Singh, S. Kumaran, Microstructure, Mechanical and Bio-corrosion Behaviour of Thermomechanically Processed Mg–4Li–1Ca Alloy, *Trans. Indian Inst. Met.* 72 (2019) 1635–1638. <https://doi.org/10.1007/s12666-019-01599-y>.
- [39] N. Sriraman, S. Kumaran, Processing and understanding of light-weight Mg–4Li–xCa (0, 0.5 and 1) alloy for bio-degradable implant applications, *Mater. Today Proc.* 27 (2019) 1959–1961. <https://doi.org/10.1016/j.matpr.2019.09.026>.
- [40] J. Zhang, S. Liu, R. Wu, L. Hou, M. Zhang, Recent developments in high-strength Mg–RE-based alloys: Focusing on Mg–Gd and Mg–Y systems, *J. Magnes. Alloy.* 6 (2018) 277–291. <https://doi.org/10.1016/j.jma.2018.08.001>.
- [41] P.W. Chu, E.A. Marquis, Linking the microstructure of a heat-treated WE43 Mg alloy with its corrosion behavior, *Corros. Sci.* 101 (2015) 94–104. <https://doi.org/10.1016/j.corsci.2015.09.005>.
- [42] C.H. Shih, C.Y. Huang, T.H. Hsiao, C.S. Lin, The effect of the secondary phases on the corrosion of AZ31B and WE43–T5 Mg alloys, *Corros. Sci.* 211 (2023) 110920. <https://doi.org/10.1016/j.corsci.2022.110920>.
- [43] G.S. Pereira, G.Y. Koga, J.A. Avila, I.M. Bittencourt, F. Fernandez, M.H. Miyazaki, W.J. Botta, W.W. Bose Filho, Corrosion resistance of WE43 Mg alloy in sodium chloride solution, *Mater. Chem. Phys.* 272 (2021). <https://doi.org/10.1016/j.matchemphys.2021.124930>.
- [44] M. Ascencio, M. Pegguleryuz, S. Omanovic, An investigation of the corrosion mechanisms of WE43 Mg alloy in a modified simulated body fluid solution: The influence of immersion time, *Corros. Sci.* 87 (2014) 489–503. <https://doi.org/10.1016/j.corsci.2014.07.015>.
- [45] G. Liu, J. Xu, B. Feng, J. Liu, D. Qi, W. Huang, P. Yang, S. Zhang, Comparison of Corrosion Performance of Extruded and Forged WE43 Mg Alloy, *Materials (Basel)*. 15 (2022). <https://doi.org/10.3390/ma15051622>.
- [46] A.R. Eivani, M. Mehdizade, S. Chabok, J. Zhou, Applying multi-pass friction stir

- processing to refine the microstructure and enhance the strength, ductility and corrosion resistance of WE43 magnesium alloy, *J. Mater. Res. Technol.* 12 (2021) 1946–1957. <https://doi.org/10.1016/j.jmrt.2021.03.021>.
- [47] C. Yang, N. Gupta, H. Ding, C. Xiang, Effect of microstructure on corrosion behavior of we43 magnesium alloy in as cast and heat-treated conditions, *Metals (Basel)*. 10 (2020) 1–13. <https://doi.org/10.3390/met10111552>.
- [48] Y. Tang, W. Jia, X. Liu, Q. Le, Y. Zhang, Fabrication of high strength  $\alpha$ ,  $\alpha+\beta$ ,  $\beta$  phase containing Mg-Li alloys with 0.2%Y by extruding and annealing process, *Mater. Sci. Eng. A*. 675 (2016) 55–64. <https://doi.org/10.1016/j.msea.2016.08.007>.
- [49] H. Ma, L. Wu, C. Liu, M. Liu, C. Wang, D. Li, X.Q. Chen, J. Dong, W. Ke, First-principles modeling of the hydrogen evolution reaction and its application in electrochemical corrosion of Mg, *Acta Mater.* 183 (2020) 377–389. <https://doi.org/10.1016/j.actamat.2019.11.025>.



.....  
(podpis wnioskodawcy)

Publikacje A1-A7



Article

# Effect of High Deformation without Preheating on Microstructure and Corrosion of Pure Mg

Anna Dobkowska <sup>1,\*</sup>, Bogusława Adamczyk-Cieślak <sup>1</sup>, Marlene Aydee Gonzalez Garcia <sup>1</sup>,  
Wiktor Bednarczyk <sup>1</sup>, Jenő Gubicza <sup>2</sup>, Péter Jenei <sup>2</sup>, Kamilla Mukhtarova <sup>2</sup>, Marek Tkocz <sup>3</sup>, Dariusz Kuc <sup>3</sup>  
and Jarosław Mizera <sup>1</sup>

- <sup>1</sup> Faculty of Materials Science and Engineering, Warsaw University of Technology, Woloska 141, 02-507 Warsaw, Poland; boguslawa.cieslak@pw.edu.pl (B.A.-C.); marlene\_aydee.gonzalez\_garcia.dokt@pw.edu.pl (M.A.G.G.); wiktor.bednarczyk@pw.edu.pl (W.B.); jaroslaw.mizera@pw.edu.pl (J.M.)
- <sup>2</sup> Department of Materials Physics, Eotvos Lorand University, H-1117 Budapest, Hungary; jeno.gubicza@ttk.elte.hu (J.G.); jenei.peter@ttk.elte.hu (P.J.); kamillamsh@student.elte.hu (K.M.)
- <sup>3</sup> Faculty of Materials Engineering, Silesian University of Technology, Krasinskiego 8, 40-019 Katowice, Poland; marek.tkocz@polsl.pl (M.T.); dariusz.kuc@polsl.pl (D.K.)
- \* Correspondence: anna.dobkowska@pw.edu.pl

**Abstract:** In this study, the relationship between the extrusion ratio and the corrosion resistance of pure Mg deformed using extrusion with an oscillating die (KoBo) without preheating of the initial billet was investigated. The materials investigated in this study were extruded at high deformation ratios,  $R_1$  5:1,  $R_2$  7:1, and  $R_3$  10:1, resulting in significant grain refinement from the very coarse grains formed in the initial billet to a few  $\mu\text{m}$  in the KoBo-extruded samples at room temperature, which is not typical for hexagonal structures. Our research clearly shows that KoBo extrusion improves the corrosion performance of pure Mg, but there is no straightforward dependence between the extrusion ratios and corrosion resistance improvement. Although it was expected that the smallest grain size should provide the highest corrosion resistance, the dislocation density accumulated in the grain interiors during deformation at the highest extrusion ratio,  $R_3$  10:1, supports dissolution reactions. This, in turn, provides the answers for the greater grain size observed after deformation at  $R_2$  7:1, where dynamic recovery prevailed over dynamic recrystallization. This situation led to the annihilation of dislocation, leading to better corrosion resistance of the respective alloy. Therefore, the alloy with the greatest grain size has the best corrosion resistance.

**Keywords:** pure Mg; corrosion; microstructure; extrusion ratio; KoBo



**Citation:** Dobkowska, A.; Adamczyk-Cieślak, B.; Gonzalez Garcia, M.A.; Bednarczyk, W.; Gubicza, J.; Jenei, P.; Mukhtarova, K.; Tkocz, M.; Kuc, D.; Mizera, J. Effect of High Deformation without Preheating on Microstructure and Corrosion of Pure Mg. *Metals* **2024**, *14*, 949. <https://doi.org/10.3390/met14080949>

Academic Editors: Andrii Kostryzhev, Olexandra O. Marenych and Guosong Wu

Received: 2 August 2024  
Revised: 15 August 2024  
Accepted: 19 August 2024  
Published: 21 August 2024



**Copyright:** © 2024 by the authors. Licensee MDPI, Basel, Switzerland. This article is an open access article distributed under the terms and conditions of the Creative Commons Attribution (CC BY) license (<https://creativecommons.org/licenses/by/4.0/>).

## 1. Introduction

Mg alloys, due to their advantageous ratio of light weight to high strength, tend to be excellent candidates for many industrial applications. Their use is desirable to reduce the mass of engineering systems, resulting in a reduction in CO<sub>2</sub> emissions, battery electrodes, and, of course, load-bearing degradable materials [1]. The increasing demand for lightweight structures drives modern researchers and industry to look for solutions that allow for faster, more economical, and easier methods of Mg deformation. To avoid cracking, resulting in a lack of bulk integrity, Mg and Mg alloys are deformed at elevated temperatures, where their limited slip planes are activated [2,3]. The most common conventional processing methods of Mg and Mg alloys are rolling, forging, and extrusion; their properties after deformation using these methods have been well explored [4–6]. Severe plastic deformation (SPD) methods are also well known for their significant refinement of Mg and Mg alloys [7,8]. Because Mg crystallizes in a hexagonal close-packed (hcp) structure, it has only two independent, easy-slip systems at room temperature [9], so most deformation methods are conducted at high temperatures [10]. Poor formability at room temperature is a critical factor that dramatically restricts the widespread use of Mg alloys

in industry [11]. There have been some trials concerning the deformation of Mg at room temperature by high-pressure torsion [12]; however, this method is only able to produce samples in the form of discs, which are not suitable for many industrial applications.

Lately, extrusion with an oscillating die (called KoBo) has been used to form materials that are hard to deform at ambient temperature. KoBo is a modified extrusion method, which, thanks to the oscillating die assembled at the end of the extruder, is able to significantly reduce the grain size of hcp-structured material [13]. The combination of the extrusion and oscillations of the bilaterally rotating die forces the extruded materials to enter into a state of plastic flow, enabling the grain size to be reduced and improving the mechanical properties of the alloys. During KoBo, even complicated shapes can be formed at high extrusion ratios [14,15], thereby minimizing costs and maximizing the possibilities of extrusion. Therefore, the scientific and industrial interest in this method is high. To examine the method's possibilities, many materials have been extruded at high extrusion ratios under various parameters [16,17], including the hcp-structured Mg alloys investigated by our research team [18,19]. To support the results of these investigations, numerical simulations have also been conducted [20]. Nevertheless, there are very few data regarding the corrosion behavior of alloys extruded using KoBo. The corrosion mechanisms are complex, and their characterization involves many aspects (grain size, precipitations, dislocations, various environments, residual stresses, etc.) [21]. Therefore, to minimize the impact of the alloy chemistry, and to clearly define the main parameters influencing the corrosion performance of KoBo-extruded materials, in this study, the corrosion of pure Mg is evaluated. The goal of this research was to explore the possibility of extrusion at high deformation ratios of pure Mg without preheating of the initial billet using upgraded extrusion with an oscillating die at the end of the extruder. To date, there have been no detailed investigations of the effects of KoBo processing on the subsequent microstructural and corrosion changes in pure Mg. The results of this clearly show that extrusion with an oscillating die located at the end of the extruder enables the deformation of pure Mg at high deformation ratios without preheating of the initial billet. The grain refinement obtained during KoBo processing improves the corrosion resistance of the initial billet; however, no clear relationship between grain size and corrosion rate increase was observed.

## 2. Materials and Methods

### 2.1. Materials and Extrusion Method

Pure Mg in the form of a rod with an initial diameter of  $\text{Ø}40$  mm was extruded using KoBo to a diameter of  $\text{Ø}8$ ,  $\text{Ø}6$ , or  $\text{Ø}4$  mm, giving various extrusion ratios:  $R_1$  5:1,  $R_2$  7:1, and  $R_3$  10:1 (Figure 1a). Mg with a technical purity of 99.9% was cast using a Balzers furnace in graphite molds at  $680$  °C. During KoBo processing, the material was pressed through an extruder with a bilaterally rotating die located at its end. The die moves at high speed; therefore, the material enters into a viscoplastic state (Figure 1b). The initial billet temperature was  $24$  °C. The KoBo parameters were the same as those used for other Mg alloys: a punch speed of  $0.2$  mm/s, a die oscillating angle of  $\pm 8^\circ$ , and an oscillation frequency of  $5$  Hz [18].

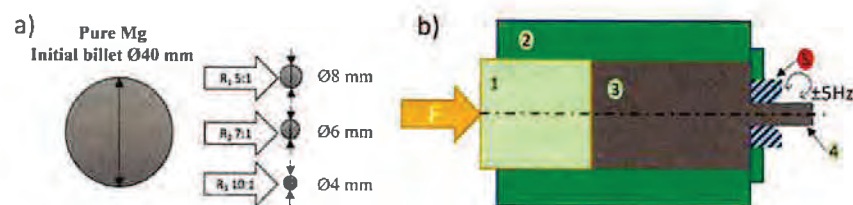


**Figure 1.** Deformation method: (a) high deformation ratios (extrusion ratios) used for pure Mg deformation investigated in this study; (b) schematic of the extrusion with an oscillating die (KoBo): 1—punch, 2—extruder, 3—initial billet, 4—final extruded material, 5—bilaterally oscillating die.

## 2.2. Microstructural Observations

Optical microscopy observations of the microstructure of the initial billet were performed using an optical microscope (AxioVision, Zeiss, Oberkochen, Germany). The microstructural characterization of the KoBo-extruded samples employed electron backscattered diffraction (EBSD) using a field-emission scanning electron microscope (FE-SEM, Hitachi SU-70, Hitachi Ltd., Tokyo, Japan) equipped with a Bruker EBSD detector (Bruker GmbH, Karlsruhe, Germany). To prepare samples for SEM observations and EBSD measurements, the extruded rods were cut into slices and polished with 1200-grit and 2400-grit SiC papers; subsequently, the surfaces perpendicular to the extrusion direction were polished with a low-energy Ar<sup>+</sup> ion-beam milling system (Hitachi IM4000 Ion Milling System, Hitachi Ltd., Tokyo, Japan) for a duration of 4 h. To avoid oxidation, measurements were performed immediately after sample preparation. The high-resolution scanning electron microscopic observations were carried out in backscattered electron mode (BSE, FE-SEM Hitachi SU-70, Hitachi Ltd., Tokyo, Japan). The EBSD data were recorded with a step size of 200 nm and processed using ATEX software (Lorraine University, Metz, France) ([www.atex-software.eu](http://www.atex-software.eu)) [22]. The crystallographic orientations of the grains are presented in the form of inverse pole figure (IPF) maps, where various colors distinguish the orientation of a given sample direction in a crystal frame. If the angle between two neighboring grains was distorted by more than 15°, then the boundary between those grains was described as a high-angle grain boundary (HAGB); when the grains were misoriented by less than 15° (a cut-off limit of 3° was selected), the boundary was described as a low-angle grain boundary (LAGB). Internal grain deformation is presented in the form of grain orientation spread (GOS) maps.

The dislocation density in the Mg samples was determined by X-ray line profile analysis (XLPA). The patterns were measured by a high-resolution rotating anode diffractometer (type: RA-MultiMax-9, manufacturer: Rigaku, Tokyo, Japan) using CuK $\alpha_1$  radiation (wavelength,  $\lambda = 0.15406$  nm). The height and width of the rectangular X-ray spot on the sample surface were 1.5 and 0.2 mm, respectively. The measured peak profiles of hcp Mg were evaluated by the convolutional multiple whole profile (CMWP) fitting procedure [23]. In this method, the diffraction pattern is fitted by the sum of a background spline and the diffraction peaks obtained as the convolution of the instrumental peaks and the theoretical line profiles related to the crystallite size and the dislocations. The instrumental peaks were measured on a NIST SRM660a LaB6 peak profile standard material. About twenty reflections of Mg appearing in the diffraction angle ( $2\theta$ ) range between 30 and 150° were evaluated. The dislocation density was determined by employing the CMWP fitting evaluation procedure on the diffraction patterns. During CMWP evaluation, the diffraction pattern was fitted by the sum of a background spline and the convolution of the instrumental pattern and the theoretical line profiles related to the parameters of the microstructure, i.e., to the crystallite size and the dislocations. The theoretical peak profile functions used in the CMWP fitting were presented in ref. [24]. In the calculation of the theoretical peak profiles, the crystallites were modelled by spheres with a log-normal size distribution, and the peak broadening caused by the strain field of dislocations was described by the Wilkens model [24]. The CMWP analysis provided the median and the lognormal variance of the crystallite size distribution and the dislocation density. Since, in the present experiments, the peak broadening caused by the crystallite size was much lower than the instrumental broadening, only the dislocation density values obtained by the CMWP method are reported in this study.

Microstructural observations of the analyzed materials were carried out using a transmission electron microscope (TEM, JEOL JEM 1200, Jeol Ltd., Tokyo, Japan) with an accelerating voltage of 120 kV. Samples cut from a cross-section perpendicular to the rod axis, in the form of discs with a diameter of 3 mm, were mechanically ground to a thickness of approximately 100  $\mu\text{m}$ . The samples were then subjected to an electrolytic thinning process using a Struers double-jet TenuPol 5 device (Struers GmbH, Willich, Germany). The electrolyte comprised a lithium chloride solution, magnesium perchlorate, methanol,

and 2-butoxy-ethanol. Electrolytic thinning was performed at  $-45\text{ }^{\circ}\text{C}$  with a voltage of approximately 90 V and a current of 100 mA. Ion milling using a Gatan 691 precision ion polishing system (PIPS, Gatan Inc., Pleasanton, CA, USA) at 3 kV for 10 min was necessary to remove the surface oxidation.

Microhardness ( $\text{HV}_{0.2}$ ) tests were performed using the Vickers method under a load of 200 g (Innovatest Falcon 500 Micro/Macro Vickers Tester, Innovatest, Wiry, Poland). Ten points in line were measured on each material.

### 2.3. Corrosion Tests

Electrochemical measurements were carried out in naturally aerated 0.01 M NaCl solution using a Gamry FAS1 potentiostat (Gamry Instruments Inc., Warminster, PA, USA) equipped with three electrodes: platinum as the counter electrode, Ag/AgCl as the reference electrode, and the measured sample as the working electrode. The electrolyte was made up using analytical-grade reagents and distilled water. The samples were immersed for 12 h, and electrochemical impedance spectroscopy was performed after 1, 6, and 12 h of immersion. Afterward, potentiodynamic polarization tests were recorded over a range of 0.2 V below  $E_{\text{OCP}}$  to 1.0 V vs. Ref (a scan rate of 5 mV/s was used), with at least three tests being conducted for each microstructural condition. The EIS and polarization curves were fitted using Gamry Echem software Version 5.58. To obtain detailed information about the corrosion damage, the corroded surfaces of the samples were observed after 1 h of immersion under open-circuit conditions using SEM (Hitachi SU-70, Hitachi Ltd., Tokyo, Japan). To remove corrosion products, the observed surfaces were chemically treated in  $\text{CrO}_3$  solution.

The corrosion rate of the investigated materials was calculated based on hydrogen evolution [25,26], and the concentration of  $\text{Mg}^{2+}$  ions in solution after the tests was measured using atomic absorption spectroscopy (AAS, GBC instrument, GBC Scientific, Keysborough, Australia). To determine the standard deviation of the measured data, three parallel samples were immersed for each extrusion condition.

## 3. Results

### 3.1. Microstructural Observations

The KoBo extrusion performed without initial preheating of the billet and at high deformation ratios resulted in significant grain refinement (Figure 2). The initial billet had a coarse-grained microstructure, which is typical for cast materials (Figure 2a). The KoBo extrusion caused a significant grain size reduction, with the distribution of grain sizes varying with respect to the changing extrusion ratio (Figure 2b–d).

The extruded microstructures show that the recrystallization intensity varied with respect to the extrusion ratio (Figure 3a–c). Interestingly, a greater extrusion ratio did not always cause a higher grain refinement. The measured grain size distribution plots are presented in Figure 2g. Surprisingly, the largest average grain size ( $d_{\text{avg}}$  3.88  $\mu\text{m}$ ) and the widest grain size spread were observed in the sample extruded to  $\text{Ø}6\text{ mm}$ ,  $R_2$  7:1 (Figure 2f), while samples subjected to a lower ( $\text{Ø}8\text{ mm}$ ,  $R_1$  5:1) or greater ( $\text{Ø}4\text{ mm}$ ,  $R_3$  10:1) reduction exhibited greater grain refinement ( $d_{\text{avg}}$  2.88  $\mu\text{m}$  and  $d_{\text{avg}}$  1.20  $\mu\text{m}$ , respectively) with a narrow grain size distribution. This trend was confirmed by the GOS map (Figure 3e). The XRD results clearly showed that the dislocation density accumulated in the sample extruded to  $\text{Ø}6\text{ mm}$  was lower than those in the other two KoBo-extruded samples (Table 1). The same trend was observed when the  $\text{GOS}_{\text{avg}}$  values were analyzed (Figure 3d–f). The dislocation densities were found to be  $(7 \pm 1) \times 10^{13}\text{ m}^{-2}$  and  $(5 \pm 1) \times 10^{13}\text{ m}^{-2}$ , respectively, for the KoBo samples extruded to  $\text{Ø}8\text{ mm}$  ( $R_1$  5:1) and to  $\text{Ø}4\text{ mm}$  ( $R_3$  10:1). Since the detection limit of the XRD method was  $10^{13}\text{ m}^{-2}$ , we were not able to obtain the numerical value of the dislocation density in the sample extruded to  $\text{Ø}6\text{ mm}$  ( $R_2$  7:1).

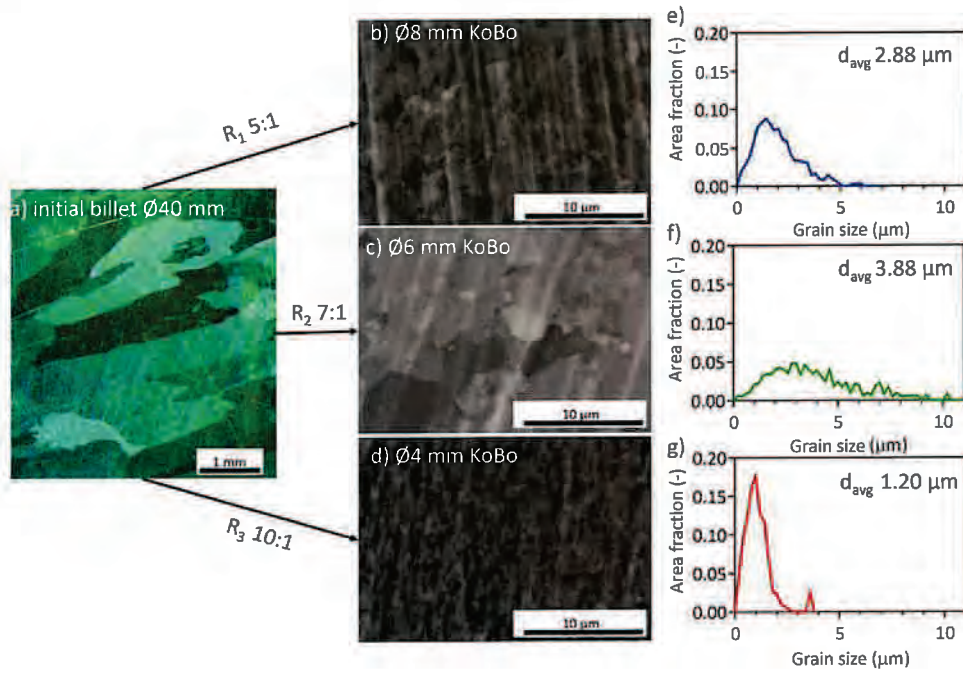


**Figure 2.** Microstructural images of pure Mg with corresponding grain size distributions: (a) initial billet (optical image), (b) KoBo-extruded to Ø8 mm ( $R_1$  5:1), (c) KoBo-extruded to Ø6 mm ( $R_2$  7:1), and (d) KoBo-extruded to Ø4 mm ( $R_3$  10:1). Grain size distribution for: (e) KoBo-extruded to Ø8 mm ( $R_1$  5:1), (f) KoBo-extruded to Ø6 mm ( $R_2$  7:1), and (g) KoBo-extruded to Ø4 mm ( $R_3$  10:1).

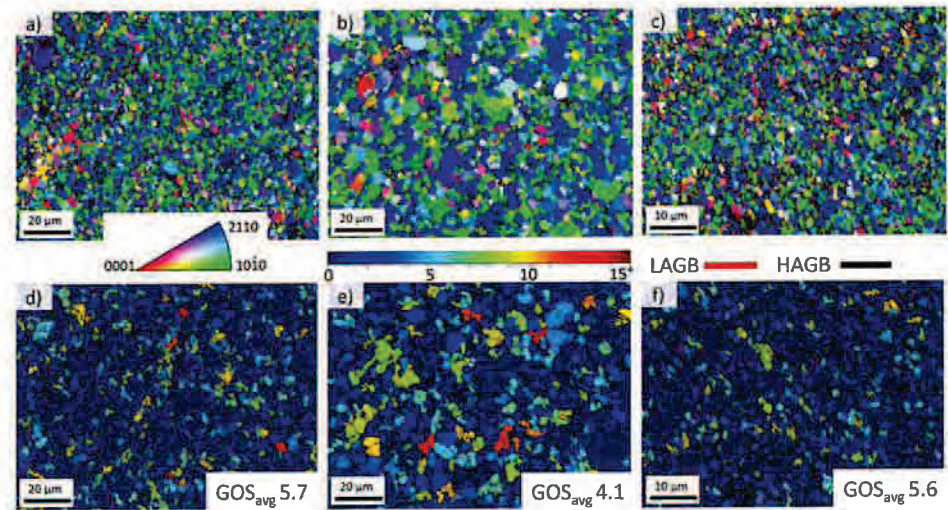


**Figure 3.** EBSD data presented in the form of inverse pole figure (IPF) maps for Mg (a) KoBo-extruded to Ø8 mm ( $R_1$  5:1), (b) KoBo-extruded to Ø6 mm ( $R_2$  7:1), and (c) KoBo-extruded to Ø4 mm ( $R_3$  10:1), with corresponding grain orientation spread (GOS) maps for Mg (d) KoBo-extruded to Ø8 mm, (e) KoBo-extruded to Ø6 mm, and (f) KoBo-extruded to Ø4 mm. Average values of the grain orientation spread ( $GOS_{avg}$ ) are given. Data were obtained from the plane perpendicular to the extrusion direction.

The orientation of the grains was random, with the majority oriented to (10-10) and to (2110) (Figure 3a–c). Moreover, the GOS distribution maps indicated around 85% undeformed grains with a GOS value of  $<5^\circ$  for the materials extruded at extrusion ratios

R<sub>1</sub> 5:1 (Figure 3d) and R<sub>3</sub> 10:1 (Figure 3f), indicating the completion of the dynamic recrystallization (DRX) processes [27–29]. After deformation at R<sub>2</sub> 7:1, the GOS map (Figure 3e) revealed a slightly lower recrystallized fraction of about 80%, with a visible substructure (LAGB) within the larger grains. All the investigated samples exhibited a {10 $\bar{1}$ 0} fiber texture, typical for extruded HCP materials, with a similar intensity for all the samples (Figure 4).

**Table 1.** Dislocation density measured using XRD (detection limit of X-ray line profile analysis is  $10^{13} \text{ m}^{-2}$ ).

Sample	Ø40 mm	Ø8 mm (R <sub>1</sub> 5:1)	Ø6 mm (R <sub>2</sub> 7:1)	Ø4 mm (R <sub>3</sub> 10:1)
Dislocation density	Below detection limit	$(7 \pm 1) \times 10^{13} \text{ m}^{-2}$	Below detection limit	$(5 \pm 1) \times 10^{13} \text{ m}^{-2}$

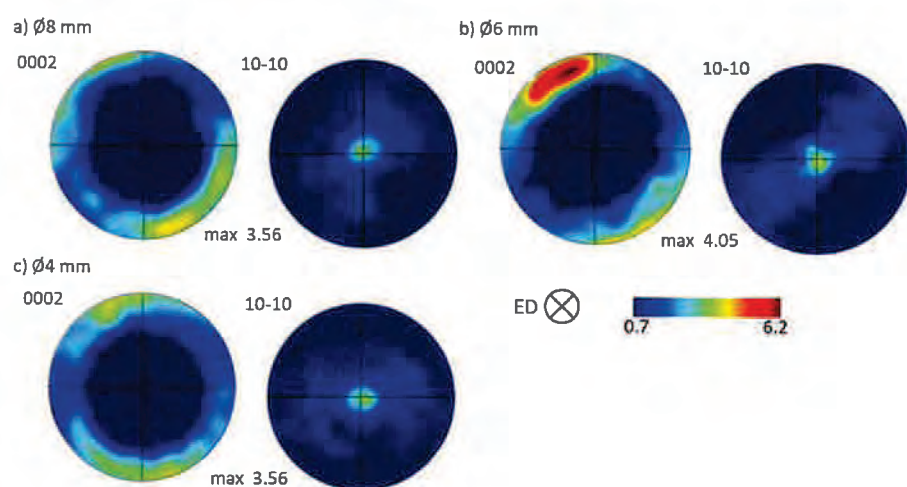


**Figure 4.** Pole figures (0002) and (10-10) obtained for pure Mg KoBo-extruded to a diameter of (a) Ø8 mm (R<sub>1</sub> 5:1), (b) Ø6 mm (R<sub>2</sub> 7:1), or (c) Ø4 mm (R<sub>3</sub> 10:1); ED—extrusion direction.

TEM images revealed that the microstructures of the extruded samples were composed of both heavily deformed areas with dislocation tangles inside (yellow arrows, Figure 5) and nearly equiaxed grains with high-angle boundaries and a low dislocation density inside them (red arrows, Figure 5). The microstructure of the sample extruded to Ø8 mm (R<sub>1</sub> 5:1) consisted of grains with various sizes (Figure 5a) and well-defined boundaries. These factors confirm that DRX takes place during KoBo extrusion [30,31]. At higher deformation ratios (R<sub>2</sub> 7:1, Ø6 mm), defects in the crystalline structure in the form of dislocations were also observed, and heavily deformed grains were formed (Figure 5b). The differing ratios of the two areas indicated that microstructural reformation during DRX and dynamic recovery (DRV) occurred with a different intensity than in the sample extruded at R<sub>1</sub> 5:1. KoBo extrusion at the highest deformation ratio (R<sub>3</sub> 10:1) did not affect microstructural reformation significantly when compared to the sample deformed at R<sub>2</sub> 7:1 (Figure 5c); however, during TEM observations, a higher number of small grains was distinguishable, which is in agreement with the EBSD data (Figure 3). The microhardness results shown in Figure 6 indicated that increasing the deformation ratio from R<sub>1</sub> 5:1 (Ø8 mm) to R<sub>2</sub> 7:1 (Ø6 mm) did not change the microhardness of the materials significantly. The average values of microhardness calculated for these samples were similar:  $40.1 \pm 1.3$  and  $41.6 \pm 1.2$ , respectively. Both materials exhibited similar microstructures, particularly with regard to the presence of areas with large, well-developed grains and smaller grains with defects inside. The highest extrusion ratio resulted in a slight increase in microhardness (about 6 HV<sub>0.2</sub>), which may be related to the smaller grain size formed.

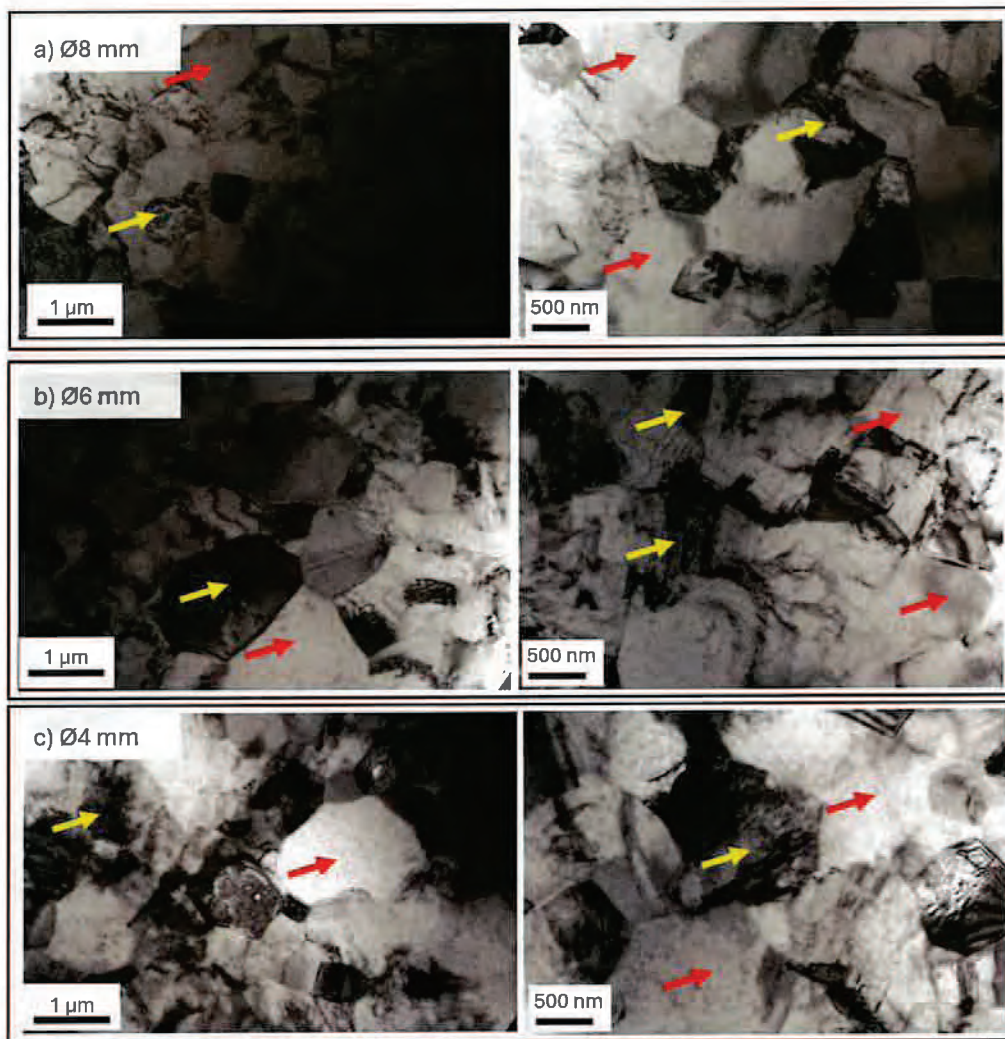


Figure 5. Bright-field TEM images obtained for pure Mg KoBo-extruded to a diameter of (a) Ø8 mm, (b) Ø6 mm, or (c) Ø4 mm. Images for each extrusion ratio are shown at two magnifications: in the first column, images taken at 30,000× are shown, while in the second column, images taken at 50,000× are depicted.

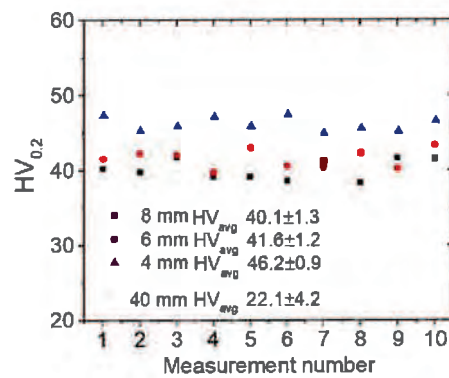
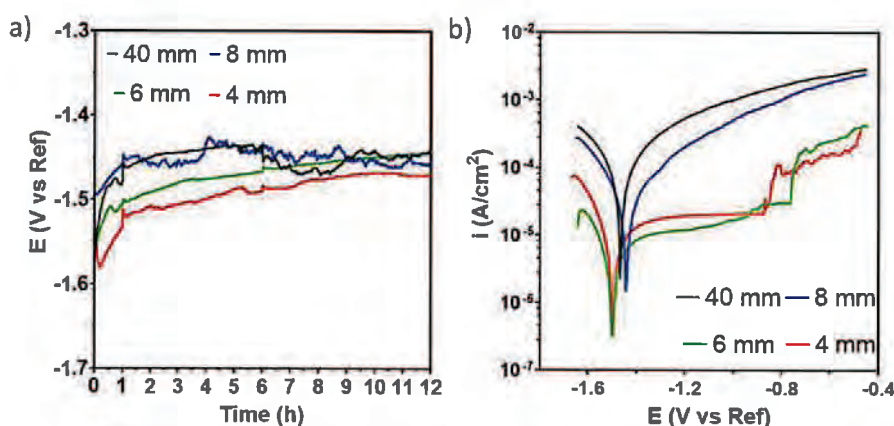


Figure 6. Microhardness profiles of the pure Mg initial billet and pure Mg KoBo-extruded to Ø8 mm, Ø6 mm, or Ø4 mm.

### 3.2. Corrosion Tests

The open circuit potential evolution during 12 h of immersion in 0.01 M NaCl is shown in Figure 7a. All the curves exhibited initial increases toward more positive values; however, oscillations were observed in the curves recorded for the initial billet and the samples extruded to  $\text{\O}8$  mm ( $R_1$  5:1). Such behavior indicates the strong anodic and cathodic reactions proceeding on the surface. This is consistent with the polarization curves, for which the highest values of the corrosion current were recorded for the initial billet and the samples extruded to  $\text{\O}8$  mm ( $R_1$  5:1) (Figure 7b). Both materials underwent active dissolution. Extrusion at higher deformation ratios ( $R_2$  7:1 and  $R_3$  10:1) changed the corrosion mechanism to a localized one. Wide plateau regions were visible on the anodic branches of the polarization curves for the samples with dimensions of  $\text{\O}6$  mm ( $R_2$  7:1) and  $\text{\O}4$  mm ( $R_3$  10:1). The higher value of  $\Delta E$  indicated a higher resistance to localized corrosion of the sample extruded to  $\text{\O}6$  mm ( $R_2$  7:1) (Table 2).



**Figure 7.** The results delivered by the electrochemical measurements performed in naturally aerated 0.01 M NaCl: (a)  $E_{\text{corr}}$  evaluation during 12 h of immersion; (b) potentiodynamic polarization curves.

**Table 2.** The electrochemical parameters calculated from the potentiodynamic polarization curves recorded in 0.01 M NaCl ( $E_{\text{corr}}$ —corrosion potential,  $E_b$ —breakdown potential).

Material	$E_{\text{corr}}$ (V/Ref)	$E_b$ (V/Ref)	$\Delta E$
Initial billet $\text{\O}40$ mm	−1.47	n/a	n/a
$\text{\O}8$ mm	−1.44	n/a	n/a
$\text{\O}6$ mm	−1.5	−0.76	0.74
$\text{\O}4$ mm	−1.5	−0.88	0.62

The Nyquist plots of the investigated alloys obtained from the EIS measurements are shown in Figure 8. In order to analyze the corrosion mechanisms of the above alloys, the corresponding equivalent circuits and the fitting data of the EIS spectra are presented in Tables 3 and 4.

$R_s$  stands for the solution resistance,  $R_{ct}$  represents the charge transfer resistance, and  $R_f$  is the film resistance. Higher values of  $R_{ct}$  and  $R_f$  indicate a better corrosion resistance of the corresponding alloy. Constant phase elements (CPEs) are used instead of an ideal capacitor to compensate for non-homogeneity in the corrosion system. Importantly,  $R_L$  (resistance) and  $L$  (inductance) describe the low-frequency inductance loop, indicating that localized corrosion has been initiated. Among the investigated materials, the highest values of resistance to corrosion were observed for the materials KoBo-extruded to  $\text{\O}6$  mm ( $R_2$  7:1) and to  $\text{\O}4$  mm ( $R_3$  10:1) and were confirmed by the highest  $R_{ct}$  and  $R_f$  values.

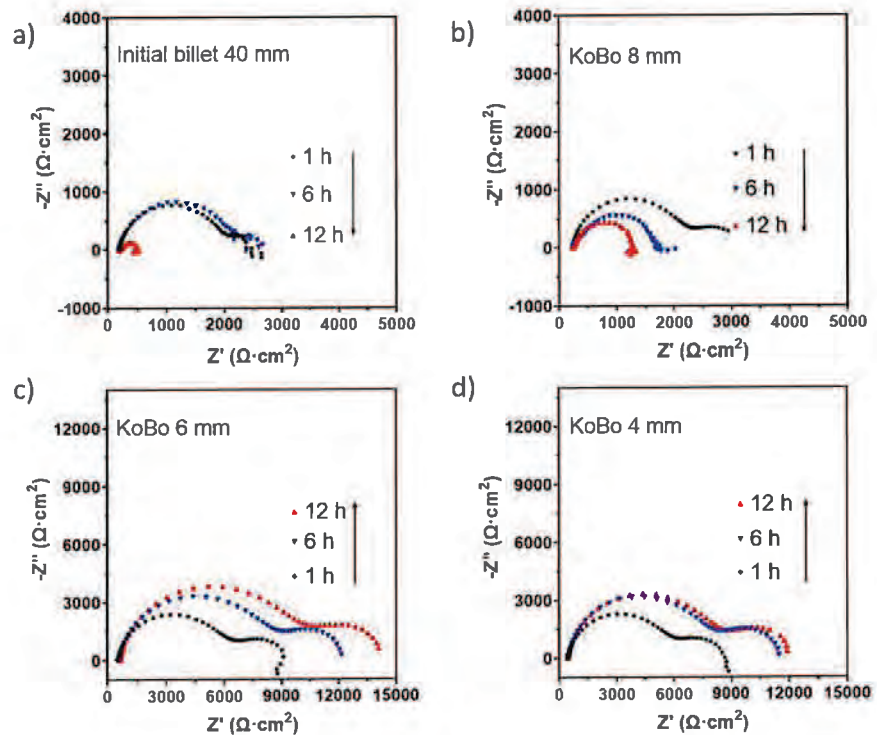


**Figure 8.** EIS results for pure Mg in naturally aerated 0.01 M NaCl delivered in the form of Nyquist plots: (a) initial billet, (b) KoBo-extruded to Ø8 mm, (c) KoBo-extruded to Ø6 mm, and (d) KoBo-extruded to Ø4 mm.

**Table 3.** Equivalent electronic circuits (EECs) used for EIS data fitting.

(a)	(b)	(c)
Ø40 mm/1 h Ø8 mm/1 h Ø6 mm/6 h Ø4 mm/6 h	Ø40 mm/6 h Ø6 mm/12 h Ø4 mm/12 h	Ø40 mm/12 h Ø6 mm/1 h Ø4 mm/1 h Ø8 mm/6 h Ø8 mm/12 h

The shape of the Nyquist plot is typical for materials with an oxide layer formed on the surface. It is worth noting that in the case of the sample extruded to Ø6 mm ( $R_2$  7:1), the corrosion resistance after 12 h was still increasing, while in the case of the sample extruded to Ø4 mm, it remained at the same level after 6 h of immersion. This is related to the passivation mechanisms occurring on the surfaces (Tables 3 and 4). The active performance of the initial billet and the sample deformed to Ø8 mm ( $R_1$  5:1) caused a weakening in their corrosion resistance with extended immersion time (Figure 8a,b). An increasing trend in the corrosion resistance with extended immersion time was shown for the samples extruded to Ø6 mm ( $R_2$  7:1) and Ø4 mm ( $R_3$  10:1) (Figure 8c,d). As shown by King et al. [32], circuit simplification enables the calculation of polarization resistance ( $R_p$ ). Given that the corrosion rate is inversely proportional to  $R_p$ , the dependence of corrosion resistance on

immersion time for the samples was calculated, and the results are shown in Figure 9. This is clear confirmation that KoBo enhances the corrosion resistance of pure Mg, with a slight increase for the sample with a diameter of Ø8 mm ( $R_2$  5:1) and a significant improvement for the material deformed to Ø6 mm ( $R_2$  7:1), though a slightly higher corrosion rate was noted for the Ø4 mm ( $R_3$  10:1) sample. Clearly, the lowest corrosion rate, regardless of the immersion time, was calculated for the Ø6 mm ( $R_2$  7:1) sample.

Table 4. Electrochemical parameters fitted for EIS results with the EECs shown in Table 3.

Sample	Immersion Time	$R_s$ ( $\Omega \cdot \text{cm}^2$ )	$R_{ct}$ ( $\Omega \cdot \text{cm}^2$ )	$CPE_{ct}$ ( $\mu\text{Ss}^a/\text{cm}^2$ )	$a$	$R_L$ ( $\Omega \cdot \text{cm}^2$ )	$L$ (H·cm <sup>2</sup> )	$R_f$ ( $\Omega \cdot \text{cm}^2$ )	$CPE_f$ ( $\mu\text{Ss}^a/\text{cm}^2$ )	$a_2$
Ø40 mm	1 h	189	380	0.003	0.83	2115	7	1906	0.00002	0.86
Ø40 mm	6 h	189	320	0.004	0.88	841	8	2085	0.0004	0.82
Ø40 mm	12 h	168	340	0.000205	0.73	1388	3130	35	0.000016	0.60
Ø8 mm	1 h	232	937	0.000202	0.75	17,520	8	2114	0.000019	0.85
Ø8 mm	6 h	247	1557	0.000054	0.73	3300	247	n/a	n/a	n/a
Ø8 mm	12 h	245	1057	0.000071	0.86	3390	52,000	n/a	n/a	n/a
Ø6 mm	1 h	506	5508	0.000004	0.89	35,000	22	5318	0.000006	0.91
Ø6 mm	6 h	569	3635	0.000006	0.81	9771	22	8099	0.000007	0.87
Ø6 mm	12 h	632	4600	0.000005	0.75	6703	20	9359	0.000006	0.88
Ø4 mm	1 h	451	2929	0.000006	0.85	8959	868,000	5425	0.000006	0.88
Ø4 mm	6 h	458	3638	0.000521	0.90	3716	12	7722	0.000006	0.86
Ø4 mm	12 h	462	3521	0.000613	0.83	4840	26	8142	0.000006	0.87

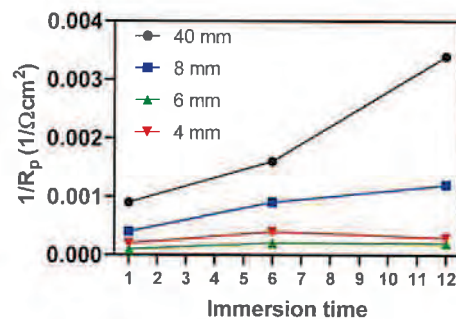
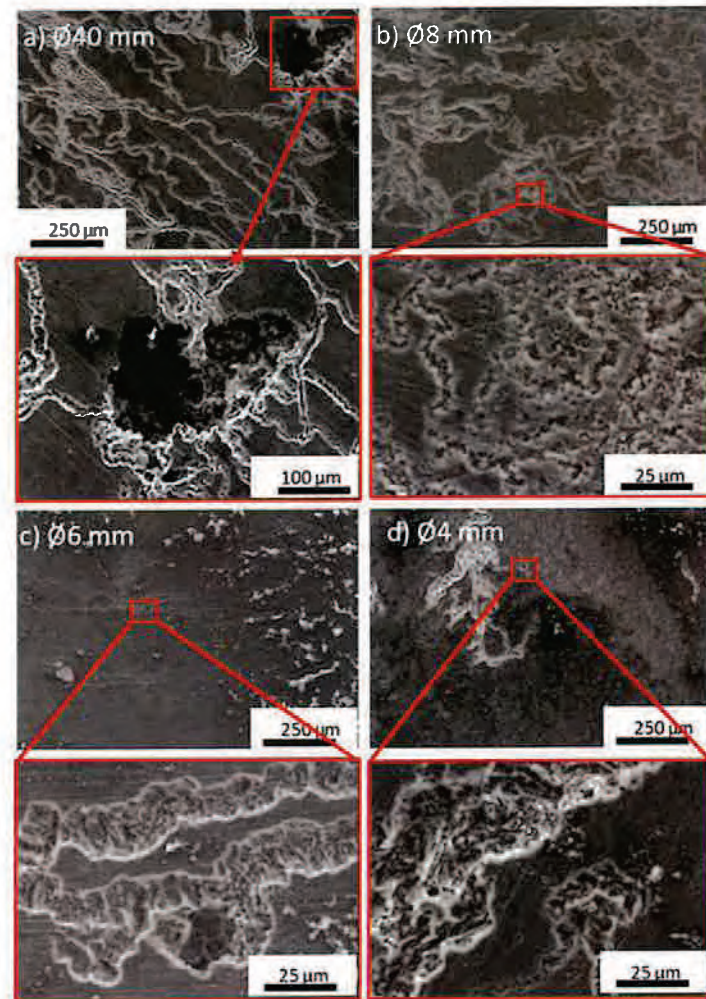


Figure 9. Typical EIS-estimated  $1/R_p$  on pure Mg (initial billet and KoBo-extruded materials) vs. time during immersion in 0.01 M NaCl.

Damage in the form of filiform corrosion with deep corrosion cavities was observed on the surface of the initial billet (Figure 10a). Corrosion with threads developing on the Mg surface was formed on the sample extruded to Ø8 mm ( $R_2$  5:1) (Figure 10b). The same type of corrosion occurred on the samples extruded at the highest extrusion ratios ( $R_2$  7:1 and  $R_3$  10:1, Figure 10c,d, respectively). The observed corrosion damage was not as deep as that observed for the initial billet. It should also be noted that the threads on the sample extruded to Ø8 mm had a different shape to those formed on the samples extruded to Ø6 mm and Ø4 mm. In the latter ones, corrosion damage propagated along privileged crystallographic planes; this type of corrosion is known as preferred crystallographic pitting [33,34].



**Figure 10.** Corrosion damage observed on the surfaces of pure Mg after corrosion product removal after 1 h immersion in naturally aerated 0.01 M NaCl: (a) initial billet ( $\text{Ø}40$  mm), (b)  $\text{Ø}8$  mm, (c)  $\text{Ø}6$  mm, and (d)  $\text{Ø}4$  mm.

#### 4. Discussion

The corrosion of Mg is a complex process and depends on the specific thermomechanical fabrication route and the resulting microstructure formed. During the last decade, researchers have tried to characterize the corrosion rate of Mg and its alloys after plastic deformation; however, their findings did not lead to a straightforward explanation concerning which microstructural components are the key factors in the mechanisms controlling their corrosion performance. The texture, dislocation density, grain size, grain distribution, and morphology of second phases are among the relevant factors; the predominance of one over another may significantly change the corrosion mechanism and the resulting corrosion rate of the materials. To simplify the complications concerning the ambiguous (cathodic/anodic) role of second phases in the corrosion of Mg alloys [35], pure Mg was investigated after KoBo extrusion. Since a similar texture intensity was observed in all the extruded samples, we can exclude this factor from further discussion. The remaining components worth consideration are the grain size, distribution, and crystallographic orientation, along with dislocation densities.

Generally speaking, in chloride-containing solution, several SPD methods improve the corrosion resistance of pure Mg via grain size reduction. Equal channel angular extrusion

(ECAE) performed on pure Mg at 200 °C reduced the grain size to ~9 μm [36], which improved the corrosion performance of the material. This result was explained by the high dislocation density, which forms more energetic crystalline defects, leading to the easier formation of a passive film on the surface. Birbilis et al. [37] showed that after equal channel angular pressing (ECAP) at 250 °C of pure Mg, the resultant more-refined grain size with a high misorientation angle promoted the formation of a more stable oxide film. Similar conditions of ECAP for pure Mg were used by Op't Hoog et al. [38], and the results showed lowered cathodic and anodic kinetics when compared to cast material. The same pure Mg samples with subsequent annealing were described in their other study [39], where the authors stated that not only does grain size reduction play a predominant role in corrosion resistance improvement, but the surface free energy and residual stress in a material are also critical. The various factors influencing pure Mg corrosion are not solely those related to the grain size and its characteristics (such as grain boundaries and crystallographic orientation) but also include the dislocation densities and strain imposed during fabrication, which seem to be especially crucial during KoBo extrusion. The dislocation density, besides high-angle grain boundaries, is of crucial importance because it can change the surface potential [40]. Everything, therefore, leads to the consideration of recrystallization intensity, which, during KoBo, depends on the extrusion ratio, thus resulting in the formation of various microstructures. Without knowledge concerning how various microstructural components formed during KoBo extrusion affect the corrosion behavior of pure Mg, we are not able to predict the corrosion performance of other Mg-based alloys fabricated using the same method. KoBo extrusion enhances the corrosion resistance of pure Mg by microstructural refinement; however, there is no clear relationship between the grain size and corrosion behavior. The corrosion resistance improvement is strongly dependent on the influence of individual microstructural components (grain size vs. dislocation density). Also, the decreasing grain size is not itself the main factor that may improve the corrosion resistance of pure Mg extruded using KoBo. During KoBo, recrystallization processes are affected by the massive plastic strain imposed during deformation. Therefore, the respective dominance of DRX vs. DRV at various extrusion ratios results in there being no linear change in the grain refinement with increasing extrusion ratio. As a result of the extrusion, the grain sizes were reduced to 2.88 μm, 3.88 μm, and 1.20 μm in the case of materials extruded to Ø8 mm (R<sub>1</sub> 5:1), Ø6 mm (R<sub>2</sub> 7:1), and Ø4 mm (R<sub>3</sub> 10:1), respectively. Therefore, considering the grain size itself, the corrosion resistance should follow the order Ø4 mm (R<sub>3</sub> 10:1) > Ø8 mm (R<sub>1</sub> 5:1) > Ø6 mm (R<sub>2</sub> 7:1). Although the smallest grain size should lead to increased passivation behavior [40], in our case, a mismatch was caused by the high dislocation density observed in the samples extruded at R<sub>1</sub> 5:1 and R<sub>3</sub> 10:1. This, in turn, provides an explanation for the greater grain size observed after deformation at R<sub>2</sub> 7:1, where, during DRV, the destruction of dislocations was observed, resulting in greater grain size formation and leading to better corrosion resistance of the corresponding alloy. This observation is opposite to the previous studies, where, with increased intensity of the plastic deformation, the dislocation intensity also increased; however, this was observed for a Mg alloy wherein second phase strengthening was also observed [41,42].

## 5. Conclusions

An attempt was made to describe the main factors influencing the corrosion resistance of KoBo-extruded pure Mg. We conclude the following:

- The KoBo method enables significant microstructural refinement for pure Mg without preheating of the initial billet, having a positive influence on its corrosion resistance.
- During KoBo deformation, there is no clear tendency for grain size reduction with increasing extrusion ratios. The grain size decreased from coarseness typical of cast material to 2.88 μm, 3.88 μm, and 1.20 μm for R<sub>1</sub> 5:1, R<sub>2</sub> 7:1, and R<sub>3</sub> 10:1.
- The corrosion resistance of the KoBo-extruded samples is related not solely to grain refinement but also to other microstructural factors, particularly the dislocation density accumulated during deformation.

**Author Contributions:** Conceptualization, A.D., D.K. and J.G.; methodology, A.D., J.G., B.A.-C., M.A.G.G. and M.T.; validation, A.D. and J.M.; formal analysis, A.D., J.G., W.B. and B.A.-C.; investigation, K.M., M.A.G.G., A.D. and P.J.; resources, M.T. and D.K.; data curation, A.D., W.B. and B.A.-C.; writing—original draft preparation, A.D., W.B., B.A.-C., J.G. and M.A.G.G.; writing—review and editing, A.D., J.G., B.A.-C., W.B., M.A.G.G. and J.M.; visualization, A.D., P.J., B.A.-C., M.A.G.G. and K.M.; supervision, A.D. and J.M.; project administration, J.M.; funding acquisition, J.M. All authors have read and agreed to the published version of the manuscript.

**Funding:** The APC was funded by the Faculty of Materials Science and Engineering, Warsaw University of Technology in Poland.

**Data Availability Statement:** The original contributions presented in the study are included in the article, further inquiries can be directed to the corresponding author.

**Conflicts of Interest:** The authors declare no conflicts of interest.

## References

- Esmaily, M.; Svensson, J.E.; Fajardo, S.; Birbilis, N.; Frankel, G.S.; Virtanen, S.; Arrabal, R.; Thomas, S.; Johansson, L.G. Fundamentals and Advances in Magnesium Alloy Corrosion. *Prog. Mater. Sci.* **2017**, *89*, 92–193. [\[CrossRef\]](#)
- Murai, T.; Matsuoka, S.I.; Miyamoto, S.; Oki, Y. Effects of Extrusion Conditions on Microstructure and Mechanical Properties of AZ31B Magnesium Alloy Extrusions. *J. Mater. Process. Technol.* **2003**, *141*, 207–212. [\[CrossRef\]](#)
- Cerreta, E.K.; Fensin, S.J.; Perez-Bergquist, S.J.; Trujillo, C.P.; Morrow, B.M.; Lopez, M.F.; Roach, C.J.; Mathaudhu, S.N.; Anghel, V.; Gray, G.T. The High-Strain-Rate Constitutive Behavior and Shear Response of Pure Magnesium and AZ31B Magnesium Alloy. *Metall. Mater. Trans. A* **2021**, *52*, 3152–3170. [\[CrossRef\]](#)
- Park, S.S.; You, B.S.; Yoon, D.J. Effect of the Extrusion Conditions on the Texture and Mechanical Properties of Indirect-Extruded Mg-3Al-1Zn Alloy. *J. Mater. Process. Technol.* **2009**, *209*, 5940–5943. [\[CrossRef\]](#)
- Wong, T.W.; Hadadzadeh, A.; Wells, M.A. High Temperature Deformation Behavior of Extruded AZ31B Magnesium Alloy. *J. Mater. Process. Technol.* **2018**, *251*, 360–368. [\[CrossRef\]](#)
- Mu, T.; Yuan, J.; Zhang, K.; Li, Y.; Li, X.; Ma, M.; Shi, G.; Sun, Z.; Zhang, K. Effect of Extrusion Ratio on Microstructures, Mechanical Properties, and High Cycle Fatigue Behavior of Mg-5Zn-1Mn Alloy. *J. Mater. Res. Technol.* **2024**, *30*, 992–1008. [\[CrossRef\]](#)
- Kasaean-Naeni, M.; Sedighi, M.; Hashemi, R. Severe Plastic Deformation (SPD) of Biodegradable Magnesium Alloys and Composites: A Review of Developments and Prospects. *J. Magnes. Alloy.* **2022**, *10*, 938–955. [\[CrossRef\]](#)
- Sepahi-Boroujeni, S.; Sepahi-Boroujeni, A. Improvements in Microstructure and Mechanical Properties of AZ80 Magnesium Alloy by Means of an Efficient, Novel Severe Plastic Deformation Process. *J. Manuf. Process.* **2016**, *24*, 71–77. [\[CrossRef\]](#)
- Hutchinson, W.B.; Barnett, M.R. Effective Values of Critical Resolved Shear Stress for Slip in Polycrystalline Magnesium and Other Hcp Metals. *Scr. Mater.* **2010**, *63*, 737–740. [\[CrossRef\]](#)
- Mansoor, P.; Dasharath, S.M. Microstructural and Mechanical Properties of Magnesium Alloy Processed by Severe Plastic Deformation (SPD)—A Review. *Mater. Today Proc.* **2020**, *20*, 145–154. [\[CrossRef\]](#)
- Imandoust, A.; Barrett, C.D.; Al-Samman, T.; Inal, K.A.; El Kadiri, H. A Review on the Effect of Rare-Earth Elements on Texture Evolution during Processing of Magnesium Alloys. *J. Mater. Sci.* **2017**, *52*, 1–29. [\[CrossRef\]](#)
- Xu, J.; Wang, X.; Shirooyeh, M.; Xing, G.; Shan, D.; Guo, B.; Langdon, T.G. Microhardness, Microstructure and Tensile Behavior of an AZ31 Magnesium Alloy Processed by High-Pressure Torsion. *J. Mater. Sci.* **2015**, *50*, 7424–7436. [\[CrossRef\]](#)
- Dobkowska, A.; Adamczyk-Cieślak, B.; Chlewicka, M.; Towarek, A.; Zielińska, A.; Koralnik, M.; Kuc, D.; Mizera, J. Evolution of Microstructure Dependent Corrosion Properties of Ultrafine AZ31 under Conditions of Extrusion with a Forward Backward Oscillating Die. *J. Mater. Res. Technol.* **2022**, *18*, 4486–4496. [\[CrossRef\]](#)
- Bochniak, W.; Korbela, A. KOBO Type Forming: Forging of Metals under Complex Conditions of the Process. *J. Mater. Process. Technol.* **2003**, *134*, 120–134. [\[CrossRef\]](#)
- Bochniak, W.; Marszowski, K.; Korbela, A. Theoretical and Practical Aspects of the Production of Thin-Walled Tubes by the KOBO Method. *J. Mater. Process. Technol.* **2005**, *169*, 44–53. [\[CrossRef\]](#)
- Bochniak, W.; Korbela, A.; Ostachowski, P.; Łagoda, M. Plastic Flow of Metals under Cyclic Change of Deformation Path Conditions. *Arch. Civ. Mech. Eng.* **2018**, *18*, 679–686. [\[CrossRef\]](#)
- Korbela, A.; Bochniak, W.; Ostachowski, P.; Błaż, L. Visco-Plastic Flow of Metal in Dynamic Conditions of Complex Strain Scheme. *Metall. Mater. Trans. A Phys. Metall. Mater. Sci.* **2011**, *42*, 2881–2897. [\[CrossRef\]](#)
- Dobkowska, A.; Zielińska, A.; Donik, Č.; Łojkowski, M.; Adamczyk-Cieślak, B. Microstructure and Properties of an AZ61 Alloy after Extrusion with a Forward-Backward Oscillating Die without Preheating of the Initial Billet. *J. Alloys Compd.* **2023**, 169843. [\[CrossRef\]](#)
- Dobkowska, A.; Adamczyk-Cieślak, B.; Koralnik, M.; Chromiński, W.; Kubasek, J.; Ciftci, J.; Kuc, D.; Mizera, J. Corrosion Behavior of Fine-Grained Mg-7.5Li-3Al-1Zn Fabricated by Extrusion with a Forward-Backward Rotating Die (KoBo). *J. Magnes. Alloy.* **2021**, *10*, 811–820. [\[CrossRef\]](#)

20. Wójcik, M.; Skrzat, A. Numerical Modelling of the KOBO Extrusion Process Using the Bodner–Partom Material Model. *Meccanica* **2022**, *57*, 2213–2230. [[CrossRef](#)]
21. Liang, J.; Liu, S.; Peng, Z.; Li, R.; Wang, B. Galvanic Corrosion Behavior of AZ31 Mg Alloy Coupled with Mild Steel: Effect of Coatings. *J. Mater. Res. Technol.* **2023**, *24*, 7745–7755. [[CrossRef](#)]
22. Beausir, B. ATEX-Software. Lorraine University, Metz, France. Available online: [www.atex-software.eu](http://www.atex-software.eu) (accessed on 12 June 2024).
23. Ribárik, G.; Gubicza, J.; Ungár, T. Correlation between Strength and Microstructure of Ball-Milled Al-Mg Alloys Determined by X-Ray Diffraction. *Mater. Sci. Eng. A* **2004**, *387–389*, 343–347. [[CrossRef](#)]
24. Gubicza, J. *X-ray Line Profile Analysis in Materials Science*; IGI Global: Hershey, PA, USA, 2014; pp. 1–343. [[CrossRef](#)]
25. Song, G.; Atrens, A. Understanding Magnesium Corrosion. A Framework for Improved Alloy Performance. *Adv. Eng. Mater.* **2003**, *5*, 837–858. [[CrossRef](#)]
26. Song, G.L.; Unocic, K.A. The Anodic Surface Film and Hydrogen Evolution on Mg. *Corros. Sci.* **2015**, *98*, 758–765. [[CrossRef](#)]
27. Jiang, M.G.; Yan, H.; Chen, R.S. Twinning, Recrystallization and Texture Development during Multi-Directional Impact Forging in an AZ61 Mg Alloy. *J. Alloys Compd.* **2015**, *650*, 399–409. [[CrossRef](#)]
28. Zeng, J.; Wang, F.; Dong, S.; Nie, X.; Fan, Y.; Dong, J. A New Dynamic Recrystallization Kinetics Model of Cast-Homogenized Magnesium Alloys. *Metall. Mater. Trans. A Phys. Metall. Mater. Sci.* **2021**, *52*, 316–331. [[CrossRef](#)]
29. Mirzadeh, H. Grain Refinement of Magnesium Alloys by Dynamic Recrystallization (DRX): A Review. *J. Mater. Res. Technol.* **2023**, *25*, 7050–7077. [[CrossRef](#)]
30. Fan, G.D.; Zheng, M.Y.; Hu, X.S.; Xu, C.; Wu, K.; Golovin, I.S. Improved Mechanical Property and Internal Friction of Pure Mg Processed by ECAP. *Mater. Sci. Eng. A* **2012**, *556*, 588–594. [[CrossRef](#)]
31. Roodposhti, P.S.; Sarkar, A.; Murty, K.L.; Scattergood, R.O. Dislocation Density Evolution during Creep of AZ31 Mg Alloy: A Study by X-ray Diffraction Line Profile Analysis. *Metallogr. Microstruct. Anal.* **2015**, *4*, 337–343. [[CrossRef](#)]
32. King, A.D.; Birbilis, N.; Scully, J.R. Accurate Electrochemical Measurement of Magnesium Corrosion Rates; A Combined Impedance, Mass-Loss and Hydrogen Collection Study. *Electrochim. Acta* **2014**, *121*, 394–406. [[CrossRef](#)]
33. Bahmani, A.; Lotfipour, M.; Taghizadeh, M.; Kim, W.J. Corrosion Behavior of Severely Plastically Deformed Mg and Mg Alloys. *J. Magnes. Alloy.* **2022**, *10*, 2607–2648. [[CrossRef](#)]
34. Pawar, S.; Slater, T.J.A.; Burnett, T.L.; Zhou, X.; Scamans, G.M.; Fan, Z.; Thompson, G.E.; Withers, P.J. Crystallographic Effects on the Corrosion of Twin Roll Cast AZ31 Mg Alloy Sheet. *Acta Mater.* **2017**, *133*, 90–99. [[CrossRef](#)]
35. Zhao, P.; Xie, T.; Ying, T.; Zhu, H.; Zeng, X. Role of Alloyed Sc on the Corrosion Behavior of Mg. *Metall. Mater. Trans. A Phys. Metall. Mater. Sci.* **2022**, *53*, 741–746. [[CrossRef](#)]
36. Li, Z.; Zhou, S.-j.; Huang, N. Effects of ECAP Processing Temperature on the Microstructure, Mechanical Properties, and Corrosion Behavior of Pure Mg. *Int. J. Miner. Metall. Mater.* **2015**, *22*, 639–647. [[CrossRef](#)]
37. Birbilis, N.; Ralston, K.D.; Virtanen, S.; Fraser, H.L.; Davies, C.H.J. Grain Character Influences on Corrosion of ECAPed Pure Magnesium. *Corros. Eng. Sci. Technol.* **2010**, *45*, 224–230. [[CrossRef](#)]
38. Op’t Hoog, C.; Birbilis, N.; Estrin, Y. Corrosion of Pure Mg as a Function of Grain Size and Processing Route. *Adv. Eng. Mater.* **2008**, *10*, 579–582. [[CrossRef](#)]
39. Ambat, R.; Aung, N.N.; Zhou, W. Evaluation of Microstructural Effects on Corrosion Behaviour of AZ91D Magnesium Alloy. *Corros. Sci.* **2000**, *42*, 1433–1455.
40. Bahmani, A.; Arthanari, S.; Shin, K.S. Formulation of Corrosion Rate of Magnesium Alloys Using Microstructural Parameters. *J. Magnes. Alloy.* **2020**, *8*, 134–149. [[CrossRef](#)]
41. Li, G.; Pan, X.; Jiang, J.; Li, J.; Xie, L.; Liu, H.; Zhang, M. Achieving Ultra-Fine Grains and High Corrosion Resistance of Al–Zn–Mg–Cu Alloy by ECAP and Post Cold Rolling. *J. Mater. Res. Technol.* **2023**, *26*, 7354–7368. [[CrossRef](#)]
42. Xue, D.; Wei, W.; Shi, W.; Guo, Y.W.; Wen, S.P.; Wu, X.L.; Huang, H.; Nie, Z.R. Effect of Cold Rolling on Mechanical and Corrosion Properties of Stabilized Al–Mg–Mn–Er–Zr Alloy. *J. Mater. Res. Technol.* **2021**, *15*, 6329–6339. [[CrossRef](#)]

**Disclaimer/Publisher’s Note:** The statements, opinions and data contained in all publications are solely those of the individual author(s) and contributor(s) and not of MDPI and/or the editor(s). MDPI and/or the editor(s) disclaim responsibility for any injury to people or property resulting from any ideas, methods, instructions or products referred to in the content.

Available online at [www.sciencedirect.com](http://www.sciencedirect.com)

**jmr&t**  
Journal of Materials Research and Technology  
journal homepage: [www.elsevier.com/locate/jmrt](http://www.elsevier.com/locate/jmrt)



## Original Article

# Evolution of microstructure dependent corrosion properties of ultrafine AZ31 under conditions of extrusion with a forward backward oscillating die



Anna Dobkowska <sup>a,\*</sup>, Bogusława Adamczyk-Cieślak <sup>a</sup>, Monika Chlewicka <sup>a</sup>,  
Aleksandra Towarek <sup>a</sup>, Aleksandra Zielińska <sup>a</sup>, Milena Koralniak <sup>a</sup>,  
Dariusz Kuc <sup>b</sup>, Jarosław Mizera <sup>a</sup>

<sup>a</sup> Faculty of Materials Science and Engineering, Warsaw University of Technology, Wołoska 141, Warsaw, 02-507, Poland

<sup>b</sup> Institute of Materials Engineering, Silesian University of Technology, Krasińskiego 8, Katowice, 40-019, Poland

## ARTICLE INFO

## Article history:

Received 17 March 2022

Accepted 24 April 2022

Available online 29 April 2022

## Keywords:

Corrosion

Grain refinement

Microstructure

Grain size distribution

Extrusion rate

Magnesium alloy

## ABSTRACT

The present work aims to elucidate the role of microstructural changes induced by the extrusion with a forward backward oscillating die, thus verifying a novel approach to developing deformation methods for Mg-based alloys at ambient temperature. The main aim of this study was to show the process which enables the reduction of the hcp-structured AZ31 rods (40 mm in diameter) to the wires with diameters of 6 mm, 4 mm and 2 mm, without initial preheating of the billet. In contrary to the studies up to date, the significant microstructure refinement led to the decline in corrosion resistance of the wires with 6 mm and 4 mm diameters slightly relative to the original material. The highest extrusion ratio resulted in the formation of an ultrafine, equiaxed microstructure, which caused a tremendous corrosion resistance decrease. The significant decline in corrosion resistance of this alloy is a result of the highest number of HAGBs and is promoted by the accumulation of tangled dislocations. Summing up, the corrosion behaviors of the extruded alloys were mainly affected by the recrystallization stage that occurred during deformation, and not by the grain size alone.

© 2022 The Author(s). Published by Elsevier B.V. This is an open access article under the CC BY license (<http://creativecommons.org/licenses/by/4.0/>).

## 1. Introduction

Magnesium-based alloys containing Al and Zn (the AZ series) are among the most commonly used lightweight alloys owing to their good castability, machining characteristics, and relatively

high tensile properties [1]. In particular, AZ31 is an attractive, commercially-used structural material; however, its hexagonal close-packed (hcp) crystalline structure limits the number of slip systems, which hinders its deformation at low temperature [2]. Therefore, numerous researchers have aimed to improve its formability at lower temperature. Most studies have focused on

\* Corresponding author

E-mail address: [anna.dobkowska@pw.edu.pl](mailto:anna.dobkowska@pw.edu.pl) (A. Dobkowska).

<https://doi.org/10.1016/j.jmrt.2022.04.131>

2238-7854/© 2022 The Author(s). Published by Elsevier B.V. This is an open access article under the CC BY license (<http://creativecommons.org/licenses/by/4.0/>).

alloying Mg-based alloys with other elements (e.g., Li [3], Y [4], or Ca [5]) or evaluating commonly applied plastic deformation parameters. In some cases, applying a combination of these methods leads to microstructural refinement, i.e., heat treatment and multi-directional forging in a channel die, shear-assisted processing and extrusion, or powder metallurgy.

In AZ-type alloys, two primary factors can improve the corrosion-stability resistance: a protective oxide layer, or the presence of precipitates, such as  $\beta$ -Mg<sub>17</sub>Al<sub>12</sub> or an AlMn phase [6,7]. Therefore, processing methods, such as severe plastic deformation (SPD), which lead to a partition or a more homogeneous distribution of the second phase particles, can reduce the corrosion rate. Many studies have evaluated the role of the well-known  $\beta$ -Mg<sub>17</sub>Al<sub>12</sub>, which precipitates preferentially along the grain boundaries and/or in the grain interiors and impacts the mechanical and corrosion properties of these alloys [8–10]. Some research groups have proposed that  $\beta$ -Mg<sub>17</sub>Al<sub>12</sub> is naturally brittle, and its presence supports cracking during low-temperature deformation [11]. Alternatively, it has been suggested that the thermal instability of  $\beta$ -Mg<sub>17</sub>Al<sub>12</sub> deteriorates the creep resistance and workability of AZ alloys at elevated temperatures [12]. In terms of the corrosion behavior,  $\beta$ -Mg<sub>17</sub>Al<sub>12</sub> either decreases the electrochemical activity of the alloy by forming a barrier against spreading corrosion reactions [13–16], or it enhances anodic reactions by promoting galvanic coupling with a matrix of the alloy or other precipitates [17].

It has been confirmed that microstructural refinement following the application of SPD methods (e.g., equal channel angular pressing, equal channel angular extrusion, severe shot peening, and extrusions performed using various parameters) improves the corrosion resistance of AZ31 alloys. Microstructural refinement promoted the formation of a protective oxide film and changed the distribution of  $\beta$ -Mg<sub>17</sub>Al<sub>12</sub>, which led to uniform corrosion with shallow penetration [18]. In contrast, some SPD methods, such as friction stir processing, decreased the corrosion properties of AZ31 by forming a bimodal grain structure [19,20].

This report presents a novel approach to obtain significant microstructural refinement in AZ31 alloys via extrusion with a forward-backward oscillating die (KoBo). KoBo has previously been used for various materials, including Al alloys [21], Ti alloys [22], Zn [23], and dual-structured MgLiAl alloys [24]. To our knowledge, all previous studies have focused on describing either the microstructure and mechanical properties, or the influence of plastic deformation on the precipitation process. It was established that KoBo significantly increased the materials' mechanical properties, but there is no scientific data indicating how KoBo influenced the corrosion resistance of the extruded materials, especially Mg-based alloys. Among SPD methods, KoBo represents a newly developed technique that enables significant alloy diameter reductions without preheating of initial billet [21,25]. It is worth noting that KoBo is often used for materials that are difficult to deform at low temperature [24,26,27]. KoBo combines traditional extrusion with oscillations of the extrusion die at a specified angle and frequency, which extrudes ingots under conditions of permanent microstructure destabilization, i.e., by applying a high deformation rate, which generates a fine-grained microstructure (typically <10  $\mu$ m) [28]. This strategy applies complex loading to the

material, involving strain from the cross-section reduction and cyclic torsion from the oscillating extrusion die. Significant grain refinement may be beneficial to improve the corrosion behavior of AZ31. Therefore, the present work aims to elucidate the role of microstructural changes induced by KoBo extrusion, thus verifying a novel approach to developing deformation methods for Mg-based alloys.

## 2. Methodology

### 2.1. Material and extrusion method

In this work, AZ31 alloys (Mg–3Al–1Zn), with the detailed composition shown in Table 1, were extruded via KoBo from an initial diameter of  $\varnothing$ 40 mm to  $\varnothing$ 6 mm,  $\varnothing$ 4 mm, and  $\varnothing$ 2 mm, which corresponds to extrusion ratios of  $R_1 = 40:6$  (deformation degree  $\lambda_1 = 44$ ; true strain  $\epsilon_1 = 1.9$ ),  $R_2 = 40:4$  ( $\lambda_2 = 100$ ;  $\epsilon_2 = 2.3$ ), and  $R_3 = 40:2$  ( $\lambda_3 = 400$ ;  $\epsilon_3 = 3.0$ ), respectively. The KoBo extrusion was performed under the following conditions: punch speed = 0.2 mm/s, die rotation angle = 8°, initial temperature of the billet = 24 °C, and die oscillation frequency = 5 Hz ( $\pm 1$  Hz).

### 2.2. Microstructure characterization

X-ray diffraction (XRD; Bruker, D8 Advance) patterns were obtained at 40 kV and 40 mA with Cu K $\alpha$  radiation to characterize the detailed alloy phase compositions. The results were recorded by stepwise scanning  $2\theta$  from 10° to 120°, with a step size of 0.02° and a count time of 10 s per step.

The microstructures of the alloys were observed using a scanning electron microscope (SEM; Hitachi, SU8000) equipped with an electron dispersive spectrometer (EDX). The extruded wires were cut into 3-mm-thick slices, polished with 1200-grit and 2400-grit SiC paper, and the surfaces perpendicular to the extrusion direction were subsequently polished using a low-energy Ar<sup>+</sup> ion beam milling system (Hitachi, IM4000 Ion Milling System) for 6 h. Images were captured immediately after sample preparation.

A transmission electron microscope (TEM; JEOL, JEM-1200EX) operating with an acceleration voltage of 120 kV was used to investigate the dislocation distribution and characterize the alloy phases in detail. The diffraction contrast in bright field (BF) mode revealed the grain size. The thin foils used for TEM observations were prepared using a Gatan Model 656 Dimple Grinder and Gatan Model 691 Precision Ion Polishing System (PIPS) at 2.5 kV. The samples were observed on the cross-section perpendicular to the extrusion direction.

### 2.3. Texture and grain size measurements

The grain sizes and their distributions were calculated based on electron back-scattered diffraction (EBSD) maps. This

**Table 1 – The chemical composition of AZ31 [29].**

Elements wt.%	Al	Zn	Mn	Si	S	P	Mg
AZ31 + 4Li $\varnothing$ 40 mm	3.28	0.91	0.26	0.12	0.01	0.01	Bal.

technique used samples prepared identical to those used for microscopic observations. Automatic EBSD scans were performed on a deformation-free surface, with a step size of 0.6  $\mu\text{m}$  at 20 kV and a sample tilt angle of 70°. For each pattern, six to seven Kikuchi bands were used to minimize indexing errors. A lower limit boundary misorientation of 2° was used. The grain sizes were calculated using a linear intercept method (HKL data acquisition software, Inca Inc.). The crystallographic orientations of the grains were presented on inverse-pole figure (IPF) maps, where various colors distinguish the orientation of a given sample direction in a crystal frame. Grain boundary characterizations were also performed. If the angle between two neighboring grains was distorted by more than 15°, then the angle between those grains was described as a high-angle grain boundary (HAGB); when the grains were misoriented by less than 15°, a low-angle grain boundary (LAGB) was created between those grains.

#### 2.4. Electrochemical measurements

Electrochemical measurements were performed in naturally aerated 0.1 M NaCl solution using a FAS1 Gamry potentiostat equipped with three electrodes: platinum as the counter electrode, Ag/AgCl as the reference electrode (Ref), and the sample was the working electrode. The electrolyte comprised analytical grade reagents and distilled water. The corrosion potential ( $E_{\text{corr}}$ ) was recorded for 1 h under open-circuit conditions. After immersion, potentiodynamic tests were conducted at a scan rate of 5 mV/s starting 0.5 V below the open-circuit potential ( $E_{\text{OCP}}$ ), and finishing at 2 V vs. Ref. At least three tests were conducted for each set of extrusion conditions. The post-corrosion sample morphologies were observed by SEM (SEM, Hitachi SU8000) after 1 h of immersion

under open-circuit conditions. The surfaces were analyzed again by SEM after immersion and removal of the corrosion products (immersion in 4%  $\text{HNO}_3$ , as described previously [30,31]).

#### 2.5. Corrosion rate measurements

To compare the alloys' corrosion resistance, the corrosion rate was calculated based on traditional mass loss measurements. Samples were polished using #4000-grit SiC paper, ultrasonically cleaned in isopropanol, and dried in air. The surface areas of the samples were measured, and they were weighed before immersion. The samples were immersed in naturally aerated 0.1 M NaCl for 1 h. After immersion, the samples were dried in air, and the corrosion products were removed by immersion in 4%  $\text{HNO}_3$  for 5 s, as described previously [30,31]. The corrosion rate was calculated using Eq. (1),

$$\text{Corrosion Rate} = \Delta m / s \cdot t \quad (1)$$

where  $\Delta m$  (g) is the mass loss,  $t$  (days) is the exposure time, and  $s$  ( $\text{m}^2$ ) is the surface area [32]. To verify the reproducibility of the results, three samples were investigated for each set of extrusion conditions.

### 3. Results

#### 3.1. Microstructure characterization

A typical bimodal microstructure with refined grains that settled around large grains formed in the AZ31 alloy extruded to  $\varnothing 6$  mm, as shown in Fig. 1a. The larger, uncrystallized grains, as well as the small grains, were oriented randomly and concentrated primarily around the pole {0001}. As shown

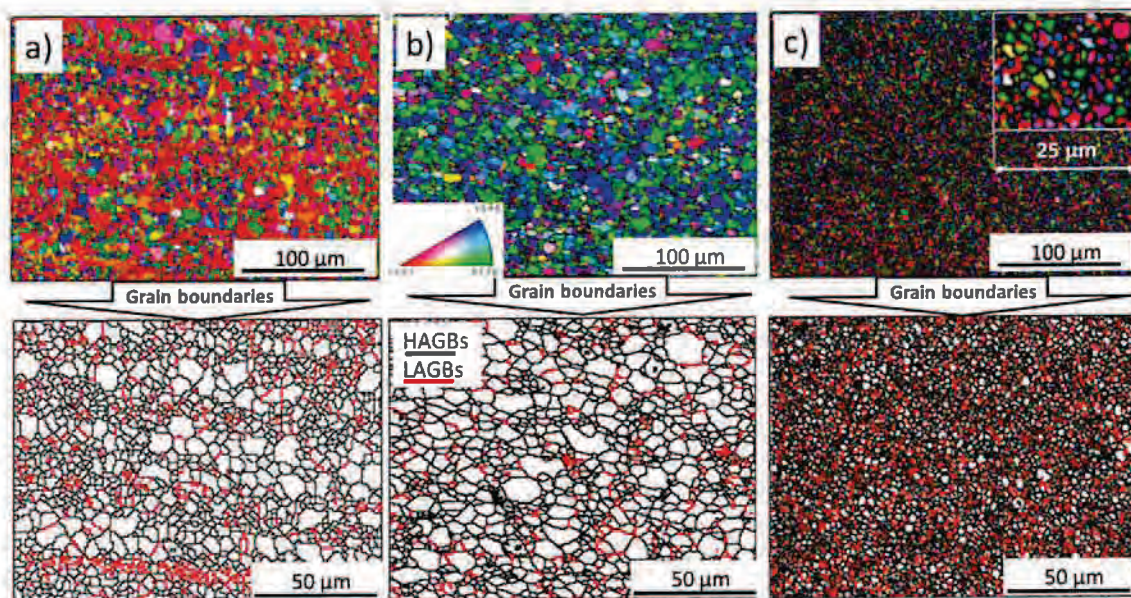


Fig. 1 – IPF maps obtained for AZ31 extruded to: a)  $\varnothing 6$  mm, b)  $\varnothing 4$  mm, and c)  $\varnothing 2$  mm, with the corresponding grain boundary distributions. The inset in panel c shows IPF map obtained for the alloy extruded to  $\varnothing 2$  mm at higher magnification.

in Fig. 2, the coarse grains are refined continuously by the dynamic recrystallization (DRX) occurring along the fine grain bands. The smallest grains formed in this alloy had diameters between 3 and 4  $\mu\text{m}$ , and they accounted for 31% of the analyzed population. Larger grains, with diameters in the range of 4–10  $\mu\text{m}$ , accounted for 69% of the population. The higher extrusion ratio (to  $\varnothing 4$  mm) also resulted in the formation of a bimodal microstructure with the grain size affected by the extrusion ratio (Fig. 1b); however, compared with the  $\varnothing 6$  mm alloy, the size and proportion of small grains changed. The higher extrusion ratio led to the formation of grains with sizes from 2 to 4 and its number increased from 31% to 56% of the population. The proportion of grains with diameters >4  $\mu\text{m}$  comprised 44% of the population. Note that in this case, the grain orientations changed significantly, and the higher deformation rate of extrusion resulted in the formation of grains whose orientations concentrated at the poles  $\{-12-10\}$  and  $\{01-10\}$ , Fig. 1b. A few very small grains were oriented to  $\{0001\}$ . In general, HAGBs formed predominantly in both

alloys. The highest extrusion ratio (to  $\varnothing 2$  mm) led to the formation of a distinct microstructure in the AZ31 alloy (Fig. 1c). The deformation sufficiently yielded an ultrafine uniform microstructure with randomly oriented grains; the average grain size was 1.88  $\mu\text{m}$ , while for the alloys extruded to  $\varnothing 6$  mm and  $\varnothing 4$  mm it was 5.03  $\mu\text{m}$  and 4.38  $\mu\text{m}$ , respectively. Similarly uniform ultrafine microstructures of AZ31 have been obtained after four passes applying accumulative back extrusion, a recent SPD method [33], or applying equal channel angular pressing at 250  $^{\circ}\text{C}$  [34]. The majority of the small grains were distorted by more than 15 $^{\circ}$  and formed HAGBs.

The XRD patterns did not reveal any other phases besides hcp-structured Mg (Fig. 3). To confirm whether there are other phases in the alloys, SEM and TEM observations were performed. The extrusion with the lowest deformation ratio resulted in the formation of coarse, irregularly-shaped, white precipitates rich in Al and Mn (Fig. 4a). Similar precipitates were observed in the alloy deformed to  $\varnothing 4$  mm (Fig. 4b). As shown in Fig. 4c, in the alloy with the lowest dimension many smaller precipitates formed with the chemical composition comparable to those existing in previous alloys. This indicates that extrusion at the highest deformation ratio resulted in the precipitates fragmentation.

Fig. 5a,b reveals a few tangled dislocations that exist in grains formed in alloy materials extruded to  $\varnothing 6$  mm and  $\varnothing 4$  mm; a slightly higher number of dislocation tangles were detected in the grains formed in the alloy extruded to  $\varnothing 4$  mm. The small grains formed in the alloys extruded at higher extrusion ratio blocked the dislocation movement at the grain boundaries, thus leading to a high concentration of tangled dislocations (Fig. 5c). The numerous dislocation tangles generated an indistinguishable granular structure.

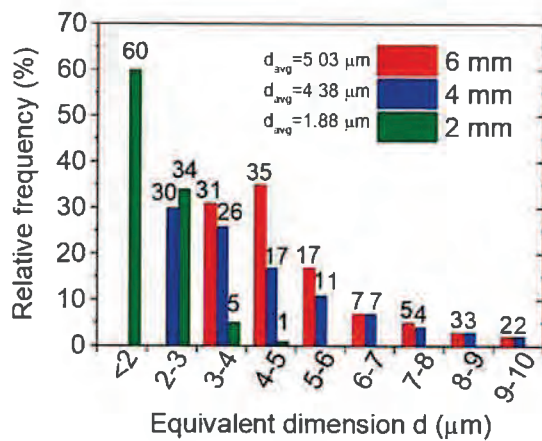


Fig. 2 – Grain size distributions for all analyzed materials calculated using a linear intercept method.

### 3.2. Corrosion behavior

Open-circuit potential testing of AZ31 alloy samples extruded to various dimensions was performed in naturally-aerated 0.1 M NaCl for 1 h (Fig. 6a). The original material had a smoothly (linearly) increasing  $E_{\text{corr}}$  from -1.49 V vs. Ref at the beginning of the immersion to -1.47 V vs. Ref at the end. The

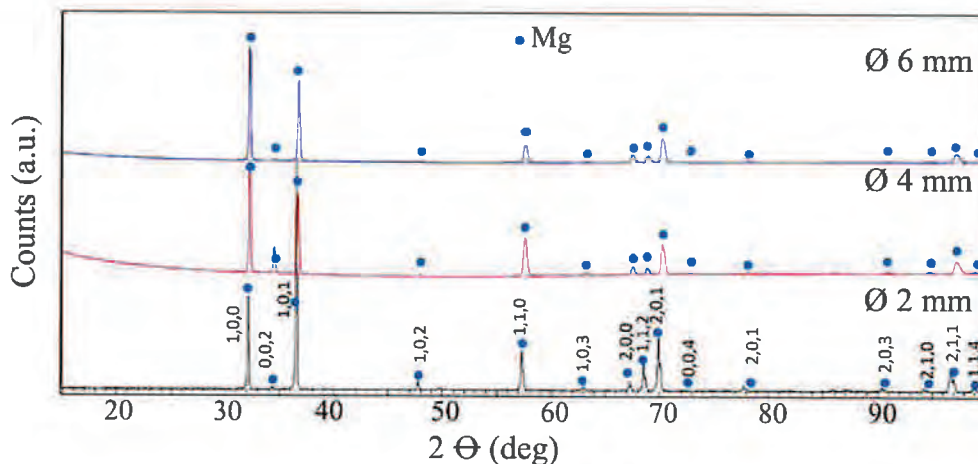


Fig. 3 – Phase composition of the AZ31 alloys extruded to  $\varnothing 6$  mm,  $\varnothing 4$  mm, and  $\varnothing 2$  mm (JCPDS 03-065-3365).



Fig. 4 – SEM microstructure images of AZ31 alloys extruded to: a) Ø6 mm, b) Ø4 mm, and c) Ø2 mm.

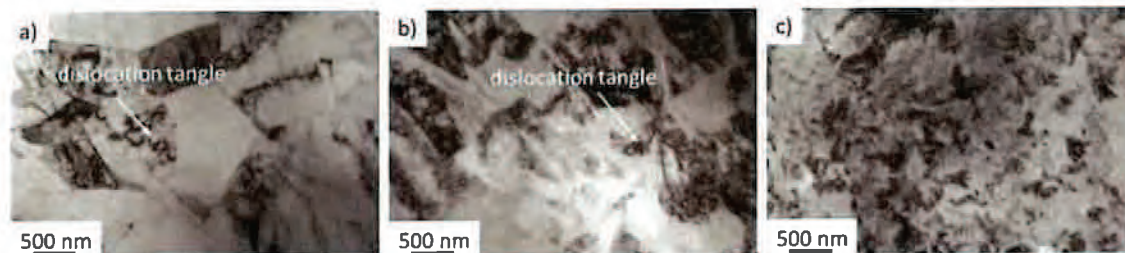


Fig. 5 – TEM micrographs of AZ31 extruded to (a) Ø6 mm, (b) Ø4 mm, and (c) Ø2 mm.

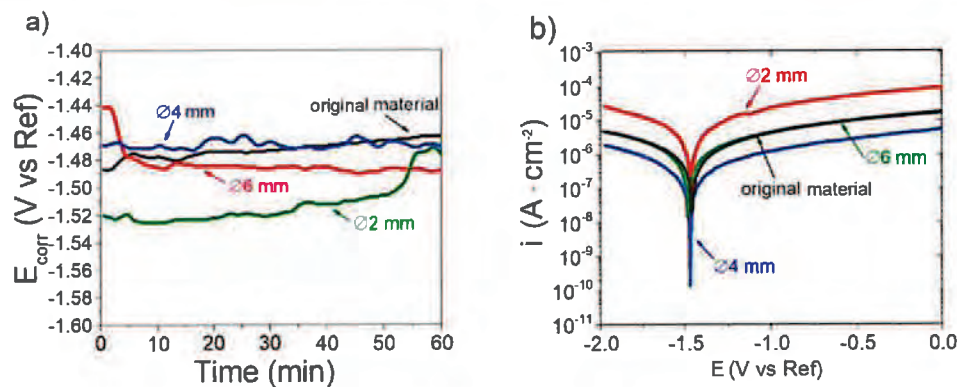


Fig. 6 – Electrochemical results: (a) corrosion potential as a function of time; b) potentiodynamic polarization curves.

sample extruded to Ø6 mm had a slightly lower  $E_{\text{corr}}$  than the original material, and the  $E_{\text{corr}}$  for that sample decreased smoothly from  $-1.44$  V vs. Ref to  $-1.49$  V vs. Ref during the first 5 min of the measurement, then remained in a near steady-state for the remainder of the hour-long experiment. Higher  $E_{\text{corr}}$  values were obtained under open-circuit conditions for the Ø4 mm sample, whose  $E_{\text{corr}}$  remained steady throughout the experiment at approximately  $-1.48$  V vs. Ref. The most negative  $E_{\text{corr}}$  (approx.  $-1.52$  V vs. Ref) was observed for the Ø2 mm extruded sample; however, after 30 min, the  $E_{\text{corr}}$  of this sample increased smoothly to  $-1.48$  V vs. Ref.

Potentiodynamic polarization curves were recorded to rationalize the  $E_{\text{corr}}$  measurements under open-circuit potential, which represents the balance between the partial anodic and cathodic reactions (Fig. 6b). All curves followed

similar trends and were characteristic for materials that undergo active dissolution; the anodic current density increased smoothly with increasing anodic potential, which indicated that the samples dissolved gradually. The curves obtained for the original material and the alloy extruded to Ø6 mm overlapped in both the cathodic and anodic regions, which suggested that both alloys exhibited very similar behavior in the analyzed solution. The cathodic side of these curves was derived from hydrogen evolution, and thus, it was concluded that the cathodic polarization current of hydrogen evolution on AZ31 extruded to Ø2 mm significantly surpassed that of the other analyzed specimens [35]. The corrosion potential shifted slightly toward more negative values for the extruded alloy, i.e., from  $E_{\text{corr}} = -1.46$  V vs. Ref for the original material to  $E_{\text{corr}} = -1.49$  V vs. Ref for the extruded alloy (Table 2). Interestingly, the cathodic and anodic components of the

**Table 2 – The characteristic parameters delivered from potentiodynamic curves.**

AZ31	$E_{\text{corr}}$ (V/Ref)	$i_{\text{corr}}$ ( $\mu\text{A} \cdot \text{cm}^{-2}$ )
Original material	-1.46	2.8
extruded to $\varnothing 6$ mm	-1.49	2.9
extruded to $\varnothing 4$ mm	-1.47	0.3 nA $\text{cm}^{-2}$
extruded to $\varnothing 2$ mm	-1.47	2.4

potentiodynamic curve for the sample with a higher extrusion ratio ( $\varnothing 4$  mm) remained at the same potential but shifted toward a more negative current density range (by one order of magnitude); this result suggested that the lower grain size distribution in the  $\varnothing 4$  mm sample rendered it less active than both the original material and the sample extruded to  $\varnothing 6$  mm. This is also confirmed by the corrosion current density with lower value calculated for the alloy extruded to  $\varnothing 4$  mm (Table 2). The current density of the sample extruded to  $\varnothing 2$  mm was an order of magnitude higher than the original material and the  $\varnothing 6$  mm alloy (thus, two orders of magnitude higher than the  $\varnothing 4$  mm extruded alloy). This indicated that the sample with the most refined grains was the most active under the analyzed conditions.

Potentiodynamic polarization is an effective technique for monitoring the instantaneous corrosion rate; however, owing to their enhanced catalytic behavior, the general corrosion rate of Mg-based alloys should be estimated based on mass loss measurements or hydrogen evolution. Therefore, to obtain more clear information regarding the corrosion behavior of AZ31 alloys extruded using KoBo, their corrosion rates were calculated based on traditional mass loss measurements. Additionally, the corrosion rate for the initial billet of AZ31 alloy (before KoBo) was calculated, and all of these results are presented in Fig. 7.

The original material exhibited the lowest corrosion rate ( $0.03 \text{ g day}^{-1} \text{ cm}^{-2}$ ), which suggested that this material had the highest corrosion resistance in 0.1 M NaCl. The AZ31 alloys extruded to  $\varnothing 6$  mm and  $\varnothing 4$  mm had higher corrosion rates ( $0.07$  and  $0.06 \text{ g day}^{-1} \text{ cm}^{-2}$ , respectively). The alloy with the highest grain refinement (extruded to  $\varnothing 2$  mm) was the most active (corrosion rate =  $1.19 \text{ g day}^{-1} \text{ cm}^{-2}$ ); this sample had a

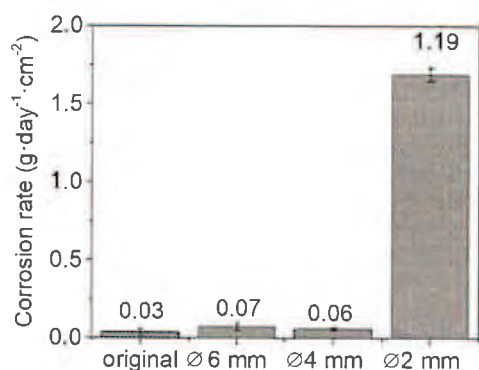


**Fig. 7 – Corrosion rates calculated from mass loss measurements for the original AZ31 and the alloys extruded via KoBo to  $\varnothing 6$  mm,  $\varnothing 4$  mm, and  $\varnothing 2$  mm.**

calculated corrosion rate nearly 40 times higher than the original material and almost 20 times higher than that calculated for alloys with bimodal grain size distributions.

### 3.3. Characterization of corroded surfaces

The corroded surfaces of samples immersed for 1 h were examined using SEM to investigate the mechanism governing their corrosion. Severe corrosion occurred on all materials; Fig. 8 a,c,e shows the overall changes in the bulk materials extruded to  $\varnothing 6$  mm,  $\varnothing 4$  mm, and  $\varnothing 2$  mm, respectively. The surface of the AZ31 extruded to  $\varnothing 6$  mm was covered with a blurry white deposition (observed at higher magnification in Fig. 8b) and contained needle-like shapes, which were identified as brucite- $\text{Mg}(\text{OH})_2$ . Severe corrosion occurred in some areas, which aligned along certain preferential paths. Similar localized corrosion damage was detected on the surface of the alloy extruded to  $\varnothing 4$  mm (Fig. 8c); however, the corrosion products were not as dense as those observed on the sample extruded to a higher dimension. Comparing Fig. 8a and c reveals that the reactions that generated corrosion products were more intense on the surface of the alloy extruded to  $\varnothing 4$  mm than on that extruded to  $\varnothing 6$  mm; these reactions resulted in a dense hydroxide film that formed on the surface of the material. For the AZ31 extruded to  $\varnothing 4$  mm, dissolution reactions did not compensate for reactions generating corrosion products; therefore, severe dissolution of the alloy surface was observed (Fig. 8d). As shown in Fig. 8e, corrosion of the alloy extruded to the lowest dimension ( $\varnothing 2$  mm) was much more severe than in the other two cases. Simultaneously, the corrosion products formed on the AZ31 extruded to  $\varnothing 2$  mm were denser than those on the surface of the  $\varnothing 6$  mm sample (Fig. 8f and b, respectively).

SEM observations confirmed that the corrosion of all samples preferentially occurred along certain paths; this phenomenon was clear on the samples' surfaces after the corrosion products were removed (Fig. 9). For the alloys extruded to  $\varnothing 6$  mm and  $\varnothing 4$  mm, corrosion proceeded along pathways that are characteristic for the material flow during KoBo deformation. These paths result from the reversible oscillations of the die (Fig. 9a and c). The alloy extruded to  $\varnothing 2$  mm was corroded more severely than the other two investigated alloys, and Fig. 9e reveals that this specimen had more visible corrosion filaments, which were generally more ordered. Despite the fact that corrosion slowly extended into the grain interiors, several deep pits also formed (Fig. 9e). The particles rich in Al and Mn remained inactive during immersion (Fig. 9b and d, inset). In addition to the severe filiform corrosion, tiny pits were created in the matrix of the alloys, as shown in Fig. 9b, d, and f. These surface observations led to the conclusion that corrosion damage depended on the recrystallization stage that took place during KoBo extrusion.

## 4. Discussion

Many studies on Mg-based alloys present a power law relationship between grain size and corrosion rate, i.e., the smaller the grain size, the better the corrosion resistance [36–38]. Additionally, many researchers declare that the corrosion

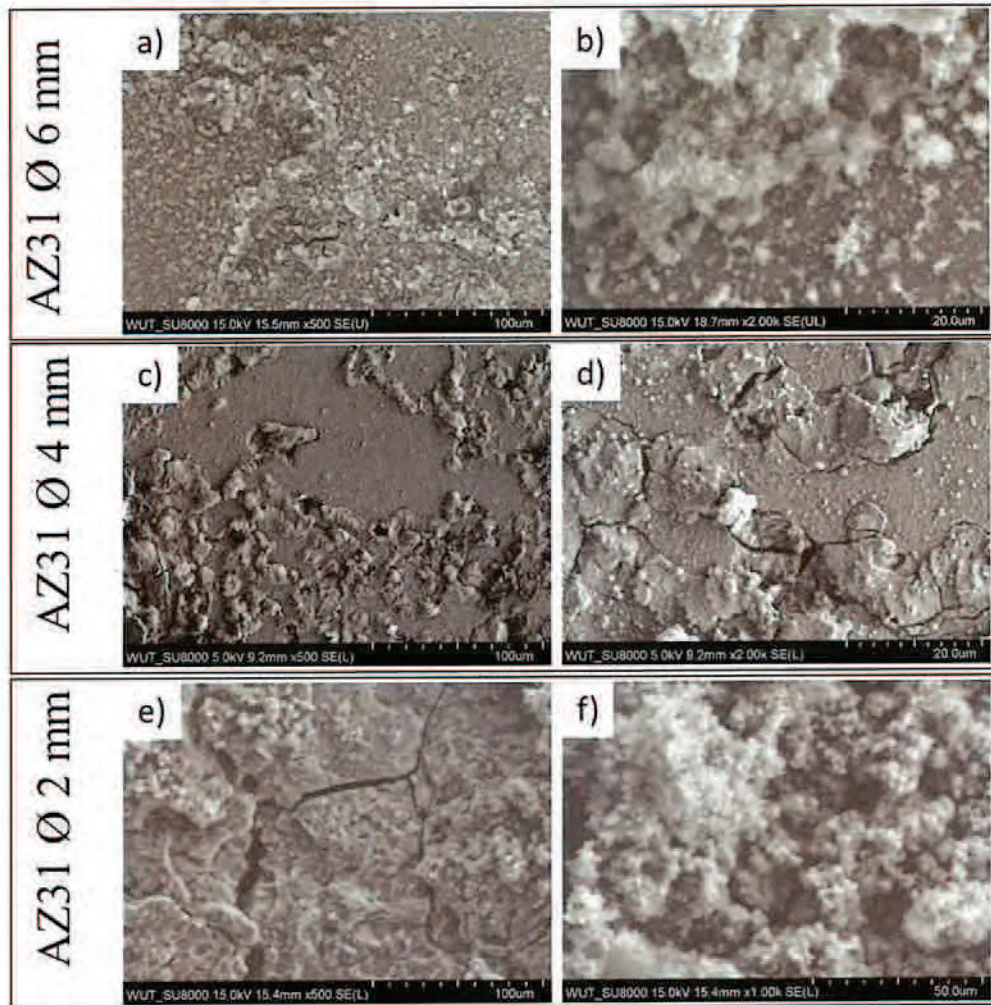


**Fig. 8 – Post-corrosion observations (after immersion for 1 h in 0.1 M NaCl) of the surface of AZ31 alloys extruded to various dimensions: SEM images at different magnifications showing the corrosion products formed on the surface of (a, b) AZ31 Ø6 mm, (c, d) AZ31 Ø4 mm, and (e, f) AZ31 Ø2 mm.**

resistance of coarse-grained Mg-based alloys can be improved through SPD techniques by forming ultrafine or fine microstructures [36,38,39]. On the basis of these suppositions, it would be reasonable to expect that AZ31 grain size reduction via KoBo would lead to an improved corrosion resistance. Nevertheless, the results presented herein reveal a contradictory relationship, i.e., in the case of AZ31, samples with smaller grains exhibit lower corrosion resistance. These results strongly suggest that other microstructural features (in addition to the grain size) must be considered when evaluating the corrosion resistance of fine and ultrafine microstructures. The KoBo-extruded materials did not exhibit higher corrosion resistance relative to the original material, and depending on the extrusion ratio, various corrosion mechanisms could be responsible for the material degradation. Those mechanisms rely on various metallurgical aspects of KoBo processing. It was observed that corrosion damage formed on the alloys extruded to Ø6 mm and Ø4 mm propagated along lines characteristic of

the reversible oscillations of the die during deformation. This suggests that the corrosion performances of those two alloys are mainly controlled by the recrystallization stage, and not by the grain size or its bimodal distribution. Nevertheless, when comparing those two materials, the effect of the grain size and its distribution must be taken into consideration. Comparing AZ31 specimens extruded to Ø6 mm and Ø4 mm reveals that a higher degree of processing resulted in slightly higher corrosion resistance. The extrusion to Ø6 mm led to the formation of a bimodal microstructure with a significantly different ratio of larger to smaller grains, relative to the Ø4 mm alloy. The microstructure of the Ø6 mm alloy comprised larger grains, similar in size to those of the Ø4 mm alloy, although the proportion of smaller grains was definitively higher in the Ø4 mm alloy. These results explain the different corrosion behaviors exhibited by these two alloys, which clearly indicates that corrosion damage on the surface depends on the spatial distribution of the potential throughout the surface of the metal.

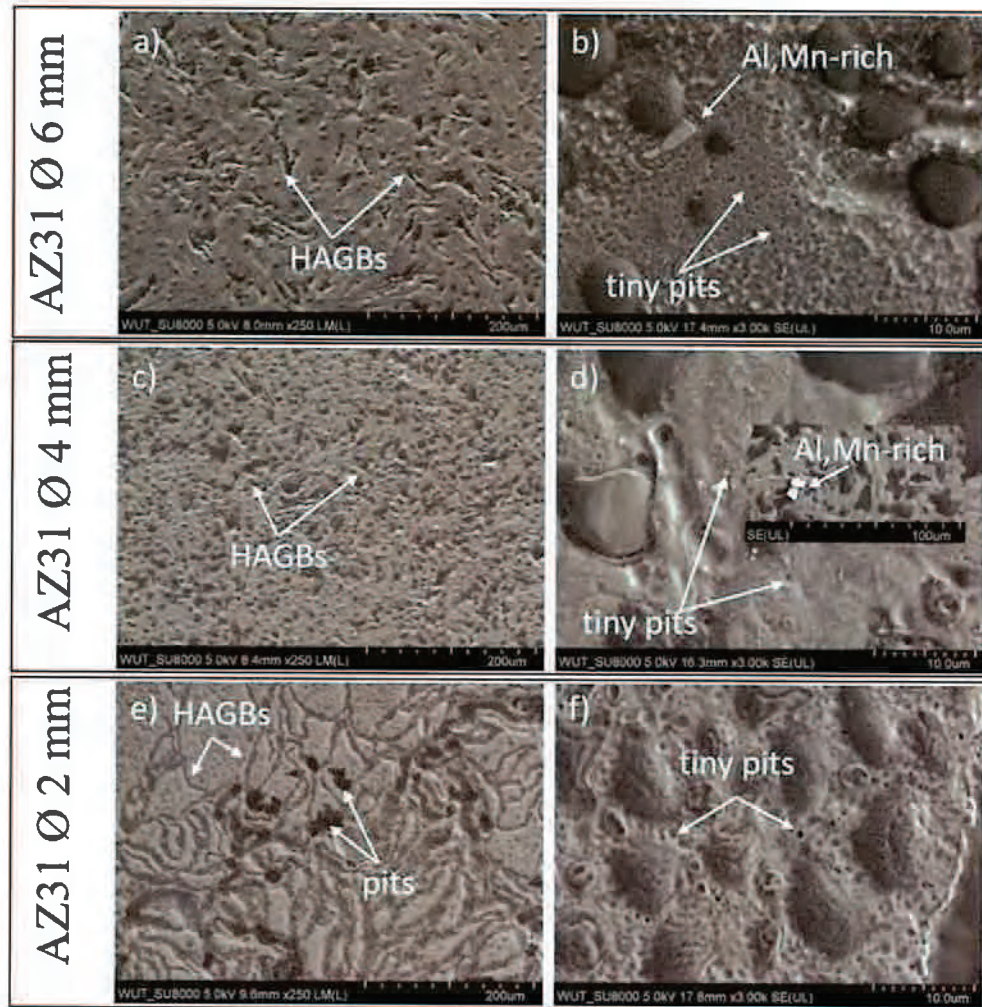


**Fig. 9** – Post-corrosion observations (after 1 h of immersion in 0.1 M NaCl) of the surfaces of AZ31 alloys extruded to various dimensions (after removal of the corrosion products): SEM images showing: a) corrosion on the surface of AZ31 Ø6 mm, b) Al, Mn-rich particles and tiny pits formed on the AZ31 Ø6 mm surface, c) corrosion on the surface of AZ31 Ø4 mm, d) tiny pits formed on the surface of AZ31 Ø4 mm (inset shows inactive Al, Mn-rich particles, e) corrosion on the surface of AZ31 Ø2 mm, and f) tiny pits formed on the surface of AZ31 Ø2 mm.

Although the mechanism of spatial distribution of the potential due to different grains refinement is not experimentally investigated in the present study, it is clear that the higher fraction of bigger grains force reactions occurred on the smaller grains to corrode faster as system is always driving to the equilibrium state.

The most active alloy in 0.1 M NaCl was the alloy deformed to Ø2 mm, which also had the most uniform and refined (ultrafine) microstructure. Notably, this alloy exhibited the worst corrosion resistance among all investigated alloys. Previous reports claimed that AZ31 alloys with the finest grains resisted corrosion better than coarse-grained counterparts [40,41], and others proposed that microstructural refinement through the formation of additional grain boundaries inhibited Mg alloy corrosion [36]. In addition, the passivity of the surface film

should be improved for the fine-grained AZ31B [42–44]. The results presented herein are in contrast to these reports and suggest that the high number of HAGBs are the main reason for the reduced corrosion resistance of the ultrafine-grained AZ31. It is well established that for heterogeneous microstructures, corrosion proceeds by forming local cells between the anode and cathode reactions, which, in the case of uniform microstructures, are identified as HAGBs (anodes) and grain interiors (cathodes) [45,46]. In the alloy with the most refined microstructure, the highest number of HAGBs resulted in the greatest corrosion initiation. Moreover, KoBo deformation generates intensively localized plastic flow in the shear bands of the metal [27]. Such a high degree of processing (i.e., in the case of the alloy deformed to Ø2 mm;  $\lambda_3 = 400$ ) may promote the activation of numerous slip systems in an hcp

AZ31 alloy, compared with lesser activation in the materials deformed at lower processing degrees ( $\lambda_1 = 44$  and  $\lambda_2 = 100$ ) [47,48]. This can lead to the accumulation of a higher deformation energy, which induces the transformation of more lattice vacancies into dislocations. The numerous tangled dislocations accumulated in the material because of their less-ordered structure have a detrimental effect on its already poor corrosion resistance by supporting further corrosion processes.

## 5. Conclusions

Based on the results presented in this work it can be concluded that:

- KoBo method enables extrusion of hexagonal Mg alloys without preheating of the initial billet at high extrusion ratio.
- KoBo extrusion resulted in a significant grain size reduction, and depending on the extrusion ratio, fine and ultra-fine microstructures were formed. The formation of fine, bimodally-distributed microstructures was observed in AZ31 alloys extruded to  $\varnothing 6$  mm ( $R_1 = 40:6$ ,  $\lambda_1 = 44$ ) and  $\varnothing 4$  mm ( $R_2 = 40:4$ ,  $\lambda_2 = 100$ ); the highest extrusion ratio (to  $\varnothing 2$  mm;  $R_3 = 40:2$ ,  $\lambda_3 = 400$ ) led to the formation of an ultrafine, equiaxed microstructure.
- The microstructural changes induced by KoBo extrusion reduced the corrosion resistance of AZ31 alloys extruded to  $\varnothing 6$  mm and  $\varnothing 4$  mm slightly relative to the original material. The corrosion behaviors of the extruded alloys were mainly affected by the recrystallization stage that occurred during KoBo deformation, and not by the grain size alone.
- The higher corrosion resistance of AZ31 extruded to  $\varnothing 4$  mm (relative to  $\varnothing 6$  mm) was related to the lower diversity of grain sizes and the more uniform crystallographic orientation of neighboring grains, as well as their mutual interactions.
- The highest degree of processing led to the highest grain refinement and the formation of an equiaxed ultrafine microstructure (in the alloy extruded to  $\varnothing 2$  mm). The lowest corrosion resistance of this alloy was caused by the highest number of HAGBs, which was promoted by the accumulation of tangled dislocations.

## Declaration of Competing Interest

The authors declare that they have no known competing financial interests or personal relationships that could have appeared to influence the work reported in this paper.

## Acknowledgements

This study was financed by the Warsaw University of Technology, Faculty of Materials Science and Engineering, from the statutory work "Materials and structures used for working under extreme conditions", Ref. No. 504/04206/1090.

## REFERENCES

- [1] Niknejad S, Liu L, Lee MY, Esmaeili S, Zhou NY. Resistance spot welding of AZ series magnesium alloys: effects of aluminum content on microstructure and mechanical properties. *Mater Sci Eng A* 2014;618:323–34. <https://doi.org/10.1016/j.msea.2014.08.013>.
- [2] Ma X, Barnett MR, Kim YH. Forward extrusion through steadily rotating conical dies. Part I: Experiments. *Int J Mech Sci* 2004;46:449–64. <https://doi.org/10.1016/j.ijmecsci.2004.03.017>.
- [3] Król M. Effect of grain refinements on the microstructure and thermal behaviour of Mg–Li–Al alloy. *J Therm Anal Calorim* 2018;133:237–46. <https://doi.org/10.1007/s10973-018-7223-x>.
- [4] Inoue A, Kawamura Y, Matsushita M, Hayashi K, Koike J. Novel hexagonal structure and ultrahigh strength of magnesium solid solution in the Mg–Zn–Y system. *J Mater Res* 2001;16:1894–900. <https://doi.org/10.1557/JMR.2001.0260>.
- [5] Liao J, Hotta M, Mori Y. Improved corrosion resistance of a high-strength Mg–Al–Mn–Ca magnesium alloy made by rapid solidification powder metallurgy. *Mater Sci Eng A* 2012;544:10–20. <https://doi.org/10.1016/j.msea.2012.02.046>.
- [6] Zeng RC, Zhang J, Huang WJ, Dietzel W, Kainer KU, Blawert C, et al. Review of studies on corrosion of magnesium alloys. *Trans Nonferrous Met Soc China* (English) 2006;16. [https://doi.org/10.1016/S1003-6326\(06\)60297-5](https://doi.org/10.1016/S1003-6326(06)60297-5).
- [7] Song G, Atrens A. Understanding magnesium corrosion. A framework for improved alloy performance. *Adv Eng Mater* 2003;5:837–58. <https://doi.org/10.1002/adem.200310405>.
- [8] Cao FR, Ding H, Li YL, Zhou G, Cui JZ. Superplasticity, dynamic grain growth and deformation mechanism in ultra-light two-phase magnesium–lithium alloys. *Mater Sci Eng A* 2010;527:2335–41. <https://doi.org/10.1016/j.msea.2009.12.029>.
- [9] Tripathi A, Murty SVSN, Narayanan PR. Microstructure and texture evolution in AZ31 magnesium alloy during caliber rolling at different temperatures. *J Magnes Alloy* 2017;5:340–7. <https://doi.org/10.1016/j.jma.2017.07.001>.
- [10] Leleu S, Rives B, Causse N, Pébère N. Corrosion rate determination of rare-earth Mg alloys in a Na<sub>2</sub>SO<sub>4</sub> solution by electrochemical measurements and inductive coupled plasma-optical emission spectroscopy. *J Magnes Alloy* 2019;7:47–57. <https://doi.org/10.1016/j.jma.2018.12.002>.
- [11] Shang L, Jung IH, Yue S, Verma R, Essadiqi E. An investigation of formation of second phases in microalloyed, AZ31 Mg alloys with Ca, Sr and Ce. *J Alloys Compd* 2010;492:173–83. <https://doi.org/10.1016/j.jallcom.2009.11.159>.
- [12] Shahbeigi Roodposhti P, Sarkar A, Murty KL, Scattergood RO. Effects of microstructure and processing methods on creep behavior of AZ91 magnesium alloy. *J Mater Eng Perform* 2016;25:3697–709. <https://doi.org/10.1007/s11665-016-2222-1>.
- [13] Dobkowska A, Adamczyk-Cieślak B, Towarek A, Maj P, Ura-Bińczuk E, Momeni M, et al. The influence of microstructure on corrosion resistance of Mg–3Al–1Zn–15Li (LAZ1531) alloy. *J Mater Eng Perform* 2020;29:2679–86. <https://doi.org/10.1007/s11665-020-04775-0>.
- [14] Martin HJ, Horstemeyer MF, Wang PT. Structure-property quantification of corrosion pitting under immersion and salt-spray environments on an extruded AZ61 magnesium alloy. *Corros Sci* 2011. <https://doi.org/10.1016/j.corsci.2010.12.025>.
- [15] Thirumalaikumarasamy D, Shanmugam K, Balasubramanian V. Comparison of the corrosion behaviour of AZ31B magnesium alloy under immersion test and potentiodynamic polarization test in NaCl solution. *J Magnes Alloy* 2014;2:36–49. <https://doi.org/10.1016/j.jma.2014.01.004>.
- [16] Kim JY, Byeon JW. Quantitative relation of discontinuous and continuous Mg<sub>17</sub>Al<sub>12</sub> precipitates with corrosion rate of

- AZ91D magnesium alloy. *Mater Char* 2021;174:111015. <https://doi.org/10.1016/j.matchar.2021.111015>.
- [17] Atrens A, Liu M, Zainal Abidin NI. Corrosion mechanism applicable to biodegradable magnesium implants. *Mater Sci Eng B Solid-State Mater Adv Technol* 2011. <https://doi.org/10.1016/j.mseb.2010.12.017>.
- [18] Cubides Y, Ivan Karayan A, Vaughan MW, Karaman I, Castaneda H. Enhanced mechanical properties and corrosion resistance of a fine-grained Mg-9Al-1Zn alloy: the role of bimodal grain structure and  $\beta$ -Mg<sub>17</sub>Al<sub>12</sub> precipitates. *Materialia* 2020;13:100840. <https://doi.org/10.1016/j.mtla.2020.100840>.
- [19] Saikrishna N, Pradeep G, Reddy K, Munirathinam B, Sunil BR. Influence of bimodal grain size distribution on the corrosion behavior of friction stir processed biodegradable AZ31 magnesium alloy. *J Magnes Alloy* 2016;4:68–76. <https://doi.org/10.1016/j.jma.2015.12.004>.
- [20] Dobkowska A, Adamczyk – Cieślak B, Kuc D, Hadasik E, Pociński T, Ura-Bińczyk E, et al. Influence of bimodal grain size distribution on the corrosion resistance of Mg-4Li-3Al-1Zn (LAZ431). *J Mater Res Technol* 2021;13:346–58. <https://doi.org/10.1016/j.jmrt.2021.04.078>.
- [21] Koprowski P, Bieda M, Boczkal S, Jarzębska A, Ostachowski P, Kawalko J, et al. AA6013 aluminium alloy deformed by forward-backward rotating die (KoBo): microstructure and mechanical properties control by changing the die oscillation frequency. *J Mater Process Technol* 2018;253:34–42. <https://doi.org/10.1016/j.jmatprotec.2017.10.043>.
- [22] Kawalko J, Bobrowski P, Koprowski P, Jarzębska A, Bieda M, Lagoda M, et al. Microstructure evolution of CP titanium during deformation in KoBo process followed by cold rolling. *J Alloys Compd* 2017;707:298–303. <https://doi.org/10.1016/j.jallcom.2016.11.202>.
- [23] Piela K, Wróbel M, Sztwiertnia K, Jaskowski M, Kawalko J, Bieda M, et al. Zinc subjected to plastic deformation by complex loading and conventional extrusion: comparison of the microstructure and mechanical properties. *Mater Des* 2017;117:111–20. <https://doi.org/10.1016/j.matdes.2016.12.056>.
- [24] Dutkiewicz J, Bobrowski P, Rusz S, Hilser O, Tański TA, Borek W, et al. Effect of various SPD techniques on structure and superplastic deformation of two phase MgLiAl alloy. *Met Mater Int* 2018;24:1077–89. <https://doi.org/10.1007/s12540-018-0118-3>.
- [25] Dobkowska A, Adamczyk – Cieślak B, Koralknik M, Chromiński W, Kubasek J, Ciftci J, et al. Corrosion behavior of fine-grained Mg-7.5Li-3Al-1Zn fabricated by extrusion with a forward-backward rotating die (KoBo). *J Magnes Alloy* 2021. <https://doi.org/10.1016/j.jma.2021.08.020>.
- [26] Maciejewski J, Mróz Z. An upper-bound analysis of axisymmetric extrusion assisted by cyclic torsion. *J Mater Process Technol* 2008;206:333–44. <https://doi.org/10.1016/j.jmatprotec.2007.12.061>.
- [27] Korbel A, Bochniak W. Refinement and control of the metal structure elements by plastic deformation. *Scripta Mater* 2004;51:755–9. <https://doi.org/10.1016/j.scriptamat.2004.06.020>.
- [28] Sztwiertnia K, Kawalko J, Bieda M, Jaskowski M, Piela K, Bochniak W. Microstructure and texture of zinc deformed by extrusion with forward-backward rotating die (KoBo). *IOP Conf Ser Mater Sci Eng* 2015;82:1–4. <https://doi.org/10.1088/1757-899X/82/1/012084>.
- [29] Dobkowska A, Koralknik M, Adamczyk-Cieślak B, Kuc D, Chromiński W, Kubasek J, et al. The effect of extrusion ratio on the corrosion resistance of ultrafine-grained Mg-4Li-3Al-Zn alloy deformed using extrusion with a forward-backward oscillating die. *J Mater Eng Perform* 2022. <https://doi.org/10.1007/s11665-022-06895-1>.
- [30] Sudholz AD, Gusieva K, Chen XB, Muddle BC, Gibson MA, Birbilis N. Electrochemical behaviour and corrosion of Mg-Y alloys. *Corros Sci* 2011;53:2277–82. <https://doi.org/10.1016/j.corsci.2011.03.010>.
- [31] Kirkland NT, Lespagnol J, Birbilis N, Staiger MP. A survey of bio-corrosion rates of magnesium alloys. *Corros Sci* 2010;52:287–91. <https://doi.org/10.1016/j.corsci.2009.09.033>.
- [32] ASTM B90/B90M-12. Standard specification for magnesium-alloy sheet and plate. 2012. [https://doi.org/10.1520/B0090\\_B0090M-12](https://doi.org/10.1520/B0090_B0090M-12).
- [33] Fatemi-Varzaneh SM, Zarei-Hanzaki A. Processing of AZ31 magnesium alloy by a new noble severe plastic deformation method. *Mater Sci Eng A* 2011;528:1334–9. <https://doi.org/10.1016/j.msea.2010.10.033>.
- [34] Eddahbi M, Del Valle JA, Pérez-Prado MT, Ruano OA. Comparison of the microstructure and thermal stability of an AZ31 alloy processed by ECAP and large strain hot rolling. *Mater Sci Eng A* 2005;410–411:308–11. <https://doi.org/10.1016/j.msea.2005.08.081>.
- [35] Chang JW, Guo XW, Fu PH, Peng LM, Ding WJ. Effect of heat treatment on corrosion and electrochemical behaviour of Mg-3Nd-0.2Zn-0.4Zr (wt.%) alloy. *Electrochim Acta* 2007;52:3160–7. <https://doi.org/10.1016/j.electacta.2006.09.069>.
- [36] Argade GR, Panigrahi SK, Mishra RS. Effects of grain size on the corrosion resistance of wrought magnesium alloys containing neodymium. *Corros Sci* 2012;58:145–51. <https://doi.org/10.1016/j.corsci.2012.01.021>.
- [37] Zhang Jie, Zhang Yang, Wu Guohua, Liu Wencai, Liang Zhang WD. Microstructure and mechanical properties of as-cast and extruded Mg-8Li-3Al-2Zn-0.5Nd alloy. *Mater Sci Eng A* 2015;621:198–203.
- [38] Hamu G Ben, Eliezer D, Wagner L. The relation between severe plastic deformation microstructure and corrosion behavior of AZ31 magnesium alloy. *J Alloys Compd* 2009;468:222–9. <https://doi.org/10.1016/j.jallcom.2008.01.084>.
- [39] Pu Z, Yang S, Song GL, Dillon OW, Puleo DA, Jawahir IS. Ultrafine-grained surface layer on Mg-Al-Zn alloy produced by cryogenic burnishing for enhanced corrosion resistance. *Scripta Mater* 2011;65:520–3. <https://doi.org/10.1016/j.scriptamat.2011.06.013>.
- [40] Alvarez-Lopez M, Pereda MD, Del Valle JA, Fernandez-Lorenzo M, Garcia-Alonso MC, Ruano OA, et al. Corrosion behaviour of AZ31 magnesium alloy with different grain sizes in simulated biological fluids. *Acta Biomater* 2010;6:1763–71. <https://doi.org/10.1016/j.actbio.2009.04.041>.
- [41] Jiang B, Xiang Q, Atrens A, Song J, Pan F. Influence of crystallographic texture and grain size on the corrosion behaviour of as-extruded Mg alloy AZ31 sheets. *Corros Sci* 2017;126:374–80. <https://doi.org/10.1016/j.corsci.2017.08.004>.
- [42] Liao J, Hotta M, Motoda SI, Shinohara T. Atmospheric corrosion of two field-exposed AZ31B magnesium alloys with different grain size. *Corros Sci* 2013;71:53–61. <https://doi.org/10.1016/j.corsci.2013.02.003>.
- [43] Aung NN, Zhou W. Effect of grain size and twins on corrosion behaviour of AZ31B magnesium alloy. *Corros Sci* 2010;52:589–94. <https://doi.org/10.1016/j.corsci.2009.10.018>.
- [44] Zhang T, Ji Z, Wu S. Effect of extrusion ratio on mechanical and corrosion properties of AZ31B alloys prepared by a solid recycling process. *Mater Des* 2011;32:2742–8. <https://doi.org/10.1016/j.matdes.2011.01.012>.
- [45] Miyamoto H, Harada K, Mimaki T, Vinogradov A, Hashimoto S. Corrosion of ultra-fine grained copper fabricated by equal-channel angular pressing. *Corros Sci* 2008;50:1215–20. <https://doi.org/10.1016/j.corsci.2008.01.024>.
- [46] Dobkowska A, Adamczyk – Cieślak B, Kubasek J, Vojtech D, Kuc D, Hadasik E, et al. Microstructure and corrosion resistance

- of a duplex structured Mg–7.5Li–3Al–1Zn. *J Magnets Alloy* 2021;9:467–77. <https://doi.org/10.1016/j.jma.2020.07.007>.
- [47] Dong H, Pan F, Jiang B, Zeng Y. Evolution of microstructure and mechanical properties of a duplex Mg-Li alloy under extrusion with an increasing ratio. *Mater Des* 2014;57:121–7. <https://doi.org/10.1016/j.matdes.2013.12.055>.
- [48] Pan F, Wang Q, Jiang B, He J, Chai Y, Xu J. An effective approach called the composite extrusion to improve the mechanical properties of AZ31 magnesium alloy sheets. *Mater Sci Eng A* 2016;655:339–45. <https://doi.org/10.1016/j.msea.2015.12.098>.



ELSEVIER

Contents lists available at ScienceDirect

Journal of Alloys and Compounds

journal homepage: [www.elsevier.com/locate/jalcom](http://www.elsevier.com/locate/jalcom)

Research article

# Microstructure and properties of an AZ61 alloy after extrusion with a forward-backward oscillating die without preheating of the initial billet



Anna Dobkowska<sup>a,\*</sup>, Aleksandra Zielińska<sup>a</sup>, Irena Paulin<sup>b</sup>, Črtomir Donik<sup>b</sup>,  
Maciej Łojkowski<sup>a</sup>, Milena Koralnik<sup>a</sup>, Bogusława Adamczyk-Cieślak<sup>a</sup>, Krystian Paradowski<sup>a</sup>,  
Marek Tkocz<sup>c</sup>, Dariusz Kuc<sup>c</sup>, Jiří Kubásek<sup>d</sup>, Matjaž Godec<sup>b</sup>, Wojciech Świąszkowski<sup>a,1</sup>

<sup>a</sup> Faculty of Materials Science and Engineering, Warsaw University of Technology, Warsaw, Poland

<sup>b</sup> Institute of Metals and Technology, Ljubljana, Slovenia

<sup>c</sup> Institute of Materials Engineering, Silesian University of Technology, Katowice, Poland

<sup>d</sup> Department of Metal and Corrosion Engineering, University of Chemical Technology, Prague, Czech Republic

## ARTICLE INFO

### Article history:

Received 21 January 2023

Received in revised form 21 March 2023

Accepted 26 March 2023

Available online 29 March 2023

### Keywords:

Magnesium alloys

Severe plastic deformation

Microstructure

Mechanical properties

Corrosion

Extrusion

High deformation ratio

## ABSTRACT

We have investigated the microstructure, mechanical and corrosion properties of an AZ61 alloy that was extruded using a newly developed technique with an oscillating die (KoBo). The KoBo method allows the extrusion of AZ61 without preheating of the initial billet at high deformation ratios. The combined SEM, EBSD and TEM investigations of the microstructure revealed significant microstructure refinement as well as changes to the intensity of the texture and the distribution of the Mg<sub>17</sub>Al<sub>12</sub> phase. The size of grains was reduced from coarse ( $d_{avg}$  20.4 μm for the initial billet) to fine ( $d_{avg}$  6.6 μm for the extrusion ratio of R<sub>1</sub> 7:1 and  $d_{avg}$  4.5 μm for R<sub>2</sub> 10:1). However, in this study, it does not improve the strength and the corrosion properties of the AZ61 alloys. The continuously precipitated Mg<sub>17</sub>Al<sub>12</sub> phase along the grain boundaries overwhelms the strengthening due to grain refinement. Intense corrosion occurs in the case of the KoBo-extruded samples, and the main mechanism of the corrosion is microgalvanic, taking place between the matrix and the Mg<sub>17</sub>Al<sub>12</sub> formed at grain boundaries.

© 2023 Elsevier B.V. All rights reserved.

## 1. Introduction

The properties of Mg-Al-Zn alloys depend on the manufacturing and the processing methods, and the resulting microstructure in terms of grain size, type, size, and distribution of precipitates, defects, etc. [1,2]. The Mg-Al-Zn alloys are commonly used in many branches of industry; however, their wide use is limited by poor corrosion resistance. This obstacle is being solved by various deformation possibilities or thermal and chemical treatments. The microstructure modification of Mg-Al-Zn alloys which includes grain refinement, homogenization of second phases distribution, decreasing of residual strain in the matrix may be achieved using severe deformation methods (SPD). The Mg-based alloys after SPD generally show an improvement of the mechanical and the corrosion properties. For example, shear-assisted processing and extrusion improved the corrosion resistance and mechanical properties [3].

The ultrafine microstructure obtained by repeated upsetting through extrusion also led to an improvement in the mechanical properties of AZ61 [4]. The same effect was found in the case of AZ61 processed by multi-temperature multi-axial forging [5], isothermal multi-axial forging [6], multi-pass equal-channel angular pressing [7], isothermal multidirectional forging with increasing strain rate [8], and equal-channel angular pressing with a 160° channel angle and electro pulsing treatment [9]. Modifications to the microstructure by adding elements such as Ca [10], Sr [11], Sc [12], Ag, Y [13] or a combination of Y and Ca [14], were also investigated in terms of corrosion and mechanical properties improvement. The addition of Ca reduced the plastic elongation when the (0001) texture strength increased [10]; Sc and Sr had a positive influence on the compressive strength [11,12]; and the addition of Ag or Y inhibited the growth of Mg<sub>17</sub>Al<sub>12</sub> and refined the grain size, which results in better mechanical and corrosion properties [13,15].

Since Mg-based alloys cannot be easily processed at room temperatures, all the deformation methods were employed at elevated temperatures. Their hexagonal structure makes them very hard to deform due to the limited slip systems which are possible to being activated at room temperature [2]. It is very difficult to reduce the

\* Corresponding authors.

E-mail addresses: [anna.dobkowska@pw.edu.pl](mailto:anna.dobkowska@pw.edu.pl) (A. Dobkowska), [wojciech.swieszkowski@pw.edu.pl](mailto:wojciech.swieszkowski@pw.edu.pl) (W. Świąszkowski).

<https://doi.org/10.1016/j.jalcom.2023.169843>

0925-8388/© 2023 Elsevier B.V. All rights reserved.

**Table 1**  
Chemical composition of AZ61 according to [22] and measured using atomic absorption spectroscopy (AAS, GBC 932 Plus Spectrometer), wt. %.

	Al	Zn	Mn	Si	Fe	Mg
Given in literature	5.92	0.49	0.15	0.037	0.0070	bal.
AAS	6.21	0.58	0.20	-	-	bal.

dimensions of Mg alloys at a high extrusion ratio at lower temperatures than used so far (approx. 180–400 °C depending on the deformation method [16,17]), and to obtain a homogeneous microstructure. The newly developed technique made us able to plastically deform the AZ61 at high extrusion ratios without preheating of the initial billet. We used extrusion with a forward-backward oscillating die (called KoBo), which, due to the fact that the material shows a plastic flow behaviour, makes it possible to significantly reduce the Mg-based alloy's dimensions [18,19]. Hence, the properties of the common Mg-Al-Zn alloy (in particular AZ61) extruded at high deformation ratios could be tested without preheating of the initial billet which has not been well developed for hexagonal structured metals so far. In this work, for the first time, the influence of the microstructure formed during the KoBo processing on the corrosion and the mechanical behaviour of AZ61 reduced from  $\varnothing 40$  mm to  $\varnothing 6$  mm and from  $\varnothing 40$  mm to  $\varnothing 4$  mm (extrusion ratios of 7:1 and 10:1) is investigated.

## 2. Materials

The Mg-6Al-1Zn magnesium alloy (AZ61) with the chemical composition given in Table 1 was extruded without preheating of the initial billet using an extruder with a forward-backward oscillating die [19–21]. KoBo is a combination of a traditional extrusion with a reversible oscillating die assembled at the end of the extruder (Fig. 1). During the interaction of the extruder and the oscillating die, the material shows plastic flow behaviour, and this enables significant microstructure refinement of the hcp-structured metals without preheating of the initial billet [19,21]. The detailed description of the method can be found in [18].

As shown in Fig. 2, the initial billet in the form of a circular rod with a diameter of 40 mm was extruded to  $\varnothing 6$  mm (extrusion ratio  $R_1$  7:1) and to  $\varnothing 4$  mm (extrusion ratio  $R_2$  10:1). The KoBo extrusion had a punch speed of 0.2 mm/s, a die rotation angle of 8° and a frequency of 5 Hz.

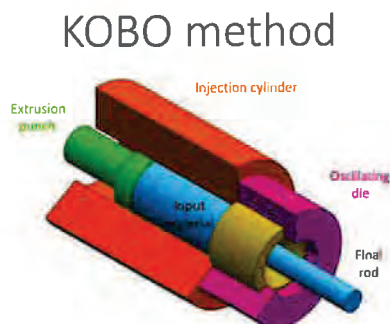


Fig. 1. Schematic of extrusion with a forward-backward oscillating die KoBo (gif file)

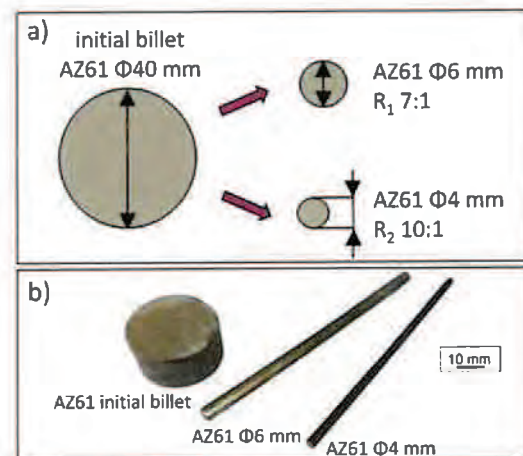


Fig. 2. Details of KoBo extrusion applied to the investigated materials: a) initial and final dimensions of the AZ61 rods extruded under various extrusion ratios, b) real life images of the extruded rods.

## 3. Methods

### 3.1. Microstructure characterization

The microstructures of the investigated materials on the surfaces perpendicular to the extrusion direction were observed using a field-emission scanning electron microscope (FE-SEM JEOL JSM 6500 F) and chemical analyses of the coarse precipitates, using energy-dispersive X-ray spectrometer (EDX, Inca Energy 400, Oxford Instruments). The samples were first ion milled in an Ar+ beam. Afterwards, electron-backscatter diffraction (EBSD) was used with a HKL Nordlys II EBSD camera and EDAX software. Inverse pole figures (IPF) with the corresponding grain-boundary (GB) distributions and the density of the geometrically necessary dislocations (GNDs) density were obtained. The low-angle grain boundary (LAGB) between two adjacent grains deviated by less than 15 degrees (subgrains). In the case when the grains deviated by more than 15 degrees, a high-angle grain boundary (HAGB) was detected. The textures of the materials were analysed based on the pole figures. The intermetallic compounds formed in the alloys were determined using X-ray diffraction (XRD, Bruker D8 Advance) operated at 40 kV and 40 mA with Cu-K $\alpha$  radiation. The results were recorded by stepwise scanning  $2\theta$  from 10° to 120°, with a step size of 0.02° and a count time of 10 s per step. The TEM observations were carried out using a JEOL JEM 1200EX microscope with an accelerating voltage of 120 kV. Thin foils were prepared using a Gatan Model 691 Precision Ion Polishing System (PIPS) with a beam voltage of 3 V inclined to the sample surface at an angle of 10 degrees.

### 3.2. Mechanical properties

The mechanical properties were described based on tensile tests performed using a Zwick/Roell Z050 tensile machine equipped with holders that allow specimens with non-standard dimensions. In this study we used micro-sized specimens, as in the work of Molak et al. [23]. Due to small dimensions of the extruded wires samples were cut along the extrusion direction. The initial strain rate was 0.01 s<sup>-1</sup>. After the tests the characteristic parameters for each material were calculated: ( $R_{0.2}$  – yield strength;  $R_m$  – tensile strength,  $A_t$  – percentage of total extension at fracture) [24]. To ensure the repeatability of the measurements, four tests were performed for each material. Fractured surfaces of the representative tensile specimens were examined with an SEM (Hitachi TM1000). The microhardness

(HV<sub>0.2</sub>) tests were done using Vickers method under the load of 200 g (Innovatest Falcon 500 Micro/Macro Vickers Tester). 10 points in line were measured on each material.

### 3.3. Corrosion performance

The corrosion measurements were based on electrochemical tests (OCP – open-circuit potential evaluation, EIS – electrochemical impedance spectroscopy, and potentiodynamic polarization tests), and corrosion-rate calculations based on the hydrogen-release method were used to describe the corrosion behaviour of the investigated materials. The measurements were made in 0.1 M naturally aerated sodium chloride solutions (0.1 M NaCl) at room temperature. The electrochemical tests were conducted using Gamry's FAS1 potentiostat with a three-electrode measuring system (a Pt electrode as the counter electrode, a saturated Ag/AgCl electrode as the reference electrode, and the sample as the working electrode). The OCP was recorded for 1 h. The potentiodynamic tests were carried out with a scan rate of 5 mV/s and a potential range from -0.5 V below E<sub>OCP</sub> to 1.5 V vs Ref. The EIS was recorded in the range from 0.01 Hz to 10 000 Hz and the data were fitted using Echem Analyst software. To ensure the reproducibility of the results, the data for each sample were collected three times. To calculate the corrosion rate the hydrogen evolved during immersion was collected. Samples polished with #4000 SiC paper were placed in a beaker and connected to a burette [25]. Hydrogen was collected in the burette through a PVC pipe installed above the beaker, equipped with a dropping funnel. The corrosion rate was calculated as follows [25]:

$$CR = \Delta m / s \cdot t \quad (1)$$

where:  $\Delta m$  is the mass loss (g) calculated from the hydrogen evolution,  $s$  is the surface area (m<sup>2</sup>), and  $t$  is the time of exposure (days). To determine the standard deviation of the measured data, three parallel samples were immersed from each material.

### 3.4. Characterization of the corroded surfaces

The samples were assessed with an SEM after immersion in 0.1 M NaCl for 1 h. To find the fine differences in the corrosion mechanisms propagating on the surfaces of the alloys the corrosion products were chemically removed by immersion in chromic acid (200 g of Cr<sub>2</sub>O<sub>3</sub> in 1 L of distilled water). The surface development of the samples was measured using an atomic force microscope (AFM, Oxford's Instrument's Asylum Research AFM MFP3D Bio). The measurement was performed with a scan size of 40  $\mu$ m and a scan rate of 0.49 Hz. The setpoint of the deflection at the contact with the surface for imaging was 0.5 V, and the set point for scratching was 5 V. Measurements were repeated three times for each sample. The obtained data were analysed using Gwyddion software. The images showing the development of the surface profiles at the selected location, and the numerical values of the mean roughness ( $S_a$ ) were exported. The mean roughness ( $S_a$ ) is the arithmetic mean of the absolute value of the height within a sampling area [48].

## 4. Results

### 4.1. Microstructure characterization

SEM observations of the investigated microstructures together with the corresponding EDX analyses are shown in Fig. 3. The material before the extrusion was composed of coarse white second phase precipitates that were enriched with Mn and Al (Fig. 3a). As the literature data shows, these are coarse Al<sub>5</sub>Mn<sub>8</sub> [26]. Other coarse precipitates were Al, Mn, and Si-rich (P2, Fig. 3a). The same type of precipitates was observed in the KoBo-extruded samples (P3, P4,

Fig. 3b, and P5, P6, Fig. 3c). XRD patterns revealed that the Mg<sub>17</sub>Al<sub>12</sub> phase exists in all the materials (Fig. 4).

For a deeper understanding of the microstructure formation during KoBo extrusion, TEM images taken in bright field were inspected (Fig. 5). The dense dislocations distributions in some individual grains are observed for both deformation ratios (see Fig. 5a – AZ61  $\varnothing$ 6 mm and Fig. 5c – AZ61  $\varnothing$ 4 mm). The small and elongated precipitates (200–300 nm) form along the grain boundaries in both KoBo-extruded materials. These precipitates are marked by the red arrows, and they are identified in terms of Mg<sub>17</sub>Al<sub>12</sub> (Fig. 5b – AZ61  $\varnothing$ 6 mm, and Fig. 5d – AZ61  $\varnothing$ 4 mm). The KoBo extrusion caused a change in the grain size of the investigated alloys (Fig. 6a–c). The EBSD data shows that the average grain size in the case of the initial billet is 20.4  $\mu$ m (Fig. 6a), while the extrusion to  $\varnothing$ 6 mm causes a grain refinement to 6.6  $\mu$ m (Fig. 6b); the highest extrusion ratio decreases the average grain size to 4.3  $\mu$ m (Fig. 6c). The grains detected in the initial billet are mostly oriented with  $\langle 10\bar{1}0 \rangle$  and  $\langle 2\bar{1}10 \rangle$  perpendicular to the extrusion direction corresponding to a strong  $\{10\bar{1}0\}$  fibre texture. The KoBo extrusion does not affect the crystallographic grain orientation. All the grain boundaries are HAGBs, with a few grains disoriented by fewer than 15 degrees (LAGBs), Fig. 6d–f. In the initial sample there is a higher GND density at the grain boundaries than in the grain interiors (Fig. 6g). A similar situation exists in the case of the KoBo-deformed samples, where a higher GND density is observed at the grain boundaries. However, due to the grain refinement resulting in a larger number of grain boundaries, the GND density is higher in the KoBo-extruded samples (Fig. 6h, i). The pole figures for  $\{0001\}$  and  $\{10\bar{1}0\}$  show typical strong texturing of the basal and prismatic planes for Mg (Fig. 7). The texture intensity for the initial billet is weaker (max 6.4) than for the KoBo-extruded samples (max 9.0 and 10.2 for  $\varnothing$ 6 mm and  $\varnothing$ 4 mm, correspondingly). Conversely, the texture components in the materials after KoBo extrusion show a difference in pole figures. The texture intensity is stronger in both KoBo-prepared samples than in the reference material.

### 4.2. Mechanical properties

The representative engineering tensile curves are depicted in Fig. 8 and the mechanical parameters calculated based on the tensile tests are listed in Table 2. The data show that the KoBo-processed samples elongated by 17 % and 15 % for the AZ61  $\varnothing$ 6 mm and AZ61  $\varnothing$ 4 mm, respectively, which is less than the elongation of the initial billet (22 %). The tensile strengths ( $R_m$ ) do not vary (having 246, 242 and 245 MPa for AZ61 initial billet, KoBo extruded to  $\varnothing$ 6 mm and  $\varnothing$ 4 mm, respectively). Nevertheless, an increase in the yield strength,  $R_{0.2}$ , is observed after the KoBo extrusion (from 101 MPa for the initial billet to 134 MPa for the AZ61  $\varnothing$ 6 mm, and to 161 MPa for AZ61  $\varnothing$ 4 mm). It is worth mentioning that with the increasing extrusion ratio, the values of the  $R_{0.2}$  also rise. The fracture surfaces are similar and contain mixed regions of plastic deformation characterized by a dimple-like morphology (marked by the red arrows in Fig. 9) and facets typical for brittle fracture (yellow arrows in Fig. 9). In the materials with smaller grain size, the free dislocation path is reduced by grain boundaries, causing the decrease in plasticity [27]. Materials prepared by KoBo also had a stronger basal texture. Such an arrangement is not favourable for basal slip during tensile loading along the extrusion direction, causing an increase in the hardness, Fig. 10 [28,29].

### 4.3. Corrosion performance

The open-circuit potential (E<sub>OCP</sub>) during 1 h of immersion in naturally aerated 0.1 M NaCl is shown in Fig. 11a. The increasing values of E<sub>OCP</sub> are characteristic of the initial billet. Such a trend indicates that the sample is in oxidising conditions. Different curves

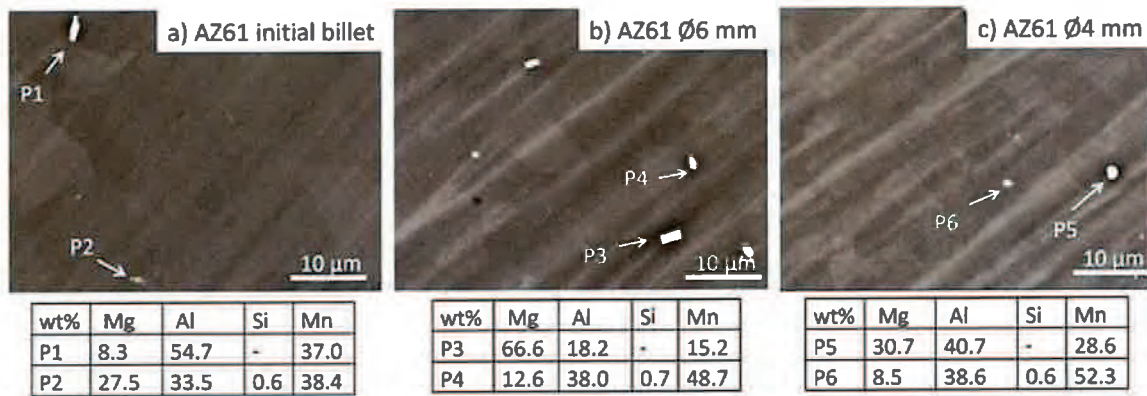


Fig. 3. SEM images of the microstructure of the investigated materials with corresponding EDX analyses: a) initial billet, b) sample after KoBo extrusion to Ø6 mm, and c) sample after KoBo extrusion to Ø4 mm. P1,P3 and P5 precipitates enriched in Al and Mn; P2, P4 and P6 precipitates enriched in Al, Si and Mn.

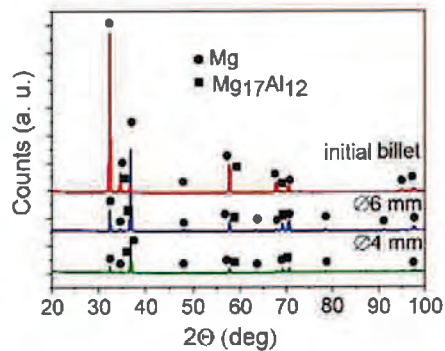


Fig. 4. XRD patterns obtained for the investigated materials: initial billet, material after KoBo extrusion to Ø6 mm, and material after KoBo extrusion to Ø4 mm.

were recorded for the KoBo-extruded samples. The alternating small ups and downs of the  $E_{OCP}$  show that the oxidation and reduction reactions are being overcompensated; however, those reactions cannot be easily explained by the  $E_{OCP}$  measurements.

The cathodic branches obtained for the initial billet and KoBo-extruded material to Ø6 mm are similar, suggesting that the cathodic reaction kinetics in both cases is not related to the microstructural differences caused by the KoBo extrusion [3], Fig. 11b. There is a shift in the cathodic branch of the potentiodynamic curve recorded for the most deformed sample. All anodic branches of the potentiodynamic curves exhibit similar shapes, with the inflection points indicating the pitting (breakdown,  $E_b$ ) potentials [3]. As shown in Table 3, the smallest difference between  $E_{corr}$  and  $E_b$  is recorded for the most refined alloy, indicating that this alloy is the least resistant to pitting corrosion. The corrosion-current density increases with the increasing KoBo-extrusion ratio, from  $79 \mu A/cm^2$  calculated for the initial billet to  $129 \mu A/cm^2$  and  $221 \mu A/cm^2$  for the KoBo extrusion to Ø6 mm and Ø4 mm, respectively (Table 3). Based on the

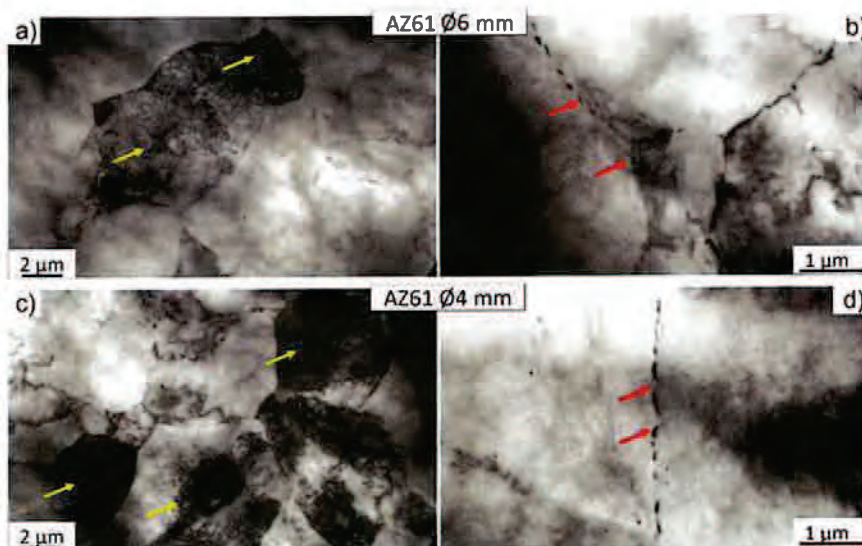


Fig. 5. Bright-field TEM images of the KoBo-extruded materials: Ø6 mm (a, b) and Ø4 mm (c, d). The dislocations are marked by the yellow arrows and the small black precipitates identified as  $Mg_{17}Al_{12}$  are marked by the red arrows.

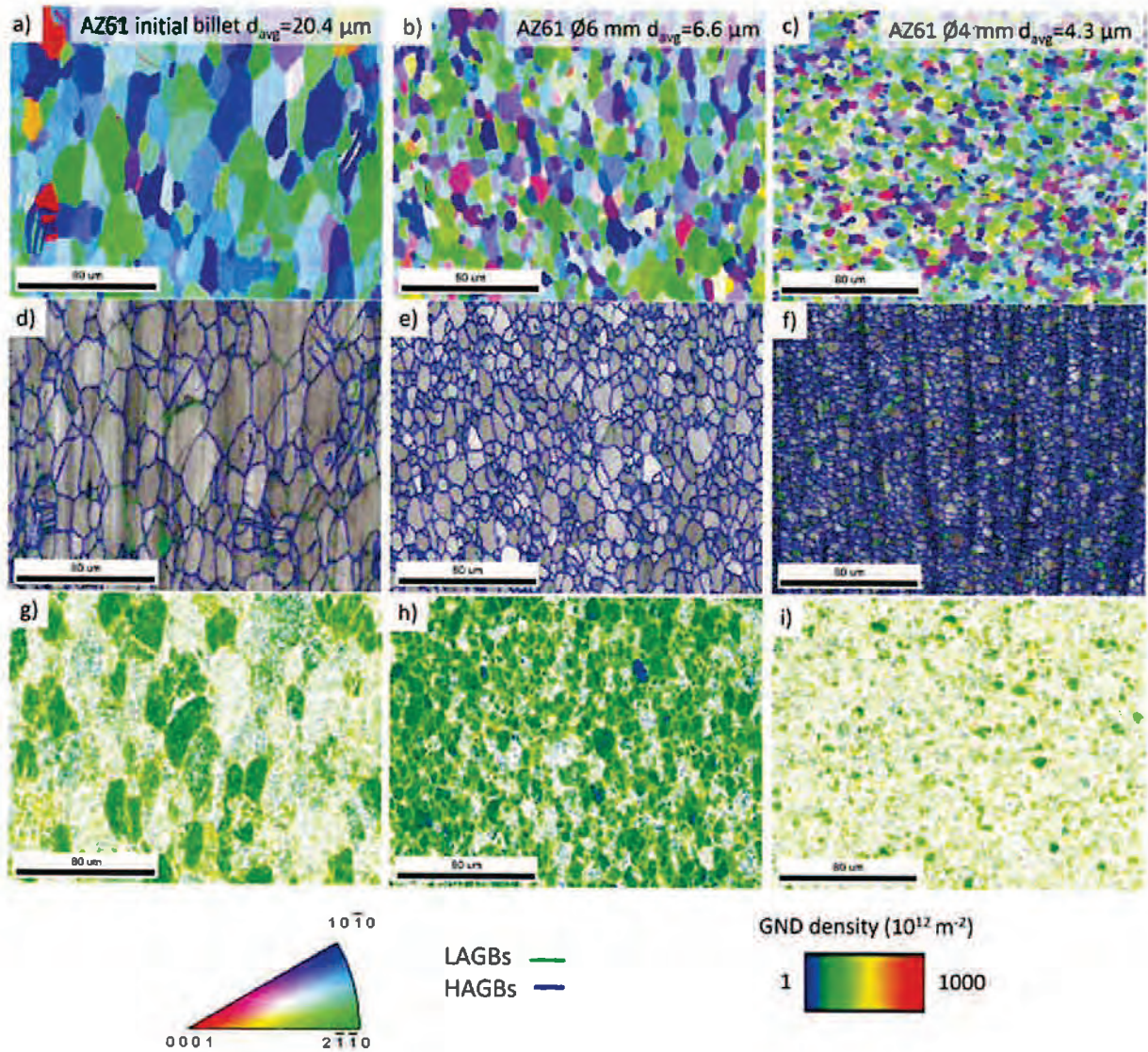


Fig. 6. Inverse pole figures (IPFs) with the average grain size (a-c), grain boundaries (GBs) distributions (d-g), geometrically necessary dislocation (GND) densities (g-i) presented for the AZ61 initial billet, the AZ61 after KoBo extrusion to Ø6 mm to Ø4 mm.

radius of the capacitive loops shown in the Nyquist plots (Fig. 11c), the corrosion resistance of the materials can be ranked as follows: initial billet > KoBo extruded to Ø6 mm > KoBo extruded to Ø4 mm. Two EECs were chosen to fit the EIS data [30–32]. The first one

shown in Fig. 11d was used to fit data for the initial billet and the AZ61 KoBo extruded to Ø6 mm. The second circuit was used for the most extruded material (Ø4 mm), Fig. 11e. In both circuits  $R_s$  represents the solution resistance,  $R_{ct}$  is the resistance of the electric-

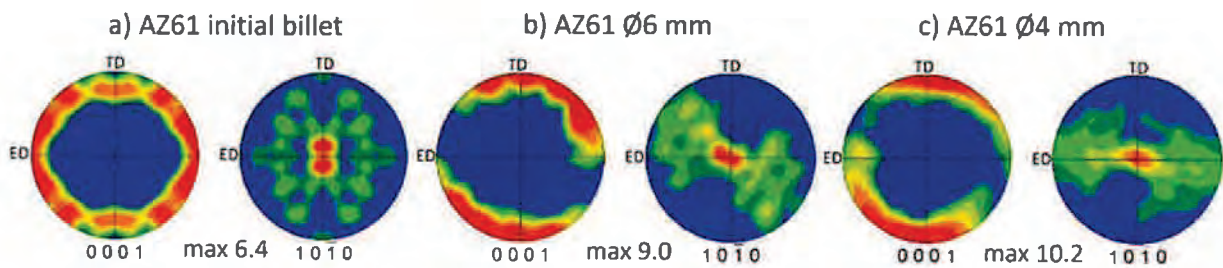


Fig. 7. Pole figures obtained for a) the AZ61 initial billet, b) the AZ61 after KoBo extrusion to Ø6 mm, and c) the AZ61 after KoBo extrusion to Ø4 mm; ED – extrusion direction.

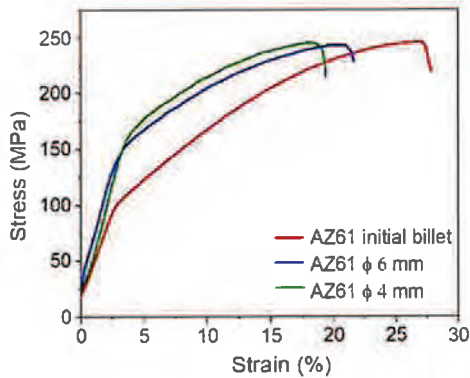


Fig. 8. The representative engineering tensile curves of the investigated materials.

**Table 2**  
Mechanical properties of the conventional and KoBo-extruded AZ61 ( $R_{0.2}$  - yield strength;  $R_m$  - tensile strength,  $A_t$  - percentage total extension at fracture).

Material	$R_{0.2}$ (MPa)	$R_m$ (MPa)	$A_t$ (%)
AZ61 Ø40 mm	101 ± 0.8	246 ± 5.4	22 ± 1.5
AZ61 Ø6 mm	134 ± 6.5	242 ± 3.5	17 ± 2.3
AZ61 Ø4 mm	161 ± 1.3	245 ± 7.7	15 ± 1.0

charge transfer through the material and electrolyte solution interface,  $CPE_{dl}$  models the properties of the double layer at the material-electrolyte interface,  $R_L$  stands for the resistance at low frequencies and is related to localized corrosion and  $L$  stands for the inductance at low frequencies and is also related to localized corrosion.  $R_f$  and  $CPE_f$  also appear in the circuit chosen for the most extruded sample, and the first represents the resistance of the passive film, while the second element describes the capacitance of the passive layer. The values of the  $R_{ct}$  confirm that the corrosion

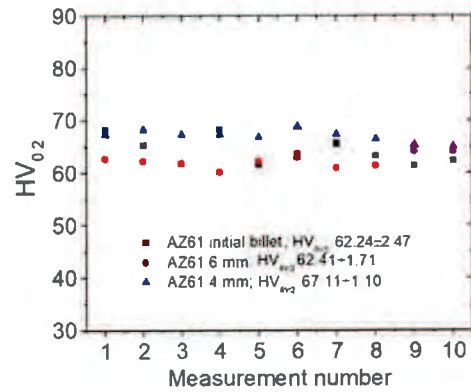


Fig. 10. Microhardness profiles of the AZ61 initial billet, AZ61 KoBo extruded to Ø6 mm and to Ø4 mm.

resistance of the AZ61 alloy extruded to Ø6 mm is slightly lower than the initial billet. However, a difference in the corrosion-resistance decrease is clearly visible for the most deformed sample (Table 4).

Fig. 12 shows the corrosion rates calculated based on the hydrogen release method and taken from the potentiodynamic polarization measurements. The corrosion rates based on the hydrogen release method and the polarization tests show the same increasing trend due to the increased extrusion ratio. The corrosion rate for the sample deformed at the highest extrusion ratio is much larger than those for the initial billet and the KoBo-extruded alloy to Ø6 mm. This agrees with the EIS results and suggests that microstructural changes caused by the deformation to Ø4 mm have a critical influence on the corrosion resistance.

As shown in Fig. 13, regardless of the extrusion ratio, the corrosion propagates through the grain boundaries. Despite the intergranular attack, multiple pits formed on the surface of the material

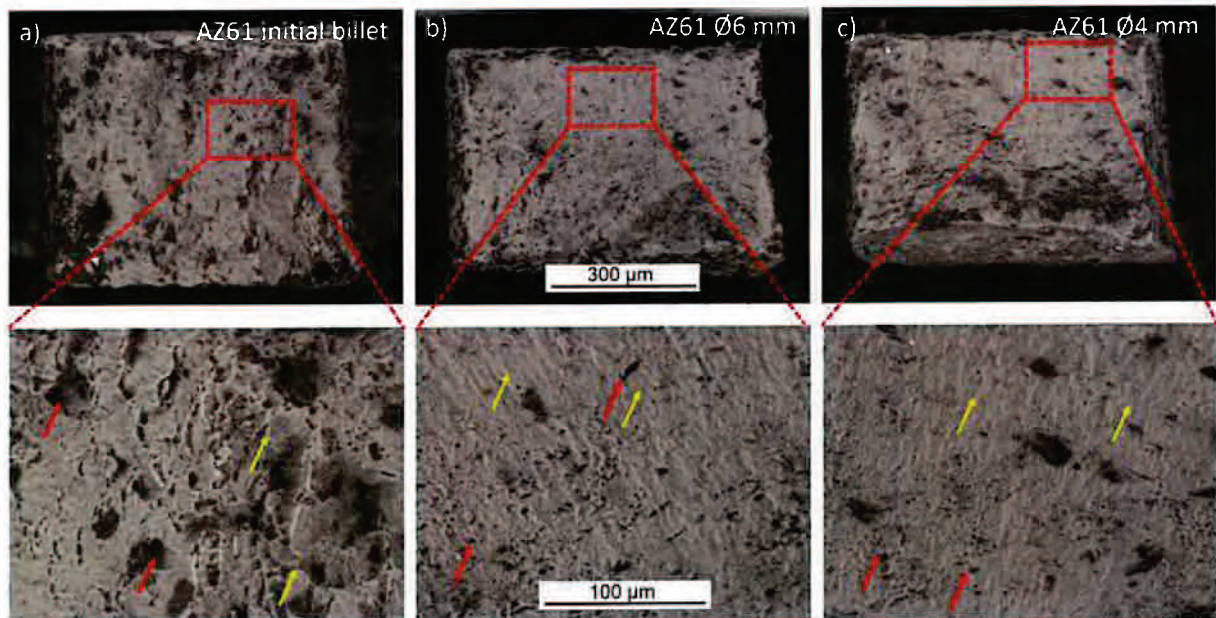


Fig. 9. Fracture surfaces of the AZ61 alloys: a) initial billet, b) KoBo extruded to Ø6 mm and c) KoBo extruded to Ø4 mm. Dimples are marked by the red arrows, and facets typical for brittle fracture are marked by the yellow arrows.

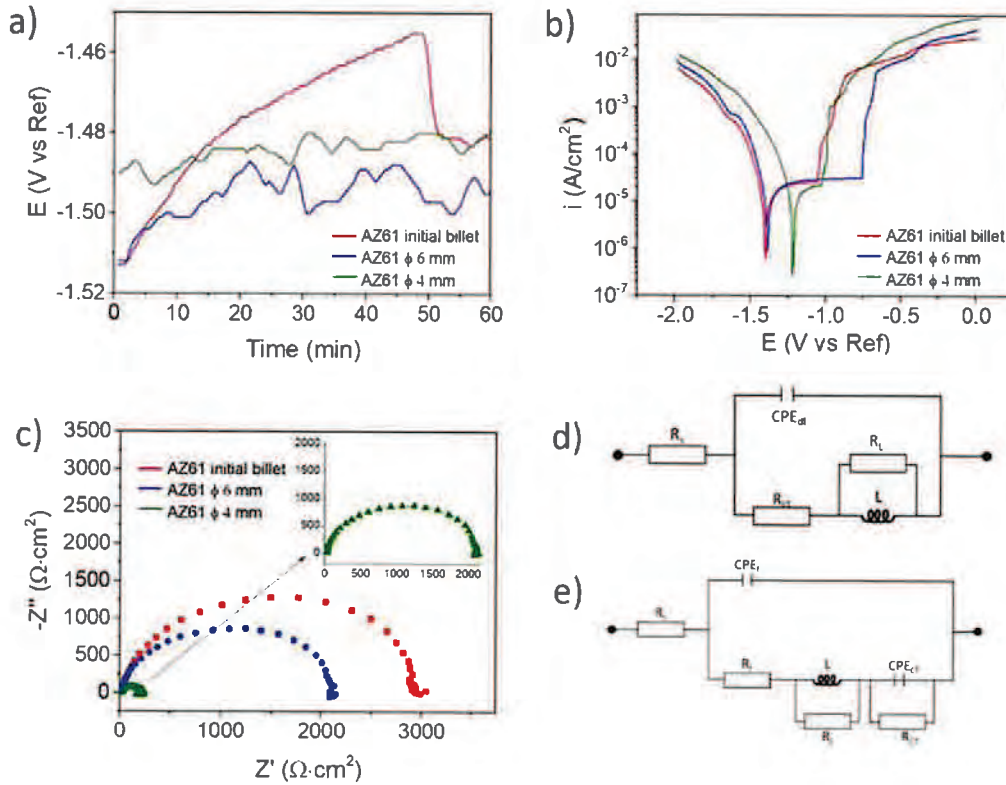


Fig. 11. Electrochemical measurements performed in 0.1-M NaCl: a) open-circuit potential, b) polarization curves, c) Nyquist plots and electronic equivalent circuits (EEC) used for EIS data fitting: d) initial billet and AZ61 KoBo extruded to  $\phi 6$  mm, e) AZ61 KoBo extruded to  $\phi 4$  mm.

Table 3  
Electrochemical parameters calculated from potentiodynamic polarization curves.

AZ61	$E_{corr}$ (V/Ref)	$E_b$ (V/Ref)	$\Delta E$	$i_{corr}$ ( $\mu A/cm^2$ )
Initial billet $\phi 40$ mm	-1.40	-1.06	0.34	79
KoBo extruded to $\phi 6$ mm	-1.39	-0.76	0.63	129
KoBo extruded to $\phi 4$ mm	-1.22	-1.03	0.20	221

prior to the extrusion (Fig. 13a). More intensive damage occurred on the surface of the  $\phi 6$ -mm KoBo-extruded sample (Fig. 13b). Here, the grain boundaries are heavily corroded, and the corrosion propagates to the grain interiors. The most corroded surface is seen in Fig. 13c, where dissolution reactions are not compensated by the passivation reactions and, as a result, the surface of the sample is heavily damaged. Moreover, many pits are formed. This is confirmed by the measured depth profile, where a higher  $S_a$  is calculated for the sample extruded to  $\phi 4$  mm ( $S_a = 75$  nm), Fig. 14. The pits are not as deep as in the material deformed to  $\phi 6$  mm, but there are many more of them.

Table 4  
Electrochemical parameters fitted for EIS results.

AZ61	$R_s$ ( $\Omega \cdot cm^2$ )	$R_{ct}$ ( $\Omega \cdot cm^2$ )	$CPE_{ct}$ ( $\mu S s^2/cm^2$ )	$a_1$	$R_L$ ( $\Omega \cdot cm^2$ )	$L$ (H $cm^2$ )	$R_i$ ( $\Omega \cdot cm^2$ )	$CPE_i$ ( $\mu S s^2/cm^2$ )	$a_2$
Initial billet	36	2977	8.7	0.92	30	4	-	-	-
KoBo $\phi 6$ mm	25	2165	10.2	0.91	1	1894	-	-	-
KoBo $\phi 4$ mm	21	37	340.1	0.93	66	24	114	9.6	0.99

### 5. Discussion

The KoBo extrusion of the AZ61 magnesium alloy modified the microstructure in terms of grain size, second phase distribution, and texture evolution. The KoBo extrusion does not improve the strength of the initial billet; however, it has an influence on the ductility of the alloy, whereas the strength of the alloys, even with the refined grains, remains at the same level. Simultaneously, the higher the extrusion ratio, the worse the corrosion behaviour. To our knowledge, such a relationship has not been previously reported among SPD methods used for hexagonal structures.

KoBo can refine the original coarse microstructure, and this is the reason for the increasing yield strength. This indicates that the strain hardening of the alloys decreases and the plastic deformation is localized more rapidly. Jiang et al. [7] and Kim et al. [33] suggested that it is probably related to the texture softening, which appreciably overwhelms the strengthening due to grain refinement. This hypothesis does not fit the results of our study, as the texture intensity of the KoBo-deformed materials is higher than that for the initial billet. This is confirmed by Zeng et al. [34] where various

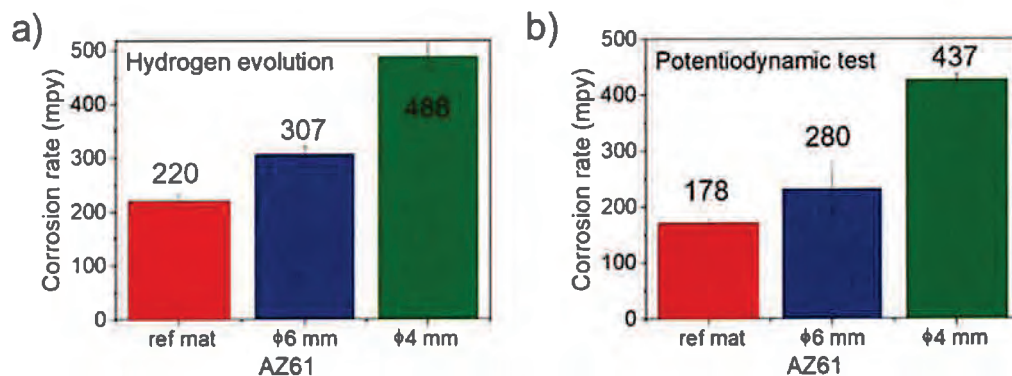


Fig. 12. Corrosion rates calculated from hydrogen release method and potentiodynamic polarization tests.

relationships between the textures and mechanical properties of the extruded Mg alloys are described. Although the grain size was reduced, no changes in the strength of the alloys was observed. We supposed that in our case it is the result of the dynamic precipitation of the  $Mg_{17}Al_{12}$  phase during the KoBo extrusion and the dislocations being accumulated around the grain boundaries, which overwhelmed the strengthening mechanism related to grain refinement. As shown in Section 4.1, the  $Mg_{17}Al_{12}$  precipitates have the same size after KoBo extrusion regardless extrusion ratio. The KoBo specimens show failure around precipitates with the neighboring regions having brittle failure. Therefore, one might say, that failure under tensile loading is initiated by the delamination or fracture of  $Mg_{17}Al_{12}$ . This phenomenon has been previously studied in details by Zha et al. [35] and Lu et al. [36]. Such behaviour would explain the ultimate strength of the samples remaining at the same level.

Microgalvanic corrosion is always an issue in the case of Mg-Al-Zn alloys [32,37,38]. Even though many reports of the role of the  $Mg_{17}Al_{12}$  phase in the corrosion of AZXX alloys exist in the literature, their results are contradictory. Surface-potential maps obtained by scanning Kelvin-probe force microscopy for the AZ91D alloy made by Pardo et al. [39] suggested that between the  $Mg_{17}Al_{12}$  and the  $\alpha(Mg)$  the galvanic coupling was not significant. The authors claimed that the potential difference between them was in the range of 10 mV, which is not enough to form a galvanic couple. Other researchers, such as Mathieu et al. [40], suggested that the  $Mg_{17}Al_{12}$  is 150 mV nobler than the  $\alpha(Mg)$  and thus is able to form microgalvanic coupling with the Mg matrix. Based on the literature review the corrosion of the Mg-Al-Zn alloys not only depends on the presence of the  $Mg_{17}Al_{12}$  phase, but also on its shape, size and distribution. Ubeda et al. [41]

stated that under anodic polarization, larger amounts of  $Mg_{17}Al_{12}$  are beneficial for durability, decreasing the Mg matrix dissolution rates. Candan et al. [42] investigated the role of the  $Mg_{17}Al_{12}$  intermetallic phase due to the increasing Al content in AZ series alloys. It was shown that the decline in the corrosion resistance of the alloys, at higher Al contents, was attributed to the amount and morphology of the  $Mg_{17}Al_{12}$  intermetallic phase, and the interruption of the continuity of the oxide film on the surface of the alloys, owing to the coarsened  $Mg_{17}Al_{12}$  intermetallic phase. None of the researchers described in a systematic way the relationship between the grain size and the distribution density of the  $Mg_{17}Al_{12}$  along the grain boundaries during deformation. Generally, considering relationship between grain size and corrosion, the smaller the grain size the better corrosion performance as high grain boundary density tends to passivate more readily [43–46]. The role of  $Mg_{17}Al_{12}$  must be also explained. As shown, with the increasing Al content, the number of  $Mg_{17}Al_{12}$  increases and this leads to the corrosion resistance improvement [32,47]. The results of our study show that the smaller the grain size, the most intense the microgalvanic corrosion, while it is promoted by the presence of fine precipitates of  $Mg_{17}Al_{12}$ . We have proven here that when the small, elongated precipitates of  $Mg_{17}Al_{12}$  are located very close to each other on the grain boundary, and the grain size is small, the current of the anodic half-reactions must be compensated by the cathodic half-reactions. This drives the system to rapid dissolution close to the  $Mg_{17}Al_{12}$ , causing the rapid dissolution of the grain interior. This mechanism is also supported by dislocation accumulation at the grain boundaries, leading to the very rapid dissolution of the surrounding areas. In this scenario, the corrosion is less severe for materials with a larger grain size.

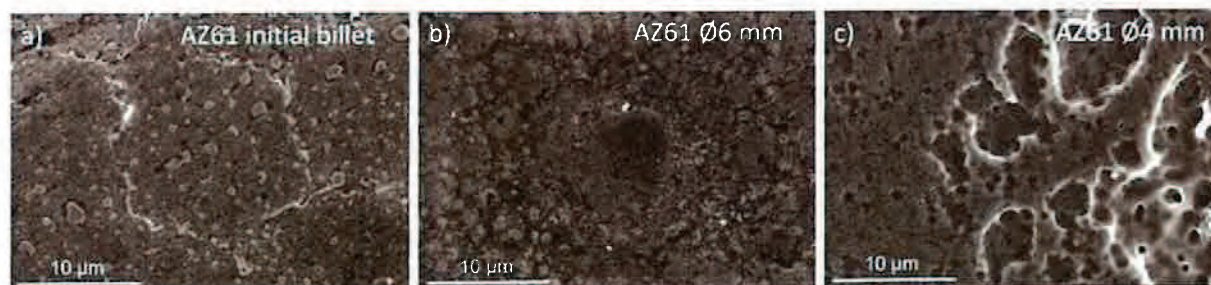


Fig. 13. SEM images of the corroded surfaces: a) initial billet, b) AZ61 extruded to Ø6 mm, c) AZ61 extruded to Ø4 mm.

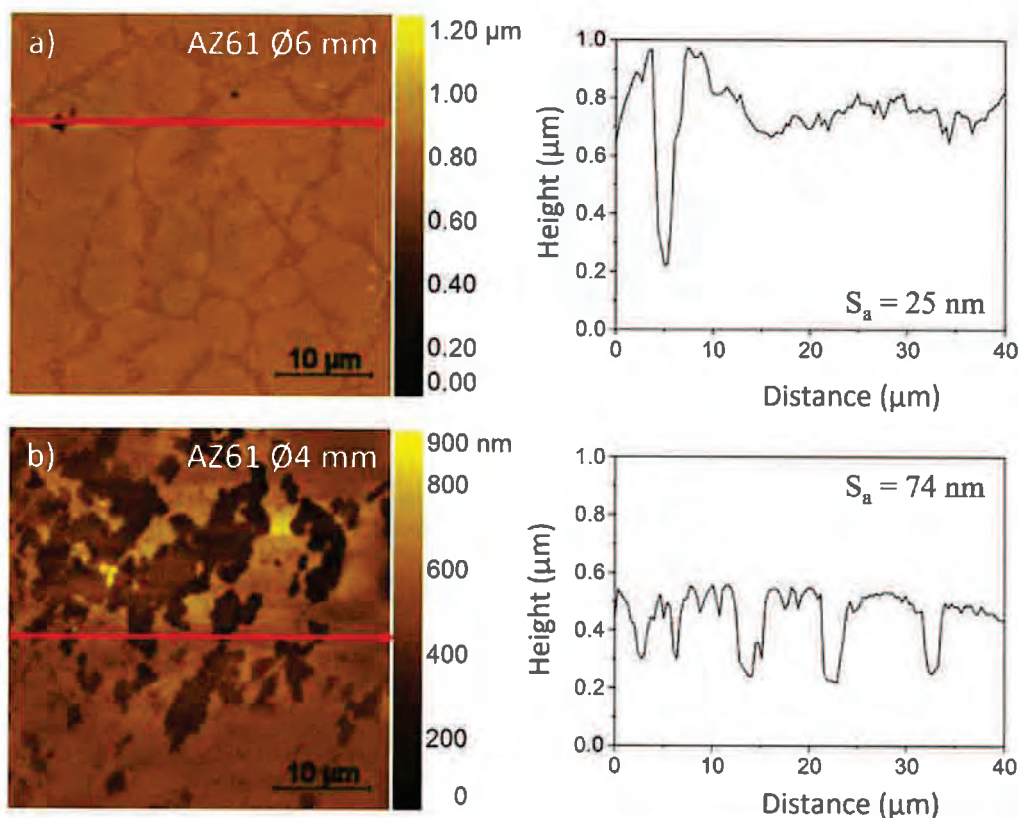


Fig. 14. AFM images with the corresponding surface development profiles extracted from the area marked by the arrow for a) AZ61 extruded to Ø6 mm, b) AZ61 extruded to Ø4 mm.

## 6. Conclusions

Based on the results the following conclusions can be drawn:

1. The KoBo extrusion results in grain refinement of AZ61 Mg alloys without preheating the initial billet (from 10.4 µm to 6.6 µm and to 4.3 µm for R 7:1 and R 10:1). The main difference is related to the distribution of the  $Mg_{17}Al_{12}$ , which in the KoBo-extruded samples is more refined and denser at the grain boundaries. The texture intensity is stronger in the KoBo-prepared samples than in the reference extruded material.
2. KoBo extrusion improves the yield strength of the alloys; however, it does not affect the strength of AZ61.
3. The corrosion resistance of the KoBo-processed materials in the chloride-containing solution was lower than the corrosion resistance of the initial billet. The decline of the corrosion properties is related to the grain refinement; the smaller the grain size, the more intense the micro galvanic corrosion, and it is promoted by the presence of fine precipitates of  $Mg_{17}Al_{12}$ .

### CRedit authorship contribution statement

**Anna Dobkowska:** Conceptualization, Methodology, Investigation, Writing – Original Draft, **Aleksandra Zielińska:** Investigation, Writing – Original Draft, **Irena Paulin:** Investigation, Writing – Review & Editing, **Črtomir Donik:** Investigation, Data Curation, **Maciej Łojkowski:** Investigation, **Milena Korallnik:** Investigation, Data Curation, **Bogusława Adamczyk-Cieślak:** Investigation, **Krystian Paradowski:** Investigation, Data Curation,

**Marek Tkocz:** Resources, **Dariusz Kuc:** Resources, **Jiří Kubásek:** Writing – Review & Editing, **Matjaž Godec:** Writing – Review & Editing, Funding acquisition, **Wojciech Świąszkowski:** Conceptualization, Supervision, Writing – Review & Editing, Funding acquisition.

### Data Availability

Data will be made available on request.

### Declaration of Competing Interest

The authors declare that they have no known competing financial interests or personal relationships that could have appeared to influence the work reported in this paper.

### Acknowledgements

This research was funded under statutory work No. 404/04727/1090 at the Faculty of Materials Science and Engineering Warsaw University of Technology in Poland, and by the Slovenian Research Agency ARRS program P2-0132 "Physics and Chemistry of Metals".

Authors would like to thank Dr. Paul McGuinness from the Institute of Metals and Technology in Slovenia for his support in language corrections, and to Mr. Jakub Ciftci, PhD Candidate at the Faculty of Materials Science and Engineering Warsaw University of Technology for assistance in 3D imaging of KoBo method.

## References

- [1] M. Avvari, S. Narendranath, M. Able, Microstructure evolution in AZ61 alloy processed by equal channel angular pressing, *Adv. Mech. Eng.* 8 (2016) 1–9, <https://doi.org/10.1177/1687814016651820>
- [2] Z. Shan, J. Yang, J. Fan, H. Zhang, Q. Zhang, Y. Wu, et al., Microstructure evolution and mechanical properties of an AZ61 alloy processed with TS-ECAP and EPT, *Mater. Sci. Eng. A* 780 (2020) 139195, <https://doi.org/10.1016/j.msea.2020.139195>
- [3] V. Beura, D. Zhang, N. Overman, J. Darsell, D.R. Herling, K. Solanki, et al., Enhanced mechanical behavior and corrosion resistance of AZ31 magnesium alloy through a novel solid-phase processing, *Corros. Sci.* 197 (2022) 110074, <https://doi.org/10.1016/j.corsci.2021.110074>
- [4] Y. Xu, L.X. Hu, Y. Sun, J.B. Jia, J.F. Jiang, Q.G. Ma, Microstructure and mechanical properties of AZ61 magnesium alloy prepared by repetitive upsetting-extrusion, *Trans. Nonferrous Met Soc. China (Engl. Ed.)* 25 (2015) 381–388, [https://doi.org/10.1016/S1003-6326\(15\)63614-7](https://doi.org/10.1016/S1003-6326(15)63614-7)
- [5] Q. Chen, D. Shu, C. Hu, Z. Zhao, B. Yuan, Grain refinement in an as-cast AZ61 magnesium alloy processed by multi-axial forging under the multi-temperature processing procedure, *Mater. Sci. Eng. A* 541 (2012) 98–104, <https://doi.org/10.1016/j.msea.2012.02.009>
- [6] X.S. Xia, M. Chen, Y.J. Lu, F.Y. Fan, C.H. Zhu, J. Huang, et al., Microstructure and mechanical properties of isothermal multi-axial forging formed AZ61 Mg alloy, *Trans. Nonferrous Met Soc. China (Engl. Ed.)* 23 (2013) 3186–3192, [https://doi.org/10.1016/S1003-6326\(13\)62851-4](https://doi.org/10.1016/S1003-6326(13)62851-4)
- [7] J. Jiang, Y. Wang, J. Qu, Microstructure and mechanical properties of AZ61 alloys with large cross-sectional size fabricated by multi-pass ECAP, *Mater. Sci. Eng. A* 560 (2013) 473–480, <https://doi.org/10.1016/j.msea.2012.09.092>
- [8] J. Li, J. Liu, Z. Cui, Microstructures and mechanical properties of AZ61 magnesium alloy after isothermal multidirectional forging with increasing strain rate, *Mater. Sci. Eng. A* 643 (2015) 32–36, <https://doi.org/10.1016/j.msea.2015.07.028>
- [9] Z. Shan, J. Yang, J. Fan, H. Zhang, Q. Zhang, Y. Wu, et al., Extraordinary mechanical properties of AZ61 alloy processed by ECAP with 160° channel angle and EPT, *J. Magnes. Alloy* 9 (2021) 548–559, <https://doi.org/10.1016/j.jma.2020.02.028>
- [10] M. Zhou, Y. Morisada, H. Fujii, Effect of Ca addition on the microstructure and the mechanical properties of asymmetric double-sided friction stir welded AZ61 magnesium alloy, *J. Magnes. Alloy* 8 (2020) 91–102, <https://doi.org/10.1016/j.jma.2020.02.001>
- [11] F. Yavari, S.G. Shabestari, Assessment of the microstructure, solidification characteristics and mechanical properties of AZ61 + xSr magnesium alloys, *Met. Mater. Trans. B Process Met. Mater. Process Sci.* 51 (2020) 3089–3097, <https://doi.org/10.1007/s11663-020-01971-0>
- [12] H. Zhang, J. Wang, H. Ma, Y. Yuan, Y. Li, Y. Liu, et al., The microstructure evolution and mechanical properties improvement of the AZ61 alloy by adding Sr, *Mater. Res. Express* (2021) 8, <https://doi.org/10.1088/2053-1591/ac315f>
- [13] J. Su, F. Guo, H. Cai, L. Liu, Study on alloying element distribution and compound structure of AZ61 magnesium alloy with yttrium, *J. Phys. Chem. Solids* 131 (2019) 125–130, <https://doi.org/10.1016/j.jpcs.2019.03.021>
- [14] C. Jun, Z. Qing, L. Qunan, Microstructure and mechanical properties of AZ61 magnesium alloys with the Y and Ca combined addition, *Int. J. Met* 12 (2018) 897–905, <https://doi.org/10.1007/s40962-018-0222-7>
- [15] C. Hu, C. Chen, M. Zhang, Effects of Ag content and heat treatment on the microstructure and properties of SLMed AZ61 Mg–Al–Zn alloy, *Appl. Phys. A Mater. Sci. Process* 127 (2021) 1–16, <https://doi.org/10.1007/s00339-021-04331-0>
- [16] S.M. Masoudpanah, R. Mahmudi, The microstructure, tensile, and shear deformation behavior of an AZ31 magnesium alloy after extrusion and equal channel angular pressing, *Mater. Des.* 31 (2010) 3512–3517, <https://doi.org/10.1016/j.matdes.2010.02.018>
- [17] H.T. Jeong, W.J. Kim, Critical review of superplastic magnesium alloys with emphasis on tensile elongation behavior and deformation mechanisms, *J. Magnes. Alloy* 10 (2022) 1133–1153, <https://doi.org/10.1016/j.jma.2022.02.009>
- [18] A. Dobkowska, B. Adamczyk – Cieslak, M. Koralnik, W. Chromiński, J. Kubasek, J. Ciftci, et al., Corrosion behavior of fine-grained Mg-7.5Li-3Al-1Zn fabricated by extrusion with a forward-backward rotating die (KoBo), *J. Magnes. Alloy* (2021), <https://doi.org/10.1016/j.jma.2021.08.020>
- [19] A. Dobkowska, M. Koralnik, B. Adamczyk-Cieslak, D. Kuc, W. Chromiński, J. Kubasek, et al., The effect of extrusion ratio on the corrosion resistance of ultrafine-grained Mg-4Li-3Al-Zn alloy deformed using extrusion with a forward-backward oscillating die, *J. Mater. Eng. Perform.* (2022), <https://doi.org/10.1007/s11665-022-06895-1>
- [20] A. Dobkowska, B. Adamczyk – Cieslak, M. Koralnik, W. Chromiński, J. Kubasek, J. Ciftci, et al., Corrosion behavior of fine-grained Mg-7.5Li-3Al-1Zn fabricated by extrusion with a forward-backward rotating die (KoBo), *J. Magnes. Alloy* 10 (2021) 811–820, <https://doi.org/10.1016/j.jma.2021.08.020>
- [21] A. Dobkowska, B. Adamczyk-Cieslak, M. Chlewicka, A. Towarek, A. Zielińska, M. Koralnik, et al., Evolution of microstructure dependent corrosion properties of ultrafine AZ31 under conditions of extrusion with a forward backward oscillating die, *J. Mater. Res. Technol.* 18 (2022) 4486–4496, <https://doi.org/10.1016/j.jmrt.2022.04.131>
- [22] I. Bednarczyk, D. Kuc, A. Tomaszewska, M. Tkocz, The effect of extrusion in the complex strain state on the microstructure and mechanical properties of MgAlZn magnesium alloys, *Arch. Met. Mater.* 65 (2020) 1121–1128, <https://doi.org/10.24425/amm.2020.133228>
- [23] R.M. Molak, K. Paradowski, T. Brynk, L. Ciupinski, Z. Pakielna, K.J. Kurzydowski, Measurement of mechanical properties in a 316L stainless steel welded joint, *Int. J. Press Vessel Pip.* 86 (2009) 43–47, <https://doi.org/10.1016/j.ijpvp.2008.11.002>
- [24] EN ISO. Metallic materials - Tensile testing - Part 1: Method of test at room temperature, vol. 1, 2020.
- [25] A. Dobkowska, L. Zrodowski, M. Chlewicka, M. Koralnik, B. Adamczyk-cie. A comparison of the microstructure-dependent corrosion of dual-structured Mg-Li alloys fabricated by powder consolidation methods: Laser powder bed fusion vs pulse plasma sintering, *J. Magnes. Alloy* (2022), <https://doi.org/10.1016/j.jma.2022.06.003>
- [26] S.M. Baek, H.J. Kim, H.Y. Jeong, S.D. Sohn, H.J. Shin, K.J. Choi, et al., Effect of alloyed Ca on the microstructure and corrosion properties of extruded AZ61 Mg alloy, *Corros. Sci.* 112 (2016) 44–53, <https://doi.org/10.1016/j.corsci.2016.07.011>
- [27] K. Singh, G. Singh, H. Singh, Investigation of microstructure and mechanical properties of friction stir welded AZ61 magnesium alloy joint, *J. Magnes. Alloy* 6 (2018) 292–298, <https://doi.org/10.1016/j.jma.2018.05.004>
- [28] H. Aghamohammadi, S.J. Hosseinipour, S.M. Rabiee, R. Jamaati, Effect of hot rolling on microstructure, crystallographic texture, and hardness of AZ31 alloy, *Mater. Chem. Phys.* 273 (2021) 125130, <https://doi.org/10.1016/j.matchemphys.2021.125130>
- [29] X.G. Qiao, Y.W. Zhao, W.M. Gan, Y. Chen, M.Y. Zheng, K. Wu, et al., Hardening mechanism of commercially pure Mg processed by high pressure torsion at room temperature, *Mater. Sci. Eng. A* 619 (2014) 95–106, <https://doi.org/10.1016/j.msea.2014.09.068>
- [30] C. Zhang, L. Wu, G. Huang, Y. Huang, B. Jiang, A. Atrens, et al., Effect of microalloyed Ca on the microstructure and corrosion behavior of extruded Mg alloy AZ31, *J. Alloy. Compd.* 823 (2020) 153844, <https://doi.org/10.1016/j.jallcom.2020.153844>
- [31] C.Q. Li, D.K. Xu, X.B. Chen, B.J. Wang, R.Z. Wu, E.H. Han, et al., Composition and microstructure dependent corrosion behaviour of Mg–Li alloys, *Electro Acta* 260 (2018) 55–64, <https://doi.org/10.1016/j.electacta.2017.11.091>
- [32] Z. Wen, C. Wu, C. Dai, F. Yang, Corrosion behaviors of Mg and its alloys with different Al contents in a modified simulated body fluid, *J. Alloy. Compd.* 488 (2009) 392–399, <https://doi.org/10.1016/j.jallcom.2009.08.147>
- [33] W.J. Kim, S.I. Hong, Y.S. Kim, S.H. Min, H.T. Jeong, J.D. Lee, Texture development and its effect on mechanical properties of an AZ61 Mg alloy fabricated by equal channel angular pressing, *Acta Mater.* 51 (2003) 3293–3307, [https://doi.org/10.1016/S1359-6454\(03\)00161-7](https://doi.org/10.1016/S1359-6454(03)00161-7)
- [34] Z. Zeng, N. Stanford, C.H.J. Davies, J.F. Nie, N. Birbilis, Magnesium extrusion alloys: a review of developments and prospects, *Int. Mater. Rev.* 64 (2019) 27–62, <https://doi.org/10.1080/09506608.2017.1421439>
- [35] M. Zha, H.M. Zhang, C. Wang, H.Y. Wang, E.B. Zhang, Q.C. Jiang, Prominent role of a high volume fraction of Mg17Al12 particles on tensile behaviors of rolled Mg–Al–Zn alloys, *J. Alloy. Compd.* 728 (2017) 682–693, <https://doi.org/10.1016/j.jallcom.2017.08.289>
- [36] M. Lu, J. Mead, Y. Wu, H. Russell, H. Huang, A study of the deformation and failure mechanisms of protective intermetallic coatings on AZ91 Mg alloys using microarc-tensile bending, *Mater. Charact.* 120 (2016) 337–344, <https://doi.org/10.1016/j.matchar.2016.09.020>
- [37] A. Atrens, M. Liu, N.I. Zainal Abidin, Corrosion mechanism applicable to biodegradable magnesium implants, *Mater. Sci. Eng. B Solid-State Mater. Adv. Technol.* (2011), <https://doi.org/10.1016/j.mseb.2010.12.017>
- [38] A. Dhanapal, S. Rajendra Boopathy, V. Balasubramanian, Influence of pH value, chloride ion concentration and immersion time on corrosion rate of friction stir welded AZ61A magnesium alloy weldments, *J. Alloy. Compd.* 523 (2012) 49–60, <https://doi.org/10.1016/j.jallcom.2012.01.070>
- [39] A. Pardo, M.C. Merino, A.E. Coy, F. Viejo, R. Ariabal, S. Feliú, Influence of microstructure and composition on the corrosion behaviour of Mg/Al alloys in chloride media, *Electro Acta* 53 (2008) 7890–7902, <https://doi.org/10.1016/j.electacta.2008.06.001>
- [40] S. Mathieu, C. Rapin, J. Steinmetz, P. Steinmetz, A corrosion study of the main constituent phases of AZ91 magnesium alloys, *Corros. Sci.* 45 (2003) 2741–2755, [https://doi.org/10.1016/S0010-938X\(03\)00109-4](https://doi.org/10.1016/S0010-938X(03)00109-4)
- [41] C. Ubeda, G. Garces, P. Adeva, I. Llorente, G.S. Frankel, S. Fajardo, The role of the beta-Mg17Al12 phase on the anomalous hydrogen evolution and anodic dissolution of AZ magnesium alloys, *Corros. Sci.* 165 (2020) 108384, <https://doi.org/10.1016/j.corsci.2019.108384>
- [42] S. Candan, E. Candan, Comparative study on corrosion behaviors of Mg–Al–Zn alloys, *Trans. Nonferrous Met Soc. China (Engl. Ed.)* 28 (2018) 642–650, [https://doi.org/10.1016/S1003-6326\(18\)64696-5](https://doi.org/10.1016/S1003-6326(18)64696-5)
- [43] K.D. Ralston, N. Birbilis, C.H.J. Davies, Revealing the relationship between grain size and corrosion rate of metals, *Scr. Mater.* 63 (2010) 1201–1204, <https://doi.org/10.1016/j.scriptamat.2010.08.035>
- [44] K.D. Ralston, N. Birbilis, Effect of grain size on corrosion, *Corrosion* 66 (2010) 1–4, <https://doi.org/10.5006/1.3462912>
- [45] S.V. Dobatkin, E.A. Lukanova, N.S. Martynenko, N.Y. Anisimova, M.V. Kiselevskiy, M.V. Gorshenkov, et al., Strength, corrosion resistance, and biocompatibility of ultrafine-grained Mg alloys after different modes of severe plastic deformation, *IOP Conf. Ser. Mater. Sci. Eng.* (2017) 194, <https://doi.org/10.1088/1757-899X/194/1/012004>
- [46] A. Witcka, A. Bogucka, A. Yamamoto, K. Máthi, T. Krajciák, J. Jaroszewicz, et al., In vitro degradation of ZM21 magnesium alloy in simulated body fluids, *Mater. Sci. Eng. C* 65 (2016) 59–69, <https://doi.org/10.1016/j.msec.2016.04.019>
- [47] C. Liu, H. Zheng, X. Gu, B. Jiang, J. Liang, Effect of severe shot peening on corrosion behavior of AZ31 and AZ91 magnesium alloys, *J. Alloy. Compd.* 770 (2019) 500–506, <https://doi.org/10.1016/j.jallcom.2018.08.141>



TECHNICAL ARTICLE

# The Effect of Extrusion Ratio on the Corrosion Resistance of Ultrafine-Grained Mg-4Li-3Al-Zn Alloy Deformed Using Extrusion with a Forward-Backward Oscillating Die

Anna Dobkowska , Milena Koralknik, Bogusława Adamczyk-Cieślak, Dariusz Kuc, Witold Chromiński, Jiri Kubasek, and Jarosław Mizera

Submitted: 3 November 2021 / Revised: 22 March 2022 / Accepted: 2 April 2022

In this study, the microstructure-dependent corrosion of fine-grained Mg-4Li-3Al-Zn alloys in the chloride containing solutions is described. The materials were processed using extrusion with a forward-backward oscillating die. The Mg-4Li-3Al-Zn alloys were extruded from  $\varnothing 40$  to  $\varnothing 4$  mm ( $R_1 = 10:1$ ,  $\lambda_1 = 100$ ), and also from  $\varnothing 40$  to  $\varnothing 1$  mm ( $R_2 = 40:1$ ,  $\lambda_2 = 1600$ ); the resulting microstructures were then analyzed. The results show that the corrosion of both alloys is strongly dependent on the processing parameters (mainly extrusion ratio), which in turn have a significant influence on the recrystallization stage. Interestingly, the higher the extrusion ratio, the lower the corrosion resistance of the alloy. The decreasing corrosion resistance of the alloy deformed at a higher extrusion ratio is related to the grain growth resulting from the more intense recrystallization processes that occurred during KoBo extrusion.

**Keywords** Mg-Li alloys, corrosion, extrusion ratio, microstructure

## 1. Introduction

Extrusion is a powerful technique which results in the improvement of many properties of metallic materials (Ref 1, 2). The recent literature suggests that grain refinement can improve the mechanical and corrosion properties of Mg and its alloys (Ref 3), however, grain refinement may also lead to reduced corrosion resistance, partly because of the increased chemical activity at energetic grain boundary regions (Ref 4). Numerous experiments have shown that severe plastic deformation (SPD) provides a useful tool for introducing significant microstructure refinement in AZ-type magnesium alloys (Ref 5). As commonly known, plastic deformation of Mg-based alloys is difficult to process due to their hcp-structure, which together with their low stacking fault energy, is the main cause of the low ductility of Mg-based alloys (Ref 6). Therefore, very important from processing point of view is to develop the room-temperature deformation method of Mg-based alloys. One of the solution is the modification of the crystal structure of Mg by Li addition, which has a significant impact on its formability at room temperature by the activation of prismatic

slip alongside basal slip, resulting in an increasing number of total available independent slip systems (Ref 7). To approach this, Mg-Li with 8 wt.% Li was processed by high-pressure torsion at room temperature, and as a result, ultrafine grains were formed (Ref 8). Mg-8Li-1Zn processed by multidirectional forging, and rolling at 573 K with refined microstructure was also described by Cao et al. (Ref 9). The ultrafine-grained Mg-9Li-1Zn alloy prepared through high-ratio-differential speed rolling had a higher strength and ductility at room temperature than its conventional counterpart (Ref 10).

The literature review indicated that there is a chance that significant microstructure refinement may also increase the corrosion resistance of Mg-Li alloys. It was found that SPD affects both the microstructure and the corrosion performance of AZ31, and as shown by Ben Hamu et al. (Ref 11) and Alvarez-Lopez et al. (Ref 12), the corrosion rate decreases with a decrease in grain size. The corrosion resistance of hot rolled Mg-4Li-1Ca was analyzed in simulated body fluids by Nene et al. (Ref 13). The results showed a significant improvement in the overall corrosion resistance of the fine-grained alloy over the coarse one. Li et al. (Ref 14) showed that the grain refinement of Mg-9Li-1Zn via friction stir processing weakened galvanic corrosion compared to the coarse-grained counterpart. Mineta et al. (Ref 15) proved that accumulative channel-die compression bonding is a powerful method to simultaneously improve the Vickers hardness and corrosion resistance of LA143.

Studies to date have shown various SPD techniques that give a significant grain refinement of Mg-based alloys, leading to an improvement in their corrosion resistance. A recently developed method for significantly reducing the grain size of Mg-based alloys at room temperature is extrusion with a forward-backward rotating die (KoBo) (Ref 16). KoBo, due to the additional reverse rotation of the matrix, is a suitable method of deformation for materials that are hard to deform at low temperature without pre-heating of the billet (Ref 17). During KoBo extrusion, the input material goes through the matrix,

Anna Dobkowska, Milena Koralknik, Bogusława Adamczyk-Cieślak, Witold Chromiński, and Jarosław Mizera, Faculty of Materials Science and Engineering, Warsaw, University of Technology, Wołoska 141, 02-507 Warsaw, Poland; Dariusz Kuc, Institute of Materials Engineering, Silesian University of Technology, Krasińskiego 8, 40-019 Katowice, Poland; Jiri Kubasek, Department of Metals and Corrosion Engineering, University of Chemistry and Technology, Technicka 5, 166 28 Prague 6, Czech Republic. Contact e-mail: anna.dobkowska@pw.edu.pl.

where an additional reversible oscillating die causes permanent destabilization of the structure and the dominance of localized plastic flow in the intersecting shear bands (Ref 17); a detailed description of the KoBo can be found in (Ref 18). In the deformed materials, fine or even nano-grained microstructure is formed, and the materials have an optimum combination of high strength and good plasticity (Ref 19–22). Our previous work focused on the characterization of the corrosion mechanisms occurred in dual phase Mg-Li (according to equilibrium phase diagram when Li concentration is more than 5.5 wt.% and less than 11wt.% Mg-Li alloys have dual phase structure) (Ref 18). Nevertheless, there is still no information regarding the corrosion performance of KoBo extruded single  $\alpha$  phase Mg-Li alloys (with less than 5.5 wt.% of Li). Therefore, in this work the microstructure and corrosion properties of fine-grained Mg-4Li-3Al-Zn (AZ31-4Li) extruded using the KoBo method at various extrusion ratios are investigated.

## 2. Materials and Methodology

### 2.1 Materials

In this paper, the Mg-4Li-3Al-1Zn (AZ31-4Li) alloy deformed at different processing parameters is investigated: extruded using KoBo from  $\varnothing 40$  mm to  $\varnothing 4$  mm giving an extrusion ratio of  $R_1 = 10:1$  and a processing degree of  $\lambda_1 = 100$ , and extruded from  $\varnothing 40$  mm to  $\varnothing 1$  mm ( $R_2 = 40:1$  and  $\lambda_2 = 1600$ ). The initial billet temperature was 24 °C. The extrusion was performed with a punch speed of 0.2 mm/s, a die oscillating angle of  $\pm 8^\circ$ , and an oscillation frequency of 5 Hz.

### 2.2 Microstructural Characterization

The chemical composition of the alloy before extrusion was performed using the high-performance wavelength dispersive x-ray fluorescence (WDXRF) Bruker S4 Explorer spectrometer. After extrusion, due to the high ability of Li to oxidation and evaporation, its relative concentration in the extruded alloys was measured using atomic absorption spectroscopy (AAS, GBC 932 Plus).

X-ray diffraction (XRD, Bruker D8 Advance) operating at 40 kV and 40 mA with Cu K $\alpha$  radiation was used to characterize the detailed phase composition of the alloys. The results were recorded by stepwise scanning  $2\theta$  from 10 to 120°, with a step size of 0.02° and a count time of 10 s per step.

To characterize the grain size and coarse precipitations formed in the alloys, high-resolution scanning electron microscopic observations were carried out in back scattered mode (SEM BSE, Hitachi SU8000). Additionally, electron backscattered (EBSD) scans were performed using scanning electron microscope (SEM, Hitachi SU70) equipped with Bruker EBSD detector. The EBSD data were recorded with a step size of 50 nm. The grain sizes were calculated using Quantax Esprit Bruker Microanalysis Software. The crystallographic orientations of grains are presented on inverse pole figure (IPF) maps, where various colors distinguish the orientation of a given sample direction in a crystal frame. High and low angle grain boundaries were also labeled on the maps; if the angle between two neighboring grains was distorted by more than 15°, then the angle between those grains was described as a high angle grain boundary (HAGB); when the grains were misoriented by

less than 15° (cut-off limit of 3° has been selected), a low angle grain boundary (LAGB) was created between those grains.

The extruded wires were cut into slices, polished with 1200-grit and 2400-grit SiC papers, and subsequently, the surfaces perpendicular to the extrusion direction were polished with a low-energy Ar<sup>+</sup> ion beam milling system (Hitachi IM4000 Ion Milling System) for 6 hours. Observations and EBSD measurements were done immediately after samples preparation.

A transmission electron microscope (TEM, JEOL JEM-1200EX) with an acceleration voltage of 120 kV was used to characterize the detailed phases formed in the alloys. The diffraction contrast in the bright field (BF) mode showed the grain size. The thin foils used for TEM observations were prepared using a Gatan Model 656 Dimple Grinder and a Gatan Model 691 Precision Ion Polishing System at 2.5 kV. The samples were observed on the cross-section perpendicular to the direction of extrusion.

### 2.3 Corrosion Tests

**2.3.1 Electrochemical Procedure.** Electrochemical measurements were carried out in naturally aerated, unstirred 0.01 M NaCl solution using a Gamry FAS1 potentiostat equipped with three electrodes: platinum as the counter electrode, Ag/AgCl as the reference electrode, and the measured sample as the working electrode. The reference electrode was inserted into a Luggin capillary, and the setup was placed in front of the Mg electrode. The electrolyte was made up using analytical grade reagents and distilled water. The corrosion potential ( $E_{\text{corr}}$ ) was recorded for 1 hour under open-circuit conditions. Potentiodynamic polarization tests were then carried out after immersion in a range of 0.5 V below  $E_{\text{OCP}}$  to 1.5 V vs. Ref (a scan rate of 5 mV/s was used). At least three tests were conducted for each microstructural condition. Polarization curves were fitted using Gamry Elchem software in Tafel mode.

**2.3.2 Characterization of Corroded Surfaces.** The corroded surfaces of the samples were observed after 1-hour immersion under open-circuit conditions using SEM, Hitachi SU8000. To describe the role of the microstructure in the corrosion resistance of both alloys, surfaces with chemically removed corrosion products were observed using SEM. After 1 hour of immersion in 0.01 M NaCl, the samples were gently removed, dried, and subsequently immersed in 4% nitric acid for 5 s to remove corrosion products.

**2.3.3 Corrosion Rate Calculation.** To make an exact comparison of the corrosion resistance of both alloys, the corrosion rate after 1 hour of immersion in the naturally aerated 0.01 M NaCl was calculated based on hydrogen evolution (Ref 23, 24). The evolved hydrogen was collected during immersion tests. To measure the hydrogen gas, samples polished up to #4000 SiC paper were placed into a beaker and connected to a burette. Hydrogen was collected in the burette through a PVC pipe installed above the beaker equipped with a dropping funnel. The corrosion rate was calculated as follows:

$$CR = \Delta m / s \cdot t \quad (\text{Eq 1})$$

where:  $\Delta m$  is the mass loss (g) calculated from hydrogen evolution,  $s$  is the surface area (m<sup>2</sup>), and  $t$  is the time of exposure (day). To determine the standard deviation of the measured data, three parallel samples were immersed for each extrusion condition.

### 3. Results

#### 3.1 Microstructural Characterization

The chemical composition of the billet before extrusion is given in Table 1, indicating that the composition of the investigated material is similar to the nominal composition of AZ31B (Ref 25). As shown in Table 2, the concentration of Li in the alloy extruded to Ø4 mm was found to be 3.32 wt.%, while in the alloy extruded to Ø1 mm it was 3.46 wt.%. The microstructures of both alloys are shown in Fig. 1(a) and (b). The SEM observations clearly revealed that ultrafine-grained microstructures with a grain size of less than 5 µm were formed in the examined alloys. Comparing Fig. 1(a) and (b), a more refined microstructure was formed in the alloy extruded to Ø4 mm, while grains of a greater size were present in the alloy extruded to Ø1 mm ( $d_{avg} = 3.24 \mu\text{m}$  for the alloy extruded to Ø4 mm,  $d_{avg} = 3.94 \mu\text{m}$  for the one extruded to Ø1 mm, Fig. 2). Coarse particles rich in Al and Mn occurred in both alloys (marked as P1, Fig. 1). They were randomly distributed in the matrix, and their chemical composition is given in Fig. 1(c). Needle-like particles rich in Si were also observed in the alloy extruded to Ø1 mm (Fig. 1b). The grains formed in the alloys have random crystallographic orientation, with the prevalence of grains oriented to  $\langle -1-210 \rangle$  direction (Fig. 2). In both alloys, more than 95% of the grain boundaries are HAGBs. It is worth to mention that the grain size of the billet before KoBo extrusion was found to be 19.42 µm.

XRD patterns (Fig. 3) revealed that only the diffraction peaks of the  $\alpha(\text{Mg})$  phase were identified for the Mg-4Li-3Al-1Zn extruded to Ø4 mm, while additional peaks arising from  $\text{Mg}_{17}\text{Al}_{12}$  were noted in the case of the alloy reduced to Ø1 mm. In order to more thoroughly characterize the microstructures of the alloys, TEM observations were made. As shown in Fig. 4(a), coarse and nearly round dark precipitates identified as AlLi were found in the alloy extruded to Ø4 mm. Their amount was too small to be revealed by XRD. The TEM observations performed for the alloy extruded to Ø1 mm confirmed the presence of small round dark precipitates of  $\text{Mg}_{17}\text{Al}_{12}$ . Additionally, small needle-like precipitates were observed, and they were indexed in terms of non-stoichiometric  $\text{Li}_{0.81}\text{Mg}_{0.19}$  (Fig. 4b).

#### 3.2 Corrosion Performance

Figure 5(a) presents the open circuit potential of each Mg-4Li-3Al-1Zn alloy in 0.01 M NaCl monitored for 1 h. The subsequent surface appearance of each sample was recorded by SEM. A more negative potential was recorded for the alloy extruded to Ø4 mm. Immediately the specimen was immersed, the potential had started to smoothly increase from  $-1.50 \text{ V/Ref}$  toward more positive values achieving  $-1.42 \text{ V/Ref}$  after 45 min of immersion. Afterward slight decrease in the potential was observed. A more positive potential was recorded for the specimens deformed at a higher degree of extrusion (starting from  $-1.40 \text{ V/Ref}$ ). The potential of the sample oscillated

throughout the immersion. Generally, a more negative potential reflects poorer corrosion resistance of the alloy in the corrosive environment (Ref 26), in the case of Mg-based alloys, the rise in open circuit potential is attributed to the phenomenon called "cathodic activation" (Ref 27). Moreover, the oscillations in the open circuit potential recorded for the alloy extruded to lower dimensions indicated more intense course of dissolution/passivation reactions than those proceeding on the alloy extruded to Ø4 mm (Ref 28).

The potentiodynamic curves of Mg-4Li-3Al-1Zn are displayed in Fig. 5(b). The cathodic side of the curves were driven by the hydrogen evolution reaction. In both cases, when the potential reached  $E_{\text{corr}}$ , the corrosion current density gradually increased with increasing anodic potential. When the potential was around 200 mV more positive than  $E_{\text{corr}}$  for the sample extruded to Ø4 mm, or around 600 mV more positive for sample extruded to Ø1 mm, the corrosion current increased abruptly, indicating the breakdown of the oxide film. The greater difference between  $E_{\text{corr}}$  and  $E_b$  occurred for the Mg-4Li-3Al-1Zn extruded to Ø1 mm, suggesting that this alloy was more resistant to localized corrosion than the other. However, the corrosion current density  $i_{\text{corr}}$  was significantly higher for the alloy extruded to Ø1 mm (Table 3), suggesting in contrast that this alloy was the more active of the two in the corrosive medium.

While potentiodynamic polarization allows a careful quantification of electrochemical kinetics, such testing is not sufficient to provide detailed information about the real-life corrosion rates of Mg-based alloys (Ref 29). One convenient and reliable method to measure the corrosion rate of Mg-based alloys is the hydrogen evolution technique, which is also used for Mg-Li alloys. The results from the hydrogen evolution technique showed that the sample extruded to Ø1 mm had double the corrosion rate, 307 g/(m<sup>2</sup>day), than the other, 135 g/(m<sup>2</sup>day) (Table 4).

The surface morphologies of the specimens after 1 hour of immersion in 0.01 M NaCl solution are shown in Fig. 6 and 7. More intense corrosion products were formed on the alloy extruded to Ø1 mm (compare Fig. 6a and 7a). When the corrosion products were removed (according to the ASTM standard G1-03 Ref 30), characteristic filiform corrosion was observed on the surface of both alloys (Fig. 6b and 7b). The mechanism of filiform corrosion formed on Mg-Li alloys in chloride containing solution has been clearly described by Song et al. (Ref 31). Similarly to those results, in our study the

**Table 2 The relative concentration of Li in the alloys after KoBo extrusion measured using AAS**

AZ31 + 4Li	Li wt.%
Extruded to Ø4 mm	3.32
Extruded to Ø1 mm	3.46

**Table 1 The chemical composition of the billet before extrusion measured using WDXRF**

Elements wt.%	Al	Zn	Mn	Si	S	P	Mg + Li
AZ31 + 4Li Ø40 mm	3.28	0.91	0.26	0.12	0.01	0.01	Bal.

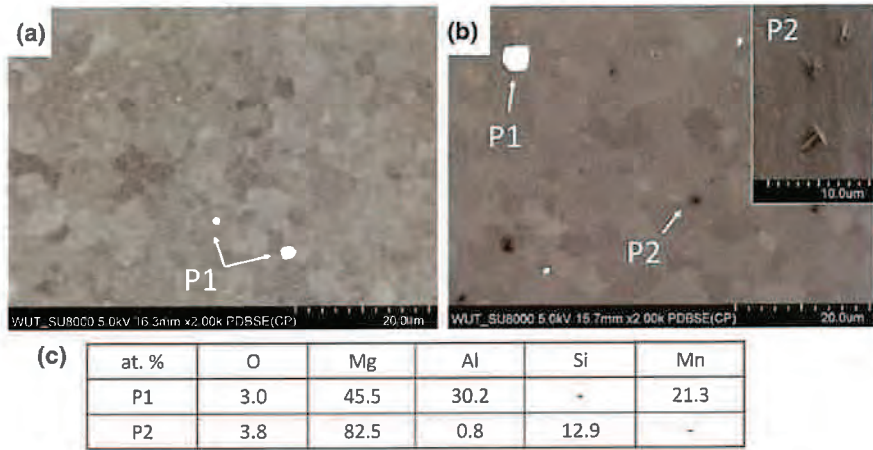


**Fig. 1** SEM images: (a) the microstructure of the alloy extruded to Ø4 mm, (b) the microstructure of the alloy extruded to Ø1 mm (P2 precipitates in SE mode are shown in the inset). (c) EDX point analyses of the precipitates are given in the table

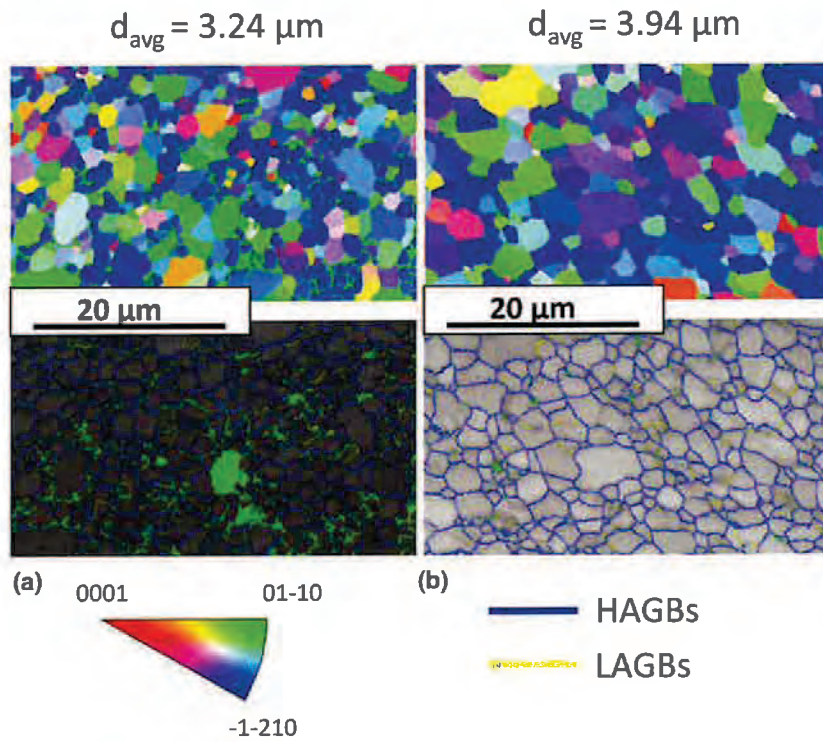


**Fig. 2** IPF maps with corresponding low and high angle grain boundaries marked in the band contrast images obtained for (a) the alloy extruded to Ø4 mm, (b) the alloy extruded to Ø1 mm; the average grain size ( $d_{avg}$ , average equivalent diameter) is given above each panel. The non-indexed areas are given in green in band contrast maps (Color figure online)

filaments were not perfectly straight, and the way they propagated appeared to be through some privileged paths. The important observation from our study is that filaments propagated into the depth of the material through crystallographically grown traces, which is visible in Fig. 7(c). This is the first time it has been noted that filiform corrosion propagates through the crystal lattice of  $\alpha(\text{Mg})$ . In random

areas, the corrosion attack propagated into the depths of the material causing deep damage (Fig. 7b). These findings indicated that the corrosion resistance of the alloy was weakened by extrusion at a higher deformation ratio, and the specimen with the lowest dimension had the lowest corrosion resistance. As observed, the precipitates rich in Al and Mn were not active during immersion in the corrosive medium (Fig. 6b).

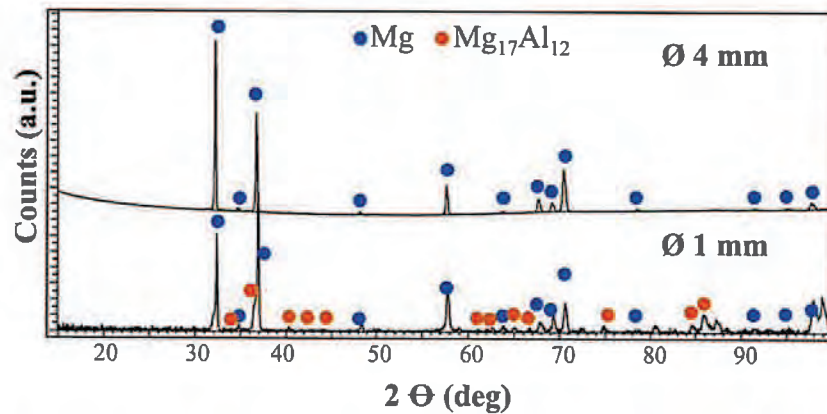


Fig. 3 XRD patterns obtained for the Mg-4Li-3Al-Zn extruded to Ø4 mm and to Ø1 mm

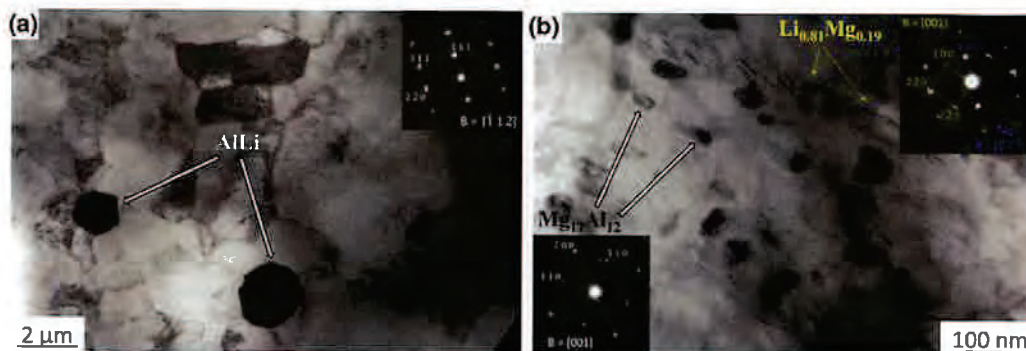


Fig. 4 TEM images in bright field and selected area diffraction (SAD) patterns obtained from second phase particles formed in Mg-4Li-3Al-1Zn: (a) extruded to Ø4 mm, (b) extruded to Ø1 mm

#### 4. Discussion

Results of this work show that the corrosion resistance of KoBo deformed fine-grained Mg-4Li-3Al-Zn alloys is dependent on the extrusion ratio. Our findings also show that the corrosion performance of Mg-4Li-3Al-Zn is a complex process and is related to a few microstructural-dependent components.

Firstly, it is important to mention that both, alloy chemistry and grain size play crucial roles in the corrosion resistance of the investigated alloys, and conversely to the results reported in reference (Ref 32), the grain size is dominant over the alloy chemistry. There are many studies showing the positive influence of grain refinement on the corrosion rate of coarse-grained Mg-based alloys (Ref 33), while there is no clear-cut information about the relationship of extrusion ratio and grain size among the refined microstructures of Mg-based alloys. As shown in this study, a higher extrusion ratio does not always lead to the greater grain refinement. The results of this study clearly show that the higher the extrusion ratio, the faster the corrosion rate of the material. The decreasing corrosion resistance of the alloy deformed at the higher extrusion ratio is related to the grain growth resulting from more intense recrystallization processes. During KoBo deformation at the higher extrusion ratio (sample extruded to Ø1 mm) effects related to material friction caused an increase in material's temperature resulting in its grain growth. As such, the corrosion

behavior of the as-extruded alloy was largely determined by the deformation of the Mg matrix phase. As shown by Korbel et al. (Ref 17), during KoBo extrusion the increase in the billet temperature, especially at high extrusion ratios, is unpredictable. Such behavior leads to intense recrystallization processes—the higher the extrusion ratio, the greater grain growth. The most likely explanation of the grain growth is that the accumulation of plastic deformation caused various dynamic recrystallization processes to occur. Depending on the deformation parameters, these processes led to dislocation structure evolution, low angle grain boundaries being formed, and their transformation to high angle grain boundaries caused grain growth in the material extruded at a higher extrusion ratio (Ref 34). This explains the grain growth observed in the alloy extruded to Ø1 mm ( $\lambda_2 = 1600$ ).

Generally, corrosion attack on Mg-Al alloys occurs at  $\alpha$ (Mg) and intermetallic particles, and a small amount of  $Mg_{17}Al_{12}$  accelerates the corrosion of the  $\alpha$ (Mg) matrix by micro-galvanic coupling (Ref 35). Therefore, the presence of the  $Mg_{17}Al_{12}$  in the alloys extruded Ø1 mm cannot be ignored, and we suppose that corrosion processes on the alloy extruded to Ø1 mm were accelerated by micro-galvanic corrosion between  $Mg_{17}Al_{12}$  and the  $\alpha$ (Mg) matrix.

Moreover, corrosion damage of the materials was dependent on the intensity of the recrystallization processes. The filaments observed on the surface of the sample deformed at a lower extrusion ratio propagated differently than those observed on

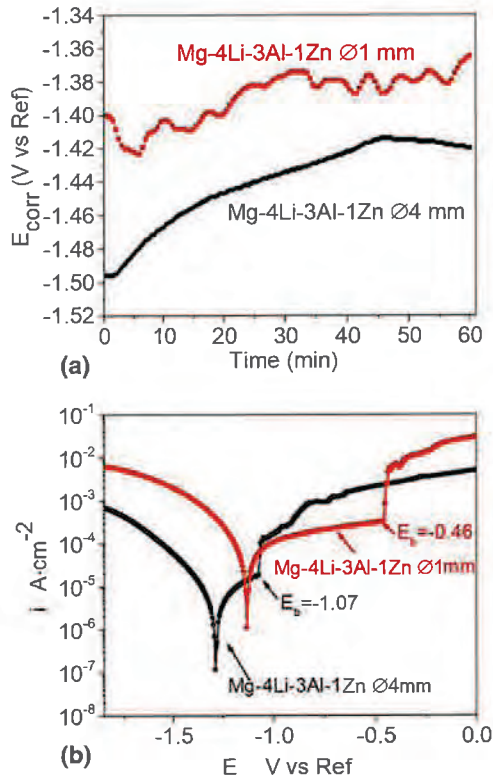


Fig. 5 The results delivered from electrochemical measurements performed in naturally aerated 0.01 M NaCl (a)  $E_{corr}$  evaluation for 1 hour; (b) potentiodynamic polarization curves

Table 3 The electrochemical parameters calculated from Tafel extrapolation based on results from potentiodynamic polarization tests recorded in 0.01 M NaCl

Materials	$E_{corr}$ , V/Ref	$i_{corr}$ , $\mu\text{A cm}^{-2}$	$\beta_v$ , mV/decade
Extruded to Ø4 mm	- 1.29	7.2	220
Extruded to Ø1 mm	- 1.13	144	297

Table 4 Corrosion rate of the Mg-4Li-3Al-1Zn alloys calculated from hydrogen evolution after 1 hour immersion in naturally aerated 0.01 M NaCl

Mg-4Li-3Al-Zn	Extruded to Ø4 mm	Extruded to Ø1 mm
Corrosion rate [ $\text{g}/(\text{m}^2\text{day})$ ]	135	307
St. deviation	9	24

the sample deformed at a higher extrusion ratio (compare Fig. 6b and 7b). The former ones were formed along lines very characteristic for reversible oscillations of the die during deformation, while the latter propagated along more ordered paths, indicating that the microstructure recrystallization was dependent on the extrusion ratio. During early stages of the deformation, slip bands were formed, and as a result of KoBo deformation they recrystallized; however, the recrystallization stage in both samples varied due to the extrusion ratio. In the sample extruded at a lower extrusion ratio ( $\lambda_1 = 100$ ), recrystallization was not as intense as in the case of the material deformed at a higher extrusion ratio ( $\lambda_2 = 1600$ ). Grains formed in the location where slip bands were formed may have different orientations than the rest of the recrystallized grains. Therefore, privileged corrosion paths occurred in these areas, leading to the formation of wave-like paths of corrosion filaments. During KoBo deformation at the higher extrusion ratio, more slip bands were formed leading to the randomization of grain orientations, and this is probably the main reason that wave-like paths were less observed.

## 5. Conclusions

- In this work, microstructure-dependent corrosion of KoBo extruded Mg-4Li-3Al-Zn alloys is described, which allows the dependence between extrusion ratio and grain size in these Mg-Li alloys to be understood.
- The KoBo extrusion of Mg-4Li-3Al-Zn from Ø40 mm to Ø4 mm ( $R_1 = 10:1$ ,  $\lambda_1 = 100$ ) and from Ø40 mm to Ø1 mm ( $R_2 = 40:1$ ,  $\lambda_2 = 1600$ ) led to significant grain refine-

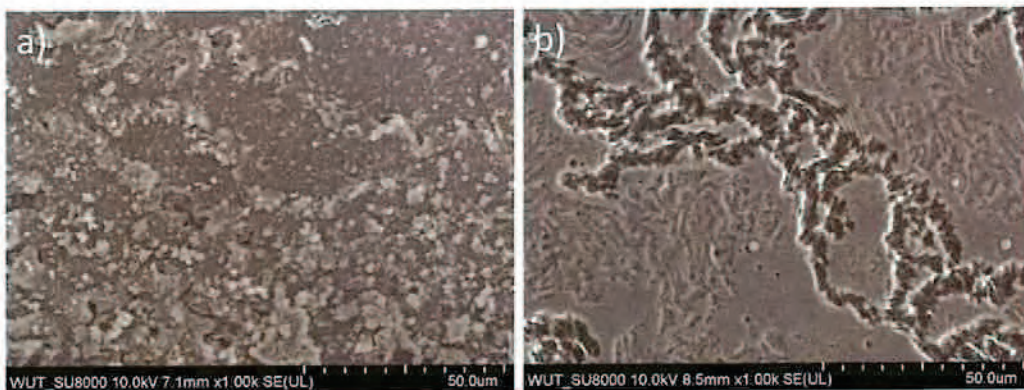
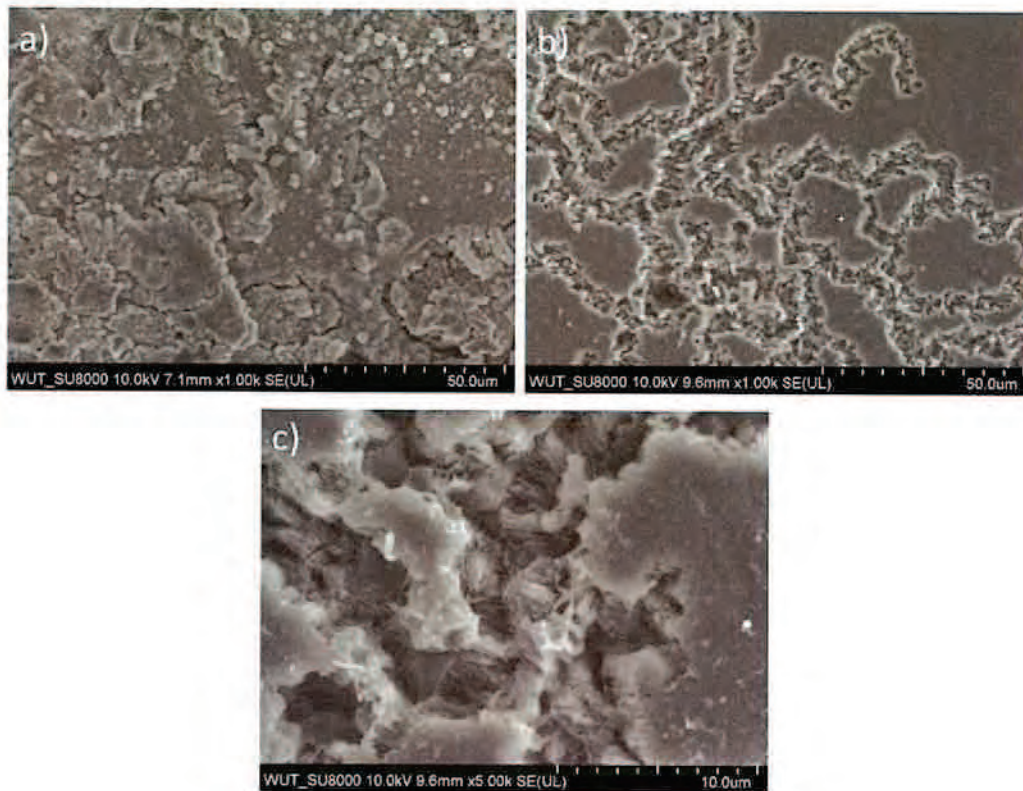


Fig. 6 Surface morphology of the Mg-4Li-3Al-1Zn alloy extruded to Ø4 mm after 1 hour immersion in naturally aerated 0.01M NaCl (a) surface morphology after immersion, (b) surface morphology after corrosion product removal



**Fig. 7** Surface morphology of the Mg-4Li-3Al-1Zn alloy extruded to  $\varnothing 1$  mm after 1 hour immersion in naturally aerated 0.01M NaCl (a) surface morphology after immersion. (b) surface morphology after corrosion product removal. (c) image showing interior of the corrosion filament

ment. Unexpectedly, the alloy extruded at a higher extrusion ratio had a poorer corrosion resistance.

- The decreased corrosion resistance of the alloy deformed at a higher extrusion ratio was related to the grain growth that resulted from the more intense recrystallization processes occurred during KoBo extrusion.
- Both alloys underwent locally distributed corrosion, and the filaments of the corrosion propagated through privileged paths that depended on the intensity of the recrystallization processes occurring in both materials. The locally spreading corrosion filaments propagated into the depth of the material through crystallographically grown traces.

## References

1. N. Soltani, H.R. Jafari Nodooshan, A. Bahrami, M.I. Pech-Canul, W. Liu and G. Wu, Effect of Hot Extrusion on Wear Properties of Al-15wt.% Mg2Si in Situ Metal Matrix Composites, *Mater. Des.*, 2014, **2014**(53), p 774–781. <https://doi.org/10.1016/j.matdes.2013.07.084>
2. R. Deaquino-Lara, N. Soltani, A. Bahrami, E. Gutiérrez-Castañeda, E. García-Sánchez and M.A.L. Hernandez-Rodríguez, Tribological Characterization of Al7075-Graphite Composites Fabricated by Mechanical Alloying and Hot Extrusion, *Mater. Des.*, 2015, **67**, p 224–231. <https://doi.org/10.1016/j.matdes.2014.11.045>
3. J.W. Seong and W.J. Kim, Development of Biodegradable Mg-Ca Alloy Sheets with Enhanced Strength and Corrosion Properties through the Refinement and Uniform Dispersion of the Mg2Ca Phase by High-Ratio Differential Speed Rolling, *Acta Biomater.*, 2015, **11**(1), p 531–542. <https://doi.org/10.1016/j.actbio.2014.09.029>
4. D. Song, A. Bin Ma, J. Jiang, P. Lin, D. Yang and J. Fan, Corrosion Behavior of Equal-Channel-Angular-Pressed Pure Magnesium in NaCl Aqueous Solution, *Corros. Sci.*, 2010, **52**(2), p 481–490. <https://doi.org/10.1016/j.corsci.2009.10.004>
5. I.A. Shahar, T. Hosaka, S. Yoshihara and B.J. Macdonald, Mechanical and Corrosion Properties of AZ31 Mg Alloy Processed by Equal-Channel Angular Pressing and Aging, *Procedia Eng.*, 2017, **184**, p 423–431
6. V. Kumar, R. Shekhar and K. Balani, Corrosion Behavior of Novel Mg-9Li-7Al-1Sn and Mg-9Li-5Al-3Sn-1Zn Alloys in NaCl Aqueous Solution, *J. Mater. Eng. Perform.*, 2015, **24**(10), p 4060–4070
7. N. Rahulan, S. Gopalan and S. Kumaran, Mechanical Behavior of Mg-Li-Al Alloys, *Mater. Today Proc.*, 2018, **5**(9), p 17935–17943
8. H. Matsumoshita, K. Edalati, M. Furui and Z. Horita, Ultrafine-Grained Magnesium-Lithium Alloy Processed by High-Pressure Torsion: Low-Temperature Superplasticity and Potential for Hydroforming, *Mater. Sci. Eng. A*, 2015, **640**, p 443–448. <https://doi.org/10.1016/j.msc.2015.05.103>
9. F. Cao, G. Xue and G. Xu, Superplasticity of a Dual-Phase-Dominated Mg-Li-Al-Zn-Sr Alloy Processed by Multidirectional Forging and Rolling, *Mater. Sci. Eng. A*, 2017, **704**, p 360–374. <https://doi.org/10.1016/j.msc.2017.08.037>
10. W.J. Kim, M.J. Kim and J.Y. Wang, Ultrafine-Grained Mg-9Li-1Zn Alloy Sheets Exhibiting Low Temperature Superplasticity, *Mater. Sci. Eng. A*, 2009, **516**(1–2), p 17–22
11. G. Ben Hamu, D. Eliczer and L. Wagner, The Relation between Severe Plastic Deformation Microstructure and Corrosion Behavior of AZ31 Magnesium Alloy, *J. Alloys Compd.*, 2009, **468**(1–2), p 222–229
12. M. Alvarez-Lopez, M.D. Pereda, J.A. Del Valle, M. Fernandez-Lorenzo, M.C. Garcia-Alonso, O.A. Ruano and M.L. Escudero, Corrosion Behaviour of AZ31 Magnesium Alloy with Different Grain

- Sizes in Simulated Biological Fluids, *Acta Biomater.*, 2010, **6**, p 1763–1771
13. T.A., S.S.S., Nenea, B.P. Kashyapa, N. Prabhua and Y. Estrina, Microstructure Refinement and Its Effect on Specific Strength and Bio-Corrosion Resistance in Ultralight Mg–4Li–1Ca (LC41) Alloy by Hot Rolling, *J. Alloys Compd.*, 2014, **615**, p 501–506
  14. G. Liu, Z. Ma, G. Wei, T. Xu, X. Zhang, Y. Yang, W. Xie and X. Peng, Microstructure Tensile Properties and Corrosion Behavior of Friction Stir Processed Mg–9Li–1Zn Alloy, *J. Mater. Process. Technol.*, 2019, **267**, p 393–402. <https://doi.org/10.1016/j.jmatprotec.2018.12.026>
  15. T. Mineta and H. Sato, Simultaneously Improved Mechanical Properties and Corrosion Resistance of Mg–Li–Al Alloy Produced by Severe Plastic Deformation, *Mater. Sci. Eng. A*, 2018, **735**, p 418–422. <https://doi.org/10.1016/j.msc.2018.08.077>
  16. J. Dutkiewicz, D. Kalita, W. Maziarz, T. Tański, W. Borck, P. Ostachowski and M. Faryna, Effect of KOB0 Extrusion and Following Cyclic Forging on Grain Refinement of Mg–9Li–2Al–0.5Sc Alloy, *Met. Mater. Int.*, 2020, **26**(7), p 1004–1014. <https://doi.org/10.1007/s12540-019-00350-y>
  17. A. Korbel, W. Bochniak, P. Ostachowski and L. Błaż, Visco-Plastic Flow of Metal in Dynamic Conditions of Complex Strain Scheme, *Metall. Mater. Trans. A Phys. Metall. Mater. Sci.*, 2011, **42**(9), p 2881–2897
  18. A. Dobkowska, B. Adamczyk-Cioślak, M. Koralnik, W. Chromiński, J. Kubasck, J. Ciftci, D. Kuc and J. Mizera, Corrosion behavior of fine-grained Mg–7.5 Li–3Al–1Zn fabricated by extrusion with a forward-backward rotating die (KoBo), *J. Magnes. Alloys*, 2021 <https://doi.org/10.1016/j.jma.2021.08.020>
  19. A. Korbel and W. Bochniak, Lüders Deformation and Superplastic Flow of Metals Extruded by KOB0 Method, *Philos. Mag.*, 2013, **93**(15), p 1883–1913
  20. I. Bednarczyk, D. Kuc, A. Tomaszewska and A. Mrugała, The Influence of Extrusion Process on the Microstructure and Mechanical Properties of Magnesium Alloys, *Arch. Metall. Mater.*, 2017, **62**(2), p 545–550
  21. J. Dutkiewicz, D. Kalita, W. Maziarz and M. Faryna, Superplastic Deformation of Mg–9Li–2Al–0.5Sc Alloy after Grain Refinement by KoBo Extrusion and Cyclic Forging, *Arch. Civ. Mech. Eng.*, 2020, **20**(4), p 1–11. <https://doi.org/10.1007/s43452-020-00128-9>
  22. I. Bednarczyk, D. Kuc, A. Tomaszewska and M. Tkocz, The Effect of Extrusion in the Complex Strain State on the Microstructure and Mechanical Properties of MgAlZn Magnesium Alloys, *Arch. Metall. Mater.*, 2020, **65**(3), p 1121–1128
  23. G. Song and A. Atrens, Understanding Magnesium Corrosion. A Framework for Improved Alloy Performance, *Adv. Eng. Mater.*, 2003, **5**(12), p 837–858
  24. G.L. Song and K.A. Unocic, The Anodic Surface Film and Hydrogen Evolution on Mg, *Corros. Sci.*, 2015, **2015**(98), p 758–765. <https://doi.org/10.1016/j.corsci.2015.05.047>
  25. ASTM B90/B90M-12, Standard Specification for Magnesium-Alloy Sheet and Plate (2012)
  26. L. Yang, Q. Jiang, M. Zheng, B. Hou and Y. Li, Corrosion Behavior of Mg–8Li–3Zn–Al Alloy in Neutral 3.5% NaCl Solution, *J. Magnes. Alloys*, 2016, **4**(1), p 22–26. <https://doi.org/10.1016/j.jma.2015.12.002>
  27. N. Birbilis, A.D. King, S. Thomas, G.S. Frankel and J.R. Scully, Evidence for Enhanced Catalytic Activity of Magnesium Arising from Anodic Dissolution, *Electrochim. Acta*, 2014, **132**, p 277–283. <https://doi.org/10.1016/j.electacta.2014.03.133>
  28. S.A. Salzman, R. Ichino and M. Okido, A Comparative Electrochemical Study of AZ31 and AZ91 Magnesium Alloy, *Int. J. Corros.*, 2010, **2010**, p 1–8
  29. C.Q. Li, D.K. Xu, X.B. Chen, B.J. Wang, R.Z. Wu, E.H. Han and N. Birbilis, Composition and Microstructure Dependent Corrosion Behaviour of Mg–Li Alloys, *Electrochim. Acta*, 2018, **260**, p 55–64
  30. ASTM Standard Practice for Preparing, Cleaning, and Evaluation Corrosion Test Specimens. ASTM (G1-90), 8 (1999)
  31. Y. Song, D. Shan, R. Chen and E. Han, Corrosion Characterization of Mg–8Li Alloy in NaCl Solution, *Corros. Sci.*, 2009, **51**, p 1087–1094
  32. G.R. Argade, S.K. Panigrahi and R.S. Mishra, Effects of Grain Size on the Corrosion Resistance of Wrought Magnesium Alloys Containing Neodymium, *Corros. Sci.*, 2012, **58**, p 145–151. <https://doi.org/10.1016/j.corsci.2012.01.021>
  33. S. Gollapudi, Grain Size Distribution Effects on the Corrosion Behaviour of Materials, *Corros. Sci.*, 2012, **62**, p 90–94. <https://doi.org/10.1016/j.corsci.2012.04.040>
  34. T. Sakai, A. Belyakov and H. Miura, Ultrafine Grain Formation in Ferritic Stainless Steel during Severe Plastic Deformation, *Metall. Mater. Trans. A Phys. Metall. Mater. Sci.*, 2008, **39**(9), p 2206–2214
  35. A. Pardo, M.C. Merino, A.E. Coy, R. Arrabal, F. Viejo and E. Matykina, Corrosion Behaviour of Magnesium/Aluminium Alloys in 3.5 Wt.% NaCl, *Corros. Sci.*, 2007, **3**, p 823–824

**Publisher's Note** Springer Nature remains neutral with regard to jurisdictional claims in published maps and institutional affiliations.



Available online at [www.sciencedirect.com](http://www.sciencedirect.com)

ScienceDirect

Journal of Magnesium and Alloys 10 (2022) 811–820



[www.elsevier.com/locate/jma](http://www.elsevier.com/locate/jma)

Full Length Article

## Corrosion behavior of fine-grained Mg-7.5Li-3Al-1Zn fabricated by extrusion with a forward-backward rotating die (KoBo)

Anna Dobkowska<sup>a,\*</sup>, Bogusława Adamczyk – Cieślak<sup>a</sup>, Milena Koralnik<sup>a</sup>, Witold Chromiński<sup>a</sup>, Jiri Kubasek<sup>b</sup>, Jakub Ciftci<sup>a</sup>, Dariusz Kuc<sup>c</sup>, Jarosław Mizera<sup>a</sup>

<sup>a</sup> Faculty of Materials Science and Engineering, Warsaw University of Technology, 141 Wołoska, St, Warsaw 02-507, Poland

<sup>b</sup> Department of Metals and Corrosion Engineering, University of Chemistry and Technology, Technicka 5, Prague 6 166 28, Czechia

<sup>c</sup> Institute of Materials Engineering, Silesian University of Technology, Krasińskiego 8, Katowice 40-019, Poland

Received 24 March 2021; received in revised form 30 June 2021; accepted 20 August 2021

Available online 6 October 2021

### Abstract

The microstructure-dependent corrosion resistance of dual structured fine-grained Mg-7.5Li-3Al-1Zn has been investigated. The alloys were extruded using extrusion with a forward-backward rotating die (KoBo, a newly developed SPD method) at two different extrusion ratios. The fine-grained microstructures formed in the alloys were characterized, and the influence of grain refinement on corrosion resistance was analyzed. For fine-grained ( $\alpha + \beta$ ) Mg-Li alloys, a higher extrusion ratio led to more intensive grain refinement; however, this relationship did not improve their corrosion resistance in a chloride-containing solution. The corrosion resistance of the alloys was mainly controlled by the refinement of  $\alpha$ (Mg) and  $\beta$ (Li), along with the distribution of second phases. The presence of MgLi<sub>2</sub>Al at grain boundaries facilitated their dissolution.

© 2021 Chongqing University. Publishing services provided by Elsevier B.V. on behalf of KeAi Communications Co. Ltd.

This is an open access article under the CC BY-NC-ND license (<http://creativecommons.org/licenses/by-nc-nd/4.0/>)

Peer review under responsibility of Chongqing University

**Keywords:** Corrosion; Grain refinement; Grain size distribution; Magnesium alloy.

### 1. Introduction

Dual-phase structured Mg-Li alloys have drawn extensive scientific attention, and they have been widely investigated in terms of their microstructure and the improvement of their mechanical properties by microstructure refinement and second-phase strengthening using plastic or thermal processing [1–9]. Many attempts have been made to evaluate the mechanical properties of ultrafine-grained ( $\alpha + \beta$ ) Mg-Li, which have been fabricated using severe plastic deformation (SPD) methods, such as high-pressure torsion [5,10], double-change

angular pressing [11], and equal-channel angular extrusion [12]. The occurrence of superplasticity was reported for dual-structured Mg-Li alloys processed by equal-channel angular pressing [13,14], heavy rolling and nitrate bath annealing [15], or forging [16]. Another method giving a possibility of significant grain refinement is a combination of an extrusion with applied additional plastic deformation by reversible torsion of the die (KoBo) [17]. The KoBo method allows a very high deformation to be obtained at room temperature and has been previously used for Mg-Li alloys [18,19].

There have been many trials to describe the corrosion resistance of dual-phase structured Mg-Li alloys; nevertheless, the associated corrosion mechanisms are quite poorly described in the literature. This phenomenon is due to the fact that the corrosion behavior of dual-structure Mg-Li is a complex process [20–24], and in addition to multiple microgalvanic processes caused by the presence of second-phase precipitation in the matrix [25,26], many other

\* Corresponding author.

E-mail addresses: [anna.dobkowska@pw.edu.pl](mailto:anna.dobkowska@pw.edu.pl) (A. Dobkowska), [boguslawa.cieslak@pw.edu.pl](mailto:boguslawa.cieslak@pw.edu.pl) (B. Adamczyk – Cieślak), [milena.koralnik@pw.edu.pl](mailto:milena.koralnik@pw.edu.pl) (M. Koralnik), [witold.chrominski@pw.edu.pl](mailto:witold.chrominski@pw.edu.pl) (W. Chromiński), [jiri.kubasek@vscht.cz](mailto:jiri.kubasek@vscht.cz) (J. Kubasek), [jakub.ciftci.stud@pw.edu.pl](mailto:jakub.ciftci.stud@pw.edu.pl) (J. Ciftci), [dariusz.kuc@polsl.pl](mailto:dariusz.kuc@polsl.pl) (D. Kuc), [jaroslaw.mizera@pw.edu.pl](mailto:jaroslaw.mizera@pw.edu.pl) (J. Mizera).

<https://doi.org/10.1016/j.jma.2021.08.020>

2213-9567/© 2021 Chongqing University. Publishing services provided by Elsevier B.V. on behalf of KeAi Communications Co. Ltd. This is an open access article under the CC BY-NC-ND license (<http://creativecommons.org/licenses/by-nc-nd/4.0/>) Peer review under responsibility of Chongqing University

microstructure-dependent mechanisms proceed simultaneously [27,28]. Pitting and filiform corrosion are the most observed types of corrosion in dual-structured Mg-Li alloys [22,23,29,30]. It should be noted that the corrosion rate of dual-structured Mg-Li alloys is the highest when compared to single  $\alpha$ -structured and single  $\beta$ -structured Mg-Li [31].

Generally, the corrosion resistance of Mg-Li alloys increases with microstructure refinement [31–34]. It has been shown that grain refinement resulting from extrusion at an extrusion ratio of 20:4:1 improved the corrosion resistance of Mg-9.29Li-0.88Ca and changed the form of corrosion from pitting to general corrosion for extruded alloys with a higher extrusion ratio [35]. In addition, it has been demonstrated that grain refinement caused by rolling supported oxide film formation [33]. Yang et al. [22] showed that in Mg-8Li-3Zn-Al in 3.5 wt.% NaCl solution,  $\text{Cl}^-$  ions led to the initiation and development of corrosion pits. It has also been noted that  $\beta(\text{Li})$ , which is more active than  $\alpha(\text{Mg})$  (since Li is a very active metal), played the major role in the corrosion behavior of Mg-Li alloys [23,36]. Another study showed that although the Volta potential of  $\alpha(\text{Mg})$  phases is much higher than that of  $\beta(\text{Li})$  phases, pitting occurrence was preferentially related to the  $\alpha(\text{Mg})$  phases, but not the ( $\beta$ )Li phases [36].

Due to their hexagonal close-packed (hcp) crystal structure, which results in a limited number of slip systems and anisotropic deformation, Mg-alloys are hard to deform [37,38]. Hence, the possibility of significant grain refinement (to fine grains with dimensions below 10  $\mu\text{m}$ ) for these materials is limited, but may be accomplished under conditions of permanent destabilization of their microstructure by methods where a high deformation rate can be applied [39]. Due to its additional reversible oscillating die at the end of its extrusion injection cylinder, extrusion with a forward-backward rotating die (KoBo) allows for the deformation at lower temperatures than used so far of materials that are hard to deform (i.e. Mg-based alloys), by the introduction of a large deformation until a viscoplastic material flow phenomenon occurs in the material [40].

The KoBo is a newly developed technique among SPD methods, which may be used for the reduction of the dimensions of Mg-based alloys [41]. Therefore, in this study the first examination of microstructure-dependent corrosion in chloride-containing solution of two Mg-7.5Li-3Al-1Zn alloys extruded via a KoBo is described.

## 2. Methodology

### 2.1. Microstructural characterization

The first step in this study was to characterize the phase compositions of the alloys. Atomic absorption spectrometry (AAS, GBC 932 Plus) was performed to calculate the Li concentration in both the analyzed materials. X-ray diffraction (XRD, Bruker D8 Advance), operating at 40 kV and 40 mA with Cu  $K\alpha$  radiation, was used to characterize the detailed phase composition of the alloys. The results were recorded by stepwise scanning  $2\theta$  from  $10^\circ$  to  $120^\circ$ , with a step size of

$0.02^\circ$  and a count time of 10 s per step. A semi-quantitative analysis of the relative concentration of the phases present in the alloys was carried out by comparing the integrated intensities of the diffraction peaks from each of the known phases.

The microstructure of the alloys was observed using a high-resolution scanning electron microscope (SEM, Hitachi SU8000). The extruded wires were cut into 3 mm-thick slices, polished with 1200-grit and 2400-grit SiC papers, and subsequently surfaces perpendicular to the extrusion direction were polished with a low-energy  $\text{Ar}^+$  ion beam milling system (Hitachi IM4000 Ion Milling System) for 6 h. Observations were carried out immediately after sample preparation.

A transmission electron microscope (TEM, JEOL JEM-1200EX) with an acceleration voltage of 120 kV was used to investigate the dislocation distribution and to characterize the details of the phases formed in the alloys. Samples in the form of thin foils were prepared using a Gatan Model 656 Dimple Grinder and a Gatan Model 691 Precision Ion Polishing System (PIPS) at 2.5 kV. The observations were carried out on cross-sections perpendicular to the extrusion direction.

### 2.2. Corrosion tests

Electrochemical measurements were carried out in naturally aerated, quiescent 0.1 M NaCl solution using an FAS1 Gamry potentiostat equipped with three electrodes: platinum as the counter electrode, saturated Ag/AgCl as the reference electrode, and the measured sample as the working electrode. The electrolyte was produced using analytical grade reagents and distilled water. The corrosion potential ( $E_{\text{corr}}$ ) was recorded for 1 h under open-circuit conditions. After immersion, potentiodynamic tests were conducted with a scan rate of 5 mV/s, starting 0.5 V below  $E_{\text{OCP}}$  and finishing at 2 V vs. Ref. The polarization curves were fitted using Gamry Echem software in Tafel mode. The post-corrosion morphology of the samples was observed after 1 h immersion under open-circuit conditions using scanning electron microscopy (SEM, Hitachi SU8000).

To compare the corrosion resistance of the alloys, the corrosion rate ( $V_c$ ) was calculated based on traditional mass loss measurements. Samples were polished up to 4000-grit SiC paper, ultrasonically cleaned in isopropanol and dried in the air. Prior to immersion, the surface area of the samples was measured, and the samples were weighted. Afterwards samples were immersed for 1 h in naturally aerated 0.1 M NaCl. After immersion, samples were dried in the air and corrosion products were removed by samples immersion in 7% solution of nitric acid ( $\text{HNO}_3$ ) for 15 s (as per [42,43]). The  $V_c$  was calculated [44]:

$$\text{Corrosion Rate} = \Delta m / s \cdot t \quad (1)$$

where:  $\Delta m$  is a mass loss (g),  $t$  is a time of exposure (day),  $s$  is a surface area ( $\text{m}^2$ ).

Corrosion rate of the investigated materials were compared with the results obtained for traditionally extruded and annealed Mg-7.5Li-3Al-1Zn alloy (coarse-grained alloy described in [45]).

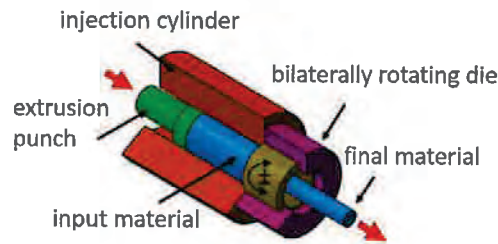


Fig. 1. Extrusion with a forward-backward rotating die (KoBo).

Table 1  
Li concentration obtained by AAS (wt.%).

Mg-7.5Li-3Al-1Zn	Li concentration (wt.%)
Ø4 mm	7.0
Ø2 mm	5.7

To describe the role of microstructure in the corrosion resistance of both alloys, the corrosion products formed on the samples as well as surfaces with chemically removed corrosion products had been chemically removed, were observed using SEM. Cross-sectional observations were also made.

### 3. Deformation method and materials

The materials examined in this study were extruded using the KoBo method. As shown in Fig. 1, during KoBo extrusion, the input material is punch-pressed through the matrix where the oscillations of the bilaterally rotating die occur. This specific combination allows for extrusion under conditions of permanent microstructure destabilization by applying a high deformation rate and leads to the formation of a fine-grained microstructure (approx.  $<10 \mu\text{m}$ ) [40,46]. The extrusion was performed under the following conditions: punch speed = 0.2 mm/s, die rotation angle =  $8^\circ$ , initial temperature of the billet =  $24^\circ\text{C}$ , and die oscillation frequency = 5 Hz ( $\pm 1$  Hz).

In this study, two fine-grained Mg-7.5Li-3Al-1Zn (AZ31 + 7.5 wt.%Li) alloys extruded using the KoBo were investigated. The first was extruded at an extrusion ratio of  $R_1 = 40:4$ , giving a deformation degree of  $\lambda_1 = 100$ , while the second was extruded at an extrusion ratio of  $R_2 = 40:2$ , giving  $\lambda_2 = 400$ .

## 4. Results

### 4.1. Microstructure characterization

As Li is a chemically active metal, it was necessary to confirm the Li concentration in the extruded rods. As listed in Table 1, the concentration of Li after extrusion to the final dimension of Ø4 mm slightly decreased from the initial amount of 7.5 wt.% to 7.0 wt.%, and to 5.7 wt.% after extrusion to Ø2 mm. Similarly to their coarse-grained counterparts [45], both materials exhibited a dual-phased structure composed of light areas of  $\alpha(\text{Mg})$  and dark areas of  $\beta(\text{Li})$ ,

Table 2

Semi-quantitative analysis obtained by XRD for the extruded Mg-7.5Li-3Al-1Zn.

Mg-7.5Li-3Al-1Zn	Relative composition (%)	
	Ø4 mm	Ø2 mm
Phase		
$\alpha(\text{Mg})$	34.1	27.2
$\beta(\text{Li})$	63.2	71.2
$\text{Mg}_{17}\text{Al}_{12}$	2.1	0.4
$\text{MgLi}_2\text{Al}$	0.4	1.0
$\text{AlLi}$	0.2	0.2

Fig. 2. The dark  $\beta(\text{Li})$  was irregularly distributed in the alloy extruded to Ø4 mm, and its twisted shape (Fig. 3a,b) may have been a result of the insufficient frequency of the die oscillation [41]; however, this hypothesis needs to be further examined. As a result of the higher degree of deformation, a more uniform microstructure formed (Fig. 2c,d). Coarse white Al,Mn-rich phases were precipitated within the matrix of both alloys (marked as P1 in Fig. 2b,d).

Moreover, various nano-sized precipitates were formed in the materials, and as shown in the XRD patterns, they were identified as  $\text{Mg}_{17}\text{Al}_{12}$ , AlLi, and  $\text{MgLi}_2\text{Al}$  (Fig. 3). To confirm their presence, TEM observations were carried out. As shown in Fig. 4a, small round  $\text{Mg}_{17}\text{Al}_{12}$  precipitates were randomly distributed in the grain interiors in the alloy extruded to Ø4 mm, Fig. 4a. Randomly distributed  $\text{Mg}_{17}\text{Al}_{12}$  precipitates, which were similar in shape, were also identified in the alloy extruded to Ø2 mm (Fig. 4c). The presence of elongated  $\text{MgLi}_2\text{Al}$  precipitates at the grain boundaries was also confirmed, and a higher number of them were formed in the alloy extruded to Ø2 mm (Fig. 4d). Additionally, the existence of round, coarse precipitates is shown in Fig. 4b. This kind of precipitates can be identified as AlLi. Unfortunately, we were not able to perform SAD to confirm its presence; however, based on our previous observations, we suppose that the observed shape and distribution can support the classification of these precipitates as AlLi [45]. Surprisingly, a few ternary precipitates of  $\text{MgLi}_2\text{Al}$  were detected in the alloy extruded to Ø4 mm (Fig. 4c). When comparing the TEM microstructure of the alloys extruded at the two extrusion ratios, it can be seen that a higher number of second phases precipitated in the alloy extruded to Ø2 mm (Fig. 5). These precipitates were formed around  $\beta(\text{Li})$ , and they are clearly visible as tiny white threads surrounding the dark areas of  $\beta(\text{Li})$  in Fig. 2b and d. Despite the differing degrees of deformation, the relative concentrations of  $\alpha(\text{Mg})$  to  $\beta(\text{Li})$  did not change significantly, and in the alloy extruded to Ø4 mm the ratio was 34.1 to 63.2%, while being 27.2 to 71.2% for Ø2 mm (Table 2).

### 4.2. Corrosion testing

The electrochemical results for both the analyzed materials, performed in naturally aerated 0.1 M NaCl, are shown in Fig. 6. The  $E_{\text{con}}$  evaluation during 1 h of immersion in naturally aerated 0.1 M NaCl for both analyzed materials is

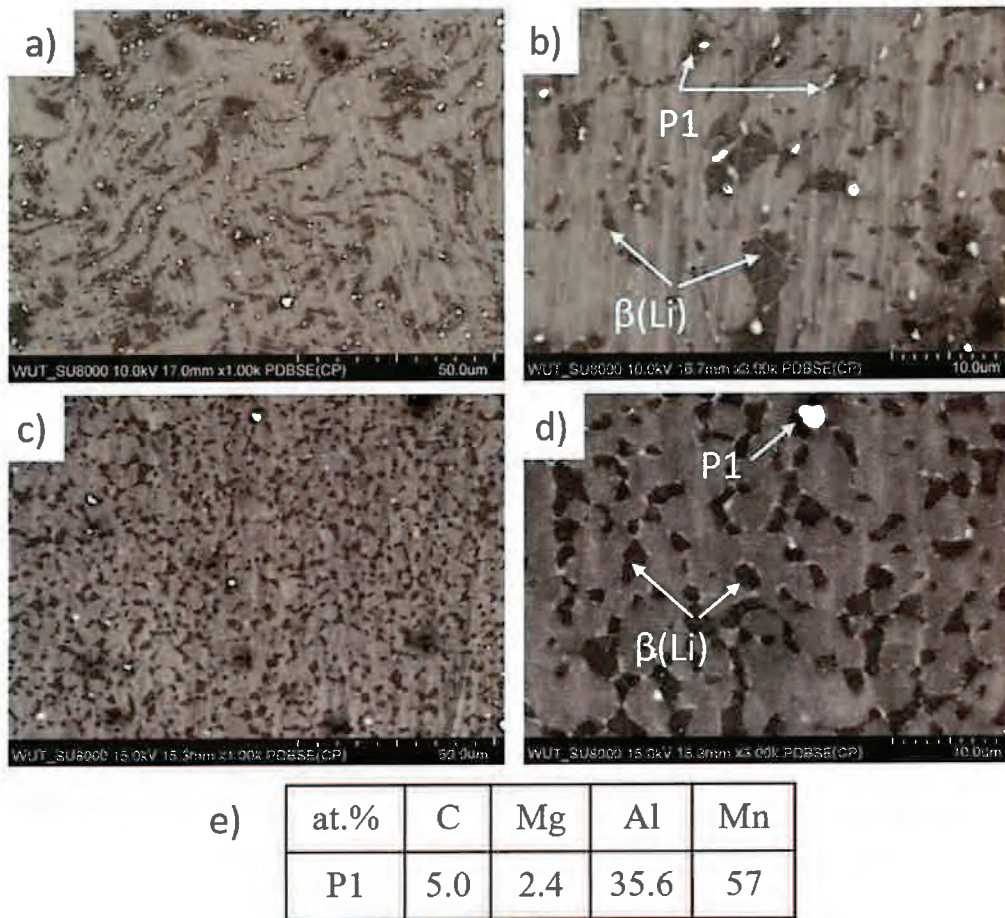


Fig. 2. SEM images showing microstructure of Mg-7.5Li-3Al-1Zn: (a) image showing overall microstructure of the alloy extruded to Ø4 mm, (b) image showing distribution of coarse precipitates in the alloy extruded to Ø4 mm, (c) image showing overall microstructure of the alloy extruded to Ø2 mm, (d) image showing distribution of coarse precipitates in the alloy extruded to Ø2 mm, (e) the representative EDX analyzes for precipitates labelled as P1.

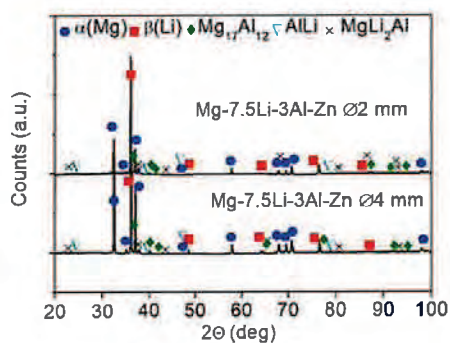


Fig. 3. XRD patterns obtained for the examined materials.

shown in Fig. 6a. Depending on the deformation ratio, the  $E_{\text{corr}}$  curves exhibited different trends. Higher values of  $E_{\text{corr}}$  were recorded for Mg-7.5Li-3Al-1Zn extruded to Ø2 mm. At the beginning of immersion, a rapid increase in  $E_{\text{corr}}$  took place, from the initial value of  $-1.53$  V/Ref to  $-1.47$  V/Ref.

During the following 3 min,  $E_{\text{corr}}$  slightly decreased, and then once again increased towards more positive values, reaching  $-1.45$  V/Ref. Subsequently, an abrupt decline occurred to  $-1.52$  V/Ref, the potential remaining around this value, in a nearly steady state, for the remainder of the experiment. Lower values of  $E_{\text{corr}}$  in the analyzed solution, suggesting a poorer resistance to the corrosive environment due to a lower equilibrium potential that made the oxidation process easier [22,47], were registered for the Mg-7.5Li-3Al-1Zn extruded to Ø4 mm. In this case, a rapid increase in  $E_{\text{corr}}$  occurred at the start of the immersion, starting below  $-1.56$  V/Ref, reaching a value of around  $-1.53$  V/Ref after 5 min of immersion, and continuing at a near steady state just above  $-1.53$  V/Ref for the remainder of the experiment. The observed initial rapid increase in the  $E_{\text{corr}}$  values for the period of <5 min of immersion is unique for Mg-based alloys, and is rather associated with “cathodic activation” than with the suppression of anodic kinetics [31,48]. Also, the variations around the steady-state value of  $E_{\text{corr}}$ , recorded for both alloys during the immersion, are attributed to the

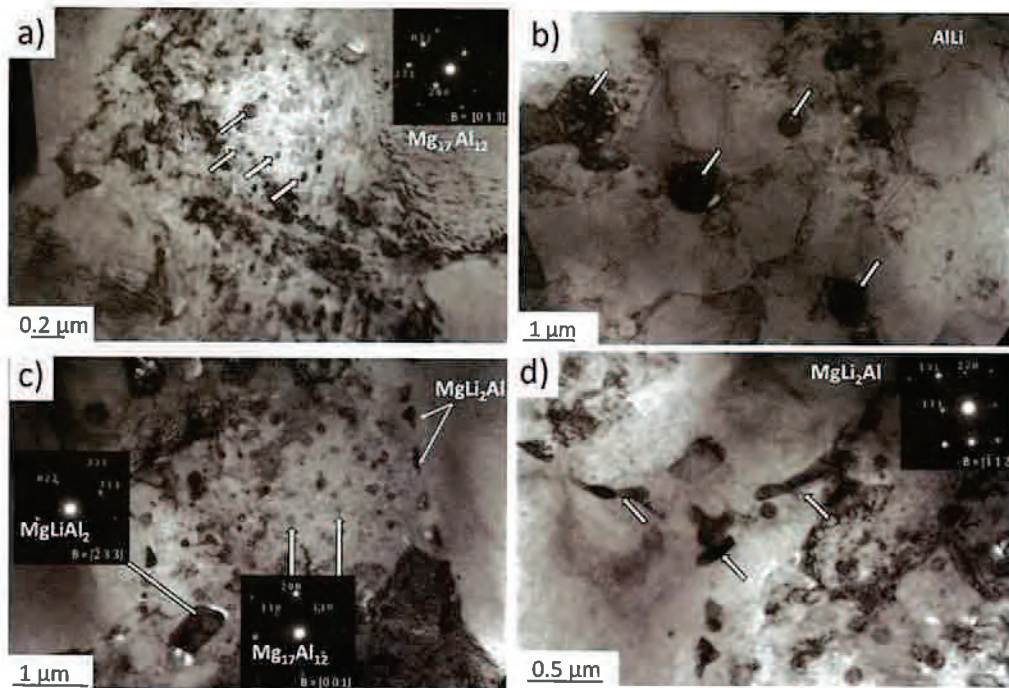


Fig. 4. TEM images in bright field and selected area diffraction (SAD) patterns obtained from the alloy extruded to  $\varnothing 4$  mm (a and b), and the alloy extruded to  $\varnothing 2$  mm (c and d).

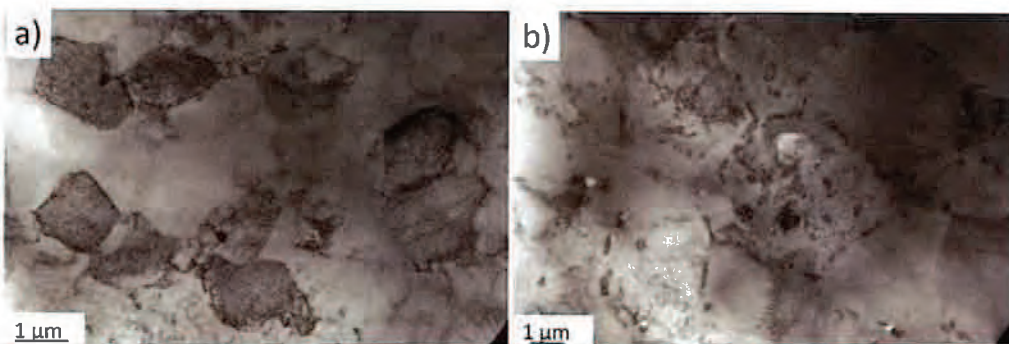


Fig. 5. TEM images of the microstructure of the alloy extruded to  $\varnothing 4$  mm (a), and the alloy extruded to  $\varnothing 2$  mm (b).

changes in anodic kinetics under the corrosion conditions [31,48,49].

Fig. 6b shows the polarization curves for the Mg-7.5Li-3Al-1Zn alloys deformed to  $\varnothing 2$  and  $\varnothing 4$  mm, and the characteristic electrochemical parameters calculated from the Tafel slopes are displayed in Table 3. The cathodic branches showed a similar trend in their slopes; however, slightly higher cathodic current densities ( $i_c$ ) were reported for Mg-7.5Li-3Al-1Zn extruded to  $\varnothing 4$  mm than for the material extruded to  $\varnothing 2$  mm. This trend suggests that the rate of water reduction is higher in the case of Mg-7.5Li-3Al-1Zn extruded to  $\varnothing 4$  mm, and may be supported by the presence of second phases that act as local cathodes [50,51]. In the anodic branches, a typical inflexion point is visible, related

to the breakdown of the protective oxide film formed on the alloys' surfaces [49,52,53]. This breakdown potential is clearly visible for both alloys; however,  $E_b$  was higher for the material extruded to  $\varnothing 2$  mm than for the material extruded to  $\varnothing 4$  mm ( $E_b = -1.24$  V/Ref for Mg-7.5Li-3Al-1Zn extruded to  $\varnothing 4$  mm, and  $E_b = -0.97$  V/Ref for Mg-7.5Li-3Al-1Zn extruded to  $\varnothing 2$  mm, respectively). The portion of the active area of the anodic slope, after reaching  $E_{corr}$  and preceding the inflexion point ( $E_b$ ), was shorter for the alloy extruded with a lower extrusion ratio (extruded to  $\varnothing 4$  mm) than for the material extruded with a higher extrusion ratio (extruded to  $\varnothing 2$  mm), as shown in Fig. 7. The greater the differences between these two values, the higher the resistance to the localized corrosion of the respective alloy. Additionally, the

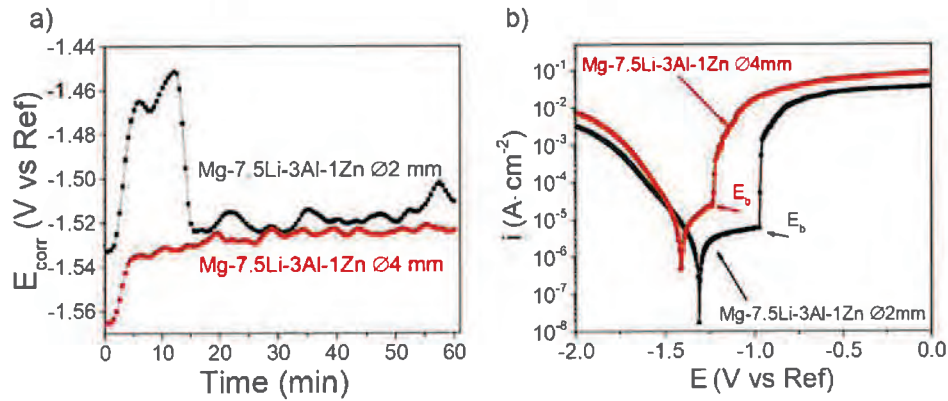


Fig. 6. The results of electrochemical measurements performed in naturally aerated 0.1 M NaCl (a)  $E_{\text{corr}}$  evaluation over 1 h. (b) potentiodynamic polarization curves.

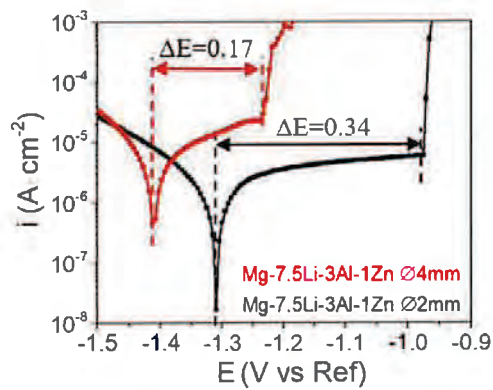


Fig. 7. The difference between  $E_{\text{corr}}$  and  $E_b$  calculated for both analyzed materials showing susceptibility to localized corrosion.

Table 3

The electrochemical parameters calculated from Tafel extrapolation based on results from potentiodynamic polarization tests recorded in 0.1 M NaCl.

Mg-7.5Li-3Al-1Zn	$E_{\text{corr}}$ (V/Ref)	$E_b$ (V/Ref)	$i_{\text{corr}}$ ( $\mu\text{A}\cdot\text{cm}^{-2}$ )
Extruded to Ø4 mm	-1.41	-1.24	9.9
Extruded to Ø2 mm	-1.31	-0.97	20.2

alloy extruded at a lower extrusion ratio (Ø4 mm) presented lower corrosion current density than that extruded with a higher extrusion ratio (Table 3).

The results for the measured mass loss rates are shown in Fig. 8. The mass loss results represent the corrosion rate directly, and as presented, the extrusion of Mg-7.5Li-3Al-1Zn to Ø4 mm made this alloy the most resistant to the 0.1 M NaCl. The corrosion rate after 1 h of immersion gave results of  $0.02\text{ g}\cdot\text{day}^{-1}\cdot\text{cm}^{-2}$ , which was significantly lower than that for coarse-grained Mg-7.5Li-3Al-1Zn ( $0.5\text{ g}\cdot\text{day}^{-1}\cdot\text{cm}^{-2}$ ). The higher extrusion ratio increased the corrosion activity of the alloy extruded to Ø2 mm, giving a corrosion rate of  $0.07\text{ g}\cdot\text{day}^{-1}\cdot\text{cm}^{-2}$  making it still lower than that calculated for its coarse-grained counterpart but higher than that the

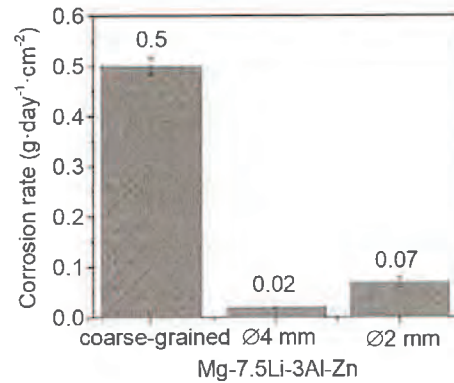


Fig. 8. Corrosion rate calculated after 1 h of immersion in 0.1 M NaCl for conventionally extruded and annealed Mg-7.5Li-3Al-1Zn (coarse-grained), and for Mg-7.5Li-3Al-1Zn KoBo extruded to Ø=4 mm and Ø=2 mm.

one obtained for the KoBo extruded alloy to Ø4 mm. This indicates, that among SPD extruded dual-structured Mg-Li alloys, higher grain refinement is not capable of reducing the corrosion rate.

#### 4.3. Post-corrosion observations

SEM images of the surface and its chemical composition (EDX) were obtained after immersion of the samples for a period of 1 h. Figs. 9 and 10 depict corrosion attack on the surface and cross-sectional observations of Mg-7.5Li-3Al-1Zn extruded to Ø4 mm and to Ø2 mm after immersion for 1 h in 0.1 M NaCl. The surface of both alloys suffered from an intense local corrosion attack aligned along some preferred paths (Figs. 9a and 10a). The SEM images of the corroded surfaces of both alloys taken with higher magnification show that localized corrosion attack was intense and led to the strong dissolution of local areas (Figs. 9b and 10b). The cross-sectional images of the samples after immersion under open-circuit conditions revealed that corrosion in Mg-7.5Li-3Al-1Zn extruded to Ø4 mm spread apparently selectively,

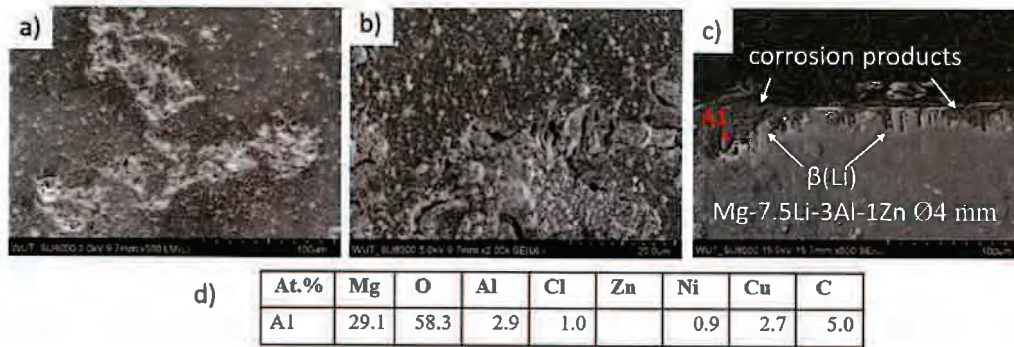


Fig. 9. SEM surface observations of Mg-7.5Li-3Al-1Zn extruded to Ø4 mm, after 1 h immersion in naturally aerated 0.1 M NaCl: (a) image showing overall corrosion after immersion, (b) image showing localized corrosion, (c) cross-sectional observations, (d) EDX analysis performed at point A1 in panel c.

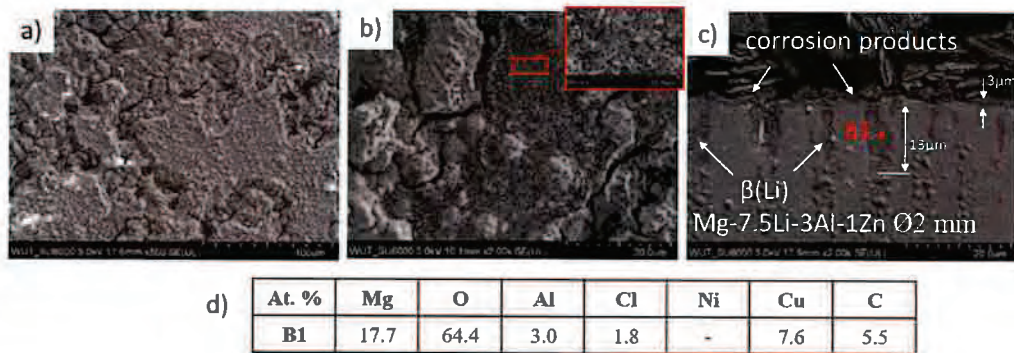


Fig. 10. Cross-sectional observations of the corrosion products formed on the Mg-7.5Li-3Al-1Zn extruded to Ø2 mm, after 1 h immersion in naturally aerated 0.1 M NaCl: (a) image showing overall corrosion after immersion, (b) image showing localized corrosion, (c) cross-sectional observations, (d) EDX analysis performed at point B1 in panel c.

and propagated into the interior of the material (Fig. 9c). The  $\alpha(\text{Mg})$  phase had a relatively higher potential of  $-2.37$  vs. SHE, whereas  $\beta(\text{Li})$  had a much lower potential of  $-3.41$  V vs. SHE [30,54]; therefore, in the case of dual-structured Mg-Li alloys,  $\beta(\text{Li})$  was more prone to dissolve than  $\alpha(\text{Mg})$ . Based on this preference, it can be claimed that the extension of corrosion proceeded through  $\beta(\text{Li})$ , as marked in Fig. 9c. In the case of the sample extruded with a higher extrusion ratio (to Ø2 mm), corrosion spreading at the sample/solution interface led to the formation of a poorly protective layer with a width of  $<3 \mu\text{m}$  and was also accompanied by selective and deep local damage to the material (Fig. 10c). EDX analyzes shown in Figs. 9d and 10d revealed that the corrosion products formed on the surfaces of both alloys were enriched in Mg and Al, suggesting that besides conglomerates with the needle-like crystals typical for brucite (shown in the inset in Fig. 10b), other compounds enriched in Al were present, which may support better passivation of the Mg-Li alloys [55,56]. Ni and Cu detected during EDX analysis were present because prior to the observations the samples were coated with Ni-Cu.

After the corrosion products were removed, it was clearly seen that the corroded areas could be identified with grain boundaries. There are two reasons of this: microgalvanic

corrosion would be expected to occur between  $\text{MgLi}_2\text{Al}$  and the grain boundary, and the grain boundaries are more prone to serve as an anode with respect to the cathodic grain interior because of their higher distortion (Fig. 11). As shown in Fig. 11b, the intergranular corrosion extends to intragranular locations, and the attack led to the dissolution of  $\beta(\text{Li})$ . Clearly, more intensive corrosion occurred at the surface of the material deformed at a higher extrusion ratio.

## 5. Discussion

The results obtained in this study gave a new insight into the corrosion of dual-structured Mg-Li alloys, which contributed to a better understanding of this process. Our combined microstructural, electrochemical, and analytical study highlighted the differences between the spreading corrosion mechanisms and evaluated the role of various microstructural features in their propagation. It would be expected that higher grain refinement would give a positive influence on the corrosion resistance of metallic materials in alkaline and near neutral solutions [35,57]. For AZ31B alloy, the effect of grain size played a significant role in the case of an untwined microstructure, for which the corrosion rate was higher when the grain size increased from  $65$  to  $250 \mu\text{m}$  [58]. Also, Li

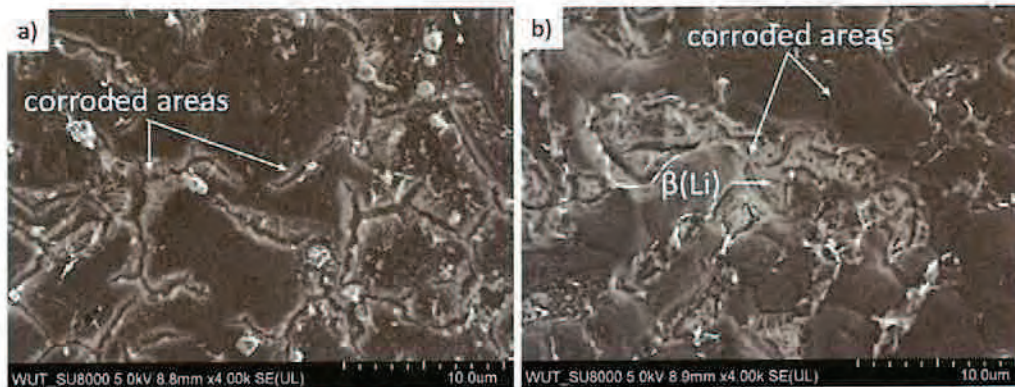


Fig. 11. Images taken after corrosion products were removed: (a) Mg-7.5Li-3Al-1Zn extruded to Ø4 mm, (b) Mg-7.5Li-3Al-1Zn extruded to Ø2 mm

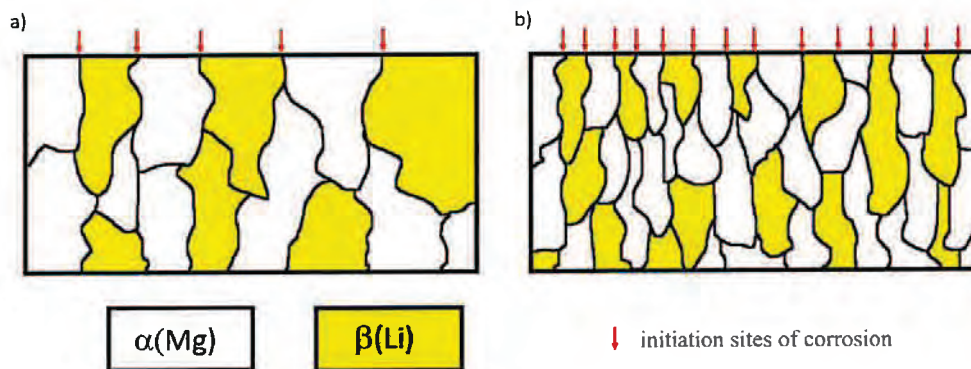


Fig. 12. The comparative images of the surfaces.

et al. [29] described the corrosion resistance of Mg-5Li alloy, which was improved due to more refined grains. The presented study shows that declaring a definitive relationship between the grain size and corrosion resistance of metallic materials, especially dual-structured ones, may be an unjustified interpretation. Grain refinement via KoBo extrusion improved the corrosion resistance of dual-structured alloys when compared to their coarse-grained counterparts. Among group of fine-grained ( $\alpha + \beta$ ) Mg-Li alloys, a higher extrusion ratio led to more intensive grain refinement; however, this relationship did not improve their corrosion resistance in chloride-containing solution. This phenomenon is attributed to two critical factors. First of all, corrosion attack on both the analyzed alloys with fine-grained structure started at the grain boundaries where  $\text{MgLi}_2\text{Al}$  was formed. The more refined structure possessed a higher number of grain boundaries with precipitated  $\text{MgLi}_2\text{Al}$  where the corrosion may be initialized, and the reactions occurring at grain boundaries were not compensated by reactions leading to the formation of a protective layer. Secondly, an important finding is that the corrosion process is extended through  $\beta(\text{Li})$ , which is more active than  $\alpha(\text{Mg})$ . A microgalvanic coupling between  $\beta(\text{Li})$  and  $\alpha(\text{Mg})$  has been previously reported [31,59]. In our previous study, we claimed that the corrosion resistance of dual-phased con-

ventionally extruded Mg-7.5Li-3Al-1Zn alloys depends on the  $\alpha(\text{Mg})$  to  $\beta(\text{Li})$  area ratio, where one acts as a cathode and drives the local system to a state of equilibrium [45]. This effect forces the second phase to actively corrode, and therefore the amount of  $\beta(\text{Li})$  and  $\alpha(\text{Mg})$  in the case of coarse-grained dual-structured Mg-Li alloys plays a predominant role in their corrosion mechanisms. In the case of fine-grained dual-structured Mg-Li alloys, regardless of the degree of deformation, the ratio of the relative concentration of  $\alpha(\text{Mg})$  to  $\beta(\text{Li})$  did not change significantly, and taking this into consideration, it is reasonable to assume that grain refinement, and the results of this refinement on both phases are major factors influencing the corrosion mechanisms in the examined alloys.

Fig. 12 summarizes the microgalvanic corrosion mechanisms in the Mg-7.5Li-3Al-1Zn alloys extruded to Ø4 and Ø2 mm. The microgalvanic processes in dual-phase Mg-Li alloys are mainly controlled by the anodic to cathodic area ratio of  $\beta(\text{Li})$   $\alpha(\text{Mg})$  [45]. Nevertheless, at the beginning of the process, in stage I, due to either the formation of a galvanic cell between the  $\text{MgLi}_2\text{Al}$  precipitate and grain boundary, or a higher distortion of the grain boundary when compared to the grain interiors, the most preferential corrosion sites were grain boundaries (marked with the red arrow in Fig. 12). Although at the beginning of immersion more sites of cor-

rosion initiation were present on the alloy with higher grain refinement, the predominant corrosion mechanism occurred during stage II, where microgalvanic corrosion proceeded between  $\alpha(\text{Mg})$  and  $\beta(\text{Li})$ , and intergranular corrosion was supplemented by an intragranular process. In this case, microgalvanic corrosion was controlled by the area ratio of cathodic to anodic grain interiors. As commonly known for heterogeneous microstructures, the corrosion system was composed of half-cell electrodes, where the phase with the lower potential was anodic, and the phase with higher potential cathodic. Therefore, after reaching stage I, anodic dissolution of  $\beta(\text{Li})$  was observed. Moreover, the higher refinement of both phases resulted in a higher number of microgalvanically coupled  $\alpha(\text{Mg})/\beta(\text{Li})$  grains with a lower area ratio than in the material where the grains were larger. In the latter case the number of microgalvanically coupled  $\alpha(\text{Mg})/\beta(\text{Li})$  grains was lower, and the area ratio of  $\alpha(\text{Mg})/\beta(\text{Li})$  was higher. This trend influenced the spatial distribution of the cathodic and anodic reactions, resulting in a higher degree of penetration for the alloy with the more refined grains.

## 6. Conclusion

In this study, through observing the microstructure and investigating the corrosion behavior of KoBo extruded Mg-7.5Li-3Al-1Zn alloys extruded to  $\varnothing 4$  and  $\varnothing 2$  mm, the effects of  $\alpha(\text{Mg})$  and  $\beta(\text{Li})$  distribution, their relative ratio, and the role of second phases have been examined. The following conclusions can be drawn:

- The KoBo extrusion to the dimension of  $\varnothing 4$  mm led to the formation of non-uniform fine-grained microstructure in dual-structured Mg-7.5Li-3Al-1Zn alloys. The increase in the extrusion ratio caused the formation of homogenous fine-grained dual-structured microstructure.
- In the case of fine-grained dual-structured Mg-Li alloys, the main roles in the corrosion mechanism were played by the refinement of  $\alpha(\text{Mg})$  and  $\beta(\text{Li})$  and the distribution of second phases. The presence of  $\text{MgLi}_2\text{Al}$  at grain boundaries facilitated their dissolution.
- For fine-grained ( $\alpha + \beta$ ) Mg-Li alloys, a higher extrusion ratio led to more intensive grain refinement; however, this relationship did not improve their corrosion resistance in chloride-containing solution.

## Reference

- [1] F. Cao, B. Zhou, X. Ding, J. Zhang, G. Xu, *J. Alloy. Compd.* 745 (2018) 436–445, doi:10.1016/j.jallcom.2018.02.185.
- [2] J. Zhao, Z. Li, W. Liu, J. Zhang, L. Zhang, Y. Tian, G. Wu, *Mater. Sci. Eng. A* 669 (2016) 87–94, doi:10.1016/j.msea.2016.05.085.
- [3] S. Li, L. Chen, J. Tang, G. Zhao, C. Zhang, *Results Phys.* 13 (2019) 102148, doi:10.1016/j.rinp.2019.02.084.
- [4] G. Liu, W. Xie, G. Wei, Y. Yang, J. Liu, T. Xu, W. Xie, X. Peng, *Materials* 11 (2018) 1–11 (Base1), doi:10.3390/ma11030408.
- [5] H. Matsunoshita, K. Edalati, M. Furui, Z. Horita, *Mater. Sci. Eng. A* 640 (2015) 443–448, doi:10.1016/j.msea.2015.05.103.
- [6] H. Haferkamp, R. Boehm, U. Holzkamp, C. Jaschik, V. Kaese, M. Niemeyer, *Mater. Trans.* 42 (2001) 1160–1166, doi:10.4028/www.scientific.net/MSF.350-351.31.
- [7] H. Dong, F. Pan, B. Jiang, Y. Zeng, *Mater. Des.* 57 (2014) 121–127, doi:10.1016/j.matdes.2013.12.055.
- [8] F. Guo, L. Liu, Y. Ma, L. Jiang, Y. Zhang, D. Zhang, F. Pan, *J. Alloy. Compd.* 813 (2020) 152117, doi:10.1016/j.jallcom.2019.152117.
- [9] Y. Zou, L. Zhang, H. Wang, X. Tong, M. Zhang, Z. Zhang, *J. Alloy. Compd.* 669 (2016) 72–78, doi:10.1016/j.jallcom.2016.01.174.
- [10] J. Xu, Q. Su, C. Wang, X. Wang, D. Shan, B. Guo, T.G. Langdon, *Adv. Eng. Mater.* 21 (2019) 1–11, doi:10.1002/adem.201800961.
- [11] G. Wei, Y. Mahmoodkhani, X. Peng, A. Hadadzadeh, T. Xu, J. Liu, W. Xie, M.A. Wells, *Mater. Des.* 90 (2016) 266–275, doi:10.1016/j.matdes.2015.10.143.
- [12] Y. Yoshida, L. Cisar, S. Kamado, Y. Kojima, *Mater. Trans.* 43 (2002) 2419–2423, doi:10.2320/matertrans.43.2419.
- [13] M. Furui, C. Xu, T. Aida, M. Inoue, H. Anada, T.G. Langdon, *Mater. Sci. Eng. A* 410–411 (2005) 439–442, doi:10.1016/j.msea.2005.08.143.
- [14] M. Furui, H. Kitamura, H. Anada, T.G. Langdon, *Acta Mater.* 55 (2007) 1083–1091, doi:10.1016/j.actamat.2006.09.027.
- [15] F.R. Cao, H. Ding, Y.L. Li, G. Zhou, J.Z. Cui, *Mater. Sci. Eng. A* 527 (2010) 2335–2341, doi:10.1016/j.msea.2009.12.029.
- [16] F. Cao, G. Xue, G. Xu, *Mater. Sci. Eng. A* 704 (2017) 360–374, doi:10.1016/j.msea.2017.08.037.
- [17] J. Kawałko, P. Bobrowski, P. Koprowski, A. Jarzębska, M. Bieda, M. Łagoda, K. Sztwiertnia, *J. Alloy. Compd.* 707 (2017) 298–303, doi:10.1016/j.jallcom.2016.11.202.
- [18] J. Dutkiewicz, D. Kalita, W. Maziarz, T. Tański, W. Borek, P. Ostachowski, M. Faryna, *Met. Mater. Int.* 26 (2020) 1004–1014, doi:10.1007/s12540-019-00350-y.
- [19] M. Król, *J. Therm. Anal. Calorim.* 133 (2018) 237–246, doi:10.1007/s10973-018-7223-x.
- [20] W.R. Zhou, Y.F. Zheng, M.A. Leeftang, J. Zhou, *Acta Biomater.* 9 (2013) 8488–8498, doi:10.1016/j.actbio.2013.01.032.
- [21] L. Gao, C. Zhang, M. Zhang, X. Huang, N. Sheng, *J. Alloy. Compd.* 468 (2009) 285–289, doi:10.1016/j.jallcom.2007.12.080.
- [22] L. Yang, Q. Jiang, M. Zheng, B. Hou, Y. Li, *J. Magnes. Alloy.* 4 (2016) 22–26, doi:10.1016/j.jma.2015.12.002.
- [23] Y. Song, D. Shan, R. Chen, E.H. Han, *Corros. Sci.* 51 (2009) 1087–1094, doi:10.1016/j.corsci.2009.03.011.
- [24] C. Zhang, X. Huang, M. Zhang, L. Gao, R. Wu, *Mater. Lett.* 62 (2008) 2181–2184, doi:10.1016/j.matlet.2007.11.045.
- [25] Y. Sun, R. Wang, C. Peng, Y. Feng, M. Yang, *Trans. Nonferrous Met. Soc. China* 27 (2017) 1455–1475 (English Ed.), doi:10.1016/S1003-6326(17)60167-5.
- [26] Z.Y. Ding, L.Y. Cui, R.C. Zeng, Y. Bin Zhao, S.K. Guan, D.K. Xu, C.G. Lin, *J. Mater. Sci. Technol.* 34 (2018) 1550–1557, doi:10.1016/j.jmst.2018.05.014.
- [27] G. Liu, Z. Ma, G. Wei, T. Xu, X. Zhang, Y. Yang, W. Xie, X. Peng, *J. Mater. Process. Technol.* 267 (2019) 393–402, doi:10.1016/j.jmatprotec.2018.12.026.
- [28] D.K. Xu, E.H. Han, *Scr. Mater.* 71 (2014) 21–24, doi:10.1016/j.scriptamat.2013.09.025.
- [29] C. Li, Y. He, H. Huang, *J. Magnes. Alloy.* 9 (2021) 569–580, doi:10.1016/j.jma.2020.02.022.
- [30] R.C. Zeng, L. Sun, Y.F. Zheng, H.Z. Cui, E.H. Han, *Corros. Sci.* 79 (2014) 69–82, doi:10.1016/j.corsci.2013.10.028.
- [31] C.Q. Li, D.K. Xu, X.B. Chen, B.J. Wang, R.Z. Wu, E.H. Han, N. Birbilis, *Electrochim. Acta* 260 (2018) 55–64, doi:10.1016/j.electacta.2017.11.091.
- [32] T. Mineta, H. Sato, *Mater. Sci. Eng. A* 735 (2018) 418–422, doi:10.1016/j.msea.2018.08.077.
- [33] Q. Xiang, B. Jiang, Y. Zhang, X. Chen, J. Song, J. Xu, L. Fang, F. Pan, *Corros. Sci.* 119 (2017) 14–22, doi:10.1016/j.corsci.2017.02.009.
- [34] B.J. Wang, D.K. Xu, X. Cai, Y.X. Qiao, L.Y. Sheng, *J. Magnes. Alloy* 9 (2021) 560–568, doi:10.1016/j.jma.2020.02.020.
- [35] R.C. Zeng, L. Sun, Y.F. Zheng, H.Z. Cui, E.H. Han, *Corros. Sci.* 79 (2014) 69–82, doi:10.1016/j.corsci.2013.10.028.

- [36] B. Wang, K. Xu, D. Xu, X. Cai, Y. Qiao, L. Sheng, *J. Mater. Sci. Technol.* 53 (2020) 102–111. doi:10.1016/j.jmst.2020.04.029.
- [37] S.R. Agnew, J.A. Horton, T.M. Lillo, D.W. Brown, *Scr. Mater.* 50 (2004) 377–381, doi:10.1016/j.scriptamat.2003.10.006.
- [38] M. Al-Maharbi, I. Karaman, I.J. Beyerlein, D. Foley, K.T. Hartwig, L.J. Keeskes, S.N. Mathaudhu, *Mater. Sci. Eng. A* 528 (2011) 7616–7627. doi:10.1016/j.msea.2011.06.043.
- [39] K. Sztwiertnia, J. Kawalko, M. Bieda, M. Jaskowski, K. Pieta, W. Bochniak, *IOP Conf. Ser. Mater. Sci. Eng.* 82 (2015) 1–4, doi:10.1088/1757-899X/82/1/012084.
- [40] I. Bednarczyk, D. Kuc, A. Tomaszewska, M. Tkocz, *Arch. Metall. Mater.* 65 (2020) 1121–1128, doi:10.24425/amm.2020.133228.
- [41] P. Koprowski, M. Bieda, S. Boczkal, A. Jarzębska, P. Ostachowski, J. Kawalko, T. Czeppe, W. Maziarz, M. Łagoda, K. Sztwiertnia, *J. Mater. Process. Technol.* 253 (2018) 34–42, doi:10.1016/j.jmatprotec.2017.10.043.
- [42] A.D. Sudholz, K. Gusieva, X.B. Chen, B.C. Muddle, M.A. Gibson, N. Birbilis, *Corros. Sci.* 53 (2011) 2277–2282, doi:10.1016/j.corsci.2011.03.010.
- [43] N.T. Kirkland, J. Lespagnol, N. Birbilis, M.P. Staiger, *Corros. Sci.* 52 (2010) 287–291. doi:10.1016/j.corsci.2009.09.033.
- [44] ASTM B90/B90M-15, 2012. doi:10.1520/B0090.
- [45] A. Dobkowska, B. Adamczyk – Cieślak, J. Kubásek, D. Vojtěch, D. Kuc, E. Hadasik, J. Mizera, *J. Magnes. Alloy.* 9 (2021) 467–477. doi:10.1016/j.jma.2020.07.007.
- [46] A. Korbel, W. Bochniak, *Scr. Mater.* 51 (2004) 755–759, doi:10.1016/j.scriptamat.2004.06.020.
- [47] E. Poorqasemi, O. Abootalebi, M. Peikari, F. Haqdar, *Corros. Sci.* 51 (2009) 1043–1054. doi:10.1016/j.corsci.2009.03.001.
- [48] N. Birbilis, A.D. King, S. Thomas, G.S. Frankel, J.R. Scully, *Electrochim. Acta* 132 (2014) 277–283, doi:10.1016/j.electacta.2014.03.133.
- [49] S. Leleu, B. Rives, N. Causse, N. Pébère, *J. Magnes. Alloy.* 7 (2019) 47–57, doi:10.1016/j.jma.2018.12.002.
- [50] R. Pinto, M.G.S. Ferreira, M.J. Carmezim, M.F. Montemor, *Electrochim. Acta* 56 (2011) 1535–1545. doi:10.1016/j.electacta.2010.09.081.
- [51] W.C. Neil, M. Forsyth, P.C. Howlett, C.R. Hutchinson, B.R.W. Hinton, *Corros. Sci.* 51 (2009) 387–394, doi:10.1016/j.corsci.2008.11.005.
- [52] G. Song, A. Atrens, D.S. John, X. WU, J. Nairn, *Corros. Sci.* 39 (1997) 1981–2004, doi:10.1016/S0010-938X(97)00090-5.
- [53] N. Hara, Y. Kobayashi, D. Kagaya, N. Akao, *Corros. Sci.* 49 (2007) 166–175, doi:10.1016/j.corsci.2006.05.033.
- [54] W.C. Kim, J.G. Kim, J.Y. Lee, H.K. Seok, *Mater. Lett.* 62 (2008) 4146–4148, doi:10.1016/j.matlet.2008.06.028.
- [55] L. Wang, T. Shinohara, B.P. Zhang, *Appl. Surf. Sci.* 256 (2010) 5807–5812, doi:10.1016/j.apsusc.2010.02.058.
- [56] A. Dobkowska, B. Adamczyk-Cieślak, A. Towarek, P. Maj, E. Ura-Bińczyk, M. Momeni, D. Kuc, E. Hadasik, J. Mizera, *J. Mater. Eng. Perform.* 29 (2020) 2679–2686, doi:10.1007/s11665-020-04775-0.
- [57] K.D. Ralston, N. Birbilis, *Corrosion* 66 (2010) 1–4, doi:10.5006/1.3462912.
- [58] N.N. Aung, W. Zhou, *Corros. Sci.* 52 (2010) 589–594, doi:10.1016/j.corsci.2009.10.018.
- [59] M.C. Lin, C.Y. Tsai, J.Y. Uan, *Corros. Sci.* 51 (2009) 2463–2472, doi:10.1016/j.corsci.2009.06.036.



## Microstructural, corrosion and mechanical properties of a WE43 alloy: conventional extrusion versus SPD

Anna Dobkowska<sup>a,\*</sup>, Aleksandra Zielińska<sup>a</sup>, Irena Paulin<sup>b</sup>, Črtomir Donik<sup>b</sup>, Milena Koralnik<sup>a</sup>, Bogusława Adamczyk – Cieślak<sup>a</sup>, Monika Wiecezorek-Czarnocka<sup>a</sup>, Dariusz Kuc<sup>c</sup>, Jiri Kubasek<sup>d</sup>, Tomasz Mikuszewski<sup>c</sup>, Matjaž Godec<sup>b</sup>, Jarosław Mizera<sup>a</sup>

<sup>a</sup> Faculty of Materials Science and Engineering, Warsaw University of Technology, Warsaw, Poland

<sup>b</sup> Institute of Metals and Technology, Ljubljana, Slovenia

<sup>c</sup> Department of Materials Technology, Silesian University of Technology, Katowice, Poland

<sup>d</sup> Department of Metal and Corrosion Engineering, University of Chemical Technology, Prague, Czech Republic

### ARTICLE INFO

#### Keywords:

WE43  
Several plastic deformation  
Microstructure  
Corrosion  
Mechanical properties

### ABSTRACT

A hexagonal close-packed-structure WE43 alloy was extruded without any preheating of the initial billet using extrusion with an oscillating die to improve the corrosion and mechanical properties. The WE43 alloy was extruded at high ratios of  $R_1$  5:1,  $R_2$  7:1 and  $R_3$  10:1. Electron back-scatter diffraction and transmission electron microscopy were used to determine the microstructural properties of the alloys. The influence of the extrusion method and the extrusion ratios on the corrosion and mechanical properties were investigated. Electrochemical tests were performed, and the corrosion damage was inspected. Tensile tests were made using micro specimens. When compared to conventional extrusion, the microstructural changes obtained with the KoBo method at  $R_1$  5:1 increased the corrosion resistance, which was not only due to the grain refinement, but also due to the intensity of the texture. A decline in the corrosion resistance of the alloys deformed at higher extrusion ratios was observed. This was a result of the massive plastic strain imposed by the KoBo die. The room-temperature mechanical properties of the KoBo-extruded alloys were improved. However, at higher temperatures the mechanical properties decreased due to the solutioning of tiny triple precipitates.

### 1. Introduction

One of the most popular alloys of the Mg-Y-RE series is WE43 (Mg–4.2Y–2.3Nd–0.6Zr, wt%), which owes its excellent mechanical properties at normal and high temperatures to two different mechanisms: precipitation and solid-solution strengthening [1,2]. While alloying elements are the main reason for the improvement in mechanical properties, their presence is problematic when analyzing the corrosion performance. The second phases formed in Mg-Y-RE alloys have different electrode potentials than the Mg matrix, which makes them either anodic or cathodic with respect to the Mg matrix, thus accelerating or slowing down the micro-galvanic processes [3–6]. The role of the second phases in the micro-galvanic corrosion of WE43 was investigated by Feng et al. [6]. They showed that the micro-galvanic effect caused by the second phases and Mg matrix in WE43 is dependent on the anions present in the corrosive solutions [3]. The corrosion

behavior of WE43 is also affected by the number of second phases, their distribution and the grain refinement [7]. Several studies proved that the greater the grain refinement, the better the corrosion resistance of WE43. For example, Eivani et al. [8] investigated the influence of the number of passes of friction-stir processing on WE43, and it was stated that with a smaller grain size, the uniformity of the protective passive layer was improved and, at the same time, the intensity of the micro-galvanic coupling leading to pitting corrosion was decreased. Soderlind et al. [9] also showed that the grain refinement that occurred during the spark plasma sintering of WE43 holds the potential for slow and homogeneous corrosion. The processing method also plays an important role in the corrosion behavior of WE43 alloys. A uniform corrosion dominates on the surface of the extruded WE43, while the forged WE43 alloy suffered from severe local galvanic corrosion with a four-times-higher corrosion rate than the extruded alloy [10].

At room temperature the basal slip has a much lower critical resolved

\* Corresponding author.

E-mail address: [anna.dobkowska@pw.edu.pl](mailto:anna.dobkowska@pw.edu.pl) (A. Dobkowska).

<https://doi.org/10.1016/j.jalcom.2023.173090>

Received 22 September 2023; Received in revised form 31 October 2023; Accepted 7 December 2023

Available online 11 December 2023

0925-8388/© 2023 Elsevier B.V. All rights reserved.

shear stress in Mg with a hexagonal close-packed crystal structure than all other deformation modes. Therefore, the number of independent, operable slip systems is limited, leading to poor ductility and formability [11]. Among the severe plastic deformation methods known for metals with hexagonal close-packed crystal structures, most are employed at higher temperature [12–16]. Therefore, it is crucial to look for solutions that allow for the cost and efficiency optimization of the Mg processing. In this study the mechanical and corrosion properties of a WE43 magnesium alloy extruded using conventional extrusion at 400 °C and forward-backwards extrusion with an oscillating die (KoBo) without preheating of the initial billet are compared. We emphasized the microstructural differences and their influence on the corrosion and mechanical properties of WE43 extruded at high deformation ratios with and without preheating of the initial billet.

## 2. Materials and methodology

### 2.1. Extrusion method and investigated materials

The chemical composition of the WE43 alloy is given in Table 1. The reference material was conventionally extruded from Ø40 mm to Ø8 mm at 400 °C using a Hydromet press [17], giving an extrusion ratio of R<sub>1</sub> 5:1 (Fig. 1a). The alloys in the form of rods with an initial dimension of Ø40 mm were extruded with an oscillating die (the so-called KoBo method [18–21]) to Ø8 mm, Ø6 mm and Ø4 mm, giving extrusion ratios R<sub>1</sub> 5:1 (true strain  $\epsilon_1 = 1.6$ ), R<sub>2</sub> 7:1 ( $\epsilon_2 = 1.9$ ) and R<sub>3</sub> 10:1 ( $\epsilon_3 = 2.3$ ), Fig. 1b. Unlike conventional extrusion, KoBo enables dimensional reduction at high rates without preheating of the initial billet (even for hexagonal structures) [20]. This is possible due to the presence of the oscillating die at the end of the extruder, which introduces material into a state of plastic flow. The investigated materials were extruded under the following conditions: punch speed of 0.2 mm/s, die rotation angle of 8°, initial temperature of the billet of 24 °C, and die oscillation frequency of 5 ± 1 Hz.

### 2.2. Microstructure characterization

The microstructures of the samples were analyzed by examining a cross-sectioned, ion-milled surface prepared using a JEOL SM-09010 Cross Section Polisher with an Ar<sup>+</sup> ion beam set to 5 kV and 30 mA. Secondary-electron imaging (SEI) and electron-backscatter diffraction (EBSD) were performed on a field-emission scanning electron microscope (FIB-SEM), Zeiss CrossBeam 550 with an EDAX Hikari Super EBSD camera using APEX software and EBSD postprocessing using OIM 8.6 software. The parameters used for the SE images and EDS analyses were a 15 kV accelerating voltage and a 2.0–5.0 nA probe current, while the EBSD analyses were performed on 70°-tilted samples and a 10-nA probe current with a step size of 0.5 µm. The crystallographic orientations of the grains are presented as inverse-pole-figure (IPF Z) maps, where the various colors indicate the orientation of a given grain in a crystal frame of reference. OIM software was used to calculate the Geometrically Necessary Dislocation Densities (GNDs) and the textures of materials based on their pole figures.

X-ray diffraction (XRD, Bruker D8 Advance) operating at 40 kV and 40 mA with Cu-K $\alpha$  radiation was used to identify the phases in the alloys. The results were recorded by stepwise scanning 2 $\theta$  from 10° to 120°, with a step size of 0.02° and a count time of 10 s per step. We used transmission electron microscopy (JEOL JEM 1200EX) to capture high-resolution images in bright-field mode. The acceleration voltage used

Table 1

Chemical composition of the WE43 alloy from energy-dispersive X-ray (EDS) measurements in wt%.

Elements	Y	Nd	Gd	Dy	Mg
WE43	4.1 ± 0.1	2.5 ± 0.1	0.5 ± 0.1	0.4 ± 0.1	bal.

was 120 kV. Thin foils were prepared using a Gatan Model 691 Precision Ion Polishing System (PIPS) with a beam voltage of 3 V inclined to the sample surface at an angle of 10°. Differential scanning calorimetry (DSC, PerkinElmer) was used to reveal the phase transitions. DSC samples with dimensions of 2 × 2 × 4 mm<sup>3</sup> were heated in Al<sub>2</sub>O<sub>3</sub> crucibles to 550 °C at a heating rate of 10 °C/min in argon (99.996%).

### 2.3. Corrosion testing

To compare the corrosion behavior of the alloys, electrochemical measurements were made in a naturally aerated, unstirred 0.1-M NaCl solution using a Gamry FAS1 potentiostat equipped with three electrodes: platinum as the counter electrode, Ag/AgCl as the reference electrode, and the measured sample as the working electrode. The electrolyte was made up using analytical grade reagents and distilled water. The corrosion potential ( $E_{\text{corr}}$ ) was recorded for 1 h in open-circuit conditions. Electrochemical impedance spectroscopy (EIS) covered a frequency range of 10 mHz to 10 kHz. Potentiodynamic polarization tests were then carried out in the range of 0.5 V below  $E_{\text{OCP}}$  to 1.5 V vs. Ref (a scan rate of 5 mV/s was used). At least three tests were conducted for each microstructural condition. The polarization curves were fitted using Gamry Elchem software in polarization-resistance mode.

The surfaces after 1 h of immersion in the 0.1 M NaCl with subsequent removal of the corrosion products were analyzed with SEM. The corrosion products were chemically removed by immersion in chromic acid (200 g of Cr<sub>2</sub>O<sub>3</sub> in 1 L of distilled water). The surface development of the samples was measured using an atomic force microscope (AFM, Oxford Instruments Asylum Research AFM MFP3D Bio). The measurement was performed with a scan size of 40 µm and a scan rate of 0.49 Hz. The data were analysed using Gwyddion software. The images showing the development of the surface profiles at the selected location and the mean roughness ( $S_a$ ) numerical values were exported. The mean roughness ( $S_a$ ) is the arithmetic mean of the absolute value of the height within a sampling area.

### 2.4. Mechanical testing

To characterize the mechanical properties, tensile tests were performed using micro-sized specimens, as in the study of Molak et al. [22] (Zwick/Roell Z050 tensile machine equipped with holders which allow measuring of specimens with non-standard dimensions). Tensile tests were performed at room temperature and 300 °C using an initial strain rate of 0.01 s<sup>-1</sup>. Afterwards, characteristic parameters for each material were calculated: (YS – yield strength; UTS – tensile strength, A<sub>t</sub> – percentage of total extension at fracture) [23]. Four tests were made for each material to ensure the repeatability of the measurements. SEM images of the fractured surfaces of the representative tensile specimens for deeper characterisation were captured (SEM, Hitachi SU70).

## 3. Results

### 3.1. Microstructure characterization

#### 3.1.1. EBSD, SEM and XRD

The microstructure of the conventionally extruded WE43 to Ø8 mm (R<sub>1</sub> 5:1) is composed of equiaxed grains with an average size of 3.9 µm (Fig. 1a). The Kobo extrusion at the same ratio as the conventionally extruded WE43 (R<sub>1</sub> 5:1) leads to greater microstructure refinement with an average grain size of 3.3 µm (Fig. 1b). The crystallographic orientations of the grains formed in both alloys are relatively random (Fig. 1a, b). Nevertheless, even a slight change in the microstructural refinement led to more accumulation of the GND at the grain boundaries in the KoBo-extruded alloy (Fig. 1i, j). The grains with an average size of 2.7 µm were formed in the Ø6-mm KoBo-deformed sample (R<sub>2</sub> 7:1), Fig. 1c, while the smallest grain size (1.8 µm) was in the material KoBo

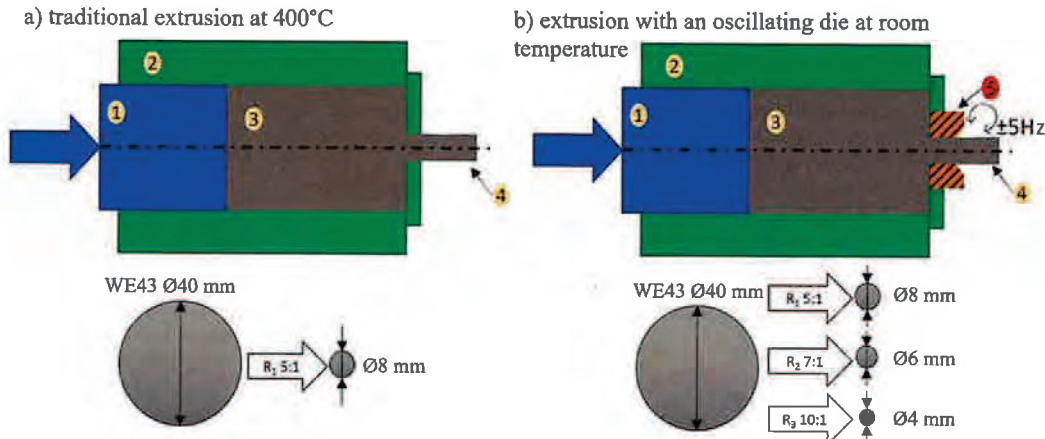


Fig. 1. Schematic of a) traditional extrusion and b) extrusion with an oscillating die (KoBo): 1 – extrusion punch, 2 – injection cylinder, 3 – initial billet, 4 – final rod, 5 – oscillating die.

extruded to  $\varnothing 4$  mm ( $R_3$  10:1), Fig. 1d. There is a change in the crystallographic orientations of the grains formed in the alloy extruded to  $\varnothing 6$  mm with a prevalence of grains oriented to  $\langle 0001 \rangle$  (red), while the highest extrusion ratio ( $\varnothing 4$  mm,  $R_3$  10:1) results in the formation of grains with random orientations (Fig. 1d). The maps showing the GND density indicate that the accumulation of dislocations occurs at the grain boundaries, however, their number is rather comparable Fig. 1j,k, l. Most of the grains formed in the investigated materials are distorted by more than  $15^\circ$ , leading to the formation of HAGBs (Fig. 1e–h). Regardless of the extrusion ratio, two types of coarse, bright precipitates are observed in each material when analyzing the SEM images (see Fig. 3a–d). The bright precipitates with irregular shapes are enriched in Nd, as shown in Fig. 3a. The precipitates that have sharp edges are

composed of Y and Nd, as shown in Fig. 2b–d. Their rectangular shape indicates that these are rare-earth hydrides [24,25]. The XRD reveals that  $Mg_{41}Nd_5$  and  $Mg_{24}Y_5$  precipitated in the conventionally and KoBo-extruded WE43 to  $\varnothing 8$  mm (Fig. 4).  $Mg_{12}Nd$  and  $Mg_{41}Nd_5$  additionally formed at higher extrusion ratios.

Fig. 5 shows pole figures of conventionally extruded (Fig. 5a) and KoBo-extruded (Fig. 5b–d) WE43 alloy. The grains in the extruded materials were mainly oriented parallel to the c axis of grains. When comparing the two types of extrusion for the same ratio of 5:1 ( $\varnothing 8$  mm), Fig. 5a and Fig. 5b reveal different textures. The conventionally extruded material has a stronger texture intensity, but also contains more randomly distributed textural components. The texture distribution in the KoBo-extruded materials is comparable for various extrusion

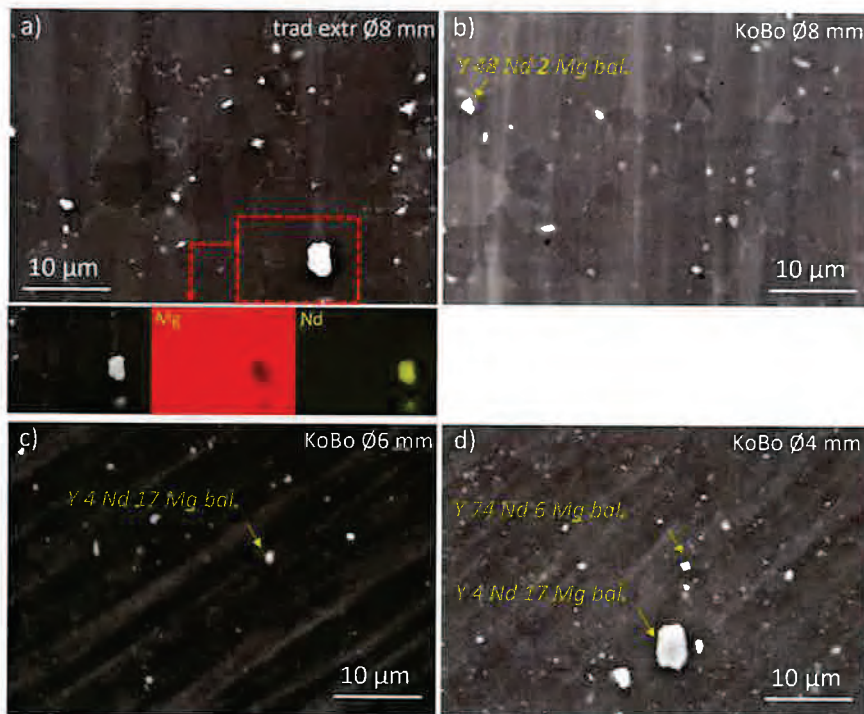


Fig. 3. SEM microstructure of the investigated alloys with the representative EDS analyses of the precipitations (in wt%).

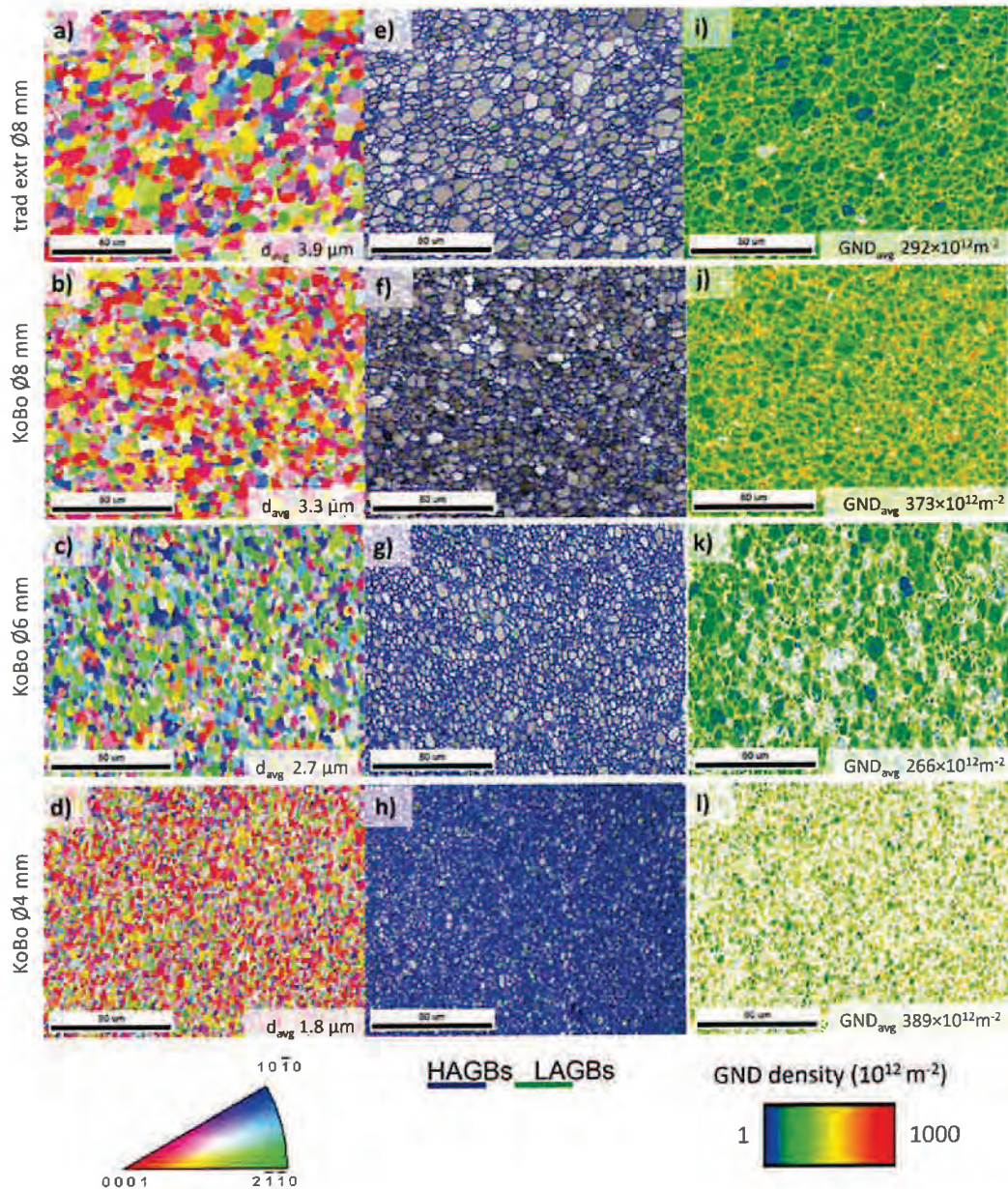


Fig. 2. Inverse-pole-figure (IPFs Z) maps with the average grain size (a–d), grain boundaries (GBs) distributions (e–h), geometrically necessary dislocation (GND) densities (i–l) with the average number of the GND density presented for the WE43 conventionally extruded to Ø8 mm, KoBo extruded to Ø8 mm, Ø6 mm and Ø4 mm. The EBSD was conducted on the surface perpendicular to the extrusion direction.

ratios (as shown in Fig. 5b–d). The material extruded at R2 7:1 (Ø6 mm) has the highest maximum texture intensity of 5.2 (Fig. 5c).

### 3.1.2. TEM observations

To gain a better understanding of the phases formed by conventional extrusion and the KoBo method, TEM observations and X-ray diffraction were carried out. As shown in Fig. 6a, besides the phases recognized with the XRD, one additional phase was detected in the conventionally extruded alloy, i.e.,  $Mg_2Y$ .  $Mg_{41}Nd_5$  has an irregular, sharp shape with an approximate size of 1 µm (Fig. 6b). The same types of precipitation observed in the KoBo-extruded alloy are round, and they are smaller than 1 µm (Fig. 6c). The  $Mg_{24}Y_5$  was detected in the WE43 KoBo-

extruded to Ø4 mm (R3 10:1), Fig. 4d. When TEM images of the materials extruded to Ø8 mm (R3 5:1) are compared, it is apparent that conventionally extruded material has only a small number of dislocations in the grain interiors (as shown in Fig. 6a, b). In the KoBo-deformed sample, more dislocations are present (as illustrated in Fig. 6c, d), which are indicated by the yellow arrows. When examining the different extrusion ratios of materials undergoing KoBo deformation, we observed that as the extrusion ratio increased, the dislocations were more tangled. These dislocations were not only present around distinct grain boundaries, but also within the grain interiors (as seen in Fig. 7b–d, indicated by the yellow arrows). A higher concentration of dislocations might support the precipitation in the samples extruded to

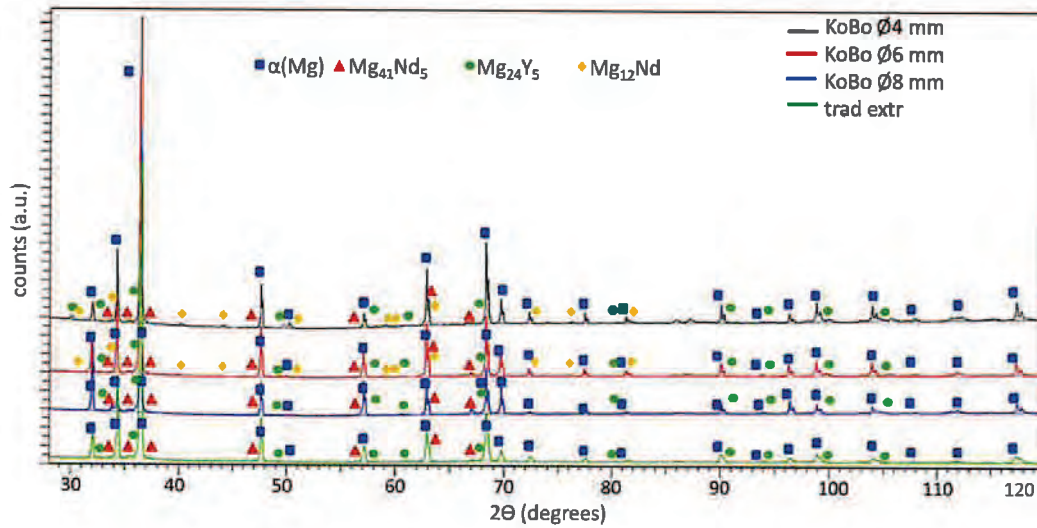


Fig. 4. Phase composition of the investigated materials analyzed with XRD.

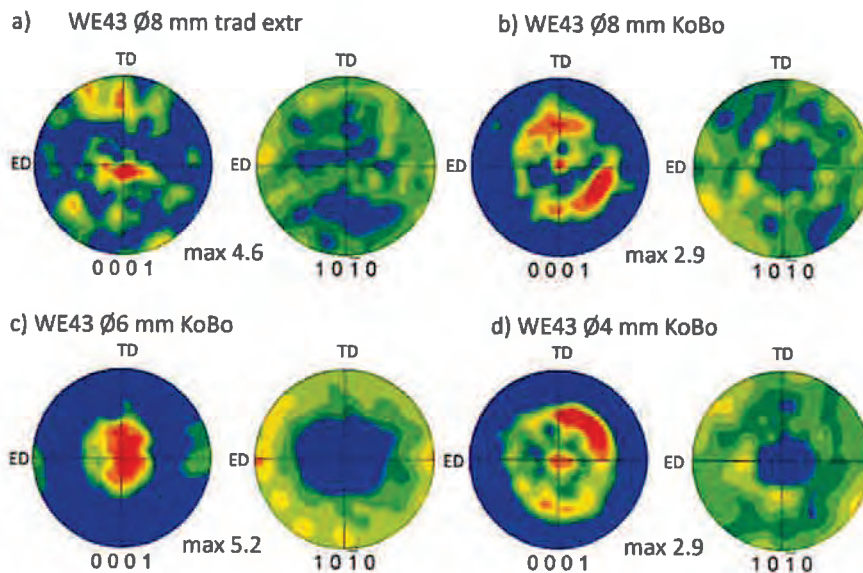


Fig. 5. Pole figures obtained for a) the WE43 conventionally extruded to Ø8 mm, and the WE43 after KoBo extrusion to b) Ø8 mm, and c) to Ø6 mm and d) to Ø4 mm; ED – extrusion direction.

Ø6 mm ( $R_2$  7:1) and Ø4 mm ( $R_3$  10:1) even during the extrusion process. Special attention should be paid to tiny, round precipitates with a size of a few nanometers that are present in the KoBo-extruded materials. A representative TEM image of the KoBo sample extruded to Ø8 mm showing those precipitates is in Fig. 8 (precipitates marked inside the red square). Behind the clearly distinguishable diffraction patterns of the  $\alpha$ (Mg) matrix, second-phase diffraction patterns are visible on the SAD pattern. Based on literature data, those tiny precipitates must be ternary precipitates with a chemical composition of Mg-Nd-Y [4,26–30].

### 3.2. Corrosion resistance

The potential evolution recorded under open-circuit conditions ( $E_{OCP}$ ) was followed for 1 h in 0.1-M NaCl for each sample, shown in Fig. 9a. At the outset, the  $E_{OCP}$  for the conventionally extruded alloy

started from  $-1.75$  V/Ref, gradually increasing during first 20 min of immersion to  $-1.68$  V/Ref, and then stabilizing. The  $E_{OCP}$  for the Ø8-mm KoBo-extruded material increased smoothly from  $-1.70$  to  $-1.67$  V/Ref. The highest values of  $E_{OCP}$  are recognized for the alloy KoBo extruded to Ø4 mm (starting from  $-1.72$  V/Ref to  $-1.57$  V/Ref), while the lowest values of  $E_{OCP}$  oscillating around  $-1.84$  V/Ref are observed for the Ø6-mm KoBo-extruded sample. The potentiodynamic curves shown in Fig. 9b indicate that all the materials undergo pitting corrosion, and that the susceptibility to localized corrosion depends on the method of deformation and the extrusion ratios. All the recorded curves have an inflection point, recognized as the breakdown potential ( $E_b$ ). Based on the values of  $E_{corr}$  and  $E_b$ , the most susceptible to pitting corrosion are the alloys extruded via KoBo to Ø6 mm and Ø4 mm (Table 2). The conventionally extruded and KoBo-extruded WE43 to Ø8 mm are the least prone to pitting. Both the cathodic and anodic branches

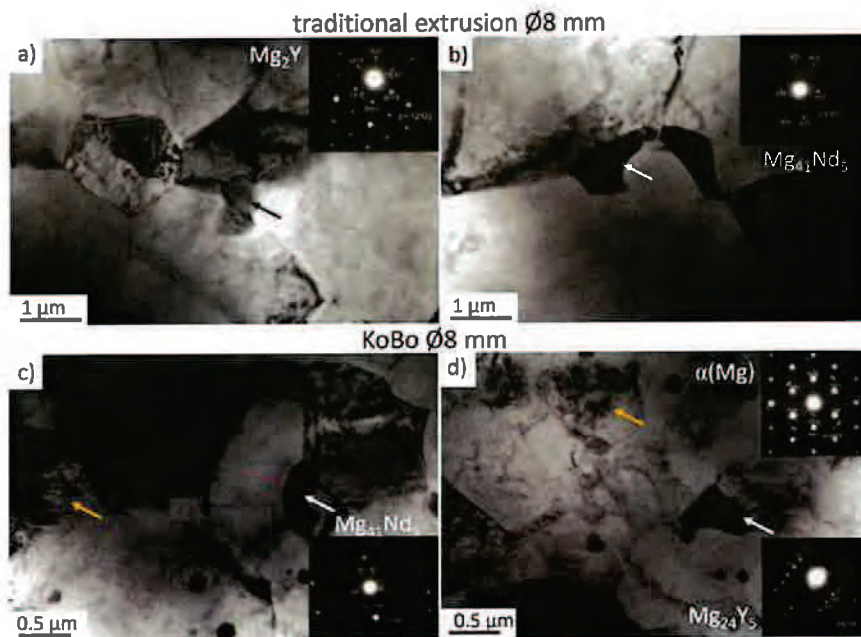


Fig. 6. Selected-area diffraction (SAD) patterns obtained from the WE43 conventionally extruded to Ø8 mm (a,b) and KoBo extruded to Ø8 mm (c,d).

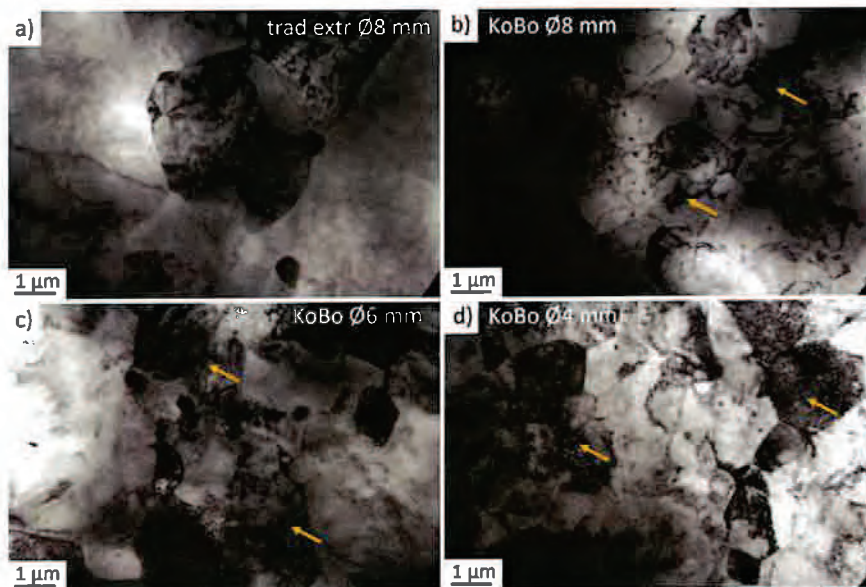


Fig. 7. TEM bright-field images of the WE43: a) conventionally extruded to Ø8 mm, b) KoBo extruded to Ø8 mm, c) KoBo extruded to Ø6 mm and d) KoBo extruded to Ø4 mm.

of the polarization curves showed an active response with the corrosion-current density,  $i_{\text{corr}}$ , determined by a Tafel extrapolation, of  $195 \mu\text{A}/\text{cm}^2$  for the reference alloy and  $191 \mu\text{A}/\text{cm}^2$ ,  $153 \mu\text{A}/\text{cm}^2$  and  $111 \mu\text{A}/\text{cm}^2$  for the KoBo-extruded material to Ø8 mm, Ø6 mm and Ø4 mm (Table 2). A change in the kinetics of the anodic processes was also observed.

Electrochemical impedance spectroscopy (EIS) was performed after 1 h of immersion in 0.1-M NaCl. Fig. 9c and d show the impedance response of the conventional and KoBo-extruded WE43. The data

presented in the form of Nyquist plots reveal the presence of two capacitive loops at high and medium frequencies and one inductive loop at low frequencies. Such a frequency response of the electrical impedance for Mg in NaCl solutions has previously been reported in several studies [31–33]. The capacitive loop at high frequencies is related to the charge-transfer double layer at the metal/electrolyte interface, while the capacitive loop at medium frequencies stands for the resistance and capacitance of the layer of corrosion products [34,35]. The medium capacitive loop originated from the diffusion through a porous solid film

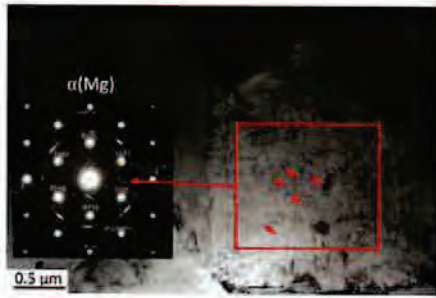


Fig. 8. TEM bright-field image of the WE43 KoBo extruded to Ø8 mm.

on the alloy surface [36]. The  $R_i$  and  $L$  at low frequencies correspond to the nucleation of localized corrosion. The magnitude of the semicircle in the high-frequency range may help to qualitatively estimate the alloys' corrosion resistance. As observed, the corrosion resistance of the KoBo-extruded material to Ø8 mm is more resistive in the analyzed solution than the same alloy conventionally extruded to the same diameter (Table 3). The KoBo-extruded WE43 to Ø4 mm and to Ø6 mm has higher activity than both alloys in the chloride-containing solution. Both the capacitive loop in the high-frequency range and the capacitive loop in

the low-frequency range decreased when the extrusion ratio was  $R_2$  7:1 and  $R_3$  5:1.

The examination of the corroded surfaces after oxide-film removal showed that localized corrosion is the predominant effect (Fig. 10). The least damage is observed on the surface of the KoBo-extruded WE43 to Ø8 mm (Fig. 10b), where some tiny pits are formed on the surface. This is also confirmed by the value of the mean roughness ( $S_a$ ), which in this case was calculated to be the lowest among the investigated materials ( $63 \pm 6$  nm). The oscillations visible in the line scan of the surface-development profile are also not significant, showing that the corrosion damage is not deeper than approximately  $0.5 \mu\text{m}$ . Greater localized damage is formed on the surface of the alloy conventionally extruded to Ø8 mm (Fig. 11a). The pits are larger than those observed in Fig. 10b,

Table 2  
Electrochemical parameters calculated from the potentiodynamic measurements.

WE43 KoBo	$E_{\text{con}}$ (V/Ref)	$E_b$ (V/Ref)	$ \Delta E $	$i_{\text{con}}$ ( $\mu\text{A}/\text{cm}^2$ )
Ø 8 mm conv. extrusion	-1.65	-1.07	0.58	195
Ø 8 mm KoBo	-1.60	-1.11	0.49	191
Ø 6 mm KoBo	-1.57	-1.32	0.25	153
Ø 4 mm KoBo	-1.54	-1.39	0.15	111

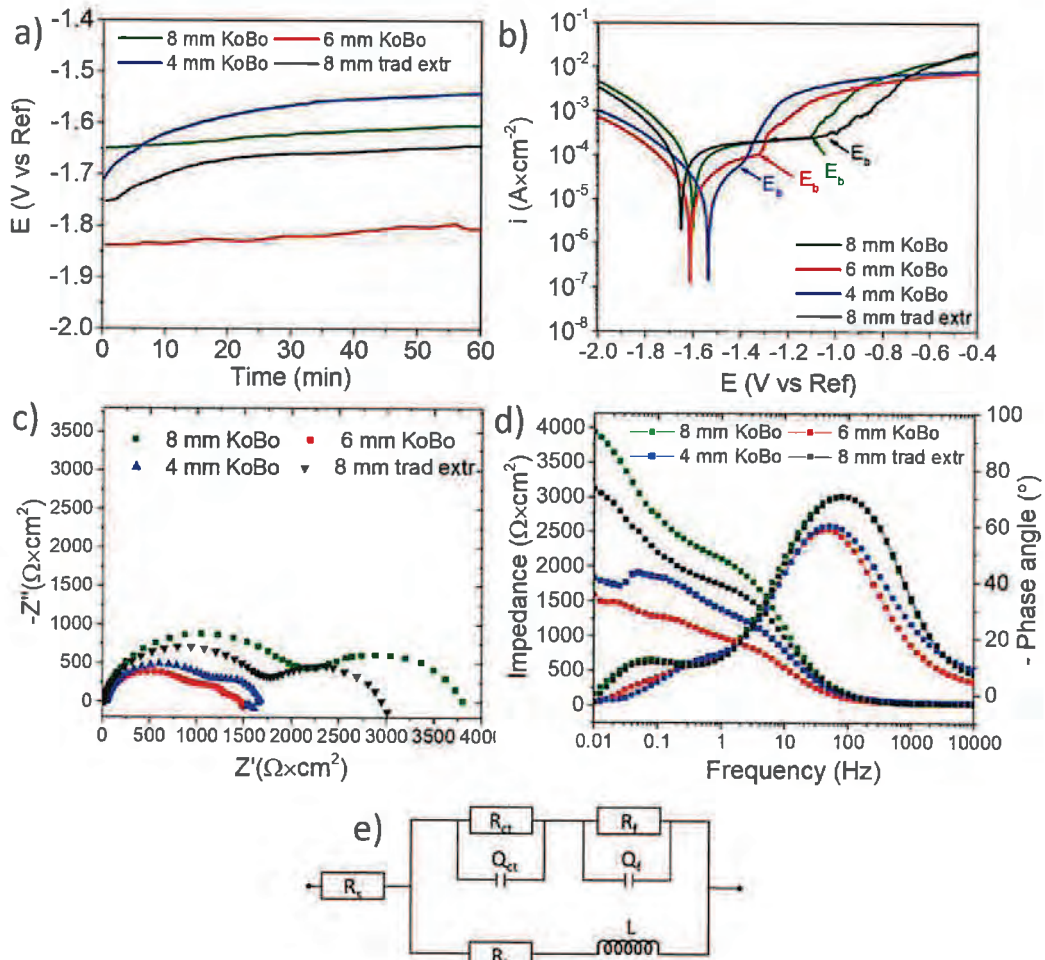
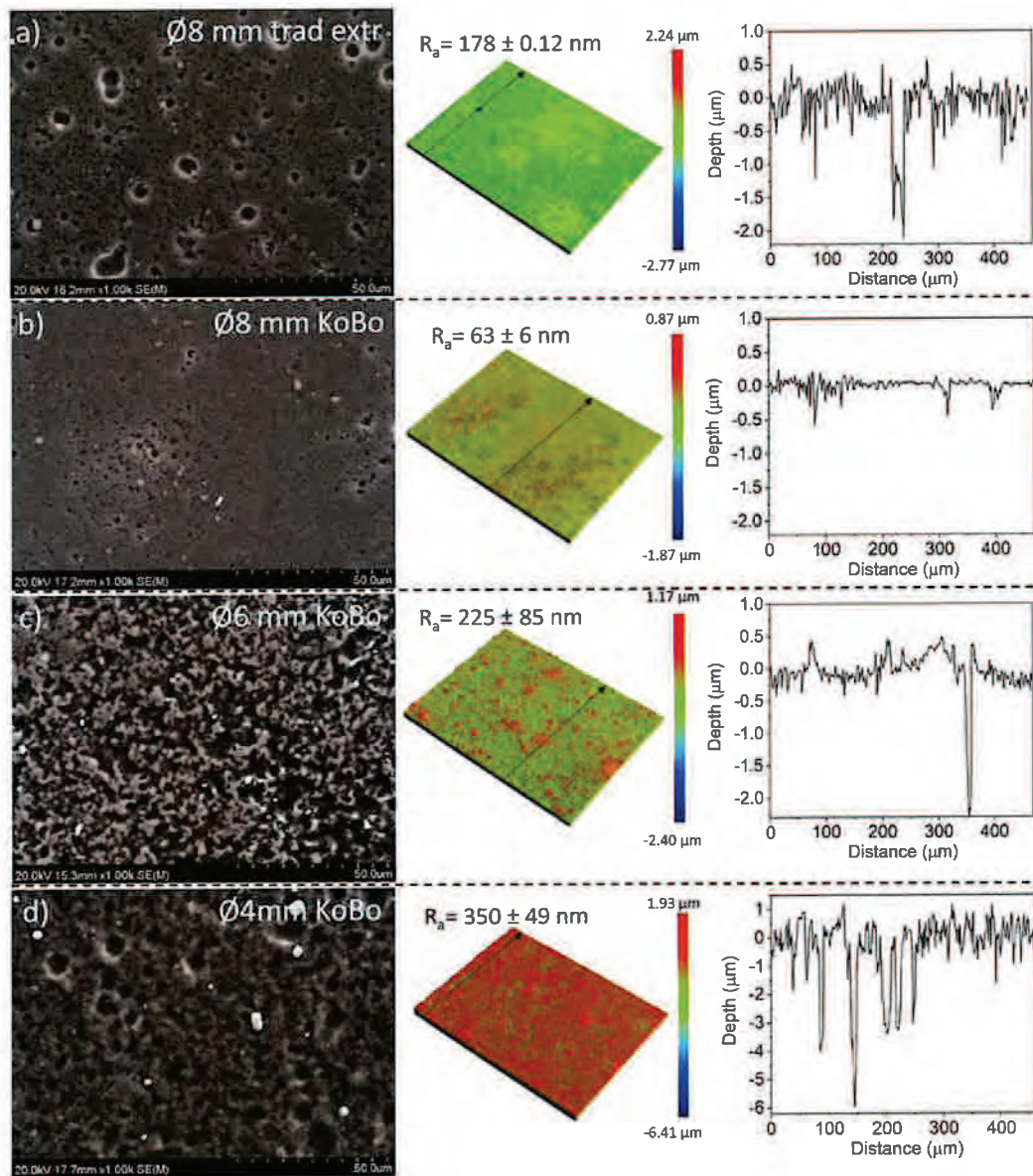


Fig. 9. Conventionally and KoBo-extruded WE43 from electrochemical testing performed in aerated 0.1-M NaCl: a)  $E_{\text{OCP}}$  evolution, b) potentiodynamic polarization curves, c) Nyquist plots, d) Bode plots, e) electrical equivalent circuit (EEC) used for data fitting.

**Table 3**  
Electrochemical parameters obtained from the electrical equivalent-circuit fitting.

WE43	$R_s$ ( $\Omega$ cm <sup>2</sup> )	$R_{ct}$ ( $\Omega$ cm <sup>2</sup> )	$Q_{ct}$ (Ss <sup>n</sup> cm <sup>-2</sup> )	$n_1$	$R_f$ ( $\Omega$ cm <sup>2</sup> )	$Q_f$ (Ss <sup>n</sup> cm <sup>-2</sup> )	$n_2$	$L$ (H cm <sup>2</sup> )	$R_L$ ( $\Omega$ cm <sup>2</sup> )
Ø 8 mm trad. extr.	24	1768	0.000017	0.95	1219	0.001633	0.84	2	1775
Ø 8 mm KoBo	26	2099	0.000017	0.90	1599	0.000145	0.83	3	2000
Ø 6 mm KoBo	48	1150	0.000026	0.88	1628	0.000939	0.68	1	1915
Ø 4 mm KoBo	18	439	0.000064	0.68	1743	0.000682	0.99	9	1639



**Fig. 10.** SEM of corroded surfaces after 1-hour immersion of WE43 in 0.1-M NaCl (corrosion products removed) with corresponding surface-development 3D images and extracted line profiles (in the areas marked by the red arrows on 3D images): a) conventionally extruded to Ø8 mm, b) KoBo extruded to Ø8 mm, c) KoBo extruded to Ø6 mm and d) KoBo extruded to Ø4 mm.

and the  $S_a$  was found to be almost three times higher, being  $178 \pm 12$  nm. The deeper pit had a depth of around 2 nm. When analysing higher extrusion ratios,  $R_2$  and  $R_3$ , the corrosion mechanism is more intense, the morphology of the samples shown in Figs. 10c and 10d is rough, having  $S_a$  of  $225 \pm 85$  and  $350 \pm 49$  nm, respectively. Also, as

presented on the line profiles, the single pits are deeper than 2 nm (for the highest extrusion ratio, it is almost 6 nm).

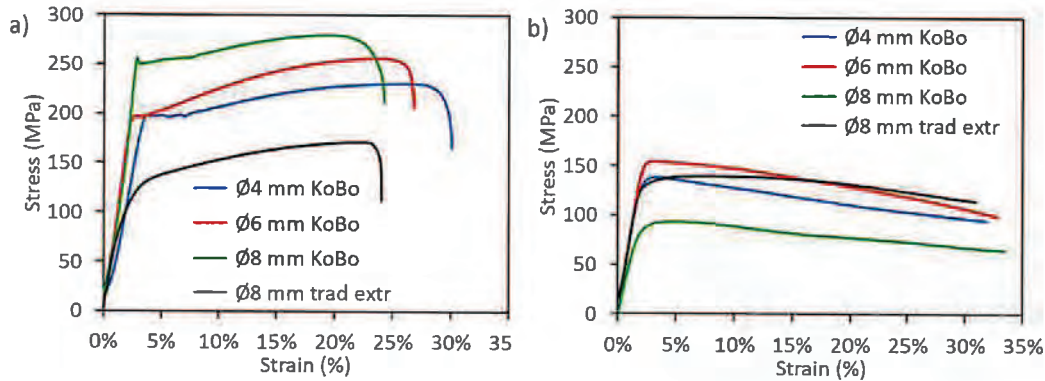


Fig. 11. Stress-strain curves taken from the tests performed for the conventionally and KoBo-extruded WE43 to Ø8 mm, Ø6 mm and Ø4 mm: a) at room temperature, b) at 300 °C.

### 3.3. Mechanical properties

Typical engineering stress-strain curves of the WE43 alloys investigated at room temperature and 300 °C are shown in Fig. 11, and the calculated mechanical properties are given in Table 4. At room temperature, the conventionally extruded WE43 has a tensile yield strength (TYS) and ultimate tensile strength (UTS) of  $80 \pm 30$  and  $165 \pm 5$  MPa, respectively. The alloys extruded to the same dimension using KoBo increased the YS to  $244 \pm 7$  MPa and the UTS to  $273 \pm 7$  MPa. Extrusion at higher ratios ( $R_2$  and  $R_3$ ) also resulted in the rise of YS and UTS to  $198 \pm 3$  MPa and  $256 \pm 1$  MPa for 6 mm and to  $210 \pm 15$  and  $250 \pm 19$ , respectively. The deformation behaviour after KoBo extrusion changed and alloys exhibited clear yield phenomenon. There is also a slight increase in the elongation values. Very similar mechanical properties at both ambient and elevated temperatures are observed for the conventionally extruded alloy. The situation changed for the KoBo-deformed materials -the mechanical properties investigated at elevated temperature decreased when compared to the properties examined at room temperature. The biggest differences are observed for the sample Kobo-extruded to Ø8 mm, where the YS is lowered from  $244 \pm 7$ – $88 \pm 4$  MPa, and UTS from  $273 \pm 7$ – $109 \pm 1$ . The other two samples also show lower values of the YS and UTS, but not with such large differences. A mixed fracture is observed on the samples fractured at room temperature (Fig. 12a–d), while typical for superplastic phenomenon, elongated tips are visible in Fig. 12e–h.

### 4. Discussion

The purpose of this study was to determine whether it was feasible to extrude WE43 at high-deformation ratios without the need to preheat the initial billet. The results indicate that such extrusion is possible and produces positive outcomes for manufacturing WE43 wires, without incurring additional costs from heating during the processing of

Table 4

Mechanical properties of the conventionally and KoBo-extruded WE43 (YS - yield strength; UTS - ultimate tensile strength,  $A_f$  - elongation to fracture).

KoBo extruded WE43	YS (MPa)	UTS (MPa)	$A_f$ (%)
Room Temperature			
Ø 8 mm traditional extrusion	$84 \pm 31$	$165 \pm 5$	$17 \pm 4$
Ø 8 mm KoBo	$244 \pm 7$	$273 \pm 7$	$20 \pm 1$
Ø 6 mm KoBo	$198 \pm 3$	$256 \pm 1$	$20 \pm 2$
Ø 4 mm KoBo	$214 \pm 15$	$252 \pm 19$	$25 \pm 1$
Elevated temperature (300 °C)			
Ø 8 mm traditional extrusion	$114 \pm 10$	$139 \pm 2$	$56 \pm 9$
Ø 8 mm KoBo	$88 \pm 4$	$109 \pm 1$	$94 \pm 2$
Ø 6 mm KoBo	$145 \pm 5$	$154 \pm 5$	$45 \pm 3$
Ø 4 mm KoBo	$116 \pm 13$	$134 \pm 13$	$78 \pm 17$

hexagonal structures. This is particularly advantageous in the medical implant industry where ultra-fine-grained WE43 is desirable because of its high strength and corrosion resistance [37].

The results show that among two different methods of extrusion at the same extrusion ratio, a better corrosion performance is observed with the KoBo-extruded sample (Ø8 mm,  $R_1$  5:1). The main factor that improves its corrosion performance is the increased grain refinement, which leads to a more uniform potentials distribution between the anodic grain boundaries and the cathodic grain interiors. However, in our opinion, it is not the only reason for the increase in the corrosion resistance of this alloy. To some extent the corrosion resistance may be controlled by the texture intensity; in our case, a lower texture intensity was measured for the KoBo-extruded sample, and it would affect the more uniform spatial distribution of the anodic and cathodic potentials on the surface of the alloys. In the conventionally extruded WE43, more rapid corrosion reactions could also be supported by the randomly distributed textural components, which in turn contribute a great deal to the surface energy, increasing the corrosion rate of the alloy [38–40].

Having in mind that KoBo enables a microstructure refinement resulting in a better corrosion resistance of the WE43 when compared to the conventional extrusion, during the next step, we investigated whether the corrosion resistance of the WE43 might be improved further by processing at higher extrusion ratios than  $R_1$  5:1. The KoBo performed better at higher extrusion ratios due to the grain refinement, but it did not improve the corrosion resistance of the alloys. This contradicts the published data, where authors showed that SPD methods improve the corrosion and mechanical properties of WE43 [8,41–43] and other Mg alloys [43–45]. In our case, the alloys with the more refined grains actively corroded in the analyzed medium, which is related to the massive plastic strain imposed during KoBo, confirmed by the high density of tangled dislocations. Grain boundaries are generally the initiation sites for corrosion; the higher number of grain boundaries, the more corrosion initiation sites formed. In this case the corrosive reactions was also enhanced by the high density of dislocations. It seems that in the case of the extrusion ratios of  $R_2$  7:1 and  $R_3$  10:1 this factor overwhelmed the role of the grain size and the textural components in those alloys, which agrees with the observations made by Zhang et al. [46]. KoBo is a specific extrusion method during which too high a deformation ratio causes the accumulation of a higher deformation energy, leading to a higher density of dislocations [20].

It is worth mentioning that bright, coarse precipitates observed during the SEM inspection are not corrosively active. Localized corrosion, in this case, can start either at the interface of the Mg matrix/grain boundaries or tangled dislocations or on the Mg matrix/double precipitates and eventually the Mg matrix/tiny triple precipitates. It is obvious that Mg in an aqueous solution is much lower than that of hydrogen and therefore forms a galvanic reaction with most metals [47].

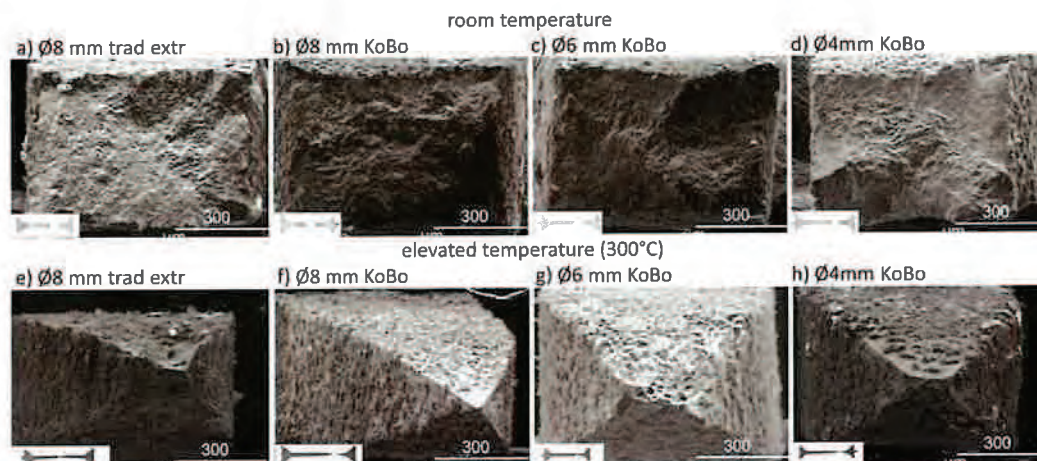


Fig. 12. Macro images and fracture characterization after tensile tests performed for WE43 conventionally extruded to Ø8 mm, and KoBo extruded to Ø8 mm, Ø6 mm and Ø4 mm at room temperature (a–d) and at 300 °C (e–h).

Several authors showed that the micro-galvanic effect between Mg and  $Mg_{24}Y_5$  or  $Mg_{41}Nd_5$  does not reduce the corrosion of WE43 because of their similar electrode potentials to Mg [48] and a capability to promote oxide-layer formation [47]. Since the specific potential of tiny triple precipitates, to the best of our knowledge, is unknown, it should be investigated further in the future. The corrosion mechanism is very complex and all the mentioned parameters play their role in the corrosion process. It is extremely difficult to completely isolate the effect of grain size on the corrosion resistance from other metallurgical parameters such as texture, the effect of precipitates or the dislocation density.

The mechanical properties of the WE43 investigated in this work are greatly influenced by the characteristic Mg-Nd-Y precipitate phases. The samples after KoBo exhibited better mechanical properties at room temperature than the conventionally extruded material, resulting from the precipitation of triple phases with a chemical composition of Mg-Y-Nd. It should be noted that during KoBo extrusion, the temperature inside the extruded material rises, creating the conditions for tiny triple phases of precipitation. There are four types of strengthening precipitate phases in Mg-Y-Nd alloys:  $\beta''$ ,  $\beta'$ ,  $\beta_1$  and equilibrium  $\beta$  [27]. Unfortunately, due to the scale of the precipitates, we were not able to determine which of the tiny precipitates were formed in the alloys. Our observations only suggest that due to the globular form observed during TEM, it might be identified with  $\beta'$  having a stoichiometry of  $Mg_{12}NdY$  [49]. Regardless of the stoichiometry, those tiny precipitates have been observed to be responsible for the strengthening effect in WE43 [50]. The triple precipitates are not thermally stable; therefore at 300 °C they solutionized, resulting in a decline in the mechanical properties of the KoBo-extruded samples. The same effect was previously noted by Li et al. [28]. The most significant decline of YS and UTS at 300 °C was further observed for the sample that was KoBo extruded to 8 mm. For the other KoBo samples, there is an evident precipitation tendency at 175 °C (peak A, Fig. 8). Such precipitation creates a barrier to dislocation slip or even helps to prevent creep, which restricts the general decline of TYS and UTS. The mechanical properties of the conventionally extruded material remained at the same level.

## 5. Conclusions

The microstructures, corrosion and mechanical properties of the WE43 alloy after conventional extrusion and extrusion with an oscillating die without preheating of the initial billet were investigated. The results are summarized as follows:

- KoBo extrusion without preheating the billet can achieve high deformation ratios and grain refinement in a WE43 alloy, but it can also cause the precipitation of small triple phases due to the temperature rise.
- KoBo extrusion at a ratio of  $R_1$  5:1 improves the corrosion behavior due to grain refinement and texture intensity. However, at higher ratios of  $R_2$  7:1 and  $R_3$  10:1, the plastic strain overwhelms the role of grain size and texture components, causing a decline in the corrosion performance.
- In the KoBo-extruded material, the triple Mg-Nd-Y precipitates have a strengthening effect. However, at 300 °C, the mechanical properties decrease due to the solutioning of the precipitates.

## CRedit authorship contribution statement

**Anna Dobkowska:** Conceptualization, Methodology, Investigation, Writing – original draft, Writing – review & editing. **Aleksandra Zielinska:** Investigation. **Irena Paulin:** Investigation, Writing – original draft. **Črtomir Donik:** Investigation, Formal analysis. **Milena Koralničnik:** Investigation. **Bogusława Adamczyk – Cieślak:** Investigation. **Monika Wiczorek:** Investigation. **Dariusz Kuc:** Resources. **Jiri Kubasek:** Investigation, Formal analysis. **Tomasz Mikuszewski:** Resources. **Matjaž Godec:** Funding acquisition. **Jarosław Mizera:** Funding acquisition.

## Declaration of Competing Interest

The authors declare that they have no known competing financial interests or personal relationships that could have appeared to influence the work reported in this paper.

## Data Availability

Data will be made available on request.

## Acknowledgements

This work was financially supported by the Slovenian Research and Innovation Agency (Project No. L2-3164 and core funding No. P2-0132) and by the Czech Science Foundation (Project no. GA22-22248S).

## References

- [1] B. Milkereit, L. Burgschat, R.H. Kemsies, A. Springer, C. Schick, O. Kessler, In situ differential scanning calorimetry analysis of dissolution and precipitation kinetics in Mg-Y-RE alloy WE43, *J. Magnes. Alloy*, 7 (2019) 1–14, <https://doi.org/10.1016/j.jma.2019.01.002>.
- [2] R.K. Sabat, P.K. Samal, M. Ahamed S, Effect of strain path on the evolution of microstructure, texture and tensile properties of WE43 alloy, *Mater. Sci. Eng. A*, 715 (2018) 348–358, <https://doi.org/10.1016/j.msea.2018.01.018>.
- [3] J. Liu, D. Bian, Y. Zheng, X. Chu, Y. Lin, M. Wang, Z. Lin, M. Li, Y. Zhang, S. Guan, Comparative in vitro study on binary Mg-RE (Sc, Y, La, Ce, Pr, Nd, Sm, Eu, Gd, Tb, Dy, Ho, Er, Tm, Yb and Lu) alloy systems, *Acta Biomater.* 102 (2020) 508–528, <https://doi.org/10.1016/j.actbio.2019.11.013>.
- [4] D. Dvorský, J. Kubásek, K. Hosová, M. Cavojský, D. Vojtěch, Microstructure, mechanical, corrosion, and ignition properties of WE43 alloy prepared by different processes, *Metals* 11 (2021) 728, <https://doi.org/10.3390/met11050728>.
- [5] C. Yang, N. Gupta, H. Ding, C. Xiang, Effect of microstructure on corrosion behavior of we43 magnesium alloy in as cast and heat-treated conditions, *Metals* 10 (2020) 1–13, <https://doi.org/10.3390/met10111552>.
- [6] B. Feng, G. Liu, P. Yang, S. Huang, D. Qi, P. Chen, C. Wang, J. Du, S. Zhang, J. Liu, Different role of second phase in the micro-galvanic corrosion of WE43 Mg alloy in NaCl and Na<sub>2</sub>SO<sub>4</sub> solution, *J. Magnes. Alloy*, (2021), <https://doi.org/10.1016/j.jma.2020.12.013>.
- [7] G. Ben-Hamu, D. Eliezer, K.S. Shin, S. Cohen, The relation between microstructure and corrosion behavior of Mg-Y-RE-Zr alloys, *J. Alloy. Compd.* 431 (2007) 269–276, <https://doi.org/10.1016/j.jallcom.2006.05.075>.
- [8] A.R. Eivani, M. Mehdiade, S. Chabok, J. Zhou, Applying multi-pass friction stir processing to refine the microstructure and enhance the strength, ductility and corrosion resistance of WE43 magnesium alloy, *J. Mater. Res. Technol.* 12 (2021) 1946–1957, <https://doi.org/10.1016/j.jmrt.2021.03.021>.
- [9] J. Soderlind, M. Cibova, R. Schaublin, S. Risbud, J.F. Löffler, Towards refining microstructures of biodegradable magnesium alloy WE43 by spark plasma sintering, *Acta Biomater.* 98 (2019) 67–80, <https://doi.org/10.1016/j.actbio.2019.06.045>.
- [10] G. Liu, J. Xu, B. Feng, J. Liu, D. Qi, W. Huang, P. Yang, S. Zhang, Comparison of corrosion performance of extruded and forged WE43 Mg alloy, *Materials* 15 (2022), <https://doi.org/10.3390/ma15051622>.
- [11] Z. Chen, S. Daly, Automated identification of deformation twin systems in Mg WE43 from SEM DIC, *Mater. Charact.* 169 (2020), 110628, <https://doi.org/10.1016/j.matchar.2020.110628>.
- [12] S.V. Dobatkin, E.A. Lukyanova, N.S. Martynenko, N.Y. Anisimova, M. V. Kiselevskiy, M.V. Gorshenkov, N.Y. Yurchenko, G.J. Raab, V.S. Yusupov, N. Birbilis, G.A. Salishchev, Y.Z. Estrin, Strength, corrosion resistance, and biocompatibility of ultrafine-grained Mg alloys after different modes of severe plastic deformation, *IOP Conf. Ser. Mater. Sci. Eng.* 194 (2017), <https://doi.org/10.1088/1757-899X/194/1/012004>.
- [13] Y.H. Kang, X.X. Wang, N. Zhang, H. Yan, R.S. Chen, Effect of pre-deformation on microstructure and mechanical properties of WE43 magnesium alloy, *Mater. Sci. Eng. A*, 689 (2017) 435–445, <https://doi.org/10.1016/j.msea.2017.02.082>.
- [14] A. Salandari-Rabori, A. Zarei-Hanzaki, S.M. Fatemi, M. Ghambari, M. Moghaddam, Microstructure and superior mechanical properties of a multi-axially forged WE magnesium alloy, *J. Alloy. Compd.* 693 (2017) 406–413, <https://doi.org/10.1016/j.jallcom.2016.09.198>.
- [15] S.K. Panigrahi, W. Yuan, R.S. Mishra, R. DeLorme, B. Davis, R.A. Howell, K. Cho, A study on the combined effect of forging and aging in Mg-Y-RE alloy, *Mater. Sci. Eng. A*, 530 (2011) 28–35, <https://doi.org/10.1016/j.msea.2011.08.065>.
- [16] J.J. Bhattacharyya, F. Wang, P.J. McQuade, S.R. Agnew, Deformation and fracture behavior of Mg alloy, WE43, after various aging heat treatments, *Mater. Sci. Eng. A*, 705 (2017) 79–88, <https://doi.org/10.1016/j.msea.2017.08.067>.
- [17] I. Bednarczyk, D. Kuc, The Influence of the Deformation Method on the Microstructure and Properties of Magnesium Alloy Mg-Y-RE-Zr, *Materials* 15 (2022), <https://doi.org/10.3390/ma15062017>.
- [18] A. Dobkowska, B. Adamczyk – Cieślak, M. Koralnik, W. Chromiński, J. Kubasek, J. Cifci, D. Kuc, J. Mizera, Corrosion behavior of fine-grained Mg-7.5Li-3Al-1Zn fabricated by extrusion with a forward-backward rotating die (KoBo), *J. Magnes. Alloy*, (2021), <https://doi.org/10.1016/j.jma.2021.08.020>.
- [19] A. Dobkowska, M. Koralnik, B. Adamczyk-Cieślak, D. Kuc, W. Chromiński, J. Kubasek, J. Mizera, The effect of extrusion ratio on the corrosion resistance of ultrafine-grained Mg-4Li-3Al-Zn alloy deformed using extrusion with a forward-backward oscillating die, *J. Mater. Eng. Perform.* (2022), <https://doi.org/10.1007/s11665-022-06895-1>.
- [20] A. Dobkowska, B. Adamczyk-Cieślak, M. Chlewicka, A. Towarek, A. Zielińska, M. Koralnik, D. Kuc, J. Mizera, Evolution of microstructure dependent corrosion properties of ultrafine AZ31 under conditions of extrusion with a forward backward oscillating die, *J. Mater. Res. Technol.* 18 (2022) 4486–4496, <https://doi.org/10.1016/j.jmrt.2022.04.131>.
- [21] A. Gusak, M. Danielewski, A. Korbel, M. Bochniak, N. Storozhuk, Elementary model of severe plastic deformation by KoBo process, *J. Appl. Phys.* 115 (2014), <https://doi.org/10.1063/1.4861870>.
- [22] R.M. Molak, K. Paradowski, T. Brynk, L. Ciupinski, Z. Pakielna, K.J. Kurzydowski, Measurement of mechanical properties in a 316L stainless steel welded joint, *Int. J. Press. Vessel. Pip.* 86 (2009) 43–47, [https://doi.org/10.1016/j.jvpp.2008.11.002](https://doi.org/10.1016/j.jjvpp.2008.11.002).
- [23] EN ISO, Metallic materials - Tensile testing - Part 1: Method of test at room temperature, 2020, <http://sklep.pkn.pl/pn-en-iso-6892-1-2016-09e.html>.
- [24] P. Minárik, J. Veselý, R. Král, J. Bohlen, J. Kubásek, M. Janeček, J. Stráská, Exceptional mechanical properties of ultra-fine grain Mg-4Y-3RE alloy processed by ECAP, *Mater. Sci. Eng. A*, 708 (2017) 193–198, <https://doi.org/10.1016/j.msea.2017.09.106>.
- [25] S.M. Zhu, J.F. Nie, M.A. Gibson, M.A. Easton, On the unexpected formation of rare earth hydrides in magnesium-rare earth casting alloys, *Scr. Mater.* 77 (2014) 21–24, <https://doi.org/10.1016/j.scriptamat.2014.01.007>.
- [26] J.F. Nie, B.C. Muddle, Precipitation in magnesium alloy WE54 during isothermal ageing at 250°C, *Scr. Mater.* 40 (1999) 1089–1094, [https://doi.org/10.1016/S1359-6462\(99\)00084-6](https://doi.org/10.1016/S1359-6462(99)00084-6).
- [27] J.F. Nie, B.C. Muddle, Characterisation of strengthening precipitate phases in a Mg-Y-Nd alloy, *Acta Mater.* 48 (2000) 1691–1703, [https://doi.org/10.1016/S1359-6454\(00\)00013-6](https://doi.org/10.1016/S1359-6454(00)00013-6).
- [28] H. Li, F. Lv, X. Liang, Y. Qi, Z. Zhu, K. Zhang, Effect of heat treatment on microstructures and mechanical properties of a cast Mg-Y-Nd-Zr alloy, *Mater. Sci. Eng. A*, 667 (2016) 409–416, <https://doi.org/10.1016/j.msea.2016.05.014>.
- [29] L. Rogal, G. Garzel, Semi-solid state mixing of Mg-Zn-RE alloys—microstructure and mechanical properties, *J. Mater. Process. Technol.* 264 (2019) 352–365, <https://doi.org/10.1016/j.jmatprotec.2018.09.012>.
- [30] H.F. Sun, C.J. Li, W. Bin Fang, Evolution of microstructure and mechanical properties of Mg-3.0Zn-0.2Ca-0.5Y alloy by extrusion at various temperatures, *J. Mater. Process. Technol.* 229 (2016) 633–640, <https://doi.org/10.1016/j.jmatprotec.2015.10.021>.
- [31] Y. Zhao, G. Wu, Q. Lu, J. Wu, R. Xu, K.W.K. Yeung, P.K. Chu, Improved surface corrosion resistance of WE43 magnesium alloy by dual titanium and oxygen ion implantation, *Thin Solid Films* 529 (2013) 407–411, <https://doi.org/10.1016/j.tsf.2012.05.046>.
- [32] B. Hadzima, M. Mhaede, F. Pastorek, Electrochemical characteristics of calcium-phosphatized AZ31 magnesium alloy in 0.9% NaCl solution, *J. Mater. Sci. Mater. Med.* 25 (2014) 1227–1237, <https://doi.org/10.1007/s10856-014-5161-0>.
- [33] F. Cao, Z. Shi, J. Hofstetter, P.J. Uggowitzer, G. Song, M. Liu, A. Atrens, Corrosion of ultra-high-purity Mg in 3.5% NaCl solution saturated with Mg(OH)<sub>2</sub>, *Corros. Sci.* (2013), <https://doi.org/10.1016/j.corsci.2013.05.018>.
- [34] M.I. James, G. Wu, Y. Zhao, D.R. McKenzie, M.M.M. Bilek, P.K. Chu, Electrochemical corrosion behavior of biodegradable Mg-Y-RE and Mg-Zn-Zr alloys in Ringer's solution and simulated body fluid, *Corros. Sci.* 91 (2015) 160–184, <https://doi.org/10.1016/j.corsci.2014.11.015>.
- [35] F. Cao, Z. Shi, G.L. Song, M. Liu, A. Atrens, Corrosion behaviour in salt spray and in 3.5% NaCl solution saturated with Mg(OH)<sub>2</sub> of as-cast and solution heat-treated binary Mg-X alloys: X=Mn, Sn, Ca, Zn, Al, Zr, Si, Sr, *Corros. Sci.* (2013), <https://doi.org/10.1016/j.corsci.2013.06.030>.
- [36] Y. Song, D. Shan, R. Chen, E.-H. Han, Corrosion characterization of Mg-8Li alloy in NaCl solution, *Corros. Sci.* 51 (2009) 1087–1094, <https://doi.org/10.1016/j.corsci.2009.03.011>.
- [37] W. Ali, M. Li, L. Tillmann, T. Mayer, C. González, J. Llorca, A. Kopp, Bioabsorbable WE43 Mg alloy wires modified by continuous plasma-electrolytic oxidation for implant applications. Part I: Processing, microstructure and mechanical properties, *Biomater. Adv.* 146 (2023), <https://doi.org/10.1016/j.bioadv.2023.213314>.
- [38] R. Xin, Y. Luo, A. Zuo, J. Gao, Q. Liu, Texture effect on corrosion behavior of AZ31 Mg alloy in simulated physiological environment, *Mater. Lett.* (2012), <https://doi.org/10.1016/j.matlet.2011.11.032>.
- [39] R. Xin, B. Li, L. Li, Q. Liu, Influence of texture on corrosion rate of AZ31 Mg alloy in 3.5wt% NaCl, *Mater. Des.* 32 (2011) 4548–4552, <https://doi.org/10.1016/j.matsdes.2011.04.031>.
- [40] B. Jiang, Q. Xiang, A. Atrens, J. Song, F. Pan, Influence of crystallographic texture and grain size on the corrosion behaviour of as-extruded Mg alloy AZ31 sheets, *Corros. Sci.* 126 (2017) 374–380, <https://doi.org/10.1016/j.corsci.2017.08.004>.
- [41] Y. Zhang, M. Gao, I.P. Etim, L. Tan, K. Yang, Optimising the torsional properties and corrosion resistance of biodegradable WE43 Mg alloy by ECAP and subsequent ageing, *Mater. Technol.* 35 (2020) 402–410, <https://doi.org/10.1080/10667857.2019.1688539>.
- [42] A. Maqbool, N.F. Lone, T. Ahmad, N.Z. Khan, A.N. Siddiquee, Effect of hybrid reinforcement and number of passes on microstructure, mechanical and corrosion behavior of WE43 Mg alloy based metal matrix composite, *J. Manuf. Process.* 89 (2023) 170–181, <https://doi.org/10.1016/j.jmapro.2023.01.070>.
- [43] A. Bahmani, M. Lotfipour, M. Taghizadeh, W.J. Kim, Corrosion behavior of severely plastically deformed Mg and Mg alloys, *J. Magnes. Alloy*, 10 (2022) 2607–2648, <https://doi.org/10.1016/j.jma.2022.09.007>.
- [44] T. Zhang, Z. Ji, S. Wu, Effect of extrusion ratio on mechanical and corrosion properties of AZ31B alloys prepared by a solid recycling process, *Mater. Des.* 32 (2011) 2742–2748, <https://doi.org/10.1016/j.matsdes.2011.01.012>.
- [45] J. Vrátná, B. Hadzima, M. Bukovina, M. Janeček, Room temperature corrosion properties of AZ31 magnesium alloy processed by extrusion and equal channel angular pressing, *J. Mater. Sci.* 48 (2013) 4510–4516, <https://doi.org/10.1007/s10853-013-7173-4>.
- [46] T. Zhang, Y. Shao, G. Meng, Z. Cui, F. Wang, Corrosion of hot extrusion AZ91 magnesium alloy: I-relation between the microstructure and corrosion behavior, *Corros. Sci.* 53 (2011) 1960–1968, <https://doi.org/10.1016/j.corsci.2011.02.015>.
- [47] J. Liu, B. Yin, F. Song, B. Liu, B. Peng, P. Wen, Y. Tian, Y. Zheng, X. Ma, C. Wang, Improving corrosion resistance of additively manufactured WE43 magnesium alloy by high temperature oxidation for biodegradable applications, *J. Magnes. Alloy*, (2022), <https://doi.org/10.1016/j.jma.2022.08.009>.
- [48] G.S. Pereira, G.Y. Koga, J.A. Avila, L.M. Bittencourt, F. Fernandez, M.H. Miyazaki, W.L. Botta, W.W. Bose Filho, Corrosion resistance of WE43 Mg alloy in sodium

- chloride solution, *Mater. Chem. Phys.* 272 (2021). <https://doi.org/10.1016/j.matchemphys.2021.124930>.
- [49] J.-F. Nie, Precipitation and hardening in magnesium alloys, *Metall. Mater. Trans. A.* 43 (2012), <https://doi.org/10.1007/s11661-012-1217-2>.
- [50] R. Xin, L. Li, K. Zeng, B. Song, Q. Liu, Structural examination of aging precipitation in a Mg-Y-Nd alloy at different temperatures, *Mater. Charact.* 62 (2011) 535–539, <https://doi.org/10.1016/j.matchar.2011.03.007>.



Article

# On the Possibility of the Deformation of Mg and Alloys Without Preheating of Initial Billets: Understanding Their Corrosion Performance via Electrochemical Tests

Anna Dobkowska <sup>1,\*</sup> and Jiri Kubasek <sup>2,\*</sup>

<sup>1</sup> Faculty of Materials Science and Engineering, Warsaw University of Technology, Woloska, 02-507 Warsaw, Poland

<sup>2</sup> Department of Metals and Corrosion Engineering, University of Chemistry and Technology, Technicka 5, 168 28 Prague 6, Czech Republic

\* Correspondence: anna.dobkowska@pw.edu.pl (A.D.); jiri.kubasek@vscht.cz (J.K.)

**Abstract:** Due to limited slip systems activated at room temperature, the plastic deformation of Mg and its alloys without any preheating of initial billets is significantly limited. To overcome those issues, new methods of severe plastic deformation are discovered and developed. One such example is extrusion with an oscillating die, called KoBo. This method, due to the oscillations of reversible die located at the end of extruded, introduces material into the plastic flow, and thus, enables deformation without preheating of the initial billets of metals that are hard to deform. Such solution is important from an industrial point of view and may lead to serious savings and reduction in carbon dioxide emission to the atmosphere. Therefore, this paper focuses on the possibility of KoBo extrusion of hcp-structured Mg alloys with different chemical compositions and includes comparison of their corrosion resistance using short-term electrochemical tests. In order to have a broad view of the problem presented, we compared the electrochemical behavior of the following groups of Mg materials: pure Mg, Mg-Al-Zn, Mg-Li, and Mg-Y-RE. It was stated that the KoBo method performed at room temperature improves the corrosion resistance of pure Mg when compared to the initial billet and the alloys which belong to the Mg-Al-Zn, Mg-Li, and Mg-Y-RE series. The presented study shows that different corrosion trends are observed for traditionally deformed alloys, and they significantly vary from nascent developments, such as KoBo extrusion. Therefore, it is crucial to widely study those methods because it may be a path leading to long-lasting solution to the formability limitations of Mg-based metallic systems.

**Keywords:** magnesium alloys; plastic deformation; microstructure; corrosion



**Citation:** Dobkowska, A.; Kubasek, J. On the Possibility of the Deformation of Mg and Alloys Without Preheating of Initial Billets: Understanding Their Corrosion Performance via Electrochemical Tests. *Materials* **2024**, *17*, 6182. <https://doi.org/10.3390/ma17246182>

Academic Editor: Xiaogang Li

Received: 12 November 2024

Revised: 3 December 2024

Accepted: 16 December 2024

Published: 18 December 2024



**Copyright:** © 2024 by the authors. Licensee MDPI, Basel, Switzerland. This article is an open access article distributed under the terms and conditions of the Creative Commons Attribution (CC BY) license (<https://creativecommons.org/licenses/by/4.0/>).

## 1. Introduction

The most appropriate way to describe the role of grain size in the corrosion behavior of materials after deformation is to analyze pure metals to avoid the effect of second phases and their anodic or cathodic contribution to corrosion mechanisms. Pure Mg has a standard potential of  $-2.373$  V vs. SHE, while its free corrosion potential is more positive (toward  $-1.6$  V), indicating that a surface layer is present on the pure Mg, limiting its contact with the solution [1,2]. This corrosion layer is not fully protective, but limits corrosion reactions on the substrate of Mg metal to some extent. To date, many researchers focused on finding clear relationship between grain size and corrosion behavior for Mg alloys [3–6]. As is commonly known, grain size is a predominant factor affecting corrosion resistance, and it might be expected that a universal law describing it would exist. Unfortunately, this is impossible for plastically deformed polycrystalline materials because grain refinement itself is also related to the dislocation density and distribution, as well as the internal strain induced during deformation [7]. Another important factor is the tremendous role of an intermetallic phase,  $\beta$ -Mg<sub>17</sub>Al<sub>12</sub>, in mechanical and corrosion properties, which

has already been described [8–10]. When AZ61 (6 wt.% Al, 1 wt.% Zn) was subjected to ECAP, precipitation strengthening was observed [11]. The large proportion of  $\beta$ -Mg<sub>17</sub>Al<sub>12</sub> hindered dislocation movement, leading to an increased dislocation density, thus causing work hardening. Nevertheless, such a large amount of this type of intermetallic phase may promote corrosion reactions by forming microgalvanic reactions with the Mg matrix [12]. From the opposite point of view,  $\beta$ -Mg<sub>17</sub>Al<sub>12</sub> may form a barrier against spreading corrosion reactions [13–15]. Therefore, the dual role of  $\beta$ -Mg<sub>17</sub>Al<sub>12</sub> in the corrosion resistance of AZ-type alloys needs to be further examined. When it comes to dual-phase structured Mg-Li alloys, two crucial factors dominating their corrosion performance have been recently described. Zeng et al. [16] suggested that Li leads to the formation of a thin film, which may play a protective role on the surface. It was also proposed that corrosion of the dual-phase structured AZ31+7.5Li traditionally extruded at 350 °C is a result of microgalvanic interaction between the  $\alpha$ (Mg) and  $\beta$ (Li) phases and their relative distribution [17]. The more equal the fractions of  $\alpha$ (Mg) and  $\beta$ (Li), the less intense were the resulting corrosion reactions. Besides the mentioned factors, texture intensity also affects the corrosion behavior especially in alloys containing Y and RE as alloying elements.

All of the above mentioned factors are typical for Mg alloys plastically deformed at high temperature. Lastly, our research groups proved that Mg and its alloys may be formed without preheating of the initial billet which is very unusual for hcp-structured metals [18]. The method used for the plastic deformation of Mg alloys at room temperature is a modified extrusion with an oscillating die located at the end of extruded (as described in [19], called KoBo. Since Mg and its alloys are characterized by poor corrosion characteristics, which limit their widespread use in industrial applications, it is of crucial importance to carry out a systematic study about the factors affecting their corrosion after extrusion using nascent developments, such as KoBo, which may lead to many economic benefits in industrial applications (elimination of furnaces from production routes, reduction in gas emission, faster deformation processes, etc.). Therefore, the main aim of this paper is to select and describe the predominant factors influencing various groups of KoBo-deformed Mg alloys and to specify the most corrosion-resistant group of Mg alloys after KoBo extrusion based on fast electrochemical corrosion tests.

## 2. Materials and Methods

The electrochemical behavior indicating corrosion resistance of various Mg alloys processed using extrusion with an oscillating die (KoBo) without preheating of the initial billet is investigated and compared. The materials for this research were selected based on our previous studies, where the corrosion resistance of pure Mg [20], AZ31 [21], AZ61 [22], AZ31+4Li [23], AZ31+7.5Li [24], and WE43 [25] extruded using KoBo at various extrusion ratios has been described. For this research, the alloys with the highest corrosion resistance analyzed in the previous studies have been chosen, and they are specified in Table 1.

**Table 1.** Selection of Mg materials in order to make a comparative analysis of their corrosion resistance.

Materials	Pure Mg	AZ31	AZ61	AZ31+4Li	AZ31+7.5Li	WE43
Extrusion ratio	7:1	10:1	7:1	10:1	10:1	5:1

The electrochemical measurements were performed in naturally aerated 0.01 M NaCl solution using a Gamry FAS1 600+ potentiostat equipped with three electrodes: platinum as the counter electrode, Ag/AgCl as the reference electrode, and the measured sample as the working electrode. The electrolyte was made up using analytical-grade reagents and distilled water. The samples were immersed for 1 h, and electrochemical impedance spectroscopy was performed over a frequency range of 0.01 Hz–10,000 Hz. Immediately afterward, potentiodynamic polarization tests were carried out over a range from 0.2 V below  $E_{OCP}$  to 1.0 V vs. Ref (a scan rate of 5 mV/s was used). At least three tests were performed for each alloy. The EIS and polarization curves were fitted using the Gamry Echem software

version 5.58. Corrosion damage was characterized after 1 h of immersion in 0.1 M NaCl. Before electrochemical tests, samples were polished using water-free diamond suspensions (3 and 1  $\mu\text{m}$ ). The morphology of corrosion damage was observed, after chemical removal of the corrosion products in aqueous  $\text{CrO}_3$  solution (4 min, 180 g/L  $\text{CrO}_3$ ), using a scanning electron microscope (SEM, Hitachi SU8000, Japan). Additionally, the corrosion rate of the materials was calculated using the hydrogen release method [26–29]. To ensure the reproducibility of the results, at least three specimens from each composition were tested.

### 3. Results

The evaluation of the open circuit potential ( $E_{\text{OCP}}$ ) of the investigated materials during 1 h of immersion in 0.1 M NaCl is presented in Figure 1. The highest values of the  $E_{\text{OCP}}$  were observed for AZ31 and AZ61, and their average values were  $-1.45$  V/Ref and  $-1.46$  V/Ref, respectively. The 4 and 7.5 wt.% of Li addition shifted the  $E_{\text{OCP}}$  toward negative values:  $-1.53$  V/Ref and  $-1.54$  V/Ref, respectively. The lowest values of  $E_{\text{OCP}}$  were observed for pure Mg and WE43:  $-1.56$  V/Ref and  $-1.65$  V/Ref, respectively. Inspection of the anodic branch of the polarization curves in Figure 2 determined the active dissolution of the AZ61, while the rest of the alloys underwent localized corrosion. A characteristic plateau was observed on the anodic branch of AZ31, WE43, pure Mg, AZ31+4Li, and AZ31+7.5Li, and a typical inflection point indicating the breakdown potential,  $E_b$ , was also noted (labeled by the red arrows in Figure 2). The difference between  $E_b$  and  $E_{\text{corr}}$  describes the resistivity to pitting corrosion,  $\Delta E$  [30,31]; the broader the difference, the higher the resistance to pitting. The numerical values of the resistivity to pitting are shown in Table 2. Undoubtedly, the highest pitting susceptibilities were in the cases of pure Mg and the alloys with Li addition. The most stable corrosion layers were formed on the AZ31 and WE43.

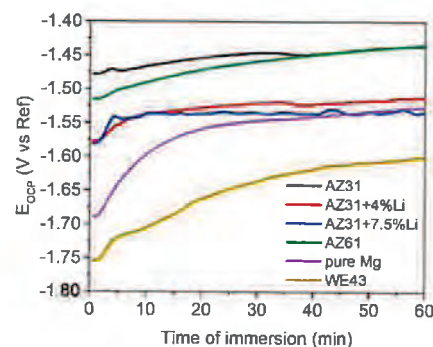


Figure 1. Open circuit potential ( $E_{\text{OCP}}$ ) evolution during 1 h of immersion in naturally aerated 0.1 M NaCl.

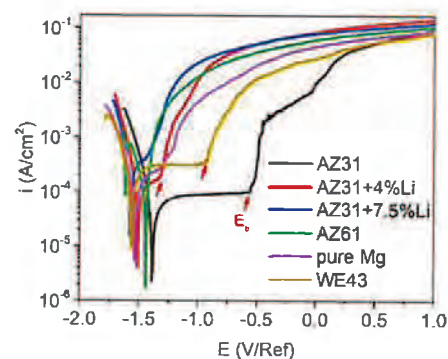


Figure 2. Potentiodynamic polarization curves recorded after 1 h of immersion in naturally aerated 0.1 M NaCl.

**Table 2.** The characteristic parameters calculated based on the extrapolation of linear polarization ( $E_{\text{corr}}$ —corrosion potential,  $E_b$ —breakdown potential).

Parameters	Pure Mg	AZ31	AZ61	AZ31+4Li	AZ31+7.5Li	WE43
$E_{\text{corr}}$ (V vs. Ref)	−1.54	−1.39	−1.44	−1.51	−1.58	−1.57
$E_b$ (V vs. Ref)	−1.34	−0.56	-	−1.33	−1.45	−0.94
$\Delta E$	0.20	0.83	-	0.18	0.13	0.63

The Nyquist plots recorded for the investigated materials after 1 h of immersion in naturally aerated 0.1 M NaCl are shown in Figure 3a, while corresponding Bode plots are depicted in Figure 3b. All samples exhibited two semicircles, corresponding to two time constants, with the exception of AZ31+7.5Li, where the small radius of the Nyquist plot and intense inductive loop may indicate strong localized corrosion and/or precipitation of corrosion products on the surface. The Nyquist plots for pure Mg, AZ31, AZ61, AZ31+4Li, and WE43 were composed of two semicircles registered at a high and medium frequency range. The first one was related to the charge transfer resistance at the double layer interface, while the second one corresponded to the corrosion products' layer [32,33]. The equivalent electrical circuits given in Figure 3c,d were used to fit data for these samples. Here,  $R_s$  is the solution resistance;  $R_{ct}$  is the charge transfer resistance, and the corresponding capacitance is defined by the constant phase element ( $CPE_{ct}$ ). The  $R_f$  and  $CPE_f$  variables stand for the resistance of the corrosion products' layer. In the given equivalent electrical circuits, CPE is used to compensate for the nonuniformity of the corrosion system [34]. The results from the fitting are depicted in Table 2. The equivalent electrical circuits given in Figure 3d were used to fit the data recorded for AZ31+7.5Li. They were composed of a capacitive loop described by  $R_{ct}$  and  $CPE_{ct}$  and an inductive loop defined by  $R_L$  and  $L$ , with the latter loop being most probably related to the initial stage of localized corrosion [35,36], although it can also be related to the precipitation of corrosion products. The behavior of the analyzed samples, with the exception of Mg-7.5Li, was very similar to each other in the analyzed medium and exhibited the presence of a protective film. The complex nature of the fitted data was supported by the corrosion rate calculated based on hydrogen release tests, Figure 4. Both the EIS results and estimated corrosion rates showed a similar tendency with respect to the corrosion behavior of the investigated materials. The least resistant was dual-structured AZ31+7.5Li, where strong dissolution of the alloy was observed. Its corrosion rate was found to be  $23.2 \pm 1.2$  mm/year. The rest of the materials were less active in the analyzed solution. The most resistant were AZ31 and AZ31+4Li, with corrosion rates of  $11.0 \pm 0.9$  mm/year and  $11.0 \pm 2.1$  mm/year, respectively. The higher standard deviation out of these two samples was observed for the alloy containing Li. These alloys exhibited the highest values of  $R_{CT}$  and  $R_f$ , suggesting that the most stable corrosion product layers are formed on their surfaces (Table 3). Less resistant than AZ31 and AZ31+4Li were AZ61, WE43, and pure Mg, and their corrosion rates were comparable to each other:  $16.0 \pm 2.2$ ,  $14.4 \pm 1.2$ , and  $16.0 \pm 1.1$  mm/year, respectively.

**Table 3.** Parameters fitted from EIS results using data shown in Figure 3.

Materials	$R_s$ ( $\Omega \cdot \text{cm}^2$ )	$R_{ct}$ ( $\Omega \cdot \text{cm}^2$ )	$CPE_{ct}$ ( $\mu\text{Ss}^n/\text{cm}^2$ )	$a_1$	$R_L$ ( $\Omega \cdot \text{cm}^2$ )	$L$ ( $\text{H} \cdot \text{cm}^2$ )	$R_f$ ( $\Omega \cdot \text{cm}^2$ )	$CPE_f$ ( $\mu\text{Ss}^n/\text{cm}^2$ )	$a_2$
Pure Mg	61	1242	0.000018	0.94	N/A	N/A	634	0.000840	0.84
AZ31	22	2266	0.000008	0.85	N/A	N/A	1420	0.000120	0.86
AZ61	10	1454	0.000019	0.94	N/A	N/A	1016	0.001688	0.72
AZ31+4Li	17	2357	0.000009	0.93	N/A	N/A	1603	0.000155	0.71
AZ31+7.5Li	17	183	0.000025	0.88	691	182	N/A	N/A	N/A
WE43	14	1201	0.000027	0.92	N/A	N/A	1294	0.001756	0.76

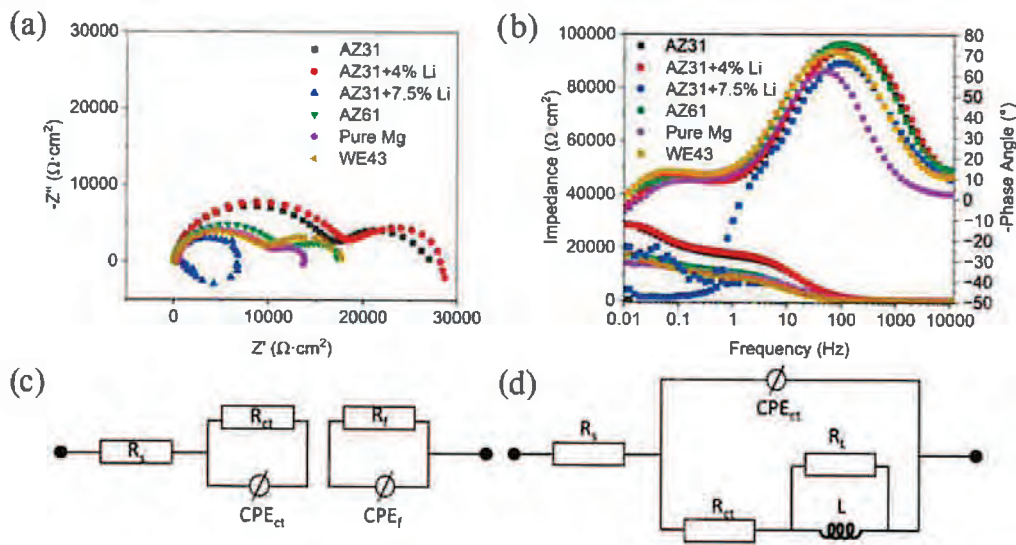


**Figure 3.** Electrochemical impedance spectroscopy (EIS) results recorded after 1 h of immersion in naturally aerated 0.1 M NaCl and presented in the form of (a) Nyquist plots, (b) Bode plots, (c) equivalent electrical circuit used for pure Mg, AZ31, AZ61, AZ31+4Li, and WE43 fitting, and (d) equivalent electrical circuit used for AZ31+7.5Li fitting.

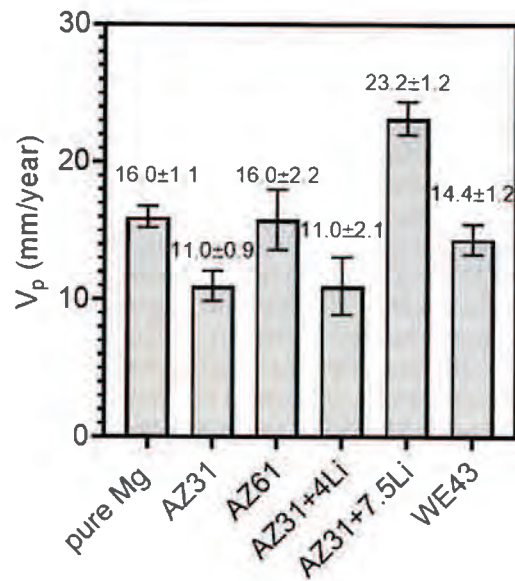


**Figure 4.** Corrosion rate calculated based on the hydrogen release method.

Figure 5a–f show the surface morphologies of the corroded samples after removing the corrosion products. Many small and round pits were observed on the surface of pure Mg (Figure 5a); in random locations, they propagated into the depth of the material (inset in Figure 5a). In the case of AZ31 (Figure 5b) and AZ61 (Figure 5c), besides small round pits, larger and deeper pitting holes interlinked with one another on the surface were observed. The pits propagated on the surface of AZ31 are as deep as those formed on pure Mg (inset in Figure 5b). As shown in the inset in Figure 5c, corrosion damage in triple points was formed on the AZ61. The surface of the AZ31 with Li was more damaged; however, the corrosion damage differed depending on the amount of Li present. On the surface of the single- $\alpha$ (Mg)-phase AZ31+4Li, corrosion in the form of threads proceeding along the

grain boundaries was observed (Figure 5d). The dual-phase structured alloy exhibited a different mode of degradation related to microgalvanic corrosion between the  $\alpha$ (Mg) and  $\beta$ (Li) phases (Figure 5e). This phenomenon is explained in detail in our previous study [24]. In the case of WE43, the corrosion mechanism propagated along the grain boundaries (Figure 5f). The corroded grain boundaries are depicted at higher magnification in the inset in Figure 5f.

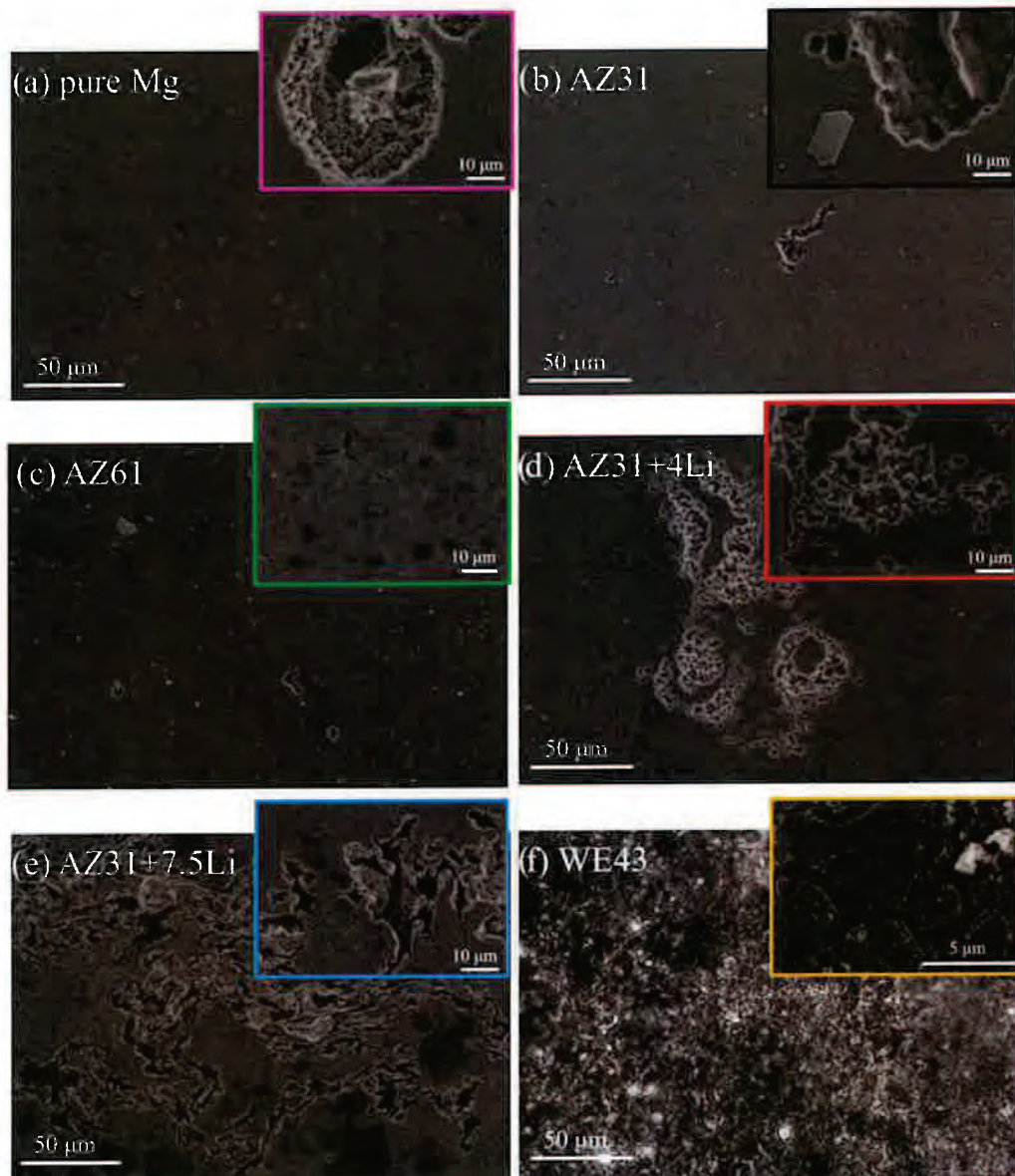


**Figure 5.** Corrosion damage characterization after chemical removal of corrosion products after 1 h of immersion in 0.1 M NaCl: (a) pure Mg, (b) AZ31, (c) AZ61, (d) AZ31+4Li, (e) AZ31+7.5Li, and (f) WE43.

#### 4. Discussion

The extrusion with an oscillating die (KoBo) method exhibits great potential for Mg alloy deformation without preheating of the initial billet. It may significantly reduce the

grain size and redistribute secondary phases in the microstructure. It is noteworthy that the grain refinement does not depend on the extrusion ratio, but on the intensity of dynamic recrystallization (DRX) triggered by the oscillations of the reversible die. As a result of this phenomenon, the corrosion resistance of Mg alloys changes in a nonlinear manner. Of course, the corrosion resistance of KoBo-extruded alloys is dependent on the alloy chemistry, but based on the data published so far, the predominant role seems to be played by grain size and dislocation distribution.

Based on the presented results of electrochemical behavior and hydrogen release, the corrosion resistance of the analyzed materials may be ordered as follows: AZ31 > AZ31+4Li >> WE43 > pure Mg > AZ61 >>> AZ31+7.5Li. The order of the corrosion resistance of each material were analyzed based on the detailed description of the microstructure presented in our previous works, and the results are shortly summarized in Table 4.

**Table 4.** Summary of the basic microstructural features characteristic for the investigated materials.

Material	Phase Structure	Grain Size ( $\mu\text{m}$ )	Second Phases	Grain Orientation	Ref.
Pure Mg	$\alpha(\text{Mg})$ phase	3.88 $\mu\text{m}$ ; uniformly distributed	N/A	(10 $\bar{1}$ 0) and (2110)	[21]
AZ31	$\alpha(\text{Mg})$ phase	4.38 $\mu\text{m}$ ; uniformly distributed	Coarse $\text{Al}_5\text{Mn}_8$	(10 $\bar{1}$ 0) and (2110) with some randomly present (0001)	[21]
AZ61	$\alpha(\text{Mg})$ phase	6.6 $\mu\text{m}$ uniformly distributed	Coarse $\text{Al}_5\text{Mn}_8$ and nano $\beta\text{-Mg}_{17}\text{Al}_{12}$ located at grain boundaries	(10 $\bar{1}$ 0) and (2110)	[22]
AZ31+4Li	$\alpha(\text{Mg})$ phase	3.24 $\mu\text{m}$ ; uniformly distributed	Coarse AlLi and $\beta\text{-Mg}_{17}\text{Al}_{12}$ (nano) distributed in the grain interiors	(10 $\bar{1}$ 0) and (2110)	[23]
AZ31+7.5Li	$\alpha(\text{Mg})+\beta(\text{Li})$	No EBSD data, based on SEM a few $\mu\text{m}$	Coarse AlLi and $\text{MgLi}_2\text{Al}$ with size around 1 $\mu\text{m}$ , $\beta\text{-Mg}_{17}\text{Al}_{12}$ (nano) distributed in the grain interiors	No EBSD data	[24]
WE43	$\alpha(\text{Mg})$ phase	3.3 $\mu\text{m}$ ; uniformly distributed	$\text{Mg}_{41}\text{Nd}_5$ , $\text{Mg}_{24}\text{Y}_5$ , $\text{Mg}_{12}\text{Nd}$ , and nano ternary Mg-Nd-Y	Random	[25]

As per results of this work, lower corrosion rate estimated via electrochemical measurements was observed for  $\alpha(\text{Mg})$  alloys than for dual-structured  $\alpha(\text{Mg})+\beta(\text{Li})$  alloys. The most resistant in the analyzed medium was AZ31. As shown in [21], it has a grain size of 4.38  $\mu\text{m}$  and a preferential orientation of the grain toward (10 $\bar{1}$ 0) and (2110). The Al fully dissolved in the solution, and no  $\beta\text{-Mg}_{17}\text{Al}_{12}$  was formed. Similar level of corrosion resistance was observed for the AZ31 alloyed with 4 wt.% of Li. In this case, nanosized  $\beta\text{-Mg}_{17}\text{Al}_{12}$  distributed in the grain interiors was observed, creating a barrier against spreading corrosion reactions caused by the Li in the alloy [23]. Lower corrosion resistance and also corrosion products being formed on the surface in some kind of “protective” layer, was characteristic for WE43, pure Mg, and AZ61. The presence of nanosized  $\beta\text{-Mg}_{17}\text{Al}_{12}$  at the grain boundaries promotes microgalvanic corrosion in AZ61, thus lowering its corrosion resistance when compared to AZ31 [22]. Surprisingly, pure Mg had a higher corrosion rate than AZ31. Since the grain sizes for pure Mg and AZ31 were similar, the factor favoring higher corrosion resistance lay in the crystallographic orientation of the grains formed in AZ31. In this case, besides grains oriented to (10 $\bar{1}$ 0) and (2110), grains with a (0001) orientation were present. In this relation, the grains with an (0001) orientation parallel to the corroded surface are more corrosion resistant than grains with orientations (10 $\bar{1}$ 0) and (2110) [37].

During KoBo, materials enters to the state of plastic flow, therefore the reversibly oscillating of the die at the end of the extruded enables deformation of Mg alloys. Simultaneously, the presence of the complex strain conditions formed as a result of the die oscillations resulted in the accumulation of high density of defects in the microstructure of the extruded material. This in turn led to the pile up of dislocations in the refined grains. As stated in [21], in the KoBo extruded AZ31 alloy, the main factors affecting corrosion resistance were dislocation density and its distribution. Consequently, despite the KoBo extrusion reducing grain size from a coarse to a micrometer scale, it did not improve the

corrosion resistance of the alloy. A similar situation was observed for the AZ61 [22,38]; however, strong microgalvanic reactions between  $\beta$ -Mg<sub>17</sub>Al<sub>12</sub> and the Mg matrix occurred, overwhelming the role of other microstructural components in its corrosion resistance [39]. WE43 has a completely different chemical composition than that of the other Mg alloys, and here, the predominant role in the corrosion mechanism may be caused by the presence of tiny precipitates located in this alloy [25], which has a corrosion resistance similar to AZ61 and pure Mg. Nevertheless, the role of small second phases must be further analyzed.

## 5. Conclusions

Based on the performed tests and reviewed data, the following may be concluded:

- KoBo extrusion enables the deformation of Mg and its alloys without preheating of the initial billet. The obtained materials are without cracking and reduce the diameter of the ingots significantly, resulting in the production of long elements, such as rods or wires. The next step of the KoBo improvement should be research on the possibility of thin-walled structure fabrication;
- KoBo extrusion improves the corrosion resistance of the initial ingots of Mg and its alloys; however, there is no clear relationship between grain refinement and corrosion resistance improvement, and smaller grain size does not always lead to higher corrosion resistance. The properties of the specific alloy must be treated as a separate case, since the intensity of the dynamic recrystallization is related to the extrusion ratio and strain induced by the reversible die;
- The corrosion resistance of the KoBo-extruded alloys depends mainly on the alloy chemistry and its microstructure; however, it is also dominated by the formation of stresses during extrusion with an oscillating die. Importantly, we do not have any clear information about the specific temperature inside the extruder. The effect of the internal heating resulting from the friction of the material and the extruder during processing should be further investigated;
- In the current research on magnesium alloys, the imperative issue of balancing the structural characteristics and mechanical properties of the alloys remains to be resolved. A reduction in the deformation temperature of Mg alloys will generate savings and reduce CO<sub>2</sub> gas emissions, which is crucial to ensure the sustainable growth of industry.

**Author Contributions:** Conceptualization, methodology, supervision, formal analysis, investigation, and writing—original draft preparation, A.D.; investigations, editing of the original draft, resources, and funding acquisition, J.K. All authors have read and agreed to the published version of the manuscript.

**Funding:** This research was partially funded by the Czech Science Foundation (GACR), project number 22-22248S.

**Institutional Review Board Statement:** Not applicable.

**Informed Consent Statement:** Not applicable.

**Data Availability Statement:** The original contributions presented in this study are included in the article. Further inquiries can be directed to the corresponding authors.

**Conflicts of Interest:** The authors declare no conflicts of interest.

## References

1. Atrens, A.; Song, G.L.; Cao, F.; Shi, Z.; Bowen, P.K. Advances in Mg Corrosion and Research Suggestions. *J. Magnes. Alloys* **2013**, *1*, 177–200. [CrossRef]
2. Atrens, A.; Song, G.L.; Liu, M.; Shi, Z.; Cao, F.; Dargusch, M.S. Review of Recent Developments in the Field of Magnesium Corrosion. *Adv. Eng. Mater.* **2015**, *17*, 400–453. [CrossRef]
3. Ralston, K.D.; Birbilis, N.; Davies, C.H.J. Revealing the Relationship between Grain Size and Corrosion Rate of Metals. *Scr. Mater.* **2010**, *63*, 1201–1204. [CrossRef]

4. Bahmani, A.; Arthanari, S.; Shin, K.S. Formulation of Corrosion Rate of Magnesium Alloys Using Microstructural Parameters. *J. Magnes. Alloys* **2020**, *8*, 134–149. [[CrossRef](#)]
5. Ben-Hamu, G.; Eliezer, D.; Shin, K.S.; Cohen, S. The Relation between Microstructure and Corrosion Behavior of Mg-Y-RE-Zr Alloys. *J. Alloys Compd.* **2007**, *431*, 269–276. [[CrossRef](#)]
6. Wang, L.; Shinohara, T.; Zhang, B.P. Influence of Chloride, Sulfate and Bicarbonate Anions on the Corrosion Behavior of AZ31 Magnesium Alloy. *J. Alloys Compd.* **2010**, *496*, 500–507. [[CrossRef](#)]
7. Miyamoto, H. Corrosion of Ultrafine Grained Materials by Severe Plastic Deformation, an Overview. *Mater. Trans.* **2016**, *57*, 559–572. [[CrossRef](#)]
8. Hoog, C.O.; Birbilis, N.; Estrin, Y. Corrosion of Pure Mg as a Function of Grain Size and Processing Route. *Adv. Eng. Mater.* **2008**, *10*, 579–582. [[CrossRef](#)]
9. Jiang, B.; Xiang, Q.; Atrens, A.; Song, J.; Pan, F. Influence of Crystallographic Texture and Grain Size on the Corrosion Behaviour of As-Extruded Mg Alloy AZ31 Sheets. *Corros. Sci.* **2017**, *126*, 374–380. [[CrossRef](#)]
10. Gollapudi, S. Grain Size Distribution Effects on the Corrosion Behaviour of Materials. *Corros. Sci.* **2012**, *62*, 90–94. [[CrossRef](#)]
11. Shan, Z.; Yang, J.; Fan, J.; Zhang, H.; Zhang, Q.; Wu, Y.; Dong, H. Microstructure Evolution and Mechanical Properties of an AZ61 Alloy Processed with TS-ECAP and EPT. *Mater. Sci. Eng. A* **2020**, *780*, 139195. [[CrossRef](#)]
12. Atrens, A.; Liu, M.; Zainal Abidin, N.I. Corrosion Mechanism Applicable to Biodegradable Magnesium Implants. *Mater. Sci. Eng. B Solid-State Mater. Adv. Technol.* **2011**, *176*, 1609–1636. [[CrossRef](#)]
13. Lunder, O.; Lein, J.E.; Aune, T.K.; Nisancioglu, K. Role of Mg17Al12 phase in the Corrosion of Mg Alloy AZ91. *Corrosion* **1989**, *45*, 741–748. [[CrossRef](#)]
14. Pardo, A.; Merino, M.C.; Coy, A.E.; Viejo, F.; Arrabal, R.; Feliú, S. Influence of Microstructure and Composition on the Corrosion Behaviour of Mg/Al Alloys in Chloride Media. *Electrochim. Acta* **2008**, *53*, 7890–7902. [[CrossRef](#)]
15. Ubeda, C.; Garces, G.; Adeva, P.; Llorente, I.; Frankel, G.S.; Fajardo, S. The Role of the Beta-Mg17Al12 Phase on the Anomalous Hydrogen Evolution and Anodic Dissolution of AZ Magnesium Alloys. *Corros. Sci.* **2020**, *165*, 108384. [[CrossRef](#)]
16. Zeng, R.C.; Sun, L.; Zheng, Y.F.; Cui, H.Z.; Han, E.H. Corrosion and Characterisation of Dual Phase Mg-Li-Ca Alloy in Hank's Solution: The Influence of Microstructural Features. *Corros. Sci.* **2014**, *79*, 69–82. [[CrossRef](#)]
17. Dobkowska, A.; Adamczyk-Cieślak, B.; Kubásek, J.; Vojtěch, D.; Kuc, D.; Hadasik, E.; Mizera, J. Microstructure and Corrosion Resistance of a Duplex Structured Mg-7.5Li-3Al-1Zn. *J. Magnes. Alloys* **2021**, *9*, 467–477. [[CrossRef](#)]
18. Dutkiewicz, J.; Kalita, D.; Maziarz, W.; Tański, T.; Borek, W.; Ostachowski, P.; Faryna, M. Effect of KOBO Extrusion and Following Cyclic Forging on Grain Refinement of Mg-9Li-2Al-0.5Sc Alloy. *Met. Mater. Int. Korean Inst. Met. Mater.* **2020**, *26*, 1004–1014. [[CrossRef](#)]
19. Bochniak, W.; Korbel, A. KOBO Type Forming: Forging of Metals under Complex Conditions of the Process. *J. Mater. Process. Technol.* **2003**, *134*, 120–134. [[CrossRef](#)]
20. Dobkowska, A.; Adamczyk-cie, B.; Aydee, M.; Garcia, G. Effect of High Deformation without Preheating on Microstructure and Corrosion of Pure Mg. *Metals* **2024**, *14*, 949. [[CrossRef](#)]
21. Dobkowska, A.; Adamczyk-Cieślak, B.; Chlewicka, M.; Towarek, A.; Zielińska, A.; Korallnik, M.; Kuc, D.; Mizera, J. Evolution of Microstructure Dependent Corrosion Properties of Ultrafine AZ31 under Conditions of Extrusion with a Forward Backward Oscillating Die. *J. Mater. Res. Technol.* **2022**, *18*, 4486–4496. [[CrossRef](#)]
22. Dobkowska, A.; Zielińska, A.; Donik, Č.; Łojkowski, M.; Adamczyk-Cieślak, B. Microstructure and Properties of an AZ61 Alloy after Extrusion with a Forward-Backward Oscillating Die without Preheating of the Initial Billet. *J. Alloys Compd.* **2023**, *952*, 169843. [[CrossRef](#)]
23. Dobkowska, A.; Korallnik, M.; Adamczyk-Cieślak, B.; Kuc, D.; Chromiński, W.; Kubasek, J.; Mizera, J. The Effect of Extrusion Ratio on the Corrosion Resistance of Ultrafine-Grained Mg-4Li-3Al-Zn Alloy Deformed Using Extrusion with a Forward-Backward Oscillating Die. *J. Mater. Eng. Perform.* **2022**, *31*, 8932–8939. [[CrossRef](#)]
24. Dobkowska, A.; Adamczyk-Cieślak, B.; Korallnik, M.; Chromiński, W.; Kubasek, J.; Ciftci, J.; Kuc, D.; Mizera, J. Corrosion Behavior of Fine-Grained Mg-7.5Li-3Al-1Zn Fabricated by Extrusion with a Forward-Backward Rotating Die (KoBo). *J. Magnes. Alloys* **2021**, *10*, 811–820. [[CrossRef](#)]
25. Dobkowska, A.; Zielińska, A.; Paulin, I.; Donik, C.; Korallnik, M.; Adamczyk-Cieślak, B.; Wieczorek-Czarnocka, M.; Kuc, D.; Kubasek, J.; Mikuszewski, T.; et al. Microstructural, Corrosion and Mechanical Properties of a WE43 Alloy: Conventional Extrusion versus SPD. *J. Alloys Compd.* **2024**, *976*, 173090. [[CrossRef](#)]
26. Kirkland, N.; Birbilis, N.; Staiger, M. Assessing the Corrosion of Biodegradable Magnesium Implants: A Critical Review of Current Methodologies and Their Limitations. *Acta Biomater.* **2012**, *61*, 65–69. [[CrossRef](#)]
27. Birbilis, N.; King, A.D.; Thomas, S.; Frankel, G.S.; Scully, J.R. Evidence for Enhanced Catalytic Activity of Magnesium Arising from Anodic Dissolution. *Electrochim. Acta* **2014**, *132*, 277–283. [[CrossRef](#)]
28. Ghali, E.; Dietzel, W.; Kainer, K.-U. Testing of General and Localized Corrosion of Magnesium Alloys: A Critical Review. *J. Mater. Eng. Perform.* **2004**, *13*, 517–529. [[CrossRef](#)]
29. Jeong, Y.S.; Kim, W.J. Enhancement of Mechanical Properties and Corrosion Resistance of Mg-Ca Alloys through Microstructural Refinement by Indirect Extrusion. *Corros. Sci.* **2014**, *82*, 392–403. [[CrossRef](#)]
30. Esmailzadeh, S.; Aliofkhaeaei, M.; Sarlak, H. Interpretation of Cyclic Potentiodynamic Polarization Test Results for Study of Corrosion Behavior of Metals: A Review. *Prot. Met. Phys. Chem. Surfaces* **2018**, *54*, 976–989. [[CrossRef](#)]

31. Benedetti, A.; Cirisano, F.; Delucchi, M.; Faimali, M.; Ferrari, M. Potentiodynamic Study of Al-Mg Alloy with Superhydrophobic Coating in Photobiologically Active/Not Active Natural Seawater. *Colloids Surfaces B Biointerfaces* **2016**, *137*, 167–175. [[CrossRef](#)] [[PubMed](#)]
32. King, A.D.; Birbilis, N.; Scully, J.R. Accurate Electrochemical Measurement of Magnesium Corrosion Rates; A Combined Impedance, Mass-Loss and Hydrogen Collection Study. *Electrochim. Acta* **2014**, *121*, 394–406. [[CrossRef](#)]
33. Li, C.Q.; Xu, D.K.; Chen, X.B.; Wang, B.J.; Wu, R.Z.; Han, E.H.; Birbilis, N. Composition and Microstructure Dependent Corrosion Behaviour of Mg-Li Alloys. *Electrochim. Acta* **2018**, *260*, 55–64. [[CrossRef](#)]
34. Jamesh, M.I.; Wu, G.; Zhao, Y.; McKenzie, D.R.; Bilek, M.M.M.; Chu, P.K. Electrochemical Corrosion Behavior of Biodegradable Mg-Y-RE and Mg-Zn-Zr Alloys in Ringer's Solution and Simulated Body Fluid. *Corros. Sci.* **2015**, *91*, 160–184. [[CrossRef](#)]
35. Xu, D.K.; Han, E.H. Effect of Quasicrystalline Phase on Improving the Corrosion Resistance of a Duplex Structured Mg-Li Alloy. *Scr. Mater.* **2014**, *71*, 21–24.
36. Tian, G.; Wang, J.; Xue, C.; Wang, S.; Yang, X.; Su, H.; Li, Q.; Li, X.; Yan, C.; Yang, Z. Improving Corrosion Resistance of Mg-Li Alloys by Sn Microalloying. *J. Mater. Res. Technol.* **2023**, *26*, 199–217. [[CrossRef](#)]
37. Ma, H.; Wu, L.; Liu, C.; Liu, M.; Wang, C.; Li, D.; Chen, X.Q.; Dong, J.; Ke, W. First-Principles Modeling of the Hydrogen Evolution Reaction and Its Application in Electrochemical Corrosion of Mg. *Acta Mater.* **2020**, *183*, 377–389. [[CrossRef](#)]
38. Bahmani, A.; Lotfipour, M.; Taghizadeh, M.; Kim, W.J. Corrosion Behavior of Severely Plastically Deformed Mg and Mg Alloys. *J. Magnes. Alloys* **2022**, *10*, 2607–2648. [[CrossRef](#)]
39. Atrens, A.; Liu, M. Corrosion of Magnesium (Mg) Alloys and Metallurgical Influence. *Corros. Magnes. Alloys* **2011**, 117–165. [[CrossRef](#)]

**Disclaimer/Publisher's Note:** The statements, opinions and data contained in all publications are solely those of the individual author(s) and contributor(s) and not of MDPI and/or the editor(s). MDPI and/or the editor(s) disclaim responsibility for any injury to people or property resulting from any ideas, methods, instructions or products referred to in the content.

Wykaz osiągnięć naukowych albo artystycznych, stanowiący znaczny wkład w rozwój określonej dyscypliny w języku polskim



## Spis treści

<b>I. WYKAZ OSIĄGNIĘĆ NAUKOWYCH ALBO ARTYSTYCZNYCH, o których mowa w art. 219 ust. 1. pkt 2 Ustawy</b> .....	2
1. Monografie naukowe, zgodnie z art. 219 ust. 1. pkt 2a ustawy.....	2
2. Cykl powiązanych tematycznie artykułów naukowych, zgodnie z art. 219 ust. 1. pkt 2b ustawy.....	2
3. Zrealizowane oryginalne osiągnięcia projektowe, konstrukcyjne, technologiczne lub artystyczne, zgodnie z art. 219 ust. 1. pkt 2c ustawy.....	3
4. Inne, niż wymienione w pkt. I.1-3, osiągnięcia naukowe lub artystyczne .....	3
<b>II. WYKAZ AKTYWNOŚCI NAUKOWEJ ALBO ARTYSTYCZNEJ</b> .....	7
1. Wykaz członkostwa w redakcjach naukowych monografii .....	7
2. Wykaz wystąpień na krajowych lub międzynarodowych konferencjach naukowych lub artystycznych, z wyszczególnieniem przedstawionych wykładów na zaproszenie i wykładów plenarnych.....	7
3. Wykaz udziału w komitetach organizacyjnych i naukowych konferencji krajowych lub międzynarodowych, z podaniem pełnionej funkcji. ....	9
4. Wykaz uczestnictwa w pracach zespołów badawczych realizujących projekty finansowane w drodze konkursów krajowych lub zagranicznych, z podziałem na projekty zrealizowane i będące w toku realizacji, oraz z uwzględnieniem informacji o pełnionej funkcji w ramach prac zespołów. ....	9
5. Wykaz członkostwa w międzynarodowych lub krajowych organizacjach i towarzystwach naukowych wraz z informacją o pełnionych funkcjach.....	10
6. Wykaz staży w instytucjach naukowych lub artystycznych, w tym zagranicznych, z podaniem miejsca, terminu, czasu trwania stażu i jego charakteru.....	11
7. Wykaz członkostwa w komitetach redakcyjnych i radach naukowych czasopism wraz z informacją o pełnionych funkcjach.....	11
8. Wykaz recenzowanych prac naukowych lub artystycznych, w szczególności publikowanych w czasopismach międzynarodowych.....	11
9. Wykaz uczestnictwa w programach europejskich lub innych programach międzynarodowych.	11
10. Wykaz udziału w zespołach badawczych, realizujących projekty inne niż określone w pkt. II.4.	11
11. Wykaz uczestnictwa w zespołach oceniających wnioski o finansowanie badań, wnioski o przyznanie nagród naukowych, wnioski w innych konkursach mających charakter naukowy lub dydaktyczny.....	12
<b>III. WSPÓLPRZA Z OTOCZENIEM SPOŁECZNYM I GOSPODARCZYM</b> .....	12
1. Wykaz dorobku technologicznego.....	12
2. Współpraca z sektorem gospodarczym.....	12
3. Wykaz uzyskanych praw własności przemysłowej, w tym uzyskanych patentów krajowych lub międzynarodowych.....	12
4. Wykaz wdrożonych technologii. ....	13
5. Wykaz wykonanych ekspertyz lub innych opracowań wykonanych na zamówienie instytucji publicznych lub przedsiębiorców. ....	13
6. Wykaz udziału w zespołach eksperckich lub konkursowych.....	13
7. Wykaz projektów artystycznych realizowanych ze środowiskami pozaartystycznymi. ....	13
<b>IV. DANE NAUKOMETRYCZNE</b> .....	14
1. Informacja o punktacji Impact Factor (stan na dzień 10.01.2025 r.).....	14
2. Informacja o liczbie cytowań publikacji wnioskodawcy, z oddzielnym uwzględnieniem autocytowań (stan na dzień 10.01.2025 r.) .....	14
3. Informacja o posiadanym indeksie Hirscha (stan na dzień 10.01.2025 r.).....	14

**I. WYKAZ OSIĄGNIĘĆ NAUKOWYCH ALBO ARTYSTYCZNYCH,  
o których mowa w art. 219 ust. 1. pkt 2 Ustawy**

**1. Monografie naukowe, zgodnie z art. 219 ust. 1. pkt 2a ustawy.**  
brak

**2. Cykl powiązanych tematycznie artykułów naukowych, zgodnie z art. 219 ust. 1. pkt 2b ustawy.**

**Tytuł: Wpływ mikrostruktury na kształtowanie odporności korozyjnej Mg i jego stopów odkształcanych metodą wyciskania współbieżnego z oscylującą matrycą**

**A1. A. Dobkowska, B. Adamczyk-Cieślak, M. Gonzalez, W. Bednarczyk, J. Gubicza, P. Jenei, K. Mukhartova, M. Tkocz, D. Kuc, J. Mizera, Evaluation of microstructure-dependent corrosion of pure Mg extruded at high deformation ratios without preheating of the initial billet using KoBo Metals 2024, 14, 949. <https://doi.org/10.3390/met14080949>, IF = 2,6, 70 pkt MNiSW**

**A2. A. Dobkowska, B. Adamczyk-Cieślak, M. Chlewicka, A. Towarek, A. Zielińska, M. Koralnik, D. Kuc, J. Mizera, Evolution of microstructure dependent corrosion properties of ultrafine AZ31 under conditions of extrusion with a forward backward oscillating die, J. Mater. Res. Technol. 18 (2022) 4486–4496. <https://doi.org/10.1016/j.jmrt.2022.04.131>, IF 6,4; 100 pkt MNiSW**

**A3. A. Dobkowska, A. Zielińska, Č. Donik, M. Łojkowski, B. Adamczyk-Cieślak, Microstructure and properties of an AZ61 alloy after extrusion with a forward-backward oscillating die without preheating of the initial billet, J. Alloys Compd. (2023) 169843. <https://doi.org/10.1016/j.jallcom.2023.169843>, IF 6,2; 140 pkt MNiSW**

**A4. A. Dobkowska, M. Koralnik, B. Adamczyk-Cieślak, D. Kuc, W. Chromiński, J. Kubasek, J. Mizera, The Effect of Extrusion Ratio on the Corrosion Resistance of Ultrafine-Grained Mg-4Li-3Al-Zn Alloy Deformed Using Extrusion with a Forward-Backward Oscillating Die, J. Mater. Eng. Perform. (2022). <https://doi.org/10.1007/s11665-022-06895-1>, IF 2,3; 70 pkt MNiSW**

**A5. A. Dobkowska, B. Adamczyk – Cieślak, M. Koralnik, W. Chromiński, J. Kubasek, J. Ciftci, D. Kuc, J. Mizera, Corrosion behavior of fine-grained Mg-7.5Li-3Al-1Zn fabricated by extrusion with a forward-backward rotating die (KoBo), J. Magnes. Alloy. 10 (2022) 811–820. <https://doi.org/10.1016/j.jma.2021.08.020>, IF 17,6; 100 pkt MNiSW**

**A6. A. Dobkowska, A. Zielińska, I. Paulin, C. Donik, M. Koralnik, B. Adamczyk-Cieślak, M. Wieczorek-Czarnocka, D. Kuc, J. Kubasek, T. Mikuszewski, M. Godec, J. Mizera, Microstructural, corrosion and mechanical properties of a WE43 alloy : conventional extrusion versus SPD, J. Alloys Compd. 976 (2024). <https://doi.org/10.1016/j.jallcom.2023.173090>, IF 6,2; 100 pkt MNiSW**

**A7. A. Dobkowska, J. Kubasek, On the possibility of the deformation of Mg and alloys without preheating of initial billets: understanding their corrosion performance via electrochemical tests, Materials (Basel). 17 (2024) 1–10. <https://doi.org/10.3390/ma17246182>, IF 3,1; 140 pkt MNiSW**

3. **Zrealizowane oryginalne osiągnięcia projektowe, konstrukcyjne, technologiczne lub artystyczne, zgodnie z art. 219 ust. 1. pkt 2c ustawy**

brak

4. **Inne, niż wymienione w pkt. 1.1-3, osiągnięcia naukowe lub artystyczne**

*Rozdział w monografii naukowej*

**A. Dobkowska**, E. Ura-Bińczyk, J. Mizera, J. Banaś, B. Mazurkiewicz, W. Solarski, Rozdział 6: Dobór materiałów orurowania odwiertów na bazie oceny kinetyki degradacji w monografii [w:] Praca zbiorowa pod redakcją Jana Lubasia „Opracowanie optymalnych koncepcji zagospodarowania złóż niekonwencjonalnych”, Tom II, Instytut Nafty i Gazu – Państwowy - Instytut Badawczy, 2018. ISSN 23532718, ISBN 978-83-65649-30-0

*Wykaz opublikowanych artykułów w czasopismach naukowych oprócz pozycji wymienionych w pkt. 1.2*

*Po uzyskaniu stopnia doktora*

1. **Dobkowska Anna**, Lofaj Francisek, González García Marlene Aydee, Martinez, Kulikowski Krzysztof, Paradiso Alessia, Idaszek Joanna, Gubicza Jenő, Jenei Peter, Kabátová Margarita, Kvetková Lenka, Lisnichuk Marek, Inoue Shinou, Kawamura Yoshishito, Święszkowski Wojciech, Structural, mechanical, corrosion, and early biological assessment of tantalum nitride coatings deposited by reactive HiTUS, Surf. Coatings Technol. 493 (2024). <https://doi.org/10.1016/j.surfcoat.2024.131267>, IF 5,3; 100 pkt MNiSW
2. Martinez Guerrero Diana Clemencia, Borkam-Schuster Anke, Helmholtz Heiko, **Dobkowska Anna**, B. Luthringer-Feyerabend, Płociński Tomasz, Willumeit-Römer Regine, Święszkowski Wojciech, Bone cells influence the degradation interface of pure Mg and WE43 materials: Insights from multimodal in vitro analysis, Acta Biomater. 187 (2024) 471–490. <https://doi.org/10.1016/j.actbio.2024.08.015>, IF 9,4; 140 pkt MNiSW
3. **Dobkowska Anna**, Kruszewski Mirosław Jakub, Ciftci Jakub, Morończyk Bartosz, Zgłobicka Izabela, Zybała Rafał, and Żrodowski Łukasz: Microstructure and Corrosion of Mg-Based Composites Produced from Custom-Made Powders of AZ31 and Ti6Al4V via Pulse Plasma Sintering. Materials, vol. 17, nr 7, 2024. <https://doi.org/10.3390/ma17071602>, IF 3,748; 140 pkt MNiSW
4. Idaszek Joanna, Wysocki Bartłomiej, Ura-Bińczyk Ewa, **Dobkowska Anna**, Nowak Wojciech, Yamamoto Akiko, Sułka Grzegorz, Święszkowski Wojciech: Graded or Random – Effect of Pore Distribution in 3D Titanium Scaffolds on Corrosion Performance and Response of HMSCs, Biomaterials Advances, vol. 163, nr art. 213955, 2024, <https://doi.org/10.1016/j.bioadv.2024.213955>, IF 7,9; 40 pkt MNiSW
5. Majchrowicz Kamil, Romelczyk, Baishya Barbara, Wieczorek Czarnockam Monika, **Dobkowska Anna**, Raga Krzysztof, Filip Ryszard, Pakieła Zbigniew: Determination of the Fracture Toughness of Carburized Pyrowear 53 Steel for Planetary Gears by the Small Punch Test Method, Archives of Civil and Mechanical Engineering, vol. 9. 2024, <https://doi.org/10.1007/s43452-024-00992-9>, IF 4,4; 140 pkt MNiSW

6. Bednarczyk Iwona, **Dobkowska Anna**, Hilšer Ondrej, Rusz Stanislav, Pastrňák Martin, Čada Radoslav, Jabłońska Monika, Tkocz Marek, Kowalczyk Karolina, Pałgan Daria, Necas David, Mizera Jarosław: Influence of temperature and number of passes during twist channel angular pressing (TCAP) on the microstructural, mechanical, and corrosion properties of Mg – 4Li – Ca, Archives of Civil and Mechanical Engineering, vol. 24, 2024, s. 1–15. <https://doi.org/10.1007/s43452-024-00903-y>, IF 4,4; 140 pkt MNiSW
7. Martinez Guerrero Diana Clemencia, **Dobkowska Anna**, Marek Romy, Ćwieka Hanna, Jaroszewicz Jakub, Płociński Tomasz, Donik Ārtomir, Helmholtz Heiko, Luthringer-Feyerabend Berengere, Zeller-Plumhoff Berit, Willumeit-Römer Regine, Świąszkowski Wojciech: In vitro and in vivo degradation behavior of Mg-0.45Zn-0.45Ca (ZX00) screws for orthopedic applications, Bioactive Materials, vol. 28, 2023, s. 132-154, DOI:10.1016/j.bioactmat.2023.05.004, IF 18,56; 200 pkt MNiSW
8. Zgłobicka Izabela, **Dobkowska Anna**, Zielińska Aleksandra, Borucinska Ewa, Kruszewski Mirosław Jakub, Zybala Rafał, Płociński Tomasz, Idaszek Joanna, Jaroszewicz Jakub, Paradowski Krystian, Adamczyk-Cieślak Bogusława, Nikiforow Kostiantyn, Bucholc Bartosz, Świąszkowski Wojciech, Kurzydłowski Krzysztof: In-depth analysis of the influence of bio-silica filler (*Didymosphenia geminata* frustules) on the properties of Mg matrix composites, Journal of Magnesium and Alloys, vol. 11, nr 8, 2023, s. 2853-2871, DOI:10.1016/j.jma.2023.08.001, IF 10,088; 100 pkt MNiSW
9. Źrodowski Łukasz, Wróblewski Rafał, Leonowicz Marcin, Morończyk Bartosz, Choma Tomasz, Ciftci Jakub, Świąszkowski Wojciech, **Dobkowska Anna**, Ura-Bińczyk Ewa, Błyskun Piotr, Jaroszewicz Jakub, Krawczyńska Agnieszka, Kulikowski Krzysztof, Wysocki Bartłomiej, Cetner Tomasz: How to control the crystallization of metallic glasses during laser powder bed fusion? Towards part-specific 3D printing of in situ composites, Additive Manufacturing, vol. 76, 2023, 103775, s. 1-40, DOI:10.1016/j.addma.2023.103775, IF 10,998; 200 pkt MNiSW
10. Chlewicka Monika, **Dobkowska Anna**, Sitek Ryszard, Adamczyk-Cieślak Bogusława, Mizera Jarosław: Microstructure and corrosion resistance characteristics of Ti–AlN composite produced by selective laser melting, Materials and Corrosion-Werkstoffe und Korrosion, vol. 73, 2022, s. 451-459, DOI:10.1002/maco.202112703, IF 2,097; 100 pkt MNiSW
11. **Dobkowska Anna**, Źrodowski Łukasz, Chlewicka Monika, Korallnik Milena, Adamczyk-Cieślak Bogusława, Ciftci Jakub, Morończyk Bartosz, Kruszewski Mirosław Jakub, Jaroszewicz Jakub, Kuc Dariusz, Świąszkowski Wojciech, Mizera Jarosław: A comparison of the microstructure-dependent corrosion of dual-structured Mg-Li alloys fabricated by powder consolidation methods: Laser powder bed fusion vs pulse plasma sintering, Journal of Magnesium and Alloys, 2022, DOI:10.1016/j.jma.2022.06.003, IF 10,088; 100 pkt MNiSW
12. Pałgan Daria, **Dobkowska Anna**, Zielińska Aleksandra, Drozdenko Daria, Máthis Kristián, Świąszkowski Wojciech: The Role of LPSO Structures in Corrosion Resistance of Mg-Y-Zn Alloys, Crystals, vol. 12, nr 12, 2022, 1723, s. 1-14, DOI:10.3390/cryst12121723, IF 2,589; 70 pkt MNiSW
13. Ura-Bińczyk Ewa, **Dobkowska Anna**, Bazarnik Piotr, Ciftci Jakub, Krawczyńska Agnieszka, Chromiński Witold, Wejrzanowski Tomasz, Molak Rafał, Sitek Ryszard, Płociński Tomasz, Jaroszewicz Jakub, Mizera Jarosław: Effect of annealing

on the mechanical and corrosion properties of 316L stainless steel manufactured by laser powder bed fusion, *Materials Science and Engineering A-Structural Materials Properties Microstructure And Processing*, vol. 860, 2022, 144263, s. 1-9, DOI:10.1016/j.msea.2022.144263, IF 5,234; 140 pkt MNiSW

14. Chmielewska Agnieszka, **Dobkowska Anna**, Kijeńska-Gawrońska Ewa, Jakubczak Michał, Krawczyńska Agnieszka, Choińska Emilia, Jastrzębska Agnieszka, Dean David, Wysocki Bartłomiej, Świąszkowski Wojciech: Biological and Corrosion Evaluation of In Situ Alloyed NiTi Fabricated through Laser Powder Bed Fusion (LPBF), *International Journal of Molecular Sciences*, vol. 22, nr 24, 2021, 13209, s. 1-16, DOI:10.3390/ijms222413209, IF 6,208; 140 pkt MNiSW
15. **Dobkowska Anna**, Castillo Millicent Dayle H., Turnbull Joseph P., Ramamurthy Sridhar, Zagidulin Dmitrij, Moser Desmond E., Behazin Mehran, Keech Peter G., Shoemith David W., Noël James J.: A comparison of the corrosion behaviour of copper materials in dilute nitric acid, *Corrosion Science*, vol. 192, 2021, 109778, s. 1-12, DOI:10.1016/j.corsci.2021.109778, IF 7,205; 140 pkt MNiSW
16. **Dobkowska Anna**, Sotniczuk Agata, Bazarnik Piotr, Mizera Jarosław, Garbacz Halina: Corrosion Behavior of Cold-Formed AA5754 Alloy Sheets, *Materials*, vol. 14, nr 2, 2021, s. 1-14, DOI:10.3390/ma14020394, IF 3,748; 140 pkt MNiSW
17. **Dobkowska Anna**, Adamczyk-Cieślak Bogusława, Kubasek Jiri, Dalibor Vojtech, Kuc Dariusz, Hadasik Eugeniusz, Mizera Jarosław: Microstructure and corrosion resistance of a duplex structured Mg–7.5Li–3Al–1Zn, *Journal of Magnesium and Alloys*, Elsevier B.V, vol. 9, nr 2, 2021, s. 467-477, DOI:10.1016/j.jma.2020.07.007, IF 10,088; 100 pkt MNiSW
18. Ura-Bińczyk Ewa, **Dobkowska Anna**, Andrzejczuk Mariusz, Roguska Agata, Mazurkiewicz Bogusław, SolarSKI Wojciech, Balcer Marek, Lewandowska Małgorzata, Banaś Jacek: Application of LPR and EIS techniques for on-site corrosion monitoring at the geothermal plant in Central Poland, *Materials and Corrosion-Werkstoffe und Korrosion*, 2021, DOI:10.1002/maco.202112340, IF 2,097; 100 pkt MNiSW
19. **Dobkowska Anna**, Adamczyk – Cieślak Bogusława, Kuc Dariusz, Hadasik Eugeniusz, Płociński Tomasz, Ura-Bińczyk Ewa, Mizera Jarosław, Influence of bimodal grain size distribution on the corrosion resistance of Mg–4Li–3Al–1Zn (LAZ431), *J. Mater. Res. Technol.* 13 (2021) 346–358. <https://doi.org/10.1016/j.jmrt.2021.04.078>, IF 6,2; 100 pkt MNiSW
20. **Dobkowska Anna**, Adamczyk-Cieślak Bogusława, Mizera Jarosław: A critical review of corrosion rate calculations of Mg-Al-Li alloys using traditional mass loss measurements, *Ochrona przed Korozją, SIGMA-NOT*, vol. 63, nr 2, 2020, s. 38-41, DOI:10.15199/40.2020.2.1, 40 pkt MNiSW
21. **Dobkowska Anna**, Adamczyk-Cieślak Bogusława, Towarek Aleksandra, Maj Piotr, Ura-Bińczyk Ewa, Momeni Mojtaba, Kuc Dariusz, Hadasik Eugeniusz, Mizera Jarosław: The Influence of Microstructure on Corrosion Resistance of Mg-3Al-1Zn-15Li (LAZ1531) Alloy, *Journal of Materials Engineering and Performance*, Springer New York LLC, vol. 29, 2020, s. 2679-2686, DOI:10.1007/s11665-020-04775-0, IF 1,819, 70 pkt MNiSW
22. Korallnik Milena, **Dobkowska Anna**, Adamczyk-Cieślak Bogusława, Mizera Jarosław: The influence of the microstructural evolution on the corrosion resistance of

- cold drawn copper single crystals in NaCl, Archives of Metallurgy and Materials, Akademia Gorniczo-Hutnicza im. Stanisława Staszica, vol. 65, nr 1, 2020, s. 55-64, DOI:10.24425/amm.2019.131096, IF 0,767; 40 pkt MNiSW
23. Nowak Marek, Mizera Jarosław, Kłyszewski Andrzej, **Dobkowska Anna**, Boczek Sonia, Kozik Anna, Koprowski Paweł: Nickel composite coatings reinforced nano SiC particles, Archives of Metallurgy and Materials, Akademia Gorniczo-Hutnicza im. Stanisława Staszica, vol. 65, nr 2, 2020, s. 935-940, DOI:10.24425/amm.2020.132841, IF 0,767; 40 pkt MNiSW
24. Chlewicka Monika, Cieślak Grzegorz, **Dobkowska Anna**, Mizera Jarosław: The impact of different volume fractions of crystalline structures on the electrochemical behaviour of Mg<sub>67</sub>Zn<sub>29</sub>Ca<sub>4</sub> alloys for biomedical applications, Corrosion Engineering Science and Technology, vol. 54, nr 8, 2019, s. 659-665, DOI:10.1080/1478422X.2019.1655199, IF 1,706; 40 pkt MNiSW
25. Nowak Marek, Mizera Jarosław, Kłyszewski Andrzej, **Dobkowska Anna**, Boczek Sonia, Kozik Anna, Koprowski Paweł: Effect of Various Organic Additives in Galvanic Bath on Properties of Ni-SiC Composite Coatings, Archives of Metallurgy and Materials, Akademia Gorniczo-Hutnicza im. Stanisława Staszica, vol. 64, nr 4, 2019, s. 1-7, DOI:10.24425/amm.2019.130098, IF 0,586; 40 pkt MNiSW
26. Towarek Aleksandra, **Dobkowska Anna**, Zdunek Joanna, Jurczak Wojciech, Mizera Jarosław: The influence of Mg addition and hydrostatic extrusion HE on the repassivation ability of pure Al, AlMg<sub>1</sub> and AlMg<sub>3</sub> model alloys in 3.5 wt-% NaCl, Corrosion Engineering Science and Technology, 2019, s. 1-7, DOI:10.1080/1478422X.2019.1655285, IF 1,706; 40 pkt MNiSW

#### *Przed uzyskaniem stopnia doktora*

27. Ura-Bińczyk Ewa, **Dobkowska Anna**, Płocińska Magdalena, Płociński Tomasz, Adamczyk-Cieślak Bogusława, Mazurkiewicz Bogusław, Solarz Wojciech, Banaś Jacek, Mizera Jarosław: The influence of grain refinement on the corrosion rate of carbon steels in fracturing fluids used in shale gas production, Materials and Corrosion-Werkstoffe und Korrosion, vol. 68, nr 11, 2017, s. 1190-1199, DOI:10.1002/maco.201709494, IF 1,259; 30 pkt MNiSW
28. **Dobkowska Anna**, Adamczyk-Cieślak Bogusława, Mizera Jarosław, Kurzydłowski Krzysztof, Kiełbus Andrzej: The comparison of the microstructure and corrosion resistance of sand cast aluminum alloys, Archives of Metallurgy and Materials, Akademia Gorniczo-Hutnicza im. Stanisława Staszica, vol. 61, nr 1, 2016, s. 209-212, DOI:10.1515/amm-2016-0038, IF 0,571; 30 pkt MNiSW
29. Pastuszek Monika, Cieślak Grzegorz, **Dobkowska Anna**, Mizera Jarosław, Kurzydłowski Krzysztof: The Development of Rapidly Solidified Magnesium – Copper Ribbons, Archives of Metallurgy and Materials, Akademia Gorniczo-Hutnicza im. Stanisława Staszica, vol. 61, 2016, s. 1083-1088, DOI:10.1515/amm-2016-0182, IF 0,571; 30 pkt MNiSW

## II. WYKAZ AKTYWNOŚCI NAUKOWEJ ALBO ARTYSTYCZNEJ

### 1. Wykaz członkostwa w redakcjach naukowych monografii.

brak

### 2. Wykaz wystąpień na krajowych lub międzynarodowych konferencjach naukowych lub artystycznych, z wyszczególnieniem przedstawionych wykładów na zaproszenie i wykładów plenarnych.

#### Po uzyskaniu stopnia doktora

##### Wykłady na zaproszenie

18.04.2024 **A. Dobkowska**, Corrosion of Mg-Li alloys: how to control corrosion resistance of Mg alloys?, Upsalla University, Szwecja

17.11.2022 **A. Dobkowska**, "Review of Mg-Li alloys", Institute of Metals and Technology, Ljubljana, Slovenia

18.11.2022 **A. Dobkowska**, University of Ljubljana, "Microstructure dependent corrosion of Mg-Li alloys", Faculty of Natural Sciences and Engineering, Slovenia

16.04.2021 **A. Dobkowska**, J.J. Noel, "Effect of microstructural features on corrosion resistance of pure Cu" University of Chemistry and Technology, Prague, Czech Republic

##### Wystąpienia konferencyjne

**A. Dobkowska**, A. Zielińska, J. Ciftci, L. Żrodowski, W. Świąszkowski, *On the possibilities of the Mg-based powders preparation for laser powder bed fusion processing*, 29<sup>th</sup> International Conference on Materials and Technology, 2-4.10.2024, Portoroz, Słowenia

**A. Dobkowska**, A. Zielińska, D. Necas, C. Donik, *Influence of powder preparation on corrosion behaviour of ODS austenitic steels with Y<sub>2</sub>O<sub>3</sub> addition*, 1-5.09.2024, Eurocorr, Paris, France,

**A. Dobkowska**, D. Martinez, M Gonzalez, W. Świąszkowski, *Influence of annealing on corrosion resistance of Mg-Zn-Y-Al alloys containing LPSO phases*, V4-Japan Meeting 4-6.12.2023, Magnesium Research Center, Kumamoto University, Kumamoto, Japonia

**A. Dobkowska**, D. Martinez, A. Zielińska, W. Świąszkowski, *Microstructure dependent corrosion of newly developed Mg-Zn-Y-Al alloys containing LPSO phases*, 28<sup>th</sup> International Conference on Materials and Technology, 11-13.10.2023, Portoroz, Słowenia

I. Zgłobicka, **A. Dobkowska**, *Nowoczesne materiały funkcjonalne. Kompozyty przyszłości*, Seminarium Polskiego Towarzystwa Mechaniki Teoretycznej i Stosowanej, 23-25.03.2023, Hołny Mejera, Polska

**A. Dobkowska**, J. Mizera, *Microstructure dependent corrosion of Mg-Li alloys*, Advanced Materials Science, Berlin, Germany, oral presentation, 14-15.06.2021, Berlin, Niemcy

**A. Dobkowska**, S. Ramamurthy, M. Behazin, J.J. Noel, *Effect of impurities on copper corrosion behaviour*, PostDoctoral School, The University of Western Ontario,

**A. Dobkowska**, M. Castillo, S. Ramamurthy, D. Zagidulin, M. Behazin, D. W. Shoesmith, J.J. Noel, *The corrosion resistance of copper with different oxygen contents in nitric acidic*

solutions, University Network of Excellence in Nuclear Engineering, UNENE, 12-13. 12.2019, Toronto, Kanada

**A. Dobkowska**, B. Adamczyk-Cieślak, E. Ura-Bińczyk, P. Maj, A. Towarek, J. Kubasek, J. Grzonka, Dalibor Vojtech, Jarosław Mizera *Influence of microstructure evaluation on corrosion resistance of AZ31-15Li alloys*, 27-29.05.2019 Corrosion, Warszawa, Polska

### **Przed uzyskaniem stopnia doktora**

#### **Wystąpienia konferencyjne**

**A. Dobkowska**, R. Sitek, P. Wiśniewski, M. Koralnik, J. Mizera, *Microstructure characterization of ceramic shell molds*, 11-15. 09.2017, The 11<sup>th</sup> International Symposium on Applied Plasma Science, Warsaw, Polska

**A. Dobkowska**, R. Sitek, K. Żaba, J. Mizera, *The role of thermal imaging camera in the identification defects of multilayer ceramic molds*, 19-27.08.2017, XXVI International Materials Research Congress, Cancun, Meksyk

**A. Dobkowska**, R. Sitek, K. Żaba, J. Mizera, *The role of thermal imaging camera in the identification of defects of multilayer ceramic molds*, 7-15.03.2017, The 24th Annual Meeting of Institute of Applied Plasma Science, Hanoi, Vietnam

**A. Dobkowska**, B. Adamczyk – Cieślak, J. Mizera, *Wpływ obróbki cieplnej na odporność korozyjną stopów magnezu z litem*, 23 – 24.11.2016, Konferencja Naukowa „Młodzi Naukowcy”, Oleśnica, Polska

J. Mizera E. Ura – Bińczyk, **A. Dobkowska**, *Dobór materiałów orurowania odwiertów na bazie oceny kinetyki degradacji*, 19-22.09.2016, Geopetrol 2016, Zakopane – Kościelisko, Polska

**A. Dobkowska**, E. Ura-Bińczyk, J. Mizera, W. Solarski, B. Mazurkiewicz, J. Banaś, *The corrosion resistance of casing pipes used in the shale gas production systems*, 10-15.09.2016 Eurocorr, Montpollier, Francja

**A. Dobkowska**, E. Ura – Bińczyk, J. Mizera, K.J. Kurzydłowski, B. Mazurkiewicz, W. Solarski, J. Banaś, *The corrosion resistance of casing pipes used in the shale gas production systems – influence of metallurgical features*, 05-08.06.2016, XXI Physical Metallurgy and Materials Science Conference, Advanced Materials and Technologies, Rawa Mazowiecka, Polska

**A. Dobkowska**, M. Bochenek, E. Ura – Bińczyk, J. Mizera, B. Mazurkiewicz, W. Solarski, J. Banaś, *Corrosion resistance of steel pipes for use as casing for wells in natural gas industry*, 20 – 24.09.2015, Euromat, Warsaw, Polska

**A. Dobkowska**, B. Adamczyk – Cieślak, J. Mizera, M. Nowak, *Neutral salt spray tests on new generation Mg – Li alloys*, 16 – 19.04.2015, International Advances in Applied Physics and Materials, Science Congress & Exhibition APMAS, Oludeniz, Turcja

**A. Dobkowska**, B. Adamczyk – Cieślak, J. Mizera, D. Vojtech and J. Kubasek *Corrosion resistance of ultra-light Mg-Li alloys. The influence of microstructural features*, 12 – 15.04.2015 Faraday Discussion, Londyn, UK

A. Dobkowska, B. Adamczyk – Cieślak, J. Mizera, J. Kubasek, D. Wojtech, *Corrosion behaviour of magnesium lithium alloys in NaCl solution*, 18-21.11.2014 International Scientific Conference Corrosion 2014, Gliwice, Polska

A. Dobkowska, B. Adamczyk – Cieślak, J. Mizera, *Analiza mikrostruktury odlewniczych stopów aluminium*, 23-27.09.2014 Szkoła Inżynierii Materiałowej, Ryto, Polska

A. Dobkowska, B. Adamczyk – Cieslak, J. Mizera, A. Kiełbus, *The characterization of microstructure of hypoeutectic AlSi10Mg sand casting alloy*, 11-12.08.2014 Conference on Mining, Materials and Metallurgical Engineering MMME, Praga, Czechy

A. Dobkowska, B. Adamczyk - Cieslak, J. Mizera, J. Kubasek, D. Wojtech, *The corrosion Resistance of New Generation Mg-Li Alloys*, 20-25.07.2014 Junior Euromat, Sevilla Szwajcaria

A. Dobkowska, J. Zdunek, J. Mizera, *Wpływ przeróbki plastycznej na odporność korozyjną i właściwości mechaniczne modelowego stopu aluminium – lit*, 24 – 27.09.2013 Szkoła Inżynierii Materiałowej, Ryto, Polska

A. Dobkowska, B. Adamczyk – Cieślak, J. Mizera, K.J. Kurzydłowski, *Porównanie odporności korozyjnej stopów AZ91D i WE43 w środowisku zawierającym 3,5% jonów chlorkowych*, 24 – 26.04.2013 Metale lekkie 2013, Niepołomice, Polska

A. Dobkowska, B. Adamczyk – Cieślak, J. Kamiński, J. Smolik, J. Mizera, K.J. Kurzydłowski, *Odporność korozyjna stopów magnezu AZ91D wytwarzanych różnymi metodami*, 24 – 27.09.2012, Szkoła Inżynierii Materiałowej, Kraków, Polska

### **3. Wykaz udziału w komitetach organizacyjnych i naukowych konferencji krajowych lub międzynarodowych, z podaniem pełnionej funkcji.**

- 2-4.10.2024 Chairman for Young Session podczas 29<sup>th</sup> International Conference on Materials and Technology w Portoroz
- 11-13.10.2023 Chairman for Young Session podczas 28<sup>th</sup> International Conference on Materials and Technology w Portoroz
- 19-22.09.2022 Pomoc w organizacji konferencji European Materials Research Society Fall Meeting and Exhibit w Warszawie

### **4. Wykaz uczestnictwa w pracach zespołów badawczych realizujących projekty finansowane w drodze konkursów krajowych lub zagranicznych, z podziałem na projekty zrealizowane i będące w toku realizacji, oraz z uwzględnieniem informacji o pełnionej funkcji w ramach prac zespołów.**

#### **Projekty badawcze będące w toku realizacji**

- 1) „Opracowanie innowacyjnego biomateriału na bazie Mg o wysokiej plastyczności i kontrolowanym stopniu degradacji poprzez zmianę mechanizmów formowania mikrostruktury w trakcie stapiania laserowego w złożu proszkowym (LPBF) do zastosowań na płytce do osteosyntezy kości żuchwy”, pełniona funkcja: kierownik, grant badawczy dla młodych naukowców Materials For Young-2 przyznawany przez IDUB PW, okres realizacji 08.2024-12.2025
- 2) „Nowe stale ODS do zastosowań w ekstremalnych warunkach z wykorzystaniem ultradźwiękowej dyspersji nano-tlenków w połączeniu z SLM i PPS”, Narodowe Centrum

Nauki, OPUS LAP 22, pełniona funkcja: wykonawca, pomysłodawca i główna autorka projektu, projekt międzynarodowy realizowany w ramach konsorcjum trzech jednostek naukowo-badawczych: Politechnika Warszawska (lider), Wyższa Szkoła Chemiczno Technologiczna w Pradze, Czechy oraz Instytut Metali i Technologii, Ljubljana, Słowenia, okres realizacji: 01.2023 – 12.2025

- 3) „Rozwój zaawansowanych stopów magnezu przeznaczonych do pracy w warunkach ekstremalnych”, Narodowe Centrum Badań i Rozwoju, MagMax, Visegrad Group V4, pełniona funkcja: wykonawca i autorka projektu, projekt realizowany w międzynarodowym konsorcjum naukowym: Magnesium Research Center, Kumamoto University, Japonia, Eotvos Lorand University, Węgry, Charles University, Czechy, Institute of Materials Research Slovak Academy of Science, Słowacja, okres realizacji: 02.2022 – 01.2025

#### ***Projekty badawcze zrealizowane po uzyskaniu stopnia doktora***

- 4) „Nowe możliwości kształtowania mikrostruktury oraz właściwości (bio)korozyjnych i mechanicznych kompozytów na bazie Mg wzmocnionych cząstkami nHA”, grant wewnętrzny Rady Dyscypliny Naukowej wspierający prowadzenie działalności naukowej w dyscyplinie inżynieria materiałowa, pełniona funkcja: kierownik i autorka projektu, okres realizacji: 03.2023 – 08.2024
- 5) „Nowe możliwości kształtowania mikrostruktury i właściwości korozyjnych dwufazowych stopów Mg-Li, Narodowe Centrum Nauki, Miniatura 6, pełniona funkcja: kierownik i autorka projektu, okres realizacji: 08.2022 – 08.2023
- 6) „Właściwości magnezowych kompozytów metalicznych: właściwości stopu AZ31 modyfikowanego proszkami Ti i Ti6Al4V”, grant dziekański, pełniona funkcja: kierownik i autorka projektu, , projekt realizowany na Wydziale Inżynierii Materiałowej, okres realizacji: 03.2022 – 12.2022
- 7) Nuclear Waste Management Organization, Toronto, Kanada, Effect of impurities on copper corrosion behaviour”, pełniona funkcja: wykonawca typu post doc, zakończony, projekt prowadzony we współpracy jednostek badawczo-naukowych oraz przemysłowych: Western University, Kanada i Nuclear Waste Management Organization, Kanada, okres realizacji: 05.2018 – 05.2020

#### ***Projekty badawcze zrealizowane przed uzyskaniem stopnia doktora***

- 8) „Opracowanie optymalnych koncepcji zagospodarowania złóż niekonwencjonalnych z uwzględnieniem aspektów środowiskowych i społecznych”, Program Blue Gas I - Polski Gas Łupkowy NCBR, projekt BG1/ResDev/13, wykonawca, okres realizacji: 10.2013 – 09.2016
- 9) „Opracowanie metod modelowania geologicznego oraz monitorowania erozyjнокorozyjnego zużycia materiałów z uwzględnieniem korozji mikrobiologicznej MIC w instalacjach wydobywania gazu łupkowego”, Program Badań Stosowanych NCBR, PBS1/A2/11/2012, wykonawca, okres realizacji: 01.2013 – 12.2015

#### **5. Wykaz członkostwa w międzynarodowych lub krajowych organizacjach i towarzystwach naukowych wraz z informacją o pełnionych funkcjach.**

od 2022	Członek <b>Polskiego Towarzystwa Mechaniki Teoretycznej i Stosowanej</b>
2018-2020	Członek <b>Electrochemical Society</b>
2016-2018	Członek <b>Royal Society of Chemistry</b>

**6. Wykaz staży w instytucjach naukowych lub artystycznych, w tym zagranicznych, z podaniem miejsca, terminu, czasu trwania stażu i jego charakteru.**

***Krajowe i zagraniczne staże po uzyskaniu stopnia doktora***

- 11-22.04.2023 Institute of Metals and Technology, Ljubljana, Slovenia (Miniatura)
- 1-22.11.2022 Institute of Metals and Technology, Ljubljana, Slovenia (Mobility PW)
- 12-27.03. 2022 Institute of Metals and Technology, Ljubljana, Slovenia
- 1.06.2018-30.06.2020 Chemistry Department, University of Western Ontario, London, Ontario, Kanada

***Krajowe i zagraniczne staże przed uzyskaniem stopnia doktora***

- 01.06.2015 – 30.07.2015 Faculty of Chemical Technology, Department of Metals and Corrosion engineering, University of Chemistry and Technology, Praga, Czechy
- 31.03.2014-04.04.2014 Spring school *Modelling of corrosion for nuclear reactors*, INSTN, Saclay, Francja
- 01.10.2013 – 30.11.2013 Faculty of Chemical Technology, Department of Metals and Corrosion engineering, University of Chemistry and Technology, Praga, Czechy

**7. Wykaz członkostwa w komitetach redakcyjnych i radach naukowych czasopism wraz z informacją o pełnionych funkcjach.**

Członek Międzynarodowej Rady Naukowej czasopisma „Materials and Technology” ISSN 1580-3414

**8. Wykaz recenzowanych prac naukowych lub artystycznych, w szczególności publikowanych w czasopismach międzynarodowych.**

Lista recenzowanych, w ramach dotychczasowej pracy naukowej, artykułów w czasopismach (w tym indeksowanych na liście JCR) została przedstawiona poniżej.

L.p.	Czasopismo	Okres	Liczba recenzji
1	Materials Science and Engineering A	2024	1
2	Acta Biomaterialia	2024	2
3	Surface and Coatings Technology	2024	1
4	Journal of Magnesium and Alloys (ISSN 2213-9567 )	2021-2022	11
5	Journal of Alloys and Compounds (ISSN 1873-4669)	2019-2021	3
6	Archives of Metallurgy and Materials (ISSN 1733-3490)	2023	1
7	Materials Today Communications	2023	1
8	Materials (ISSN 1996-1944)	2020-2023	3
9	Ochrona przed korozją (ISSN 0473-7733)	2019-2020	3

**9. Wykaz uczestnictwa w programach europejskich lub innych programach międzynarodowych.**

brak

**10. Wykaz udziału w zespołach badawczych, realizujących projekty inne niż określone w pkt. II.4.**

brak

### 11. Wykaz uczestnictwa w zespołach oceniających wnioski o finansowanie badań, wnioski o przyznanie nagród naukowych, wnioski w innych konkursach mających charakter naukowy lub dydaktyczny.

Od roku 2023 członek Academic Advisory Committee w konkursie stypendialnym „The Kościuszko Foundation – Exchange to US”.

## III. WSPÓLPRAC Z OTOCZENIEM SPOŁECZNYM I GOSPODARCZYM

### 1. Wykaz dorobku technologicznego.

brak

### 2. Współpraca z sektorem gospodarczym.

#### Współpraca z firmami z sektora gospodarczego w zakresie opracowywania rozwiązań materiałowych

- ✓ **Thornmann Recycling Sp z o.o., Toruń, Polska** – optymalizacja składów chemicznych kompozytów szklanych i węglowych służących do produktów małej infrastruktury drogowej. W ramach współpracy uzyskano patent nr PL 237042 Sposób wytwarzania elementów o strukturze kompozytowej desek, paneli i palet typu euro z odpadów kompozytów szklanych i węglowych, Piotr Widuch (50%), Anna Dobkowska (50%)
- ✓ **Amazemet Sp z o.o., Warszawa, Polska** – opracowanie sposobu atomizacji ultralekkich stopów na bazie Mg; współpraca potwierdzona publikacją naukową **Dobkowska A., Żrodowski Ł., Chlewicka M., Korallnik M., Adamczyk-Cieślak B., Ciftci J., Morończyk B., Kruszewski M., Jaroszewicz J., Kuc D., Świąszkowski W., Mizera J.**: A comparison of the microstructure-dependent corrosion of dual-structured Mg-Li alloys fabricated by powder consolidation methods: Laser powder bed fusion vs pulse plasma sintering, *Journal of Magnesium and Alloys*, Elsevier B.V, 2022, DOI:10.1016/j.jma.2022.06.003, IF = 10,088 100 pkt MNiSW oraz złożeniem wniosku o udzielenie patentu na wynalazek nr P.437777: A.Dobkowska, Ł. Żrodowski, J.Mizera, Sposób wytwarzania stopów Mg-Li-Al-Zn o ultra niskiej gęstości i ich zastosowanie”;
- ✓ **Sanok Rubber Company S.A. , Sanok, Polska** - współpraca w zakresie opracowania składu i ocena właściwości mieszanek kompozytowych modyfikowanych cząstkami wymuszającymi efekt piezorezystywny, oraz oceny właściwości mieszanek kompozytowych modyfikowanych dodatkiem cząstek magnetycznych finansowana przez Wydział Inżynierii Materiałowej PW w roku 2023 w projekcie „Właściwości mieszanek kompozytowych o szczególnych właściwościach”. Współpraca poparta złożeniem wniosku o finansowanie w zakresie opracowania powłok barierowych na tłokach i korkach do zastosowań farmaceutycznych w ramach projektu FENG „Budowanie przewagi konkurencyjnej Sanok Rubber Company Spółka Akcyjna w oparciu o innowacje produktowe będące wynikiem prac badawczo rozwojowych oraz wdrożenie w przedsiębiorstwie działań prośrodowiskowych”, nabór FENG.01.01-IP.01-002/23

### 3. Wykaz uzyskanych praw własności przemysłowej, w tym uzyskanych patentów krajowych lub międzynarodowych.

PL 237042 Sposób wytwarzania elementów o strukturze kompozytowej desek, paneli i palet typu euro z odpadów kompozytów szklanych i węglowych, Piotr Widuch (50%), Anna Dobkowska (50%)

#### **4. Wykaz wdrożonych technologii.**

Współpraca w uzyskaniu aprobaty technicznej IBDiM „Zwieńczenia z utwardzalnych tworzyw sztucznych do wpustów i studzienek” przez firmę Thormann Recycling Sp z o.o.

#### **5. Wykaz wykonanych ekspertyz lub innych opracowań wykonanych na zamówienie instytucji publicznych lub przedsiębiorców.**

- ✓ Współpraca z Tramwajami Warszawskimi w celu opracowania ekspertyzy „Określenie przyczyny pęknięć szyny rowkowej o profilu 60R2 w gatunku stali R260 wg EN 14811”, Warszawa 2024
- ✓ Współpraca z Laboratorium Badań dla Przemysłu WIM PW w zakresie badań korozyjnych; np. „Wykonanie badań i ocena warstwy tlenkowej stali typu 40H w celu optymalizacji procesu oksydowania elementów konstrukcyjnych, zlecający Fabryka Broni Łucznicz Sp z o.o., Radom, 2022

#### **6. Wykaz udziału w zespołach eksperckich lub konkursowych.**

brak

#### **7. Wykaz projektów artystycznych realizowanych ze środowiskami pozaartystycznymi.**

brak

#### IV. DANE NAUKOMETRYCZNE

##### 1. Informacja o punktacji Impact Factor (stan na dzień 10.01.2025 r.)

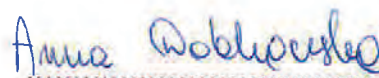
Wg Bazy Wiedzy Politechniki Warszawskiej	
Sumaryczny Impact Factor	193,889

##### 2. Informacja o liczbie cytowań publikacji wnioskodawcy, z oddzielnym uwzględnieniem autocytowań (stan na dzień 10.01.2025 r.)

Cytowania wg bazy	ogółem	bez autocytowań
Web of Science	269	220
Scopus	301	248
Google Scholar	344	316

##### 3. Informacja o posiadanym indeksie Hirscha (stan na dzień 10.01.2025 r.)

Baza	indeks Hirscha
Web of Science	9
Scopus	9
Google Scholar	10



(podpis wnioskodawcy)

Publikacja potwierdzająca inne osiągnięcia naukowe dotycząca  
wytwarzania proszków ze stopów Mg niedostępnych w sprzedaży  
komercyjnej





Available online at [www.sciencedirect.com](http://www.sciencedirect.com)

ScienceDirect

Journal of Magnesium and Alloys 10 (2022) 3553–3564



[www.elsevier.com/locate/jma](http://www.elsevier.com/locate/jma)

Full Length Article

# A comparison of the microstructure-dependent corrosion of dual-structured Mg-Li alloys fabricated by powder consolidation methods: Laser powder bed fusion vs pulse plasma sintering

Anna Dobkowska<sup>a,\*</sup>, Łukasz Żrodowski<sup>a</sup>, Monika Chlewicka<sup>a</sup>, Milena Korallnik<sup>a</sup>, Bogusława Adamczyk-Cieślak<sup>a</sup>, Jakub Ciftci<sup>a</sup>, Bartosz Morończyk<sup>a</sup>, Mirosław Kruszewski<sup>a</sup>, Jakub Jaroszewicz<sup>a</sup>, Dariusz Kuc<sup>b</sup>, Wojciech Świąszkowski<sup>a</sup>, Jarosław Mizera<sup>a</sup>

<sup>a</sup> Faculty of Materials Science and Engineering, Warsaw University of Technology, 141 Woloska, 02-507 Warsaw, Poland

<sup>b</sup> Institute of Materials Engineering, Silesian University of Technology, Krasinskiego 8, 40-019 Katowice, Poland

Received 18 January 2022; received in revised form 3 June 2022; accepted 12 June 2022

Available online 10 July 2022

## Abstract

In this study, powder metallurgy methods were used to fabricate Mg-7.5Li-3Al-Zn alloys from repowdered extruded alloys. Extruded alloys were powdered using ultrasonic atomization, and then laser powder bed fusion (LPBF) and pulse plasma sintering (PPS) were used to consolidate the bulk materials. A comparison of the properties of the fabricated alloys with those of a conventionally extruded one was carried out using methods that characterized the microstructure and corrosion resistance. When compared to their conventionally extruded counterpart, LPBF and PPS materials exhibited refined microstructures with low enrichment in AlLi and coarse Al, Zn, Mn precipitates. The main drawback of the LPBF alloy, printed for the needs of this study, was its porosity, which had a negative effect on its corrosion. The presence of unrecrystallized particle boundaries in the PPS alloy was also unbeneficial with regard to corrosion. The advantage of the LPBF and PPS processes was the ability to change the proportion of  $\alpha$ (Mg) to  $\beta$ (Li), which when the complete consolidation of the material is achievable, may increase the corrosion resistance of dual-structured Mg-Li alloys. The results show that powder metallurgy routes have a wide potential to be used for the manufacture of Mg-Li based alloys.

© 2022 Chongqing University. Publishing services provided by Elsevier B.V. on behalf of KeAi Communications Co. Ltd.

This is an open access article under the CC BY-NC-ND license (<http://creativecommons.org/licenses/by-nc-nd/4.0/>)

Peer review under responsibility of Chongqing University

**Keywords:** Additive manufacturing; Laser Powder Bed Fusion (LPBF); Pulse Plasma Sintering (PPS); Corrosion; Mg-Li alloys.

## 1. Introduction

The modern construction requirements of industries such as transportation focus on the reduction of their environmental impact and the lowering of energy costs. Such considerations have led to an increased interest in lightweight materials, such as magnesium alloys [1]. They offer high relative strength and stiffness, good damping characteristics, high

thermal and electrical conductivity, and (most importantly) the lowest weight among construction metals [2,3]. However, their widespread use is restricted by two important factors [4–6]: low corrosion resistance leading to a rapid degradation of the elements within, and secondly, poor ductility and formability, which stem from the close-packed hexagonal structure restricting the number of independent slip systems in operation [7–10]. The latter problem results in difficulties in obtaining more complex shapes using traditional manufacturing methods and raises the necessity to employ non-conventional techniques. Two types of approach that allow near-net-shape processing can be considered as alterna-

\* Corresponding author.

E-mail addresses: [anna.dobkowska@pw.edu.pl](mailto:anna.dobkowska@pw.edu.pl), [adobkow@uwo.ca](mailto:adobkow@uwo.ca) (A. Dobkowska).

tive: non-conventional powder metallurgy [11–14] and additive manufacturing [6,15–22]. Such techniques are extremely important in the biomedical industry where both a high structural integrity of the material and a wide freedom for customization to perfectly match anatomical geometries are desired [23].

Powder metallurgy and additive manufacturing routes offer attractive alternatives to conventional manufacturing of Mg alloys, and researchers to date have prepared and investigated the properties of the following Mg-based alloys: Mg–Al–Zn (AZ31, AZ61, AZ91) [24–26], Mg–Zn–Zr (mostly ZK60) [27–29], and those containing REE, such as WE43 or AE42 [30,31]. Generally, powder sintering methods exhibit many advantages in terms of microstructure modification, such as the limited formation of a strong texture and the prevention of unwanted changes to the materials, such as unfavorable grain growth or the formation of deleterious intermetallic phases [32,33]. The decisive factors with regard to the development of the aforementioned processes for the preparation of the Mg-based alloys are achieving superior mechanical properties and an improvement in the corrosion resistance of Mg alloys when compared to their traditionally cast counterparts [33,34]. For example, it was shown that AZ91D produced by wire and arc additive manufacturing exhibited higher corrosion resistance than the equivalent cast alloy [16]. Similarly, laser powder bed fusion (LPBF) produced ZK60 that was more corrosion resistant than a traditionally cast alloy [35]. Since there are also disadvantages in the form of significant degradation and the early loss of mechanical stability of the produced materials, Kopp et al. [36] proposed suitable post-processing methods for the preservation of the long-term stability of mechanical properties modified by heat treatment or plasma electrolytic oxidation of WE43 fabricated through laser powder bed fusion. Yang et al. [37] used additive manufacturing to prepare Mg-based composite with mesoporous bioglass, which shows enhanced corrosion properties in terms of orthopedic application.

In view of the microstructural considerations, the key issue in the design and production of Mg-based alloys is a full understanding and control of the properties of the powders used for consolidation [17]. Secondly, strict environmental restrictions drive researchers and technologists to look for methods to reuse post-production waste materials. Therefore, the concept behind this study was to explore the possibilities of reusing traditionally extruded Mg–Li based alloys through atomization of the base alloy and reconsolidation it, using novel manufacturing methods. To the best of our knowledge this is the first study regarding the fabrication of Mg-based alloys with Li as the main alloying element using LPBF and PPS. The main goal of this paper was to describe the differences in the corrosion resistance of the dual-structured Mg–7.5Li–3Al–Zn alloy fabricated by traditional extrusion and that produced by powder consolidation methods. This is the first study showing the possibility of the fabrication of dual structured Mg–Li alloys using powder metallurgy methods.

## 2. Materials and methodology

### 2.1. Material fabrication

#### 2.1.1. Reference material

The reference material was a dual-structured Mg–7.5Li–3Al–1Zn alloy prepared utilizing traditional casting and conventional extrusion. For casting, the AZ31B alloy was smelted, and 7.5 wt.% high-purity Li was added. The alloy was cast, extruded to a dimension of Ø20 mm, and subsequently annealed at 350 °C for 1 h. The microstructure and corrosion performance of the alloy was previously described by our research group in reference [38]. As stated in this work, Li addition decrease the density and increase formability leading to the higher number of methods that can be used for plastic deformation of Mg–Li alloys. All these aspects result in fabrication of the Mg–Li alloys with higher plasticity and strength than traditional Mg-based alloys.

#### 2.1.2. Atomization

The extruded Mg–7.5Li–3Al–1Zn was powdered by ultrasonic atomization using a rePowder device (AMAZEMET, Poland). 57.7 g of the alloy was melted in a graphite crucible at a heating rate of 150 K/min up to 1023 K and kept for 2 min at this temperature under an Ar atmosphere. Subsequently, the molten alloy was treated with a Ti6Al4V sonotrode, which vibrated at 40 kHz average frequency and 15 µm amplitude. As a result of a 40 s atomization process, 52 g of powder was produced. The powder was collected under an inert atmosphere and after sieving through a 100 µm sieve, a total mass of 48 g of powder was inserted into the laser melting machine.

#### 2.1.3. Powder metallurgy methods (LPBF and PPS)

LPBF 3D printing was carried out using a Realizer 50 (DMG MORI, Japan) laser melting machine equipped with a 120 W continuous wave 1064 nm laser. The process was carried out under an inert atmosphere of Ar 5.0 on a pure Mg build plate without preheating. After a preliminary study of the parameters, a sample of 15 × 15 × 3 mm was prepared with a 25 µm powder layer, 100 µm hatch distance, 80 mm/s scanning speed, and 15 W laser power without hatch rotation between the layers. During the process, extensive fuming was observed.

A second batch of samples was produced using powder prepared in the same way as for LPBF. The powder was consolidated using PPS, which is a novel current-assisted powder metallurgy technique (details may be found in reference [39]). The consolidation process was carried out under vacuum ( $5 \cdot 10^{-3}$  Pa) at 350 °C for 5 min under a pressure of 50 MPa.

### 2.2. Microstructural characterization

Scanning electron microscopes (SEM, Hitachi SU8000 and Hitachi SU70) were used to show the shape, distribution

and microstructure of the powder particles. To show the microstructure of the particles, powder was mixed with an acrylic resin, and the specimen was milled in Ar<sup>+</sup> beam using ion-beam milling system (Hitachi IM4000). The particle size distribution (PSD) was measured using a Horiba Partica LA-950 laser scattering particle size distribution analyzer.

To analyze the phase composition of the alloys, X-ray diffraction (XRD, Bruker D8 Advance) operating at 40 kV and 40 mA with Cu K $\alpha$  radiation was utilized. The results were recorded by stepwise scanning  $2\theta$  from 10° to 120°, with a step size of 0.02° and a count time of 10 s per step. Based on the registered patterns, by comparing the integrated intensities of the diffraction peaks from each of the known phases, a semi-quantitative determination of their relative concentration was carried out. The relative concentration of Li in the investigated alloys was measured by atomic absorption spectroscopy (AAS, GBC 932 Plus) with an air oxidizing flame and a wavelength of 670.8 nm.

The samples' microstructure was observed with the Hitachi SU8000 SEM using tunneling contrast on the ion-milled surfaces. The ion milling was carried out utilizing a low-energy Ar<sup>+</sup> ion-beam milling system (Hitachi IM4000) over 4 h. To avoid surface oxidation (due to the high activity of Li), observations were taken immediately after sample preparation. The TEM observations were carried out using JEOL JEM 1200EX microscope with an acceleration voltage of 120 kV. Thin foils were prepared using a Gatan Model 691 Precision Ion Polishing System (PIPS) with a beam voltage of 3 V inclined to the sample surface at angle of 10°. The samples were scanned using a microfocused X-ray tomographic system (MicroXCT-400, Xradia - Zeiss), at 40 kV and 200  $\mu$ A. For each sample, 1200 projection images were recorded with an exposure time of 5 s and a magnification objective of 4  $\times$ . The volume was reconstructed using the supplied manufacturer software and was then exported to Avizo Fire (Thermo Fisher Scientific) for further 3D image analysis and porosity evaluation. The voxel size was the same for all samples (5  $\times$  5  $\times$  5  $\mu$ m).

In order to investigate the mechanical properties, the test of microhardness was performed. Vickers microhardness testing was conducted under a load of 200 g using Innovatest Falcon 500 Micro/Macro Vickers Tester. 10 points were measured on each material.

### 2.3. Corrosion performance

#### 2.3.1. Electrochemical testing

The corrosion potential under open-circuit conditions, electrochemical impedance spectroscopy (EIS), and potentiodynamic measurements were carried out in naturally aerated, quiescent 0.01 M NaCl solution using an Autolab PGSTAT 302N potentiostat equipped with three electrodes: Pt as the counter electrode, Ag/AgCl as the reference electrode, and the measured sample as the working electrode. The corrosive medium was freshly prepared using analytical grade reagents and distilled water. The corrosion potential was recorded for 1 h, then EIS measurements and potentiodynamic tests were performed. The EIS measurements were recorded in a fre-

Table 1

Li concentration measured by AAS (wt.%) and Zn concentration measured by EDX (wt.%).

Material	Li% (wt.%)	Zn% (wt.%)
Powder	7.4 $\pm$ 0.4	0.9 $\pm$ 0.2
LPBF	7.5 $\pm$ 0.4	0.8 $\pm$ 0.1
PPS	7.3 $\pm$ 0.4	0.9 $\pm$ 0.1

quency range from 0.01 to 10,000 Hz. The potentiodynamic tests were conducted from 0.5 V below E<sub>OCP</sub> to 1.5 V vs. Ref with a scan rate of 5 mV. To ensure the reproducibility of the results, the data for each sample was collected three times. Nova 2.1.5 software was used to fit the data. To give a further view on the corrosion processes that occurred on the surface of the sample, high resolution SEM observations were carried out after immersion under open-circuit conditions (Hitachi SU8000, Japan). Two kinds of observation were performed: on the surfaces with the corrosion products as they were formed, and on the surfaces with chemically removed corrosion products. The corrosion products were removed by immersion in 4% nitric acid for 5 s as per references [40,41].

#### 2.3.2. Hydrogen evolution method

The evolved hydrogen was collected during immersion tests. To measure the hydrogen gas, samples polished with up to #4000 SiC paper were placed in a beaker and connected to a burette. Hydrogen was collected in the burette through a PVC pipe installed above the beaker equipped with a dropping funnel. The corrosion rate was calculated as follows [42]:

$$CR = \frac{\Delta m}{s \cdot t} \quad (1)$$

where:  $\Delta m$  is the mass loss (g) calculated from hydrogen evolution,  $s$  is the surface area (m<sup>2</sup>),  $t$  is the time of exposure (days). To determine the standard deviation of the measured data, three parallel samples were immersed from each material.

## 3. Results

### 3.1. Particle size and distribution

The shape and chemical analysis of the powder were analyzed by SEM/EDX and AAS. As shown in Fig. 1a, the particles of the repowdered alloy were spherical, and no agglomerates were observed. The morphology of a single particle is shown in Fig. 1b, and an EDX analysis revealed that the particle was composed of Mg, Al, and Zn (Fig. 1d and e). AAS results confirmed that no Li evaporation and/or oxidation was observed during atomization of the extruded ingot, and it was found to be around 7.4 wt.%; Zn depletion did not take place either during atomization (Table 1). The phase composition of the powder, namely  $\alpha$ (Mg),  $\beta$ (Li), AlLi, and MgLi<sub>2</sub>Al, is depicted in Fig. 2a. The cross-sectional SEM observations of the powder showed that pores were present in the outer regions of the particles (Fig. 1c), and the microstructure of the

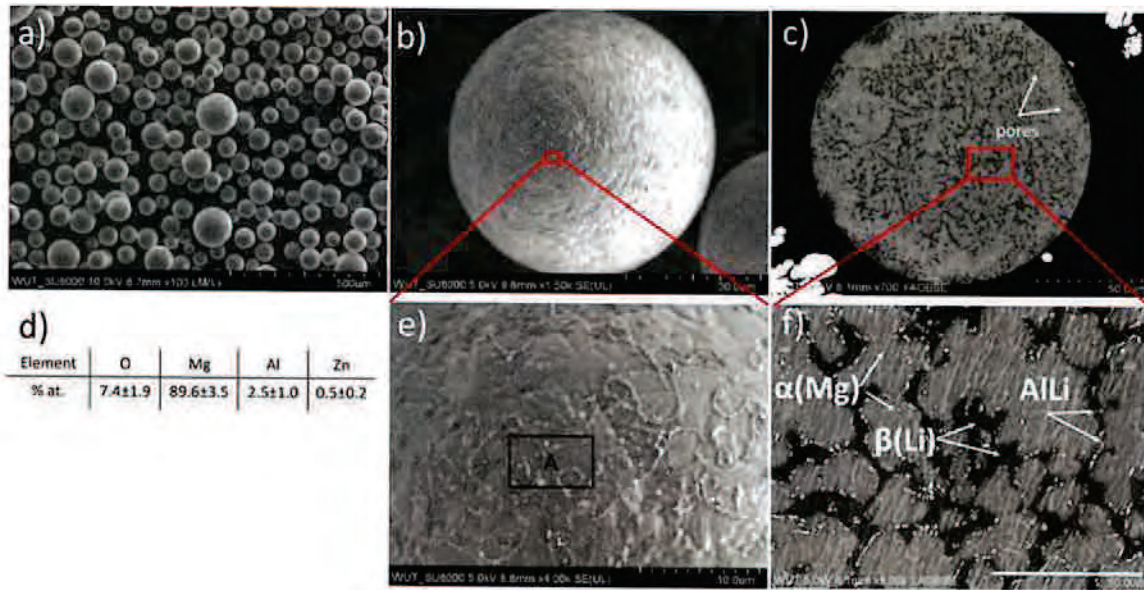


Fig. 1. SEM of powdered Mg-7.5Li-3Al-Zn alloy: a) the overall image of the powder, b) single particle image, c) the microstructure of the powder, d) EDX analyses made in area A, e) magnified area from the panel b), f) magnified area of the powder microstructure.

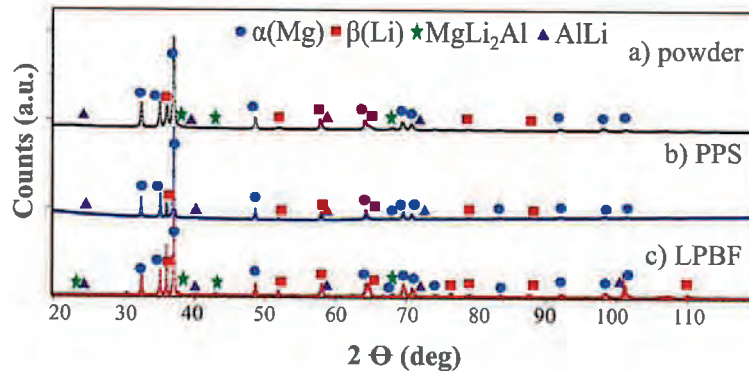


Fig. 2. XRD patterns recorded for a) powdered Mg-7.5Li-3Al-Zn, b) PPS alloy and c) LPBF - produced alloy.

Table 2

Relative phase composition (%) of the powder, PPS and LPBF alloys calculated based on XRD measurements.

	$\alpha(\text{Mg})$	$\beta(\text{Li})$	Precipitates
Powder	80	19	1
LPBF	58	39	3
PPS	85	13	2

particle was composed of  $\alpha(\text{Mg})$  and  $\beta(\text{Li})$  with the 80% of  $\alpha(\text{Mg})$  and 19% of  $\beta(\text{Li})$ , Table 2. AlLi particles were also visible in the microstructure of the powder (Fig. 1f). For sample consolidation, a powder with a size from 29 to 200  $\mu\text{m}$  was used with the frequency shown in Fig. 3. The average diameter of the particles was 70  $\mu\text{m}$ . 10% of the powder particles had a size below 48  $\mu\text{m}$ , while  $D_{90}$  is a parameter indicating that 90% of the particles had a size below 95  $\mu\text{m}$ .

### 3.2. Microstructure of the manufactured samples

As shown in Fig. 4a, the extruded Mg-7.5Li-3Al-Zn alloy exhibited a dual-phase microstructure where the dark phase was  $\beta(\text{Li})$  and the light one  $\alpha(\text{Mg})$ . The results published in our previous study [38] showed that the relative volume fractions of  $\alpha(\text{Mg})$  and  $\beta(\text{Li})$  were calculated to be 65% to 35%, respectively, and coarse white precipitates marked as P1, rich in Al, Zn, and Mn, were formed in the alloy. We also found AlLi,  $\text{MgLi}_2\text{Al}$ , and  $\text{Mg}_{17}\text{Al}_{12}$  in the extruded alloy. The LPBF- and PPS-produced alloys also had dual-phase structures; however, the shape, size, and distribution of the phases changed due to the various processing routes (compare Fig. 4a-c). It is worth to mention that the Li concentration in both alloys remained at the same level as indicated in the powder (Table 1). The microstructure of the 3D-

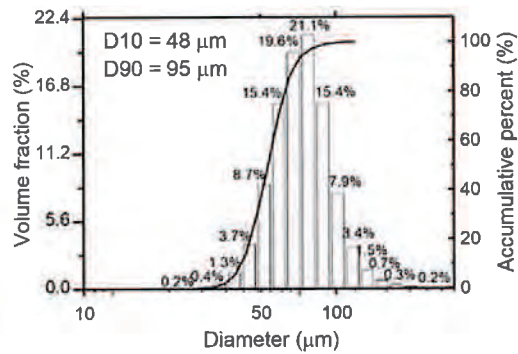


Fig. 3. PSD obtained using laser-scattering particle size distribution analyzer.

printed sample appeared as refined unevenly shaped grains, with the dark areas of  $\beta(\text{Li})$  surrounded by the  $\alpha(\text{Mg})$  matrix (Fig. 4b). Irregularly shaped pores (Fig. 4b) were also clearly distinguished in this microstructure. Coarse white precipitates P1 and the presence of tiny white AlLi areas were revealed (confirmed by combined SEM and XRD, magnified Figs. 4b and 2c, correspondingly). The PPS sintered alloy exhibited a microstructure similar to that presented by Dvorsky et al. [31] for WE43 sintered by spark plasma sintering. Individual particles were clearly visible, and the areas between them were not fully recrystallized (shown as “particle interface” in Fig. 4c). Inside each particle,  $\beta(\text{Li})$  surrounded by  $\alpha(\text{Mg})$  could be observed (magnified Fig. 4c). In the same Fig. 4c, irregularly shaped white coarse precipitates enriched with Al, Zn, and Mn were observed [38], and tiny AlLi precipitates could also be easily recognized (confirmed by XRD, Fig. 2b). During consolidation  $\text{MgLi}_2\text{Al}$  probably solutionized into the

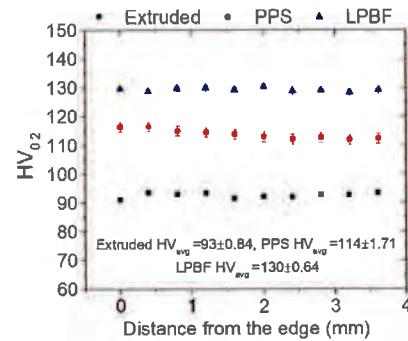


Fig. 5. Microhardness profiles of the extruded, PPS and LPBF-sintered alloys.

solid solution, therefore they were not detected in the PPS alloy. The relative concentration of the  $\alpha(\text{Mg})$  to  $\beta(\text{Li})$  changed depending on the different processing routes, being 85% to 13% for the PPS alloy, and 58% to 39% for the LPBF-printed material (Table 2). It can also be observed that together with the changing processing route the microstructure refinement occurred with the highest refinement obtained for LPBF sintered sample (Fig. 4). With the increasing microstructure refinement, microhardness of the alloys also changed, and it increased from 93 HV<sub>0.2</sub> for the extruded sample, to 114 HV<sub>0.2</sub> for the PPS and 130 HV<sub>0.2</sub> for the LPBF-sintered ones (Fig. 5).

Different manufacture methods led to the creation of the microstructures with significant differences clearly distinguishable in nanoscale. TEM observations revealed that nano-sized precipitations exist in both, LPBF and PPS fabricated

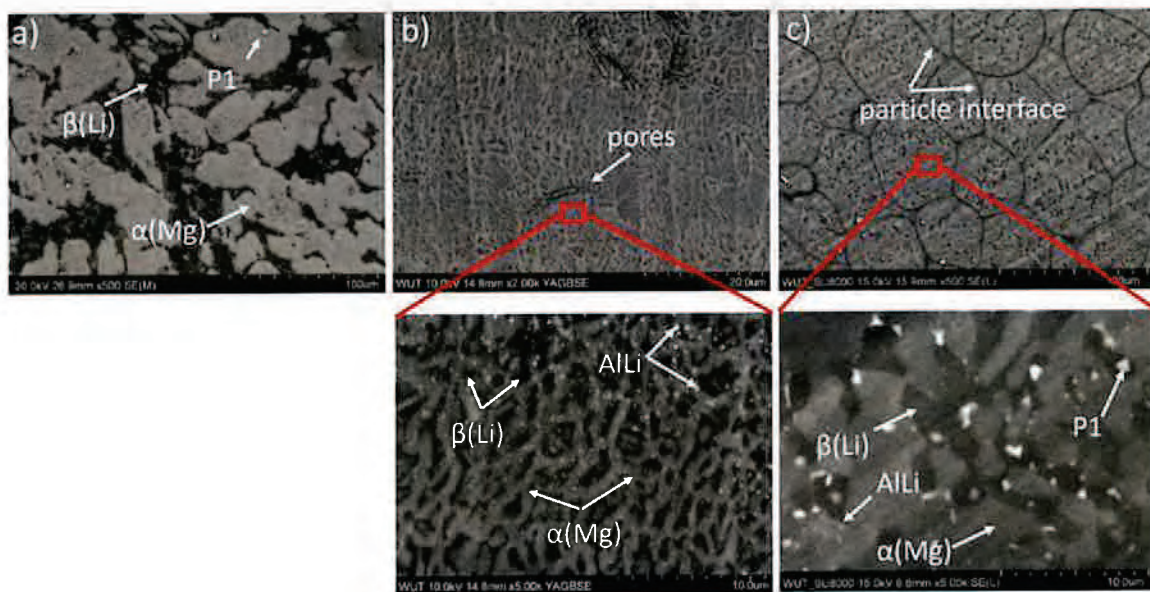


Fig. 4. SEM microstructure observations of the a) extruded alloy, b) LPBF-produced alloy, and c) PPS alloy.

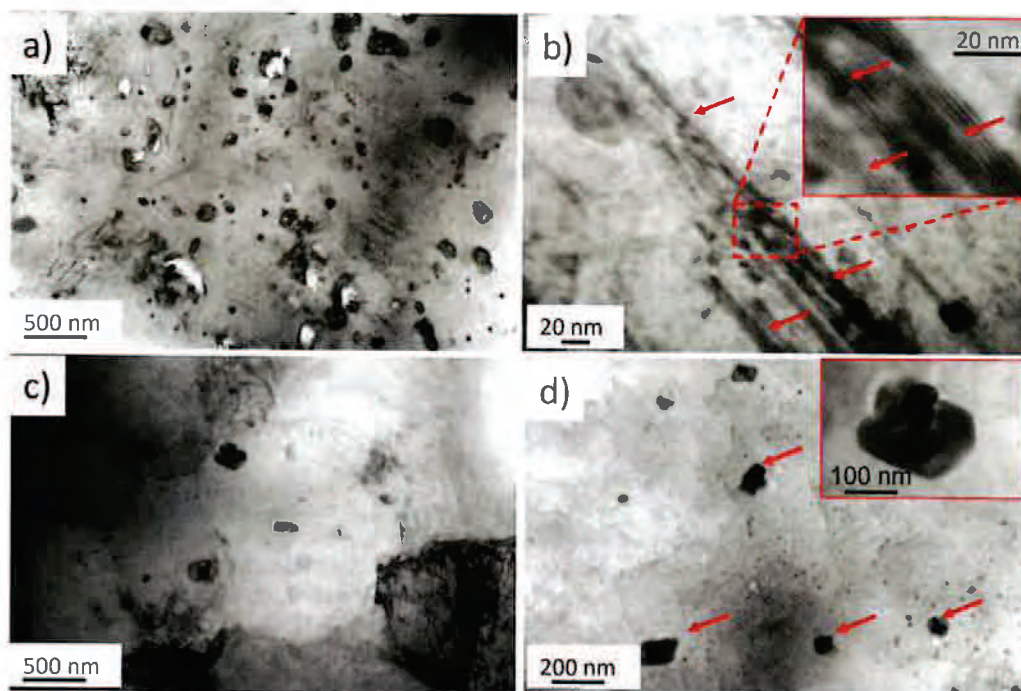


Fig. 6. TEM images in bright field obtained from the investigated alloys: a) and b) LPBF-produced alloy, c) and d) PPS sample.

samples, with the higher number of precipitates with the size of around 150 nm formed in the material fabricated by LPBF (Fig. 6a and c). There were many stacking faults in the LPBF processed material (marked by the red arrows in Fig. 6b), while formation of complex precipitates was observed in the PPS sintered sample (marked by the red arrows in Fig. 6d). The greyscale confirmed that within one location of such complex precipitate, various chemical composition could be distinguished (inset in Fig. 6d). Unfortunately, due to small size of the precipitates we were not able to perform diffraction.

Based on the XRD and SEM results, it can be stated that the precipitates formed in the alloys did not diverge qualitatively, but their quantitative distribution changed. The  $\mu$ CT measurements allowed the density and distribution of the coarse precipitates to be defined, as shown in Fig. 7. Those precipitates had a size between 5 and 30  $\mu\text{m}$ . This information combined with the SEM observations allowed us to identify the coarse precipitates with P1 in Fig. 4. The density of these precipitates formed in the traditionally extruded material was very low, being 30 precipitates per  $\text{mm}^3$  (Fig. 7a). When compared to the traditionally produced alloy, a higher density of the P1 precipitates was observed in the PPS alloy, and the highest number of precipitates was formed in the LPBF alloy ( $N = 310/\text{mm}^3$ ). Their distribution in the matrix of both alloys was nearly random.

One of the challenges faced during the production of Mg-based alloys using LPBF is minimizing porosity [43,44]. Therefore, an important issue in this research was to analyze the porosity of each of the produced materials. We did

not observe any pores formed in the extruded and PPS alloys, but a high number of closed pores were formed in the LPBF-produced alloy (Fig. 8). The calculated volume fraction of the pores was 3.51%, while their average size was found to be 28.3  $\mu\text{m}$  with a standard deviation of 18.2  $\mu\text{m}$ . We also calculated the maximum size of the pore, which was established to be 151.6  $\mu\text{m}$ . The final structure of the alloy resembled a sponge, with the pores being unreticulated. It must be mentioned that the porosity level of 3.51% in Mg-7.5Li-3Al-Zn was very high when compared other LPBF-prepared Mg alloys, such as AZ61 with a porosity of 0.8% [45], while for AZ31 a porosity level of less than 0.5% was achieved [44].

### 3.3. Corrosion behavior

The changes in open-circuit potential ( $E_{\text{OCP}}$ ) with respect to immersion time are given in Fig. 9a. The lowest values of  $E_{\text{OCP}}$  (around  $-1.42$  V/Ref) were characteristic for the extruded Mg-7.5Li-3Al-Zn alloy; the  $E_{\text{OCP}}$  of this alloy was fairly stable during the entire immersion time. The LPBF and PPS alloys exhibited higher values of  $E_{\text{OCP}}$ , which were comparable, oscillating just below  $-1.35$  V/Ref. The potentiodynamic curves shown in Fig. 9b were typical for alloys that undergo active dissolution, with a slight shift in the curve of the extruded alloy towards more negative values of potential. The parameters of corrosion potential ( $E_{\text{corr}}$ ) and corrosion current density ( $i_{\text{corr}}$ ) extrapolated using the Tafel method are depicted in Table 3. The lowest  $i_{\text{corr}}$  of 0.2  $\text{mA}/\text{cm}^2$  was calculated for the extruded alloy, while the other two alloys both

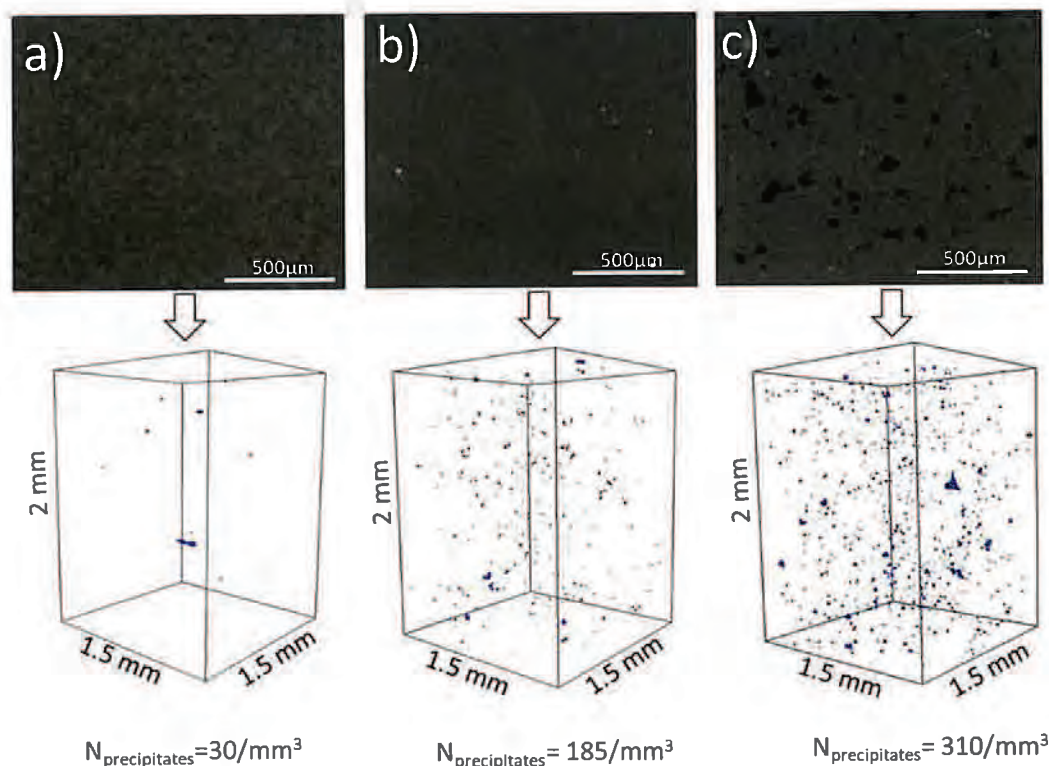


Fig. 7. Plane image of the microstructure with the corresponding 3D image showing density of pores in a) extruded Mg-7.5Li-3Al-Zn b) LPBF-produced alloy, c) PPS alloy.

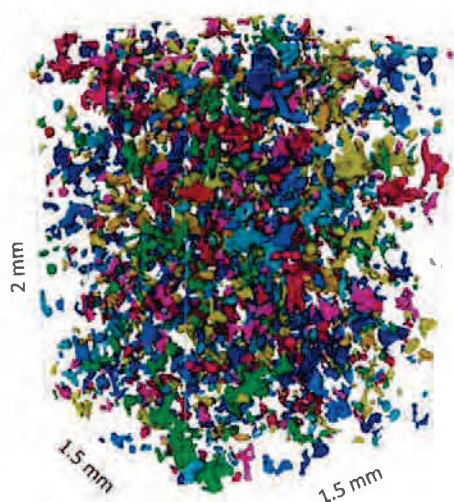


Fig. 8. Pore distribution in LPBF-produced alloy (volume fraction of pores = 3.51%, average size of the pores 28.3  $\mu\text{m}$ , stand. dev = 18.2  $\mu\text{m}$ , max size of the pore = 151.6  $\mu\text{m}$ ).

exhibited an  $i_{\text{corr}}$  of 0.5  $\text{mA}/\text{cm}^2$ . As proved by Birbilis et al. [46], because of the negative difference effect, potentiodynamic tests by themselves cannot describe the corrosion rate

Table 3

The electrochemical parameters extrapolated using Tafel method based on results from potentiodynamic polarization tests recorded in 0.01 M NaCl.

Mg-7.5Li-3Al-Zn	$E_{\text{corr}}$ (V/Ref)	$i_{\text{corr}}$ ( $\text{mA}/\text{cm}^2$ )
Extruded	-1.46	0.2
LPBF	-1.34	0.5
PPS	-1.36	0.5

Table 4

Calculated corrosion rate based on hydrogen evolution method.

Mg-7.5Li-3Al-Zn	Extruded	LPBF	PPS
Corrosion rate [ $\text{g}/(\text{m}^2\text{day})$ ]	$2.3 \times 10^3$	$3.7 \times 10^4$	$2.5 \times 10^4$
St. deviation	$6 \times 10^3$	$2 \times 10^3$	$8 \times 10^3$

of Mg-based alloys in an appropriate manner. Therefore, to have a wider view of the corrosion rates of the analyzed materials, corrosion rates were calculated based on hydrogen evolution. According to the results shown in Table 4, the samples produced via powder metallurgy methods had higher corrosion rates than the conventionally extruded alloy. The highest corrosion rate of  $3.7 \times 10^4 \text{ g}/(\text{m}^2\text{day})$  was calculated for the LPBF-printed alloy, a lower value of  $2.5 \times 10^4 \text{ g}/(\text{m}^2\text{day})$  was found for the PPS materials, and the lowest value was for the extruded alloy,  $2.3 \times 10^3 \text{ g}/(\text{m}^2\text{day})$ .

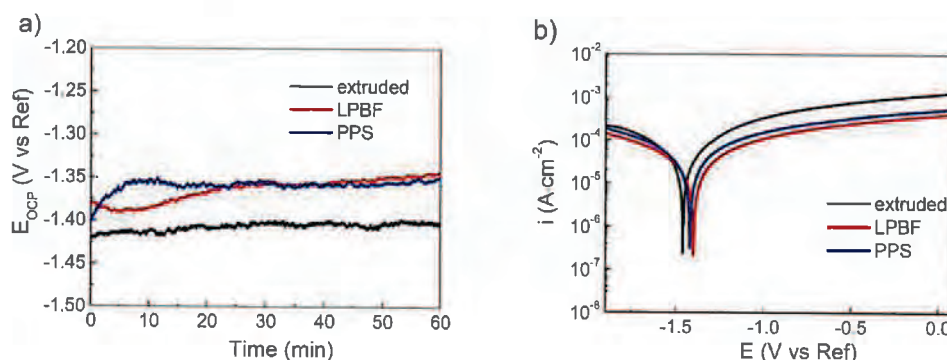


Fig. 9. Results delivered from electrochemical measurements performed in naturally aerated 0.01 M NaCl: a)  $E_{corr}$  evaluation over 1 h, b) potentiodynamic polarization curves.

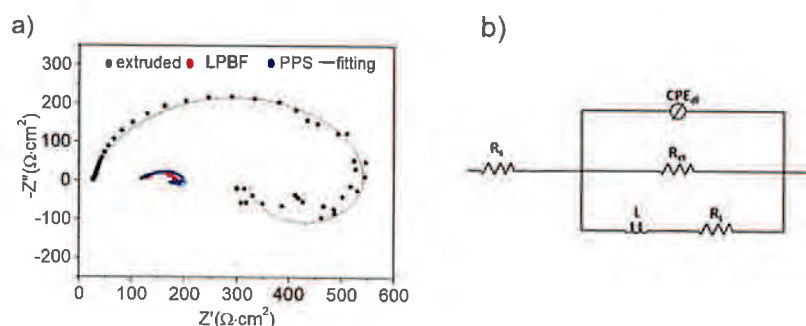


Fig. 10. The results of EIS measurements performed in naturally aerated 0.01 M NaCl: a) Nyquist plots, b) EEC used for data fitting.

Table 5  
Parameters delivered from fitting EIS data with the EEC presented in Fig. 8b.

Mg-7.5Li-3Al-Zn	$R_s$ ( $\Omega\ cm^2$ )	$R_{ct}$ ( $\Omega\ cm^2$ )	$CPE_{dl}$ ( $\mu F\cdot cm^{-2}$ )	$n_1$	$L$ (H $\cdot cm^2$ )	$R_L$ ( $\Omega\ cm^2$ )
Extruded	25	550	100	0.85	1000	650
LPBF	126	63	450	0.70	1000	250
PPS	116	94	450	0.55	777	188

The Nyquist plots presented in Fig. 10a confirmed the results from the potentiodynamic polarization and hydrogen evolution. Based on the radius of the capacitive loop, it can be stated that the extruded alloy had the highest corrosion resistance, while the LPBF and PPS alloys both had significantly lower values. In order to interpret the EIS results, the equivalent electrical circuit (EEC) shown in Fig. 10b was chosen. In this circuit,  $R_s$  is the solution resistance, while the charge transfer resistance and the electric double layer at the interface between the substrate and electrolyte are defined by  $R_{ct}$  and  $CPE_{dl}$ , respectively. The inductive character of the loop at low frequency is described by  $R_L$  and  $L$ , which stand for the resistance and the inductance related to the initiation of localized corrosion [47]. Data fitting results are given in Table 5. Since Mg-Li alloys are very active and the strong hydrogen evolution reactions that occur during immersion can disturb the results of the corrosion rate measurements, it is worthwhile to compare the corrosion rates calculated from the EIS results to those obtained from the hydrogen evolution method.

In the case of the EIS, the corrosion rate can be calculated based on the polarization resistance:

$$CR = 1/R_p \quad (1)$$

As proved by King et al. [48],  $R_p$  can be accurately determined based on the impedance of the EEC (herein presented in Fig. 8b):

$$\frac{1}{R_p} = \frac{1}{R_1} + \frac{1}{R_2} \quad (2)$$

Taking into consideration the EEC shown in Fig. 8b,  $R_p$  is a sum of:

$$\frac{1}{R_p} = \frac{1}{R_{ct}} + \frac{1}{R_L} \quad (3)$$

The measured values gave straightforward information about corrosion activity of the alloys, which followed the sequence: LPBF > PPS > extruded alloy (Table 6). These findings were highly consistent with the values of corrosion rate calculated from hydrogen evolution.



Fig. 11. Characterization of corroded surfaces of the conventionally extruded Mg-7.5Li-3Al-Zn alloy after 1 h of immersion in 0.01 M NaCl: a) surface covered with corrosion products, b) surface without corrosion products, c) surface without corrosion products shown at higher magnification.

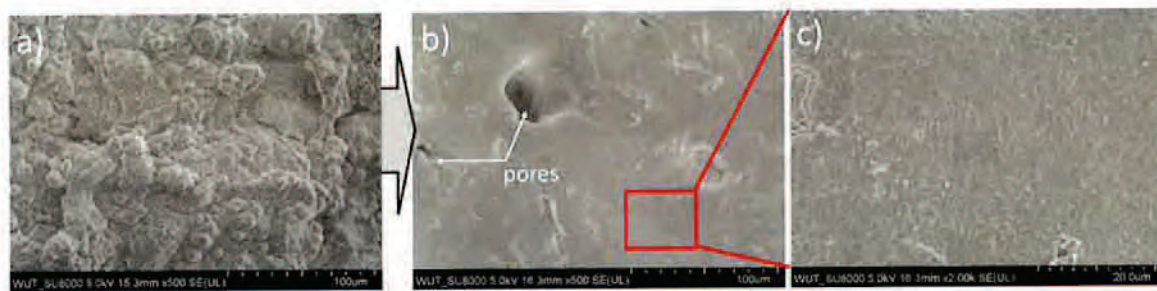


Fig. 12. Characterization of corroded surfaces of the LPBF-printed Mg-7.5Li-3Al-Zn alloy after 1 h of immersion in 0.01 M NaCl: a) surface covered with corrosion products, b) surface without corrosion products, c) surface without corrosion products shown at higher magnification.

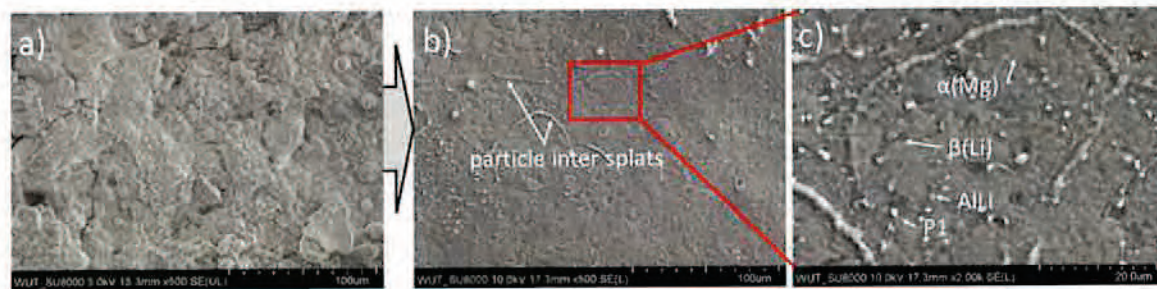


Fig. 13. Characterization of corroded surfaces of the PPS Mg-7.5Li-3Al-Zn alloy after 1 h of immersion in 0.01 M NaCl: a) surface covered with corrosion products, b) surface without corrosion products, c) surface without corrosion products shown at higher magnification.

Table 6  
Polarization resistance calculated based on EIS results.

Mg-7.5Li-3Al-Zn	$R_p$ ( $\Omega \text{ cm}^2$ )
Extruded	297
LPBF	50
PPS	62

### 3.4. Characterization of corroded surfaces

The SEM observations of corroded Mg-7.5Li-3Al-Zn alloys produced via different methods are shown in Figs. 11–13. Figs. 11a, 12a, and 13a present the surfaces of the samples covered with corrosion products after 1 h of immersion in aerated 0.01 M NaCl. The least intense corrosion products were

formed on the surface of the extruded samples (Fig. 11a). Thick layers of oxides were formed on the surfaces of the LPBF and PPS samples, with a more compact layer being formed on the LPBF-printed alloy than on the PPS one.

To obtain a better view on the corrosion mechanisms proceeding on the alloys' surfaces, the corrosion products were removed. Clearly, micro-galvanic corrosion between  $\alpha(\text{Mg})$  and  $\beta(\text{Li})$  was a dominant mechanism in the case of the extruded alloy (Fig. 11b and c), with  $\beta(\text{Li})$  being preferentially dissolved during immersion. A different situation was observed for the LPBF-printed alloy, where there was no distinguishable corrosion mechanism between the various phases; nevertheless, the printed alloy exhibited the lowest corrosion resistance among all the investigated materials. This weak corrosion resistance of the LPBF-printed alloy was a result of its

high porosity. Inside pores accumulated reactions change the pH of the solution, and local chemical variations cause rapid corrosion of these areas [49,50]. A very similar corrosion resistance was observed for the PPS alloy, where corrosion proceeded along unrecrystallized particle boundaries forming oxides, while micro-galvanic corrosion between  $\alpha(\text{Mg})$  and  $\beta(\text{Li})$  could also be seen.

#### 4. Discussion

In this study, a new approach for the manufacture of Mg-Li alloys was investigated; the microstructure and corrosion behavior of conventionally extruded Mg-7.5Li-3Al-Zn alloy were compared with those produced by powder-metallurgy techniques (LPBF and PPS). This research was carried out to elucidate the microstructure-dependent corrosion mechanisms proceeding in the dual-structured Mg-Li alloys produced from recycled powders, and the results of this work shows that powder metallurgy routes have a wide potential to be used for the manufacture of Mg-based alloys. Nevertheless, for the production of uniform, fully recrystallized, and pore-free materials, the parameters of the LPBF and PPS methods need to be further optimized and investigated.

As a result of consolidation powdered Mg-7.5Li-3Al-Zn alloy, bulk materials with various microstructures were produced. When compared to their conventionally extruded counterpart, both alloys exhibited refined microstructures with small AlLi and coarse Al,Zn,Mn enriched precipitates. The main drawback of the LPBF-printed alloy was its porosity, which had a detrimental effect on its properties. The presence of unrecrystallized particle boundaries in the PPS alloy was also unbeneficial from the point of view of corrosion. Nevertheless, the key differences observed in the microstructures of the formed alloys are important to understand, as the microstructure dictates the properties of Mg-based alloys.

As demonstrated in our previous study [38], the main corrosion mechanism in dual-structured Mg-7.5Li-3Al-Zn is the micro-galvanic corrosion processing between  $\alpha(\text{Mg})$  and  $\beta(\text{Li})$ , where the most active species (as a result of its greater reactivity) is  $\beta(\text{Li})$ . Corrosion in dual-phase structured Mg-Li alloys is clearly phase-size dependent, and when analyzing the corrosion mechanisms occurring in the Mg-7.5Li-3Al-Zn produced by LPBF and PPS, this statement is also accurate. Nevertheless, the results of this study showed that the corrosion mechanisms proceeding in these alloys were dependent not only on the variability of microstructural factors (qualitative factor), but also their number and distribution (quantitative factor). As shown, all the produced alloys were mainly composed of  $\alpha(\text{Mg})$  and  $\beta(\text{Li})$ . Not only did the relative volume fraction of  $\alpha(\text{Mg})$  and  $\beta(\text{Li})$  in each of the alloy change, but also the size of the phases, and this result is the most important factor which should be discussed when analyzing the corrosion performance of the investigated alloys. As shown in our previous study [38], the volume fraction of  $\alpha(\text{Mg})$  to  $\beta(\text{Li})$  plays a predominant role in the corrosion performance of the extruded alloy. The more uniform the proportion of

$\alpha(\text{Mg})$  compared to  $\beta(\text{Li})$ , the more uniform is the distribution of cathodic to anodic sites of corrosion. Consequently, if we were able to avoid porosity in the 3D-printed alloy, its corrosion resistance should surpass that of the conventionally extruded alloy. The volume ratios of  $\alpha(\text{Mg})$  to  $\beta(\text{Li})$  were 58% to -39% and 85% to -13% for the 3D and PPS alloys, respectively. The change in  $\alpha(\text{Mg})$  to  $\beta(\text{Li})$  volume ratio is related to the cooling rate of each method, where cooling rate during LPBF is significantly higher than cooling rate of PPS [51,52]. Additionally, the higher refinement and more uniform distribution of the  $\beta(\text{Li})$  in the  $\alpha(\text{Mg})$  matrix should support the corrosion resistance of the alloy, and LPBF is a proven technique which uses laser melting and rapid solidification to directly form fine-grained microstructure [53]. Nevertheless, the corrosion reactions occurring on the 3D-printed alloy were mainly affected by the porosity of the structure. Taking into consideration that corrosion inside the pores is increased by auto-catalytic processes because of the limited interchange of the solution inside the pores with that outside them, pores have a detrimental effect on the corrosive degradation of Mg alloys [54,55]. Moreover, in the case of the 3D printed alloy, the real surface area, because of additional internal surface area inside the pores, is significantly larger than the exposed geometric surface area. If the parameters of LPBF could be properly optimized to prevent the growth of porosity in the investigated alloys, there is a strong indication that superior corrosion resistance, because of the significant refinement of the  $\alpha(\text{Mg})$  and  $\beta(\text{Li})$  phases, may be achieved. The parameters for LPBF were chosen based on those actually used for AZ31 fabrication [53]. Due to the changed alloy chemistry, especially the presence of volatile Li, further studies have to be performed to obtain a poreless structure. Metals such as Zn cause similar problems during laser processing, and specialized machines with high gas flow rates should be used in further studies to address the issue of fuming and spatter-related porosity [50].

In the PPS alloy, microgalvanic corrosion between  $\alpha(\text{Mg})$  and  $\beta(\text{Li})$  occurred, but it was also supported by significant corrosion at the particle interfaces. Unfortunately, the parameters chosen during material consolidation did not give full microstructure recrystallization, and unrecrystallized particle-particle interfaces were still observed. Such locations, because of their different energy compared to the inner parts of the particles, are prone to corrosion. Since the size of the particles' interfaces was observed to have a major influence on the corrosion behavior of WE43 [31], the relationship between the size of the powder particles and the corrosion resistance of Mg-7.5Li-3Al-Zn should be further investigated.

Due to various techniques of powder metallurgy used for the materials fabrication, different microstructural features were formed in the alloys produced by LPBF and PPS. Results showed that high density of stacking faults were created during LPBF, and the microhardness of this alloy was also the highest among the investigated materials. Both factors can indicate that by using LPBF there is a possibility to produce Mg-3Al-7.5Li-Zn with superior mechanical properties [56].

## 5. Conclusions

- Powder metallurgy methods can be beneficial in the fabrication of ultrafine and fine-grained Mg-7.5Li-3Al-Zn alloys from atomized powders.
- Dual-phase microstructures with various degree of refinement and various volume ratio of  $\alpha$ (Mg) to  $\beta$ (Li) were formed in the alloys depending on the manufacture route. The parameters chosen for PPS of the atomized powders did not provide full recrystallization of the microstructure, and unrecrystallized particle boundaries were still present in the alloy.
- The microstructure-dependent corrosion of the produced alloys was increased by the presence of pores in the LPBF alloy and by the unrecrystallized particle boundaries revealed in the PPS alloy.
- The advantage of the LPBF and PPS processes lies in changing the proportion of  $\alpha$ (Mg) to  $\beta$ (Li), which when the complete consolidation of the material is achievable, may increase the corrosion resistance of dual-structured Mg-Li alloys.
- The high density of stacking faults can have detrimental effect in increasing microhardness of the Mg-Li materials produced using LPBF.
- The results show that powder metallurgy routes have a wide potential to be used for the manufacture of Mg-Li alloys.

## Declaration of Competing Interest

The authors declare that they have no known competing financial interests or personal relationships that could have appeared to influence the work reported in this paper.

## Data for reference

Raw data were generated at Faculty of Materials Science and Engineering, Warsaw University of Technology. Derived data supporting the findings of this study are available from the corresponding author [anna.dobkowska@pw.edu.pl](mailto:anna.dobkowska@pw.edu.pl) on request.

## References

- [1] A. Atrens, G.-L. Song, F. Cao, Z. Shi, P.K. Bowen, J. Magnes. Alloy. 1 (2013) 177–200, doi:10.1016/j.jma.2013.09.003.
- [2] A. Bussiba, A. Ben Artzy, A. Shtechman, S. Ifergan, M. Kupiec, Mater. Sci. Eng. A (2001), doi:10.1016/S0921-5093(00)01354-X.
- [3] H. Dong, F. Pan, B. Jiang, R. Li, X. Huang, Mater. Des. 65 (2015) 42–49, doi:10.1016/j.matdes.2014.08.033.
- [4] S.V.S. Prasad, S.B. Prasad, K. Verma, R.K. Mishra, V. Kumar, S. Singh, J. Magnes. Alloy. (2021), doi:10.1016/j.jma.2021.05.012.
- [5] P. Burke, G.J. Kipouros, D. Fancelli, V. Laverdiere, Can. Metall. Q. 48 (2009) 123–132, doi:10.1179/cm.2009.48.2.123.
- [6] V.S. Telang, R. Pemmada, V. Thomas, S. Ramakrishna, P. Tandon, H.S. Nanda, Curr. Opin. Biomed. Eng. 17 (2021) 100264, doi:10.1016/j.cobme.2021.100264.
- [7] T. Al-Samman, Acta Mater. 57 (2009) 2229–2242, doi:10.1016/j.actamat.2009.01.031.
- [8] Z. Drozd, Z. Trojanová, S. Kúdela, J. Alloy. Compd. 378 (2004) 192–195, doi:10.1016/j.jallcom.2004.01.040.
- [9] I. Shin, E. a. Carter, Acta Mater. 64 (2014) 198–207, doi:10.1016/j.actamat.2013.10.030.
- [10] K.K. Alaneme, E.A. Okotete, J. Magnes. Alloy. 5 (2017) 460–475, doi:10.1016/j.jma.2017.11.001.
- [11] J. Čapek, D. Vojtěch, Mater. Sci. Eng. C 35 (2014) 21–28, doi:10.1016/j.msec.2013.10.014.
- [12] P. Minárik, J. Stráský, J. Veselý, F. Lukáč, B. Hadzima, R. Král, J. Alloy. Compd. 742 (2018) 172–179, doi:10.1016/j.jallcom.2018.01.115.
- [13] P. Minárik, M. Zemková, M. Knappek, S. Šašek, J. Dittrich, F. Lukáč, J. Kozlík, R. Král, Materials 13 (2020), doi:10.3390/ma13183973.
- [14] L. Yang, T. Wang, C. Liu, Y. Ma, L. Wu, H. Yan, X. Zhao, W. Liu, J. Alloy. Compd. 870 (2021) 159473, doi:10.1016/j.jallcom.2021.159473.
- [15] M. Salehi, S. Maleksaeedi, M.L.S. Nai, M. Gupta, Addit. Manuf. 29 (2019) 100790, doi:10.1016/j.addma.2019.100790.
- [16] S. Han, M. Zielewski, D.M. Holguin, M.M. Parra, N. Kim, Appl. Sci. 8 (2018), doi:10.3390/app8081306.
- [17] M. Esmaily, Z. Zeng, A.N. Mortazavi, A. Gullino, S. Choudhary, T. Derra, F. Benn, F. D'Elia, M. Mütter, S. Thomas, A. Huang, A. Allanore, A. Kopp, N. Birbilis, Addit. Manuf. 35 (2020) 101321, doi:10.1016/j.addma.2020.101321.
- [18] J. Guo, Y. Zhou, C. Liu, Q. Wu, X. Chen, J. Lu, Materials 9 (2016), doi:10.3390/ma9100823.
- [19] M.P. Sealy, R. Karunakaran, S. Ortgies, G. Madireddy, A.P. Malshe, K.P. Rajurkar, CIRP Ann. 70 (2021) 179–182, doi:10.1016/j.cirp.2021.04.052.
- [20] X. Yang, J. Liu, Z. Wang, X. Lin, F. Liu, W. Huang, E. Liang, Mater. Sci. Eng. A 774 (2020) 138942, doi:10.1016/j.msea.2020.138942.
- [21] R. Karunakaran, S. Ortgies, A. Tamayol, F. Bobaru, M.P. Sealy, Bioact. Mater. 5 (2020) 44–54, doi:10.1016/j.bioactmat.2019.12.004.
- [22] H. Hyer, L. Zhou, G. Benson, B. McWilliams, K. Cho, Y. Sohn, Addit. Manuf. 33 (2020) 101123, doi:10.1016/j.addma.2020.101123.
- [23] R. Allavikuty, P. Gupta, T.S. Santra, J. Rengaswamy, Curr. Opin. Biomed. Eng. 18 (2021) 100276, doi:10.1016/j.cobme.2021.100276.
- [24] S. Liu, W.S. Yang, X. Shi, B. Li, S. Duan, H. Guo, J. Guo, J. Alloy. Compd. 808 (2019) 151160, doi:10.1016/j.jallcom.2019.06.261.
- [25] M. Mondet, E. Barraud, S. Lemonnier, J. Guyon, N. Allain, T. Grosdidier, Acta Mater. 119 (2016) 55–67, doi:10.1016/j.actamat.2016.08.006.
- [26] K. Wei, M. Gao, Z. Wang, X. Zeng, Mater. Sci. Eng. A 611 (2014) 212–222, doi:10.1016/j.msea.2014.05.092.
- [27] V. Manakari, G. Parande, M. Gupta, Selective laser melting of magnesium and magnesium alloy powders: a review, 2017. <https://doi.org/10.3390/met7010002>.
- [28] D. Zhang, S. Sun, D. Qiu, M.A. Gibson, M.S. Dargusch, M. Brandt, M. Qian, M. Easton, Adv. Eng. Mater. 20 (2018) 1–20, doi:10.1002/adem.201700952.
- [29] K. Wei, Z. Wang, X. Zeng, Mater. Lett. 156 (2015) 187–190, doi:10.1016/j.matlet.2015.05.074.
- [30] S. Gangireddy, B. Gwalani, K. Liu, E.J. Faierman, R.S. Mishra, Addit. Manuf. 26 (2019) 53–64, doi:10.1016/j.addma.2018.12.015.
- [31] D. Dvorský, J. Kubásek, M. Roudnická, F. Průša, D. Nečas, P. Minárik, J. Stráský, D. Vojtěch, J. Magnes. Alloy. 9 (2021) 1349–1362, doi:10.1016/j.jma.2020.12.012.
- [32] N.A. Zumdick, L. Jauer, L.C. Kersting, T.N. Kutz, J.H. Schleifenbaum, D. Zander, Mater. Character. 147 (2019) 384–397, doi:10.1016/j.matchar.2018.11.011.
- [33] S. Liu, H. Guo, Metals 10 (2020) 1–48, doi:10.3390/met10081073.
- [34] N. Madhuri, V. Jayakumar, M. Sathishkumar, Mater. Today Proc. 46 (2021) 8573–8577, doi:10.1016/j.matpr.2021.03.548.
- [35] C.L. Wu, W. Zai, H.C. Man, Mater. Today Commun. 26 (2021), doi:10.1016/j.mtcomm.2020.101922.
- [36] A. Kopp, T. Derra, M. Mütter, L. Jauer, J.H. Schleifenbaum, M. Voshage, O. Jung, R. Smeets, N. Kröger, Acta Biomater. 98 (2019) 23–35, doi:10.1016/j.actbio.2019.04.012.
- [37] Y. Yang, C. Lu, L. Shen, Z. Zhao, S. Peng, C. Shuai, J. Magnes. Alloy. (2021), doi:10.1016/j.jma.2021.04.009.

- [38] A. Dobkowska, B. Adamczyk – Cieślak, J. Kubásek, D. Vojtěch, D. Kuc, E. Hadasik, J. Mizera, J. Magnes. Alloy. 9 (2021) 467–477, doi:10.1016/j.jma.2020.07.007.
- [39] M.J. Kruszewski, R. Zybala, M.C. Ciupiński, B. Adamczyk-Cieślak, A. Michalski, M. Rajska, K.J. Kurzydowski, J. Electron. Mater. 45 (2016) 1369–1376, doi:10.1007/s11664-015-4037-5.
- [40] A.D. Sudholz, K. Gusieva, X.B. Chen, B.C. Muddle, M.A. Gibson, N. Birbilis, Corros. Sci. 53 (2011) 2277–2282, doi:10.1016/j.corsci.2011.03.010.
- [41] N.T. Kirkland, J. Lespagnol, N. Birbilis, M.P. Staiger, Corros. Sci. 52 (2010) 287–291, doi:10.1016/j.corsci.2009.09.033.
- [42] ASTM B90/B90M-12, Standard specification for magnesium-alloy sheet and plate, 2012. [https://doi.org/10.1520/B0090\\_B0090M-12](https://doi.org/10.1520/B0090_B0090M-12).
- [43] A. Pawlak, M. Rosienkiewicz, E. Chlebus, Arch. Civ. Mech. Eng. 17 (2017) 9–18, doi:10.1016/j.acmc.2016.07.007.
- [44] N. Sezer, Z. Evis, M. Koç, J. Magnes. Alloy. 9 (2021) 392–415, doi:10.1016/j.jma.2020.09.014.
- [45] S. Liu, H. Guo, Mater. Lett. 265 (2020) 127463, doi:10.1016/j.matlet.2020.127463.
- [46] N. Birbilis, A.D. King, S. Thomas, G.S. Frankel, J.R. Scully, Electrochim. Acta 132 (2014) 277–283, doi:10.1016/j.electacta.2014.03.133.
- [47] C.Q. Li, D.K. Xu, X.B. Chen, B.J. Wang, R.Z. Wu, E.H. Han, N. Birbilis, Electrochim. Acta 260 (2018) 55–64, doi:10.1016/j.electacta.2017.11.091.
- [48] A.D. King, N. Birbilis, J.R. Scully, Electrochim. Acta 121 (2014) 394–406, doi:10.1016/j.electacta.2013.12.124.
- [49] A. Dobkowska, M.D.H. Castillo, J.P. Turnbull, S. Ramamurthy, D. Zagidulin, D.E. Moser, M. Behazin, P.G. Keech, D.W. Shoesmith, J.J. Noël, Corros. Sci. 192 (2021), doi:10.1016/j.corsci.2021.109778.
- [50] F. Xie, X. He, S. Cao, M. Mei, X. Qu, Electrochim. Acta. 105 (2013) 121–129, doi:10.1016/j.electacta.2013.04.105.
- [51] P.A. Hooper, Addit. Manuf. 22 (2018) 548–559, doi:10.1016/j.addma.2018.05.032.
- [52] F. Zhang, M. Reich, O. Kessler, E. Burkel, Mater. Today 16 (2013) 192–197, doi:10.1016/j.mattod.2013.05.005.
- [53] S. Liu, H. Guo, Mater. Lett. 265 (2020) 127463, doi:10.1016/j.matlet.2020.127463.
- [54] F. Cao, Z. Shi, G.L. Song, M. Liu, M.S. Dargusch, A. Atrens, Corros. Sci. 94 (2015) 255–269, doi:10.1016/j.corsci.2015.02.002.
- [55] E. Aghion, Y. Perez, Mater. Charact. 96 (2014) 78–83, doi:10.1016/j.matchar.2014.07.012.
- [56] W.W. Jian, G.M. Cheng, W.Z. Xu, H. Yuan, M.H. Tsai, Q.D. Wang, C.C. Koch, Y.T. Zhu, S.N. Mathaudhu, Mater. Res. Lett. 1 (2013) 61–66, doi:10.1080/21663831.2013.765927.

Potwierdzenie zgłoszenia patentowego P.437777



**Kancelaria Ogólna**

Warszawa, 2021-05-05

Nasz znak: P.437777

Wasz znak: 49004

**POTWIERDZENIE**

Urząd Patentowy RP stwierdza, że dnia 2021-05-05 przyjęto w formie elektronicznej wnioszek o udzielenie patentu na wynalazek:

**Sposób wytwarzania stopów Mg-Li-Al-Zn o ultra niskiej gęstości i ich zastosowanie**

Zgłoszenie oznaczono numerem: **P.437777**

**[WIPO ST 10/C PL437777]**

Zgłaszający: **POLITECHNIKA WARSZAWSKA, Warszawa, Polska**

Dokument wystawiony automatycznie przez system teleinformatyczny UPRP.

**Pouczenie:**

1. Strony oraz ich przedstawiciele i pełnomocnicy mają obowiązek zawiadomić Urząd o każdej zmianie swojego adresu. W razie zaniedbania tego obowiązku doręczenie pisma pod dotychczasowym adresem ma skutek prawny (art. 41 kpa).
2. O zgłoszeniu wynalazku Urząd Patentowy dokonuje ogłoszenia niezwłocznie po upływie 18 miesięcy od daty pierwszeństwa do uzyskania patentu. Zgłaszający może w okresie 12 miesięcy od daty pierwszeństwa złożyć wniosek o dokonanie ogłoszenia w terminie wcześniejszym (art. 43 ustawy z dnia 30 czerwca 2000r. Prawo własności przemysłowej (Dz. U. z 2021 r. poz. 324).
3. W korespondencji należy powoływać się na nr P.437777.

**Klauzula informacyjna:**

Zgodnie z art. 13 ust. 1 i 2 Rozporządzenia Parlamentu Europejskiego i Rady (UE) 2016/679 z dnia 27 kwietnia 2016 r. w sprawie ochrony osób fizycznych w związku z przetwarzaniem danych osobowych i w sprawie swobodnego przepływu takich danych oraz uchylenia dyrektywy 95/46/WE (dalej RODO) Urząd Patentowy Rzeczypospolitej Polskiej informuje, że:

1. Administratorem Pani/Pana danych osobowych jest Urząd Patentowy Rzeczypospolitej Polskiej z siedzibą w Warszawie, adres: al. Niepodległości 188/192, 00-950 Warszawa, skrytka pocztowa 203;
2. Inspektor Ochrony Danych, dane kontaktowe: adres: al. Niepodległości 188/192, 00-950 Warszawa, tel. bezpośredni (022) 579 00 25, fax (022) 579 00 01, e-mail: iod@uprp.pl;
3. Pani/Pana dane osobowe przetwarzane będą w celu realizowania zadań Urzędu Patentowego RP określonych przepisami ustawy z dnia 30 czerwca 2000 r. Prawo własności przemysłowej;

4. Podstawą prawną przetwarzania Pani/Pana danych osobowych jest ustawa z dnia 30 czerwca 2000 r. Prawo własności przemysłowej, rozporządzenia wykonawcze do ww. ustawy, umowy międzynarodowe oraz art. 6 ust. 1 lit. c RODO;
5. Pani/Pana dane osobowe mogą być przekazywane do podmiotów publicznych na zasadach obowiązujących w przepisach prawa oraz organizacjom międzynarodowym i organom unijnym, zgodnie z obowiązującymi przepisami prawa i umowami międzynarodowymi, po upływie terminów zastrzeżonych dla nieujawniania informacji o zgłoszeniu;
6. Pani/Pana dane osobowe będą przechowywane przez okres zgodny z zasadami archiwizacji dokumentów w Urzędzie Patentowym RP;
7. Posiada Pani/Pan prawo żądania dostępu do treści swoich danych osobowych, prawo ich sprostowania oraz prawo do ograniczenia ich przetwarzania;
8. Przysługuje Pani/Panu prawo wniesienia skargi do organu nadzorczego właściwego w zakresie ochrony danych osobowych gdy uzna Pani/Pan, że przetwarzanie Pani/Pana danych osobowych narusza przepisy RODO;
9. Podanie przez Panią/Pana danych osobowych jest wymogiem ustawowym niezbędnym do dalszego procedowania przez Urząd Patentowy RP.

Publikacja potwierdzająca inne osiągnięcia naukowe dotycząca opisu  
odporności powłok miedzianych stosowanych na kontenerach  
stalowych do składowania odpadów radioaktywnych w zależności od  
metod ich wytwarzania



ELSEVIER

Contents lists available at ScienceDirect

Corrosion Science

journal homepage: [www.elsevier.com/locate/corsci](http://www.elsevier.com/locate/corsci)

## A comparison of the corrosion behaviour of copper materials in dilute nitric acid

Anna Dobkowska<sup>a,\*</sup>, Millicent Dayle H. Castillo<sup>a</sup>, Joseph P. Turnbull<sup>a</sup>, Sridhar Ramamurthy<sup>b</sup>, Dmitriy Zagidulin<sup>a</sup>, Desmond E. Moser<sup>c</sup>, Mehran Behazin<sup>d</sup>, Peter G. Keech<sup>d</sup>, David W. Shoemith<sup>a,b</sup>, James J. Noël<sup>a,b</sup>

<sup>a</sup> Department of Chemistry, The University of Western Ontario, London N6A 5B7, Canada

<sup>b</sup> Surface Science Western, The University of Western Ontario, London N6G 0J3, Canada

<sup>c</sup> Department of Earth Sciences, The University of Western Ontario, London N6A 5B7, Canada

<sup>d</sup> Nuclear Waste Management Organization, Toronto M4T 2S3, Canada

### ARTICLE INFO

#### Keywords:

Copper  
Acid corrosion  
SEM  
SIMS

### ABSTRACT

The corrosion of a number of coarse- and fine-grained copper materials has been studied in an aerated aqueous nitric acid (100 mM) solution. The materials properties and the consequences of corrosion were characterized by scanning electron microscopy, electron back scatter diffraction and confocal laser scanning microscopy. The corrosion of the coarse-grained materials was shown to be strongly influenced by the crystallographic orientations of grains. For fine-grained materials grain boundary etching at high angle grain boundaries and grain boundary pores (for cold sprayed copper) overrode the influences of texture on the corrosion rate.

### 1. Introduction

The microstructure of polycrystalline materials often has an important influence on corrosion, as has been widely described in the literature [1–8]. Corrosion initiation is commonly controlled by metallurgical factors and the inhomogeneity of structures, with the subsequent propagation mostly controlled by kinetic factors (i.e., polarization and diffusion) [9–11]. A number of studies have been devoted to investigating the effect of grain-size on corrosion of face-centered cubic (fcc) metals [3,12–20], and a review of this literature shows that the corrosion resistance improves with a reduction in grain size from coarse-grained (CG) to nanocrystalline (NC). Since grain boundaries can act as corrosion barriers, the more refined the microstructure, the higher the expected overall corrosion resistance [13,21].

An interesting insight into microstructure-dependent corrosion of metals was made by Gollapudi [22], who showed that, in a non-passivating environment, a bimodal microstructure with a higher volume fraction of coarse grains may increase the corrosion resistance of metals. These systematic studies were carried out to find the relationship between grain refinement and corrosion rate for fcc-structured metals. However, this relationship may be disrupted by other microstructural factors such as crystallographic orientation, grain boundary

distribution, discontinuities (voids or pores), or internal stress/strain that may be introduced into the material during fabrication or post-processing. Studies on the influence of grain orientation on corrosion [23–31] prove that differences in the electrochemical behaviour of grains in coarse-grained, fine-grained, and nanocrystalline materials are related to differences in the crystallographic orientations. Martinez-Lombardia et al. [23] found that for Cu in the active state,  $\langle 111 \rangle$  grains were the most reactive which is counter to expectations based on surface energies and work functions. It was also shown that the reactivity of  $\langle 100 \rangle$  grains decreased when located between  $\langle 111 \rangle$  grains, an observation consistent with those of Lapeire et al. [24].

The grain boundary misorientation angle also plays an important role in determining the corrosion resistance; with grain boundaries possessing a misorientation angle higher than  $15^\circ$  corroding faster than those with a misorientation angle below  $15^\circ$  [8,16,32]; i.e., the effect of the “special” coincidence site lattice (CSL) boundaries is a key feature [26,33–37]. It has been suggested that for low stacking fault fcc-structured metals, a higher fraction of low- $\Sigma$  CSL boundaries may enhance the corrosion resistance, especially for intergranular corrosion [33,35]. A new insight into the influence of grain boundary properties on Cu corrosion is given by Chen et al. [27], who showed that a thicker

\* Corresponding author.

E-mail address: [anna.dobkowska@pw.edu.pl](mailto:anna.dobkowska@pw.edu.pl) (A. Dobkowska).

<https://doi.org/10.1016/j.corsci.2021.109778>

Received 23 March 2021; Received in revised form 13 August 2021; Accepted 14 August 2021

Available online 17 August 2021

0010-938X/© 2021 Elsevier Ltd. All rights reserved.

passive film was formed at random grain boundaries than at coherent twin boundaries. The effect of the porosity on the corrosion resistance of fcc-structured Cu produced by cold spray deposition has also been investigated. [38], but there is a lack of evidence showing how changes in local chemistry within pores influences corrosion reactions.

The resistance of polycrystalline fcc metals to corrosion is complex and involves a number of factors for which a complete understanding has not yet been realized. Most notably the consideration of texture and grain size distribution becomes important when designing long-lived structures such as used fuel containers (UFC) for the permanent disposal of high-level nuclear waste. The UFC is a key barrier in the multi-barrier systems proposed in Canada and many other countries for the long-term containment and isolation of used nuclear fuel in a deep geologic repository (DGR). In the proposed Canadian design, used nuclear fuel will be sealed in UFCs fabricated from carbon steel vessels (ASME SA516 Gr.70) covered with an approximately 3 mm-thick Cu coating, applied by electrodeposition and cold spray deposition techniques [39,40]. For the large majority of their lifetime in a DGR, the UFCs will be exposed to anoxic conditions. However, for a brief initial period after emplacement, oxygen will be present in the DGR, trapped within the filling and sealing materials during UFC emplacement. During this relatively short period, which may last from a few weeks to a few decades, oxides of Cu may be present on the surface of the UFC [41]. An understanding of the early, oxygen-initiated corrosion behaviour of the Cu coating is important to ensure safe, long-term disposal [42–46], although the range of oxidic damage is expected to be only on the order of tens or hundreds of micrometres.

As noted above, a range of evolving exposure conditions is anticipated over the lifetime of a DGR (i.e., 1 million years). Reviews by King et al. [47] and Hall et al. [48] summarize the current understanding of container corrosion behaviour as DGR conditions evolve. In the early stages of container emplacement in a DGR, warm, humid air conditions could prevail, and with a current Canadian container thinner than those of previous container designs, gamma radiation fields on the outer surface of the container could be more significant. This could lead to the production of small amounts of HNO<sub>3</sub> by the radiolysis of aerated vapour [49,50], which may lead to small amounts of corrosion. The kinetics of this corrosion process have been studied by Turnbull et al. [51–53].

The current work compares the influence of metallurgical features such as grain size, grain distribution and the crystallographic orientations of grains, on the corrosion behaviour of pure Cu materials fabricated by various techniques. To determine how these microstructural features could influence corrosion, the extent and distribution of corrosion damage on Cu specimens after exposure to aerated HNO<sub>3</sub> solution were analysed.

## 2. Materials

Five different Cu materials were examined in this work: P-doped O-free wrought Cu (SKB Cu), electrolytic tough pitch Cu (ETP Cu), commercial wrought Cu (CW Cu), electrodeposited Cu (ED Cu), and cold spray deposited Cu (CS Cu).

The SKB Cu is a P-doped O-free wrought Cu supplied by the Swedish Nuclear Fuel and Waste Management Company (SKB, Solna, Sweden). The ETP Cu, in the form of a plate (30 cm × 30 cm × 0.5 cm), was purchased from Rolled Alloys Inc., Mississauga, Canada, and the CW Cu was a typical commercially available Cu plate material (10 cm × 3 cm × 0.5 cm, manufacturer unknown). The ED Cu was supplied in the form of a 3-mm-thick Cu coating on a 15 cm × 15 cm × 0.4 cm A516 Gr. 70 steel block substrate, by Integran Technologies Inc., Mississauga, Canada. The CS Cu was manufactured by the National Research Council of Canada, Boucherville, Canada, also in the form of a 3-mm coating on a steel substrate (A516 Gr. 70). The CS Cu was annealed at 350 °C for 1 h after deposition to relieve stresses [42,43,54].

## 3. Experimental methodology

### 3.1. Microstructural characterization

The microstructure of each material was examined by electron backscatter diffraction (EBSD) in the Zircon and Accessory Phase Laboratory, The University of Western Ontario, using a Hitachi S6600 scanning electron microscope (SEM) equipped with an Oxford Symmetry Nano EBSD detector. Cu coupons were mounted in an epoxy resin, ground with SiC papers (#600, #1200, #2500 and #4000), and then polished using 3 and 1 μm diamond suspensions in a glycol-based lubricant. Specimens were ultrasonically rinsed in methanol before electropolishing at room temperature using an electrolyte composed of HNO<sub>3</sub>:CH<sub>3</sub>OH = 1:3 by volume (HNO<sub>3</sub>, ACS reagent, 68–70%; CH<sub>3</sub>OH, ACS reagent). Using a GPR-H Series Linear D.C. Power Supply, a voltage of 10 V was applied for 10 s to specimens immersed in this solution. Prior to transfer to the SEM chamber, the surface of the specimens was flat-milled with an Ar ion beam for 6 min, using an IM4000 Hitachi Plus Ion Milling System. The EBSD data were acquired using AZtecHKL software (Oxford Instruments NanoAnalysis Group). Measurements were performed with a step scan of 0.5 μm and a working distance of 22.3 mm. The recorded data were analyzed using Oxford HKL Channel 5 software. The orientation images are shown as inverse pole figure (IPF) maps. In a polycrystalline material, two types of grain boundaries (GBs) can be distinguished. If the angle between two adjacent grains is below 15°, then the GBs are defined as low-angle grain boundaries (LAGBs) and marked in green in IPF maps. If the neighboring grains are misoriented by more than 15°, then the GB is defined as a high-angle grain boundary (HAGB) and marked in red in the IPF maps. Non-indexed areas are marked in black. The IPF maps and corresponding GB distributions obtained are shown after the processing, except for the data acquired for CS Cu which is presented in its original form.

To determine the average grain size and the relative frequency of grain sizes, we used a post-processing procedure involving a grain tolerance angle of 2° and a cut-off limit of 10 pixels. The grain size was determined using a linear intercept method. To estimate the variation in grain sizes, the coefficient of variation (C<sub>v</sub>) was calculated using the following formula:

$$C_v = \frac{\sigma}{\mu}$$

where  $\sigma$  is the standard deviation and  $\mu$  is the average grain size dimension.

To further determine the microstructure of CS Cu, SEM observations were performed on the same specimen used for EBSD measurements. The images were captured using a Hitachi S4500 field emission SEM. Dynamic secondary ion mass spectrometry (D-SIMS) was performed to determine whether oxygen was present between splats of CS Cu. Measurements were performed using a Cameca IMF-6f SIMS and an area of 250 μm × 250 μm was sputtered.

The microstructure of SKB Cu was additionally observed using an optical microscope (6000 VHS Keyence), after polishing and chemical etching using 20 mL NH<sub>4</sub>OH + 20 mL H<sub>2</sub>O + 10 mL 3% H<sub>2</sub>O<sub>2</sub>.

### 3.2. Electrochemical corrosion tests

For electrochemical measurements specimens with the dimensions 1 cm × 1 cm × 0.5 cm were cut from plate materials, tapped, threaded, and connected to steel rods covered with PTFE heat-shrink tubing. Specimens were ground with SiC papers (#600, #1200, #2500 and #4000) and polished with 3 and 1 μm diamond suspensions in a glycol-based lubricant. Prior to each electrochemical measurement, specimens were rinsed with Type-1 water, ultrasonically cleaned in methanol, and then dried with high purity Ar gas.

In this study experiments were conducted in solutions containing

100 mM HNO<sub>3</sub> to investigate the accelerated corrosion of copper surface exposed to maximum accumulated concentration of HNO<sub>3</sub> anticipated in a DGR [55], and also to facilitate the comparison with previous studies. The  $E_{\text{corr}}$  was recorded as a function of immersion time. After 24 h of immersion of coupons in an aerated HNO<sub>3</sub> solution, the polarization resistance ( $R_p$ ) of each specimen was determined by linear polarization resistance (LPR) measurements performed over a potential range of  $E_{\text{corr}} \pm 5$  mV, at a scan rate of 10 mV/min. Experiments were performed in a large volume, three-compartment electrochemical cell. A saturated calomel electrode (SCE) was used as the reference electrode (RE), a Pt wire as a counter electrode (CE), and a polished Cu specimen with 1 cm<sup>2</sup> of exposed area as a working electrode (WE). All electrochemical measurements were performed using a Solartron Analytical Modulab. The 100 mM HNO<sub>3</sub> solution was prepared using HNO<sub>3</sub> stock solution (ACS reagent, 68–70%, Fisher Scientific) and Type-1 water (18.2 MΩ·cm). To ensure the reproducibility of the results the experiments were repeated at least twice.

### 3.3. Characterization of corroded surfaces

After electrochemical measurements specimens were examined using a Hitachi SU3500 Variable Pressure SEM. The surface topography was measured and depth profiling of corroded surfaces performed using confocal laser scanning microscopy (CLSM, Zeiss LSM800 For Materials). The collected data are shown in the form of 3D images, with the attached colour scale indicating depth, and as surface profiles. In depth profiling, the deepest point detected by CLSM was adopted as zero on the ordinate (depth) axis. Imaging was performed with a 405-nm excitation laser. All measurements were performed with a 0.2 μm interval between slices. Quantitative analyses of surface profiles were based on measurements of the arithmetic mean height ( $S_a$ ) and maximum height ( $S_z$ ), where  $S_a$  describes the mean surface roughness, and  $S_z$  the height difference between the highest peak and the deepest valley within the analyzed area [56].

## 4. Results

### 4.1. Microstructural characterization

An optical image, IPF map and GB distribution for a polished and etched SKB Cu surface are shown in Fig. 1. As observed in Fig. 1a, the microstructure is characterized by coarse grains with an average size of 29 μm. The grains are randomly oriented, and almost all detected GBs reside between grains whose orientation differs by more than 15°, Fig. 1b. (Note that, due to the large grain size and the low number of grains within the field of view, the grain size distribution for this material is not shown in Fig. 3 with those of the other materials). A detailed

characterization of the microstructure of SKB Cu has been published by Li et al. [57].

ETP Cu has a random texture and exhibits a heterogeneous microstructure comprised of grains of different sizes, Fig. 2, with the majority of grain boundaries being HAGBs, Fig. 2b. The distribution of grain sizes, Fig. 3, shows that grains with an equivalent dimension below 5 μm comprise 55% of the analyzed population, and those with an equivalent dimension between 5 and 10 μm make up 31% of the population. Bigger grains contribute much smaller fractions of the population. The average grain size was estimated to be 6.1 μm, with a  $C_v$  value of 0.8.

Of the materials analyzed, CW Cu has the broadest grain size distribution, as indicated by a  $C_v$  value of ~ 1, with randomly oriented grains with an average size of 7.8 μm, Fig. 3 and Fig. 4a. HAGBs are present but LAGBs are still observed, Fig. 4b. Grains measuring below 5 μm make up 55% of all analyzed grains, with those between 5 and 10 μm comprising 20%, Fig. 3. Grains with larger sizes are also present, but in only minor amounts.

The ED Cu has a well-refined microstructure, Fig. 5, with an average grain size of 2.8 μm, Fig. 3, with the  $C_v$  value of 0.4 indicating only a small variation in grain size. Of the analyzed population, 94% of grains have an equivalent dimension below 5 μm, with those between 5 and 10 μm comprising 6% of the population. As shown by the dominance of blue and green regions, respectively, in the IPF map, Fig. 5a, the vast majority of the grains are oriented to (111) and (101). The grains oriented to (001) are smaller, and randomly distributed within the whole analyzed area. Mostly HAGBs were formed, Fig. 5b. Such a refined microstructure would provide greater strength in the Cu coating, which is critically important in optimizing the mechanical properties of the UFC [57,58].

The most refined microstructure, with an average grain size of 2.7 μm, was observed in CS Cu. During the low temperature annealing, recrystallization occurred [43,59], and ultrafine and nearly equiaxed grains were formed, Fig. 6a. The grain size in CS Cu is reasonably homogeneous ( $C_v \sim 0.4$ ), Fig. 3. As observed for ED Cu, the smallest grains, with an equivalent dimension below 5 μm, comprised the great majority of the analyzed population (95%), with the remainder between 5 and 10 μm. HAGBs were formed around recrystallized grains, but compared to ED Cu, a significantly larger number of LAGBs are present, Fig. 6b.

The indexation rate from EBSD data was 77%, with the vast majority of the non-indexed fraction due to the presence of microstructural defects (pores formed during deposition) [43]. Within the structure, pores can be observed, Fig. 7a. The observed pores can be classified according to their different shapes. Large pores, located at triple points, Fig. 7b, are around 4 μm in size. The depth of several randomly selected pores was approximately measured by subtraction of the working distance of the microscope measured when focusing on the bottom of the pore from that measured when focusing on the surface. This yielded pore depths in the

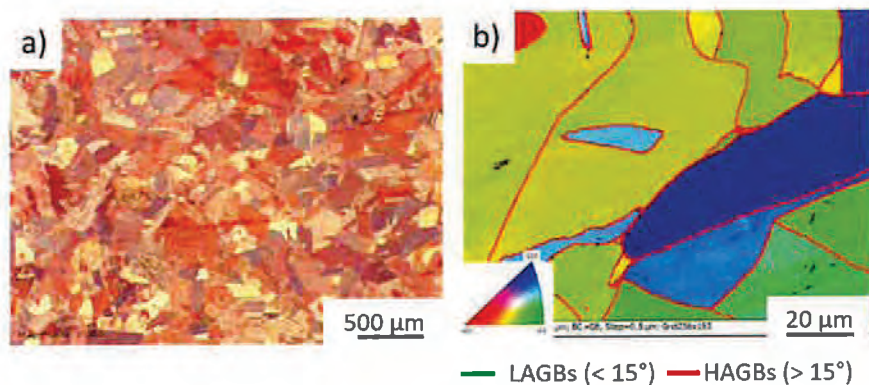


Fig. 1. Microstructure of SKB Cu; a) optical image after chemical etching; b) IPF map with corresponding GB distribution.

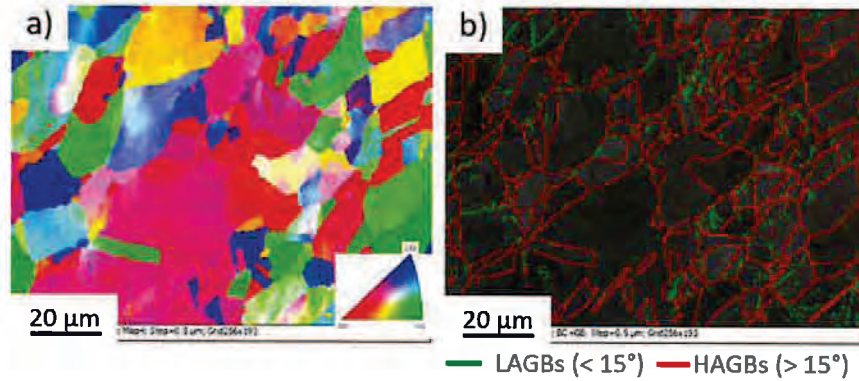


Fig. 2. EBSD maps recorded on the surface of ETP Cu: a) IPF map, b) GB distribution.

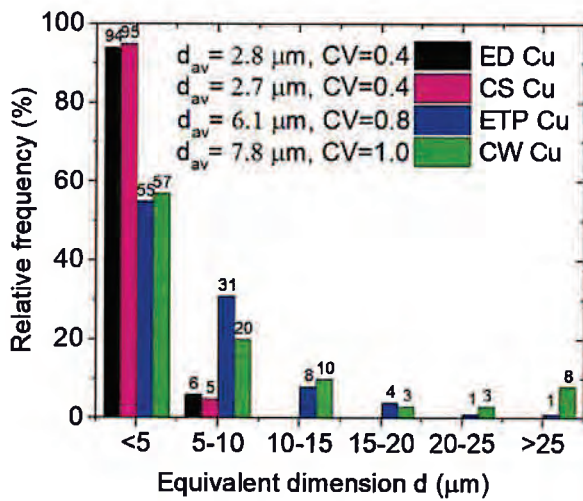


Fig. 3. Grain size distribution in different Cu materials, estimated using the linear intercept method.

range 20–46  $\mu\text{m}$ . Pores in CS Cu coatings deposited on steel have been observed previously by Yu et al. [59] and Li et al. [57]. Both studies focused on the negative influence of randomly distributed pores in CS Cu on the mechanical properties of the Cu coating.

SEM imaging showed long pores that extended along the length of

several adjacent particles located at particle boundaries, Fig. 7c, indicating weakly bonded particle-particle interfaces. Although low temperature annealing was used to minimize the porosity (350  $^{\circ}\text{C}$  for 1 h), weakly bonded areas were still present in the coating, indicating that conditions used during cold spray deposition and annealing did not lead to the complete sintering of the inter-splat areas [59]. Small grains are visible in the particle interiors suggesting that microstructural recrystallization occurred Fig. 7d; however, further studies regarding the detailed microstructure recrystallization should be undertaken.

#### 4.2. Corrosion measurements

$E_{corr}$  measurements recorded in aerated 100 mM  $\text{HNO}_3$  for 24 h are shown in Fig. 8. The evolution in  $E_{corr}$  on SKB Cu and ED Cu exhibited similar trends, a rapid, initial decrease followed by a slower longer-term increase. The initial  $E_{corr}$  decrease on ED Cu was more rapid than on SKB Cu, with the minimum potential achieved lower ( $\sim -0.05$  V/SCE) than that on SKB Cu ( $-0.04$  V/SCE to  $-0.03$  V/SCE). The ETP Cu and CW Cu also exhibited similar behaviors but were different from SKB Cu and ED Cu, with the initial decrease in  $E_{corr}$  followed by a steady increase towards steady-state values of  $\sim 0.03$  V/SCE (CW Cu) and  $\sim 0.05$  V/SCE (ETP Cu). The CS Cu exhibited very different behavior, initially rising to  $\sim 0.07$  V/SCE before decreasing slowly to  $\sim 0.03$  V/SCE, a value in the same range as achieved with CW Cu and ETP Cu.

After 24 h of exposure, when  $E_{corr}$  approached a constant value,  $R_p$  measurements were collected, Table 1. The apparent corrosion rate ( $\propto R_p^{-1}$ ) was highest on CS Cu, considerably lower on ED Cu, and of intermediate range on SKB Cu, ETP Cu and CW Cu. Moreover, all the longer-term values (i.e., after 24 h of immersion) are in the range

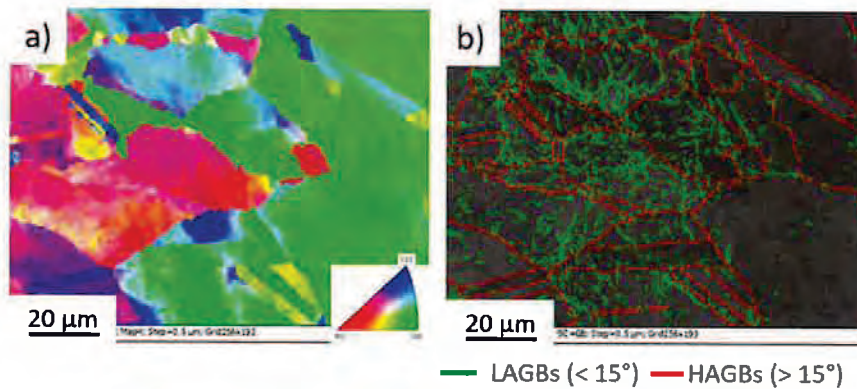


Fig. 4. EBSD maps recorded on the outer surface of CW Cu: a) IPF map, b) GB distribution.

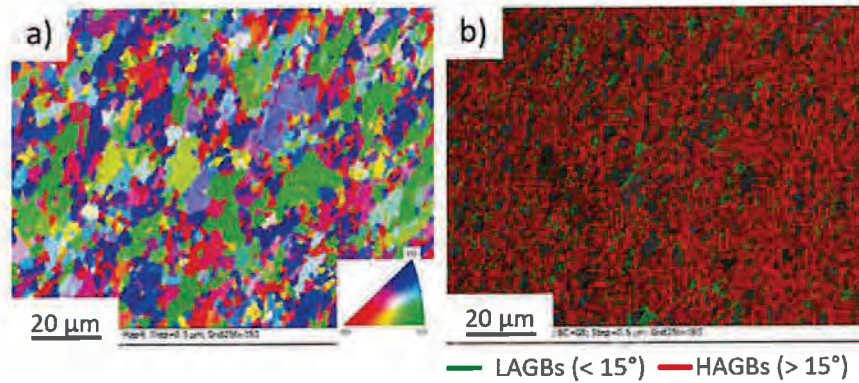


Fig. 5. EBSD maps recorded on the outer surface of ED Cu coating: a) IPF map, b) GB distribution.

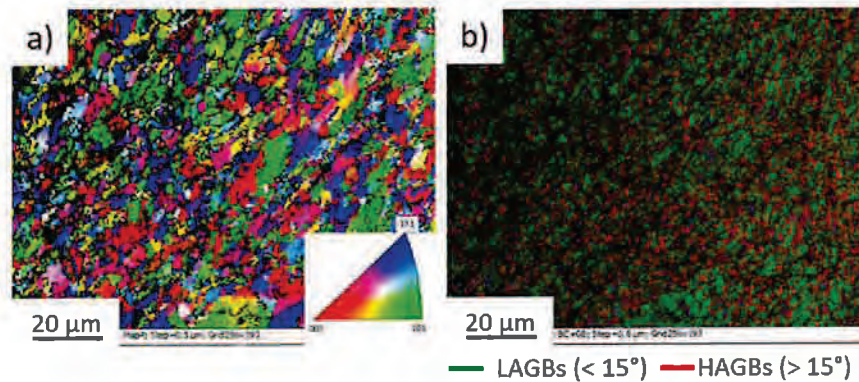


Fig. 6. EBSD maps recorded on the outer surface of CS Cu coating: a) IPF map, b) GB distribution.

(0.04 V/SCE to  $-0.04$  V/SCE) which we have observed in many experiments conducted in  $\text{HNO}_3$  solutions in the  $\text{HNO}_3$  concentration range 10–150 mM [60]. No apparent relationship between  $E_{\text{corr}}$  and  $R_p$  was observed, suggesting that the differences in  $R_p$  cannot be explained by a simple rebalancing of the relative rates of the anodic and cathodic reactions.

#### 4.3. Characterization of corroded surfaces

Fig. 9 shows that corrosion damage in aerated nitric acid was non-uniformly distributed on SKB Cu, with some grains experiencing more extensive corrosion than others. These differences were confirmed in the 3D CLSM image in Fig. 10a with the variations in depths of corrosion on individual grains shown in Fig. 10b. Measurements made on areas such as the one shown in Fig. 10a show that both  $S_a$  and  $S_z$  were greater on grain A than on grain B, Fig. 9a–c. In addition, if two adjacent grains have the same etch patterns after exposure in the test solution, then it can be supposed their exposed surfaces have similar crystallographic orientation, leading to preferential corrosion of HAGBs (Fig. 9c and d).

Examination of ETP Cu showed a texture-dependent corrosion pattern similar to that of SKB Cu, as indicated by grains A, B and C in Fig. 11a. The 3D map in Fig. 11b and the surface profile in Fig. 11c show the differences in grain etching reflecting the much lower average grain size in ETP Cu. Similar texture-dependent corrosion was observed on CW Cu, Fig. 12a–c. This is not unexpected, given similarities in their grain size distributions, Fig. 3, except for the small number of large grains present in CW Cu. Both the surface roughness ( $S_a$ ) and corrosion depth ( $S_z$ ) on CW Cu were approximately twice the values observed on ETP Cu,

which may reflect the approximate doubling in the corrosion rate of CW Cu compared to that of ETP Cu (Table 1). The SEM and CLSM images and a surface profile for ED Cu are shown in Fig. 13. Corrosion damage appeared to be greatest along grain boundaries, with the frequency of deeper penetrations indicated in the surface profile consistent with the average grain size. Since this specimen has a relatively high density of HAGBs, Fig. 5b, it was likely that corrosion initiated at these locations with the surface profile, Fig. 13c, and higher  $S_z$  value suggesting that it remained dominantly concentrated in these locations. Despite this localization of corrosion, the mean roughness ( $S_a$ ) of the ED Cu remained similar to those of the ETP Cu and CW Cu. In addition, despite the high density of corrosion-susceptible HAGBs,  $R_p$  for the ED Cu was 3–5 times higher than those of ETP Cu and CW Cu, respectively.

Examination of the corroded specimens showed that corrosion in aerated nitric acid solution was more localized on CS Cu (Fig. 14) than on the other specimens and propagated along preferential pathways. The shape and distribution of these corroded locations indicated that the most corrosion-susceptible areas were located at the pores and along the particle boundaries present in this material, Fig. 7. The CLSM surface profile showed the deepest penetrations at these locations, Fig. 14d. The maximum corrosion penetration measured in the area shown in Fig. 14b was 80  $\mu\text{m}$ , which is considerably greater than the penetration depths measured on the other specimens. Dynamic SIMS mapping by  $^{16}\text{O}$  showed that the particle boundaries were rich in O, Fig. 14c. This was most likely due to surface oxidation of the Cu particles used in the deposition process, which was retained at the particle boundaries. To examine the corrosion damage, a CLSM map and surface profile were recorded on the area marked with the black square in Fig. 14b and are

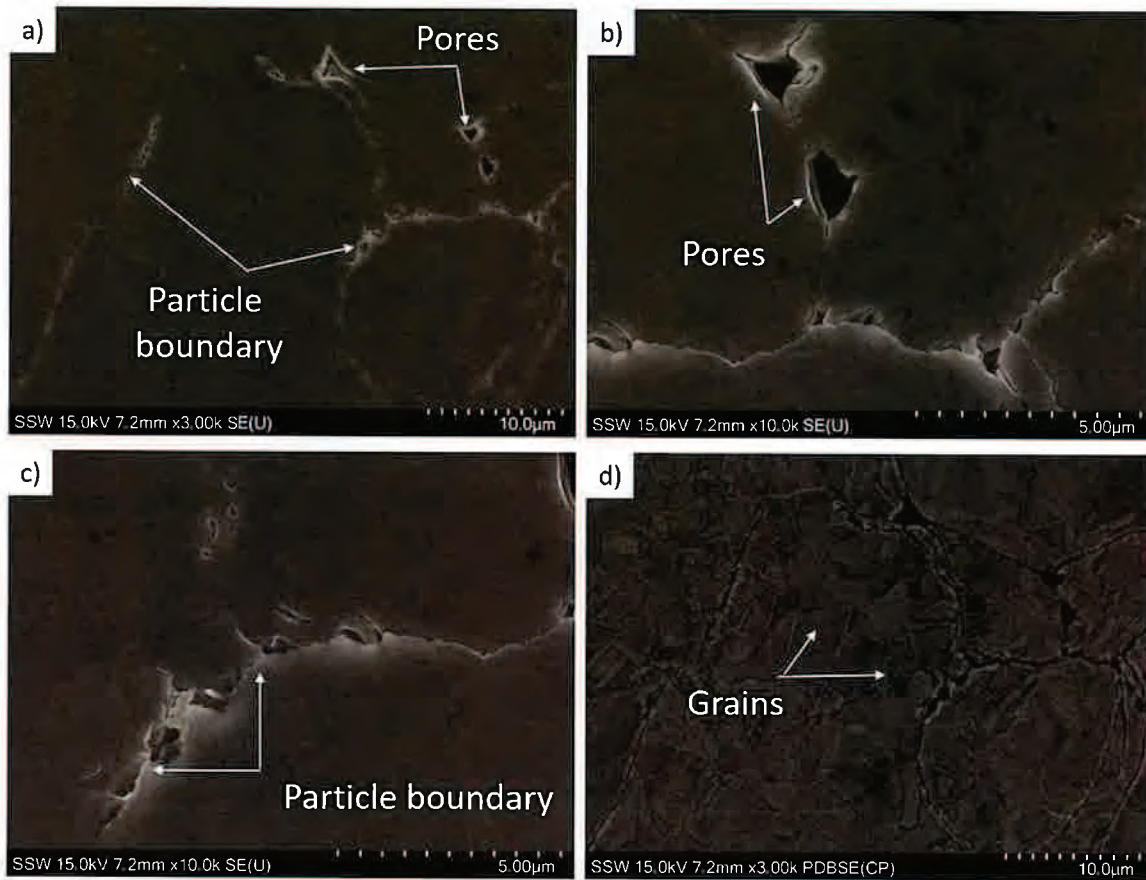


Fig. 7. SEM images recorded on the surface of the CS Cu specimen prepared for EBSD measurements: a) overall SE image, b) SE image highlighting the location of pores, c) weakly bonded particle-particle interfaces, d) BSE image taken from the same area as image 7a.

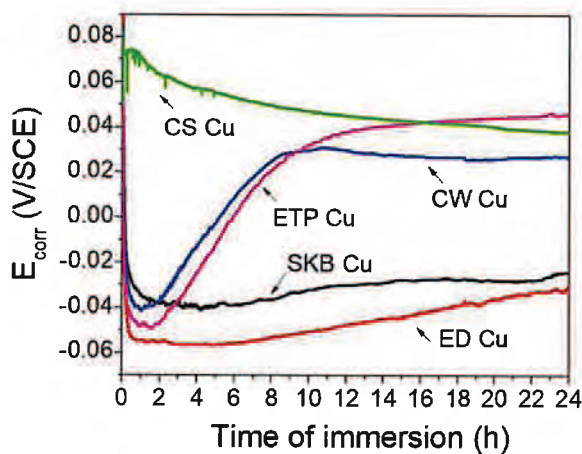


Fig. 8.  $E_{\text{corr}}$  evolution as a function of time of immersion in aerated 100 mM  $\text{HNO}_3$ .

shown in Fig. 15. The  $S_1$  and  $S_2$  values within this  $70 \mu\text{m} \times 70 \mu\text{m}$  area are  $1.7 \mu\text{m}$  and  $10 \mu\text{m}$ , respectively. Corrosion damage to the central part of a deposit particle is shown in Fig. 16.

Table 1

$R_p$  measurements after 24 h of immersion in aerated 100 mM  $\text{HNO}_3$ .

Material	Linear polarization $R_p$ ( $\Omega \text{ cm}^2$ )
ED Cu	2269
ETP Cu	712
SKB Cu	569
CW Cu	469
CS Cu	49

<sup>a</sup> due to an increasing effective area, the value may only be approximate

## 5. Discussion

The Cu specimens investigated in this study can be separated into coarse-grained (SKB Cu, ETP Cu, CW Cu) and refined grain (ED Cu, CS Cu) materials.

### 5.1. The major factors affecting the corrosion behaviour of coarse-grained Cu

The key features controlling the corrosion of the coarse-grained materials were the crystallographic orientation of grains, with variously oriented grains corroding at different rates. The rates for all 3 specimens were within a factor of 2 (Table 1), with the  $E_{\text{corr}}$  for the very large grained SKB Cu substantially lower than that for the ETP Cu and CW Cu. Miyamoto et al. [9] suggested that this dependence on texture

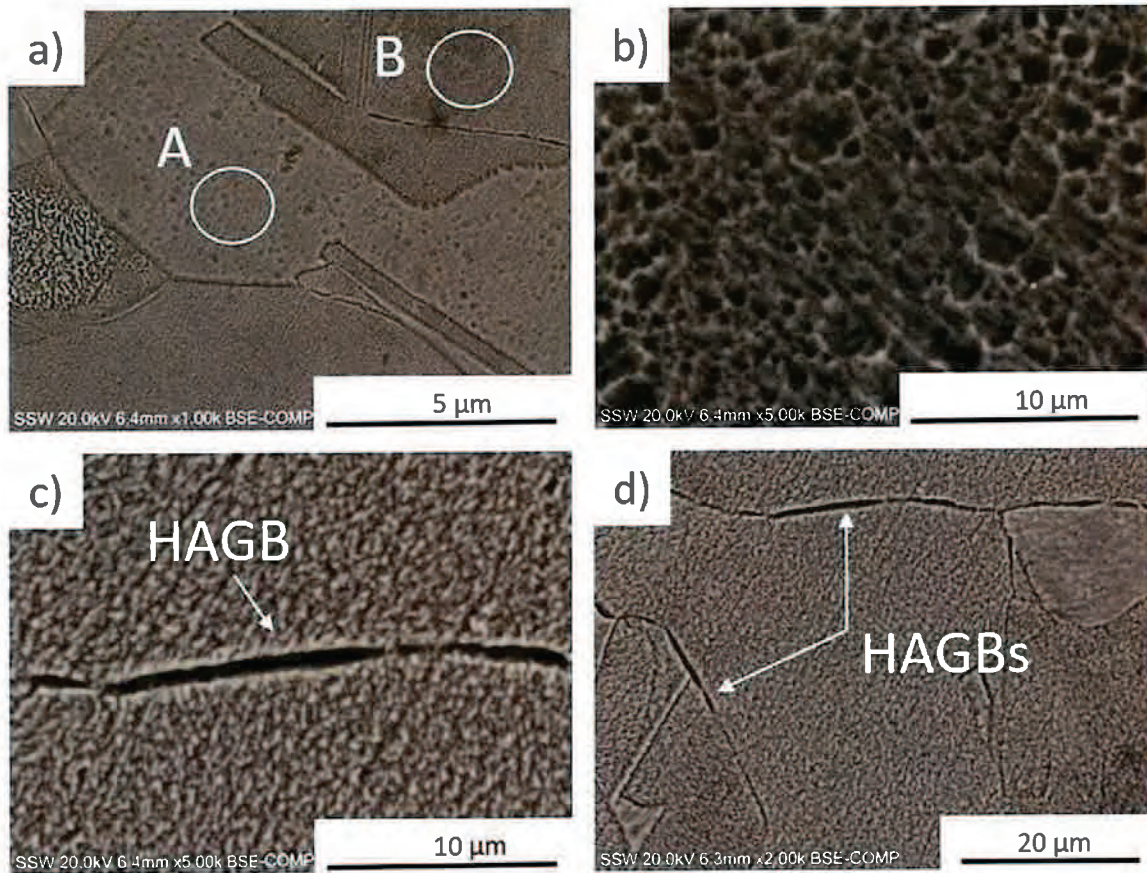


Fig. 9. SEM images of the surface of SKB Cu after immersion in  $\text{HNO}_3$  for 24 h. Areas A and B are shown with higher magnification in Fig. 9b and c, respectively. Panels c and d show preferential etching of HAGBs.

can be assigned to the establishment of anodic/cathodic separation between individual grains. They proposed that this could result from differences in surface energies between crystal planes, with the close packed  $\langle 111 \rangle$  plane having the lowest surface energy. Subsequently, Lapeire et al. [13] demonstrated that not only the grain orientation but also the orientation of neighbouring grains exhibited an influence on the corrosion behaviour of specific grains, and suggested that the greatest degree of galvanic coupling between grain interiors would be between  $\langle 001 \rangle // \text{ND}$  and  $\langle 111 \rangle // \text{ND}$  oriented grains, particularly if they were located adjacent to each other [24]. How this leads to the rebalancing of the anodic and cathodic kinetics, which would account for the lower  $E_{\text{corr}}$  for SKB Cu, is presently unclear. The variation of corrosion rate with texture will also be complicated by anion adsorption processes, which could be particularly important in  $\text{NO}_3^-$  solutions, since this anion has been shown to have different adsorption energies on different crystal planes [61].

In addition, within this group of coarse-grained materials, the very large grained SKB Cu exhibited preferential grain boundary etching of HAGBs. The higher energies at these locations make them preferential corrosion sites relative to the lower energy grain surfaces, as described by Miyamoto et al. [9], this leads to a combination of GB etching and the more visible etching of the more sensitive crystallographic planes. Miyamoto et al. [9] went on to propose that the mechanism for this effect was a type of galvanic coupling between the grains and grain boundaries.

Our results are not inconsistent with the results of Miyamoto et al. [9] and Lapeire et al. [13], and it is possible that an

intra-microstructural-feature galvanic corrosion mechanism may be responsible, though we do not yet have direct evidence for the anode-cathode separation that would confirm it.

## 5.2. The major factors affecting the corrosion behaviour of fine-grained Cu

A number of studies [16,37,62–65] have demonstrated the enhanced reactivity of HAGBs, with the corrosion rate depending on their number and distribution. However, despite the extremely high number and density of such boundaries, ED Cu was the most corrosion resistant of these materials, exhibiting a  $R_p$  value 3–6 times greater than the values recorded for the other 4 materials (Table 1). This decrease in corrosion rate, combined with a lower  $E_{\text{corr}}$  (compared to the other materials), indicates a suppression of the cathodic reaction on the ED Cu surface. Miyamoto et al. proposed that the dominant influence on the corrosion rate of fine-grained Cu is galvanic coupling between the grains, acting dominantly as cathodes, and the HAGBs which act dominantly as anodes [9]. In this scenario, a refined structure containing dominantly HAGBs will possess a low cathode (grain surface) area to anode (HAGBs) area ratio which, while dominantly supporting corrosion within the HAGBs, would limit the overall rate of corrosion penetration. That HAGB etching was observed for the large-grained SKB Cu (large ratio of grain interior to grain boundary surface area) but not the smaller-grained ETP Cu and CW Cu (smaller grain interior: grain boundary area ratio) is also in line with the results of Miyamoto et al. [9].

For the CS Cu, corrosion propagated preferentially within the

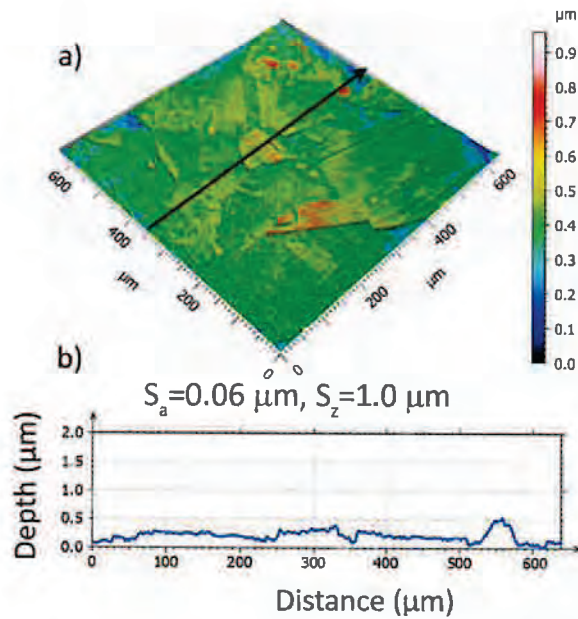


Fig. 10. CLSM image recorded on the surface of SKB Cu: a) 3D image, b) surface profile extracted from the location marked by the arrow.

particle boundaries. Despite a lower density of HAGBs than on ED Cu and a similar small grain size, the corrosion rate and  $E_{\text{corr}}$  for CS Cu were both considerably higher than those of ED Cu. This indicates faster cathodic reaction kinetics on the former than the latter material. The  $E_{\text{corr}}$  of CS Cu was approximately the same as that of the coarse-grained materials but the corrosion rate was considerably higher, a combination suggesting that both the anodic and cathodic reaction kinetics were faster on CS Cu. Although annealing has been shown to significantly decrease plastic strain within the interparticle boundaries [42], it is possible that small amounts of residual strain exerted an influence on the anodic kinetics. These observations demonstrate that any influence of

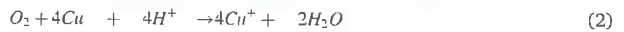
inter-structural-feature galvanic coupling was overridden by the enhanced overall cathodic and anode reaction kinetics on CS Cu.

### 5.3. Corrosion mechanism

The mechanism of Cu corrosion in aerated  $\text{HNO}_3$  has been shown to be complicated [52,53,60]. Nitrate is strongly adsorbed on Cu [61] and, in the absence of dissolved  $\text{O}_2$ , prevents corrosion either due to  $\text{NO}_3^-$  adsorption or to the formation of a protective oxide [53,61]. When dissolved  $\text{O}_2$  is present it acts as the dominant oxidant,



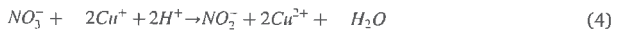
leading to the overall corrosion reaction,



with the overall reaction kinetics being first-order with respect to  $[\text{O}_2]$  but independent of  $[\text{H}^+]$  and only slightly dependent on  $[\text{NO}_3^-]$  [52,53,66]. These studies also demonstrated that corrosion supported by  $\text{H}^-$  reduction does not occur. The  $\text{Cu}^-$  produced in reaction 2 can then undergo competitive homogeneous oxidation reactions:



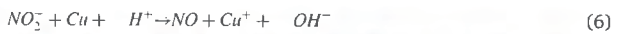
and



Reaction 4 effectively activates  $\text{NO}_3^-$  as an oxidant, since the  $\text{NO}_2^-$  formed acts as a rapid cathodic reactant [52],



supporting the overall corrosion reaction



with the  $\text{Cu}^-$  produced in reactions (2) and (6) consumed by reactions (3) and (4) to produce  $\text{Cu}^{2+}$  whose reduction on the Cu surface leads to further corrosion via comproportionation reaction (7),

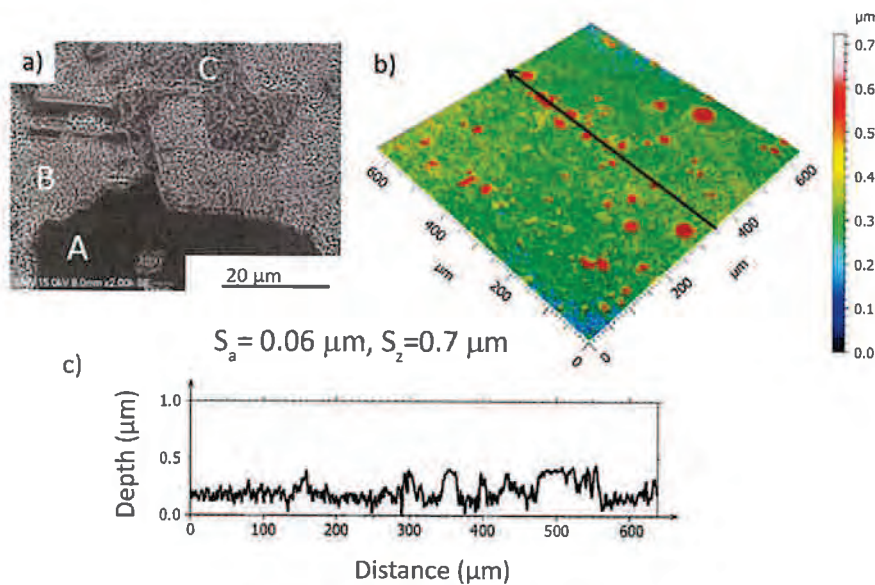


Fig. 11. Post-corrosion characterization of ETP Cu: a) SEM image, b) CLSM 3D image, d) surface profile extracted along the location marked by the arrow.

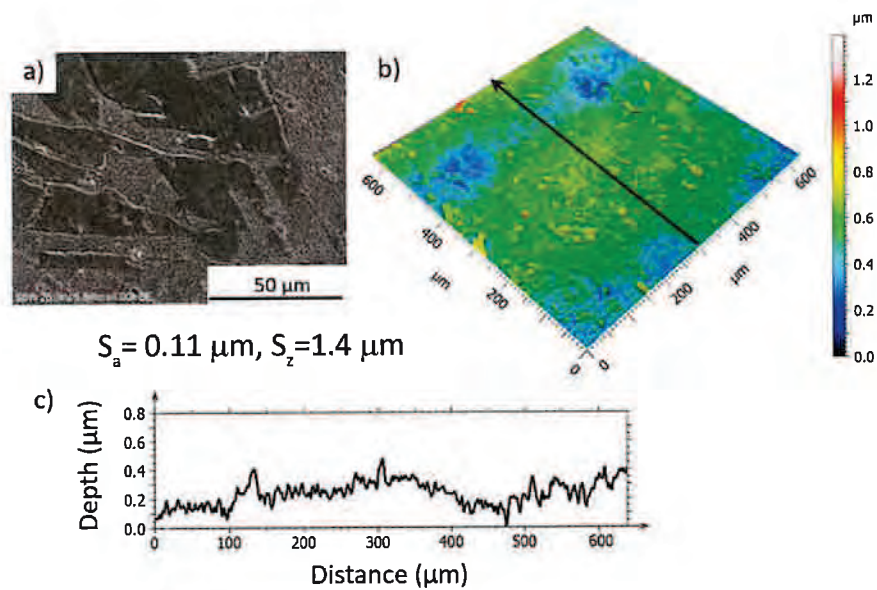


Fig. 12. Post-corrosion characterization of CW Cu: a) SEM image, b) CLSM 3D image, d) surface profile extracted along the location marked by the arrow.

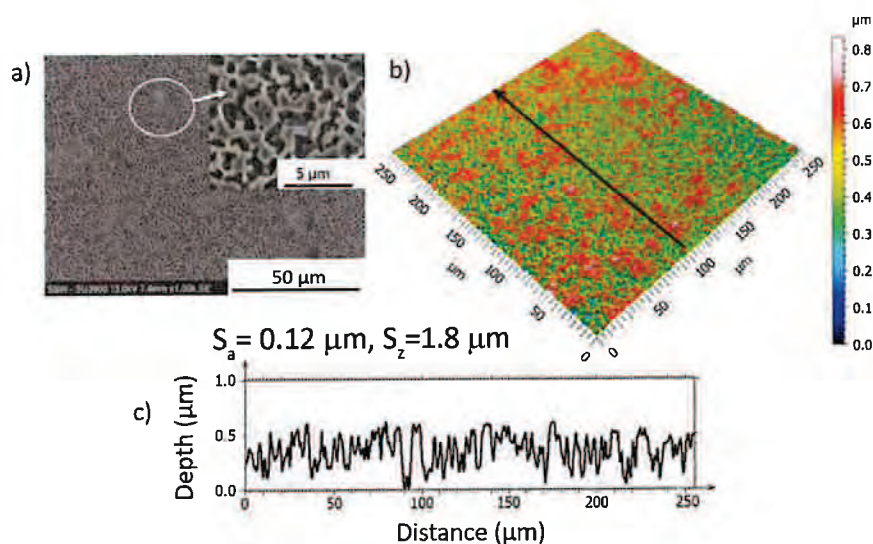


Fig. 13. Post-corrosion characterization of ED Cu: a) SEM image of the surface, b) CLSM 3D image, b) surface profile extracted from the location marked by the arrow.

and the establishment of a catalytic corrosion cycle.

Experiments involving large and small Cu surface area to solution volume ( $S_A/V$ ) ratios demonstrated that for small  $S_A/V$  ratios the latter potential oxidants ( $\text{Cu}^{2+}$  and  $\text{NO}_2^-$ ) could escape by transport to the bulk of solution, leading to their dilution at the Cu surface and limiting their involvement in the corrosion process. When the  $S_A/V$  ratio was large, such transport losses were limited and Cu corrosion accelerated by reactions (6) and (7).

This sequence of reactions offers an explanation for the promotion of corrosion occurring in the pores along particle boundaries of CS Cu, based on local  $S_A/V$  ratios. Initially, the  $\text{O}_2$  reduction reaction would occur across the whole CS Cu surface. However, due to transport limitations,  $\text{O}_2$  would become depleted within the pores and particle boundary fractures. By contrast, the  $\text{NO}_3^-$ , which in the present

experiments was present at a significantly higher concentration than  $\text{O}_2$ , would not be similarly depleted in these regions. Combined with the mass transport restrictions, and the high solubility of  $\text{Cu}^+$  in acidic solution, this would allow  $\text{Cu}^+$  and the other potential oxidants ( $\text{Cu}^{2+}$  and  $\text{NO}_2^-$ ) to accumulate in these high  $S_A/V$  ratio locations, initiating the catalytic corrosion cycle locally, particularly reactions (4), (6) and (7). Conversely, on the boldly exposed surfaces, where  $S_A/V$  ratios are smaller,  $\text{Cu}^{2+}$  and  $\text{NO}_2^-$  could escape by transport to the bulk of solution, meaning corrosion on these surfaces would be directly driven by oxygen but not by the catalytic cycle. This would lead to more rapid corrosion within pores and fractures at particle boundaries than on the open surfaces. It also suggests the possibility of developing differential  $\text{O}_2$  concentration cells between open surfaces and particle boundary pores and fractures. The presence of oxides at these locations in the form

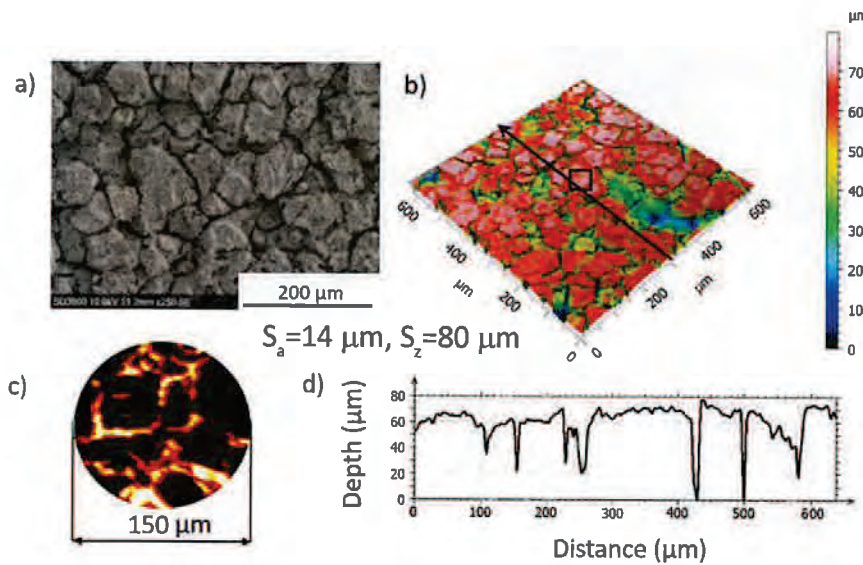


Fig. 14. Post-corrosion characterization of CS Cu: a) SEM image, b) 3D CLSM image, c) D-SIMS elemental map for  $^{16}\text{O}$ , d) surface profile extracted from the area marked by the arrow in panel b.

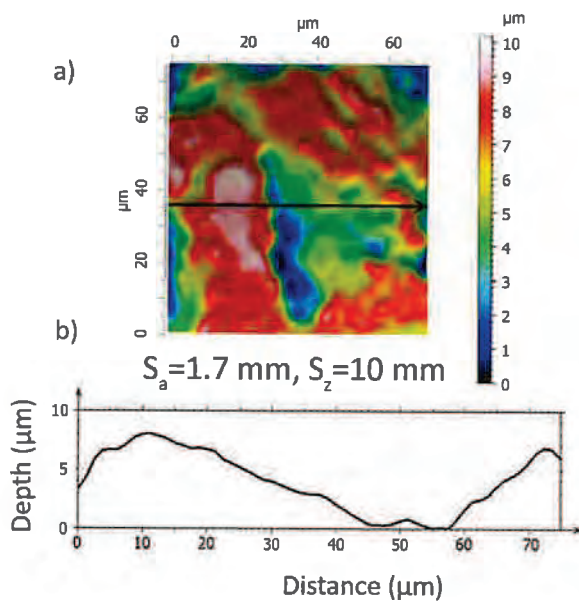


Fig. 15. Post-corrosion characterization of the area extracted from the particle of CS Cu marked by the black square in Fig. 14b: a) 3D CLSM image, b) surface profile extracted from the area marked by the arrow.

of either  $\text{Cu}_2\text{O}$  or  $\text{CuO}$  would not be expected to inhibit corrosion since they would dissolve in the acidic solution to produce  $\text{Cu}^+$  and/or  $\text{Cu}^{2+}$  both of which would accelerate the localized corrosion by reactions (4) and (7).

## 6. Conclusions

- In this work, different Cu specimens were exposed to an aerated nitric acid solution to allow us to observe an accelerated corrosion of

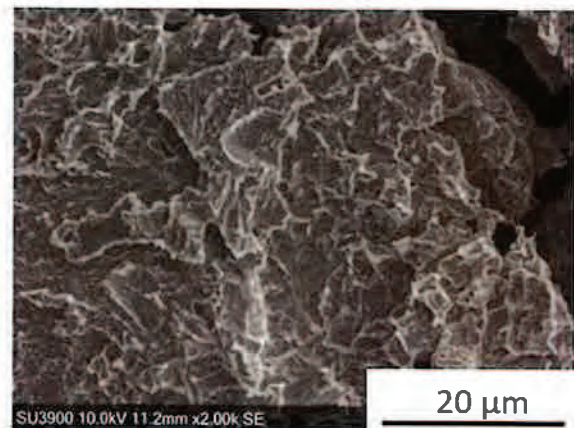


Fig. 16. SEM image showing corrosion damage in a particle interior in CS Cu after immersion for 24 h in aerated 100 mM  $\text{HNO}_3$ .

Cu in a short period of time, and to understand the reactivity of different grain structures under an aggressive condition.

- On the coarse-grained materials investigated (SKB Cu, ETP Cu, CW Cu) the corrosion behaviour was controlled by the crystallographic orientation of grains, with differently oriented grains corroding at different rates.
- On SKB Cu, the HAGBs corroded at a higher rate than did the grain surfaces, whereas preferential dissolution of grain boundaries was not prevalent on ETP Cu and CW Cu.
- On the refined-grained ED Cu, the corrosion rate was considerably lower than on the coarse-grained materials, with corrosion damage accumulating predominantly in the HAGBs.
- The corrosion rate in 100 mM nitric acid was considerably higher on CS Cu than on the coarse-grained materials, with corrosion progressing most rapidly within pores and along deposited particle boundaries. The propagation of corrosion within these locations was likely enhanced by the confinement of  $\text{Cu}^+$ , as well as oxidants  $\text{NO}_2^-$

and  $\text{Cu}^{2-}$  produced by the reaction of  $\text{NO}_3^-$  with  $\text{Cu}^-$ , giving rise to a catalytic corrosion cycle locally.

Further investigations are underway to elucidate the influence of O in oxides present on the particle boundaries of CS Cu on its corrosion behaviour.

#### CRedit authorship contribution statement

**Anna Dobkowska:** Conceptualization, Formal analysis, Investigation, Methodology, Visualization, Writing – original draft, Writing – review & editing. **Millicent Dayle H. Castillo:** Investigation. **Joseph P. Turnbull:** Methodology. **Sridhar Ramamurthy:** Data curation, Project administration. **Dmitrij Zagdulin:** Data curation, Software. **Desmond E. Moser:** Funding acquisition, Writing – review & editing. **Mehran Behazin:** Funding acquisition, Writing – review & editing. **Peter G. Keech:** Funding acquisition, Writing – review & editing. **David W. Shoesmith:** Validation, Supervision, Writing – review & editing. **James J. Noël:** Supervision, Funding acquisition, Validation, Project administration, Writing – review & editing.

#### Declaration of Competing Interest

The authors declare that they have no known competing financial interests or personal relationships that could have appeared to influence the work reported in this paper.

#### Acknowledgements

This research was mainly funded by the Nuclear Waste Management Organization (Toronto, Canada) with minor support from an NSERC Discovery Grant to Desmond E. Moser. The authors are grateful to Mr. Gary Good (Surface Science Western, ON, Canada) for his support in D-SIMS measurements, Mr. Ivan Barker (Surface Science Western, ON, Canada) for support with SEM imaging of CS Cu, and Dr. Brendt Hyde (Zircon and Accessory Phase Laboratory, University of Western Ontario, ON, Canada) for assistance with SEM-EBSD measurements.

#### References

- A. Pardo, M.C. Merino, A.E. Coy, R. Arrabal, F. Viejo, E. Matykina, Corrosion behaviour of magnesium/aluminium alloys in 3.5wt% NaCl, *Corros. Sci.* 50 (2008) 823–834, <https://doi.org/10.1016/j.corsci.2007.11.005>.
- G. Ben Hamu, D. Eliezer, L. Wagner, The relation between severe plastic deformation microstructure and corrosion behavior of AZ31 magnesium alloy, *J. Alloy. Compd.* 468 (2009) 222–229, <https://doi.org/10.1016/j.jallcom.2008.01.084>.
- G. Meng, Y. Li, Y. Shao, T. Zhang, Y. Wang, F. Wang, X. Cheng, C. Dong, X. Li, Effect of microstructures on corrosion behavior of nickel coatings: (I) abnormal grain size effect on corrosion behavior, *J. Mater. Sci. Technol.* 31 (2015) 1186–1192, <https://doi.org/10.1016/j.jmst.2015.10.011>.
- M. Alvarez-Lopez, M.D. Pereda, J.A. Del Valle, M. Fernandez-Lorenzo, M.C. Garcia-Alonso, O.A. Ruano, M.L. Escudero, Corrosion behaviour of AZ31 magnesium alloy with different grain sizes in simulated biological fluids, *Acta Biomater.* 6 (2010) 1763–1771, <https://doi.org/10.1016/j.actbio.2009.04.041>.
- R. Ly, K.T. Hartwig, H. Castaneda, Influence of dynamic recrystallization and shear banding on the localized corrosion of severely deformed Al–Mg–Si alloy, *Materialia* 4 (2018) 457–465, <https://doi.org/10.1016/j.mtl.2018.11.005>.
- T.A.-S.S.S. Nene, B.P. Kashyapa, N. Prabhua, Y. Estrina, Microstructure refinement and its effect on specific strength and bio-corrosion resistance in ultralight Mg–4Li–1Ca (IC41) alloy by hot rolling, *J. Alloy. Compd.* 615 (2014) 501–506.
- H.S. Kim, G.H. Kim, H. Kim, W.J. Kim, Enhanced corrosion resistance of high strength Mg–3Al–1Zn alloy sheets with ultrafine grains in a phosphate-buffered saline solution, *Corros. Sci.* 74 (2013) 139–148, <https://doi.org/10.1016/j.corsci.2013.04.035>.
- G.R. Argade, S.K. Panigrahi, R.S. Mishra, Effects of grain size on the corrosion resistance of wrought magnesium alloys containing neodymium, *Corros. Sci.* 58 (2012) 145–151, <https://doi.org/10.1016/j.corsci.2012.01.021>.
- H. Miyamoto, K. Harada, T. Mimaki, A. Vinogradov, S. Hashimoto, Corrosion of ultra-fine grained copper fabricated by equal-channel angular pressing, *Corros. Sci.* 50 (2008) 1215–1220, <https://doi.org/10.1016/j.corsci.2008.01.024>.
- L. Beaunier, Corrosion of grain boundaries: initiation processes and testing, *J. Phys. (Paris) Colloq.* 43 (1982) 271–282, <https://doi.org/10.1051/jphyscol:1982624>.
- L. Beaunier, M. Froment, C. Vignaud, A kinetic model for the electrochemical grooving of grain boundaries, *Electrochim. Acta* 25 (1980) 1239–1246, [https://doi.org/10.1016/0013-4686\(80\)87127-1](https://doi.org/10.1016/0013-4686(80)87127-1).
- K.D. Ralston, N. Birbilis, C.H.J. Davies, Revealing the relationship between grain size and corrosion rate of metals, *Scr. Mater.* 63 (2010) 1201–1204, <https://doi.org/10.1016/j.scriptamat.2010.08.035>.
- L. Lapeire, E. Martinez Lombardia, I. De Graeve, H. Terryn, K. Verbeke, Influence of grain size on the electrochemical behavior of pure copper, *J. Mater. Sci.* 52 (2017) 1501–1510, <https://doi.org/10.1007/s10853-016-0445-z>.
- R. Mishra, R. Balasubramanian, Effect of nanocrystalline grain size on the electrochemical and corrosion behavior of nickel, *Corros. Sci.* 46 (2004) 3019–3029, <https://doi.org/10.1016/j.corsci.2004.04.007>.
- K.D. Ralston, D. Fabjanic, N. Birbilis, Effect of grain size on corrosion of high purity aluminium, *Electrochim. Acta* 56 (2011) 1729–1736, <https://doi.org/10.1016/j.electacta.2010.09.023>.
- M. Orłowska, E. Ura-Bińczyk, L. Olejnik, M. Lewandowska, The effect of grain size and grain boundary misorientation on the corrosion resistance of commercially pure aluminium, *Corros. Sci.* 148 (2019) 57–70, <https://doi.org/10.1016/j.corsci.2018.11.035>.
- J.K. Yu, E.H. Han, L. Lu, X.J. Wei, M. Leung, Corrosion behaviors of nanocrystalline and conventional polycrystalline copper, *J. Mater. Sci.* 40 (2005) 1019–1022, <https://doi.org/10.1007/s10853-005-6524-1>.
- A.V. Syugayev, E.A. Pechina, N.V. Lyalina, S.F. Lomaeva, M.V. Mar'in, S.M. Reshetnikov, The influence of the ultrafine-grained structure on passivation of copper, *Prot. Met. Phys. Chem. Surf.* 50 (2014) 841–845, <https://doi.org/10.1134/S2070205114070168>.
- K.D. Ralston, N. Birbilis, Effect of grain size on corrosion, *Corrosion* 66 (2010) 1–4, <https://doi.org/10.5006/1.3462912>.
- R. Rofagha, R. Langer, A.M. El-Sherik, U. Erb, G. Palumbo, K.T. Aust, The corrosion behaviour of nanocrystalline nickel, *Scr. Metall. Mater.* 25 (1991) 2867–2872, [https://doi.org/10.1016/0956-716X\(91\)90171-V](https://doi.org/10.1016/0956-716X(91)90171-V).
- N.N. Aung, W. Zhou, Effect of grain size and twins on corrosion behaviour of AZ31B magnesium alloy, *Corros. Sci.* 52 (2010) 589–594, <https://doi.org/10.1016/j.corsci.2009.10.018>.
- S. Gollapudi, Grain size distribution effects on the corrosion behaviour of materials, *Corros. Sci.* 62 (2012) 90–94, <https://doi.org/10.1016/j.corsci.2012.04.040>.
- E. Martinez-Lombardia, Y. Gonzalez-Garcia, L. Lapeire, I. De Graeve, K. Verbeke, L. Kestens, J.M.C. Mol, H. Terryn, Scanning electrochemical microscopy to study the effect of crystallographic orientation on the electrochemical activity of pure copper, *Electrochim. Acta* 116 (2014) 89–96, <https://doi.org/10.1016/j.electacta.2013.11.048>.
- L. Lapeire, E. Martinez-Lombardia, K. Verbeke, I. De Graeve, L.A.L. Kestens, H. Terryn, Effect of neighboring grains on the microscopic corrosion behavior of a grain in polycrystalline copper, *Corros. Sci.* 67 (2013) 179–183, <https://doi.org/10.1016/j.corsci.2012.10.017>.
- A. Schreiber, J.W. Schultze, M.M. Lohregel, F. Kármán, E. Kálmán, Grain dependent electrochemical investigations on pure iron in acetate buffer pH 6.0, *Electrochim. Acta* 51 (2006) 2625–2630, <https://doi.org/10.1016/j.electacta.2005.07.052>.
- E. Martinez-Lombardia, L. Lapeire, I. De Graeve, K. Verbeke, L.A.L. Kestens, H. Terryn, Study of the influence of the microstructure on the corrosion properties of pure copper, *Mater. Corros.* 67 (2016) 847–856, <https://doi.org/10.1002/maco.201508719>.
- H. Chen, V. Maurice, L.H. Klein, L. Lapeire, K. Verbeke, H. Terryn, P. Marcus, Grain boundary passivation studied by in situ scanning tunneling microscopy on microcrystalline copper, *J. Solid State Electrochem.* 19 (2015) 3501–3509, <https://doi.org/10.1007/s10008-015-2787-x>.
- B. Davepon, J.W. Schultze, U. König, C. Rosenkranz, Crystallographic orientation of single grains of polycrystalline titanium and their influence on electrochemical processes, *Surf. Coat. Technol.* 169–170 (2003) 85–90, [https://doi.org/10.1016/S0257-8972\(03\)00163-4](https://doi.org/10.1016/S0257-8972(03)00163-4).
- M. Koralnik, A. Dobkowska, B. Adamczyk-Cieslak, J. Mizera, The influence of the microstructural evolution on the corrosion resistance of cold drawn copper single crystals in NaCl, *Arch. Metall. Mater.* 65 (2020) 55–64, <https://doi.org/10.24425/amm.2019.131096>.
- Z. Pu, G.L. Song, S. Yang, J.C. Outeiro, O.W. Dillon, D.A. Puleo, I.S. Jawahir, Grain refined and basal textured surface produced by burnishing for improved corrosion performance of AZ31B Mg alloy, *Corros. Sci.* 57 (2012) 192–201, <https://doi.org/10.1016/j.corsci.2011.12.018>.
- M. Liu, D. Qiu, M.C. Zhao, G. Song, A. Atrens, The effect of crystallographic orientation on the active corrosion of pure magnesium, *Scr. Mater.* 58 (2008) 421–424, <https://doi.org/10.1016/j.scriptamat.2007.10.027>.
- A. Chojnacka, J. Kawalko, H. Koscielny, J. Guspel, A. Drewienkiewicz, M. Bieda, W. Pachla, M. Kulczyk, K. Sztwiertnia, E. Beltowska-Lehman, Corrosion anisotropy of titanium deformed by the hydrostatic extrusion, *Appl. Surf. Sci.* 426 (2017) 987–994, <https://doi.org/10.1016/j.apsusc.2017.07.231>.
- E.M. Lehecky, A.M. Brennenstuhl, I. Thompson, On the relationship between grain boundary connectivity, coincident site lattice boundaries, and intergranular stress corrosion cracking, *Corros. Sci.* 46 (2004) 2383–2404, <https://doi.org/10.1016/j.corsci.2004.01.019>.
- G. Palumbo, E.M. Lehecky, P. Lin, U. Erb, K.T. Aust, A grain boundary engineering approach to materials reliability, *MRS Proc.* 458 (1996) 273, <https://doi.org/10.1557/PROC-458-273>.
- Y. Yuan, Y. Jiang, J. Zhou, G. Liu, X. Ren, Influence of grain boundary character distribution and random high angle grain boundaries networks on intergranular

- corrosion in high purity copper, *Mater. Lett.* 253 (2019) 424–426, <https://doi.org/10.1016/j.matlet.2019.07.125>.
- [36] S. Xia, H. Li, T.G. Liu, B.X. Zhou, Applying grain boundary engineering to Alloy 690 tube for enhancing intergranular corrosion resistance, *J. Nucl. Mater.* 416 (2011) 303–310, <https://doi.org/10.1016/j.jnucmat.2011.06.017>.
- [37] A. Lin, E.E. Hoffman, L.D. Marks, Effects of grain boundary misorientation and chromium segregation on corrosion of CoCrMo alloys, *Corrosion* 73 (2017) 256–267, <https://doi.org/10.5006/2233>.
- [38] T.E. Standish, Galvanic Corrosion of Copper-coated Carbon Steel for Used Nuclear Fuel Containers, The University of Western Ontario, 2019, <https://u.lib.uwo.ca/etd/6705/>.
- [39] R. Crowe, K. Birch, J. Freire-Canosa, J. Chen, D. Doyle, F. Garisto, P. Giersewski, M. Gobien, C. Hatton, N. Hunt, S. Hirschorn, M. Hobbs, M. Jensen, P. Keech, L. Kennel, E. Kremer, P. Maak, J. McKelvie, C. Medri, M. Mielcarek, A. Murchison, A. Parmenter, R. Ross, E. Sykes, T. Yang, Technical Program for Long-Term Management of Canada's Used Nuclear Fuel – Annual Report 2013, 2015.
- [40] NWMO Report, Description of a Deep Geological Repository and Centre of Expertise for Canada's Used Nuclear Fuel, 2015.
- [41] N. Giroud, Y. Tomonaga, P. Wersin, S. Briggs, F. King, T. Vogt, N. Diomidis, On the fate of oxygen in a spent fuel emplacement drift in Opalinus Clay, *Appl. Geochem.* 97 (2018) 270–278, <https://doi.org/10.1016/j.apgeochem.2018.08.011>.
- [42] T. Standish, J. Chen, R. Jacklin, P. Jakupi, S. Ramamurthy, D. Zagidulin, P. Keech, D. Shoesmith, Corrosion of copper-coated steel high level nuclear waste containers under permanent disposal conditions, *Electrochim. Acta* 211 (2016) 331–342, <https://doi.org/10.1016/j.electacta.2016.05.135>.
- [43] P. Jakupi, P.G. Keech, I. Barker, S. Ramamurthy, R.L. Jacklin, D.W. Shoesmith, D. E. Moser, Characterization of commercially cold sprayed copper coatings and determination of the effects of impacting copper powder velocities, *J. Nucl. Mater.* 466 (2015) 1–11, <https://doi.org/10.1016/j.jnucmat.2015.07.001>.
- [44] T.E. Standish, D. Zagidulin, S. Ramamurthy, P.G. Keech, D.W. Shoesmith, J.J. Noël, Synchrotron-based micro-CT investigation of oxidic corrosion of copper-coated carbon steel for potential use in a deep geological repository for used nuclear fuel, *Geosciences* 8 (2018) 360, <https://doi.org/10.3390/geosciences8100360>.
- [45] P.G. Keech, P. Vo, S. Ramamurthy, J. Chen, R. Jacklin, D.W. Shoesmith, Design and development of copper coatings for long term storage of used nuclear fuel, *Corros. Eng. Sci. Technol.* 49 (2014) 425–430, <https://doi.org/10.1179/1743278214y0000000206>.
- [46] X. Zhang, Development of the structural design basis of the long-term storage container for Canada's used nuclear fuel, in: 4th Can. Conf. Nucl. Waste Manag. Decommissioning Environ. Restor., 2013: pp. 37–41, [doi:10.1080/02626667.2013.819433](https://doi.org/10.1080/02626667.2013.819433).
- [47] F. King, C. Lilja, K. Pedersen, P. Pitkänen, M. Vähänen, An update of the state-of-the-art report on the corrosion of copper under expected conditions in a deep geologic repository, Stockholm, 2010.
- [48] D.S. Hall, M. Behazin, W.J. Binns, P.G. Keech, An evaluation of corrosion processes affecting copper-coated nuclear waste containers in a deep geological repository, *Prog. Mater. Sci.* 118 (2021), 100766, <https://doi.org/10.1016/j.pmatsci.2020.100766>.
- [49] F. King, L. Ahonen, C. Taxen, U. Vuorinen, L. Werme, Copper corrosion under expected conditions in a deep geologic repository, 2001.
- [50] R.P. Morco, J.M. Joseph, D.S. Hall, C. Medri, D.W. Shoesmith, J.C. Wren, Modelling of radiolytic production of HNO<sub>3</sub> relevant to corrosion of a used fuel container in deep geologic repository environments, *Corros. Eng. Sci. Technol.* 52 (2017) 141–147, <https://doi.org/10.1080/1478422X.2017.1340227>.
- [51] J.P. Turnbull, The Influence of Radiolytically Produced Nitric Acid on the Corrosion Resistance of Copper-Coated Used Nuclear Fuel Containers, The University of Western Ontario, 2020 [doi:https://u.lib.uwo.ca/etd/6903](https://u.lib.uwo.ca/etd/6903).
- [52] J. Turnbull, R. Szukalo, D. Zagidulin, D.W. Shoesmith, Nitrite effects on copper corrosion in nitric acid solutions, *Corros. Sci.* 179 (2021), 109147, <https://doi.org/10.1016/j.corsci.2020.109147>.
- [53] J. Turnbull, R. Szukalo, M. Behazin, D. Hall, D. Zagidulin, S. Ramamurthy, J. C. Wren, D.W. Shoesmith, The effects of cathodic reagent concentration and small solution volumes on the corrosion of copper in dilute nitric acid solutions, *Corrosion* 74 (2018) 326–336, <https://doi.org/10.5006/2655>.
- [54] M. Wu, M. Behazin, J. Nam, P. Keech, R. Morco, Internal corrosion of used fuel container, 2019, <https://www.nwmo.ca/~/media/Site/Reports/2019/02/25/22/45/NWMOTR201902-Internal-Corrosion-of-Used-Fuel-Container-ashx?la=en>.
- [55] R.P. Morco, J.M. Joseph, D.S. Hall, C. Medri, D.W. Shoesmith, J.C. Wren, Modelling of radiolytic production of HNO<sub>3</sub> relevant to corrosion of a used fuel container in deep geologic repository environments, *Corros. Eng. Sci. Technol.* 52 (2017) 141–147, <https://doi.org/10.1080/1478422X.2017.1340227>.
- [56] ISO 25178-2: Geometrical product specifications (GPS) – Surface texture: Areal – Part 2: Terms, definitions and surface texture parameters, 2012.
- [57] W. Li, B. Yu, J. Tam, J.D. Giallonardo, D. Doyle, D. Poirier, J.G. Legoux, P. Lin, G. Palumbo, U. Erb, Microstructural characterization of copper coatings in development for application to used nuclear fuel containers, *J. Nucl. Mater.* 532 (2020), 152039, <https://doi.org/10.1016/j.jnucmat.2020.152039>.
- [58] C.H. Boyle, S.A. Meguid, Mechanical performance of integrally bonded copper coatings for the long term disposal of used nuclear fuel, *Nucl. Eng. Des.* 293 (2015) 403–412, <https://doi.org/10.1016/j.nucengdes.2015.08.011>.
- [59] B. Yu, J. Tam, W. Li, H.J. Cho, J.G. Legoux, D. Poirier, J.D. Giallonardo, U. Erb, Microstructural and bulk properties evolution of cold-sprayed copper coatings after low temperature annealing, *Materialia* 7 (2019), 100356, <https://doi.org/10.1016/j.matla.2019.100356>.
- [60] J. Turnbull, R. Szukalo, D. Zagidulin, M. Biesinger, D. Shoesmith, The kinetics of copper corrosion in nitric acid, *Mater. Corros.* 72 (2021) 348–360, <https://doi.org/10.1002/maco.202011707>.
- [61] S.-E. Bae, A.A. Gewirth, Differential reactivity of Cu(111) and Cu(100) during nitrate reduction in acid electrolyte, *Faraday Discuss.* 140 (2008) 113–123, <https://doi.org/10.1039/b814058h>.
- [62] M. Maric, O. Muránsky, I. Karatchevtseva, T. Ungár, J. Hester, A. Studer, N. Scales, G. Ribárik, S. Primig, M.R. Hill, The effect of cold-rolling on the microstructure and corrosion behaviour of 316L alloy in FLiNaK molten salt, *Corros. Sci.* 142 (2018) 133–144, <https://doi.org/10.1016/j.corsci.2018.07.006>.
- [63] U. Erb, H. Gleiter, G. Schwitzgebel, The effect of boundary structure (energy) on interfacial corrosion, *Acta Met.* 30 (1982) 1377–1380, [https://doi.org/10.1016/0001-6160\(82\)90157-2](https://doi.org/10.1016/0001-6160(82)90157-2).
- [64] M. Yamashita, T. Mimaki, S. Hashimoto, S. Miura, Effect of interfacial structure and energy on corrosion and stress-corrosion-cracking in  $\alpha$ -Cu-Al alloy bicrystals, *C1-715–C1-720, J. Phys. Colloq.* 51 (1990), <https://doi.org/10.1051/jphyscol:19901114>.
- [65] H. Miyamoto, T. Mimaki, A. Vinogradov, S. Hashimoto, Intergranular corrosion of ultrafine grain copper fabricated by ECAP, *Mater. Sci. Forum* 561–565 (2007) 2385–2388, <https://doi.org/10.4028/www.scientific.net/MSF.561-565.2385>.
- [66] J. Turnbull, R. Szukalo, D. Zagidulin, M. Behazin, D.W. Shoesmith, Electronic cigarette use among patients with cancer: characteristics of electronic cigarette users and their smoking cessation outcomes (Erratum: Borderdud SP, Lj Y, Burkhalter JE, Sheffer CE and Ostroff JS). *Cancer* 121 (2015) 800, <https://doi.org/10.1002/maco.202011707>.